Studies on Plasma-Enhanced Atomic Layer Deposition of Superconducting-Insulating-Superconducting Multilayers for Use in SRF Cavities

Dissertation

zur Erlangung des Doktorgrades
an der Fakultät für Mathematik, Informatik und Naturwisschenschaften
Fachbereich Physik

der Universität Hamburg

vorgelegt von

ISABEL GONZÁLEZ DÍAZ-PALACIO

Hamburg
2025

Eidesstattliche Versicherung / Declaration on oath

Hiermit versichere ich an Eides statt, die vorliegende Dissertationsschrift selbst verfasst und keine anderen als die angegebenen Hilfsmittel und Quellen benutzt zu haben.

I hereby declare and affirm that this doctoral dissertation is my own work and that I have not used any aids and sources other than those indicated.

If electronic resources based on generative artificial intelligence (gAI) were used in the course of writing this dissertation, I confirm that my own work was the main and value-adding contribution and that complete documentation of all resources used is available in accordance with good scientific practice. I am responsible for any erroneous or distorted content, incorrect references, violations of data protection and copyright law or plagiarism that may have been generated by the gAI.

Hamburg, den _____

_____
Unterschrift

Abstract

Superconducting-Insulating-Superconducting (SIS) multilayers offer a promising approach to surpass the accelerating gradients of standard bulk Nb superconducting radio frequency (SRF) cavities, while enabling more efficient and sustainable accelerators. This dissertation contributes to the pursuit of higher accelerating gradients and improved quality factors by tailoring SRF cavities, focusing on the synthesis and characterisation of SIS multilayers to pave the way for plasma-enhanced atomic layer deposition (PEALD)-based SRF cavities. One of the biggest challenges in developing SIS-based SRF cavities is achieving conformal and uniform coatings on the cavity shape. PEALD is the most promising technique, as it allows for conformal coating of highly structured, three-dimensional substrates without shadowing effect and with sub-nm thickness precision. Furthermore, it is a mature technology already established in industrial processes. The SIS multilayers studied consisted of AlN-NbTiN deposited on planar substrates: on Nb, representing cavity-relevant conditions, and on Si to offer insights into the intrinsic material properties. The optimisation of the SIS multilayers synthesis by PEALD was carried out by studying the superconducting properties of the NbTiN thin films. Fundamental studies were conducted using various material analysis techniques to assess the film microstructure, composition, crystal structure, and superconducting performance. The PEALD-deposited thin films were found to be smooth, which is essential for sustaining high fields in SRF cavities by minimizing field enhancements and preventing early quenching or losses. The study emphasised the interface between the superconducting and insulating films. The NbTiN composition (ratio of Nb to Ti within the ternary) was confirmed to be precisely tailored by the PEALD deposition process. The superconducting performance of NbTiN films is related to the composition and crystal structure of the film. The ratio of Nb to Ti was adjusted to 3:1 for an improved superconducting transition temperature. The PEALD-deposited NbTiN films formed the phase of interest δ-NbTiN. Post-deposition thermal procedures were found to promote crystal growth and impurities outgassing, significantly enhancing the superconducting performance of NbTiN thin films. The post-deposition annealing process was optimised, with higher annealing temperatures resulting in greater enhancements. The impact of annealing on SIS multilayers—microstructure, morphology, composition, crystal structure, and superconducting performance—was evaluated. SIS multilayers produced by PEALD met the necessary criteria for potential implementation in SRF cavities and demonstrated suitability for cavity preparation processes. Nevertheless, RF performance tests are required to assess the effectiveness of SIS coatings.

Zusammenfassung

Supraleitende-Isolierende-Supraleitende (SIS) Mehrschichtsysteme bieten einen vielversprechenden Ansatz, um die Beschleunigungsgradienten herkömmlicher supraleitender Niob-Radiofrequenz (SRF)-Kavitäten zu übertreffen und gleichzeitig effizientere und nachhaltigere Beschleuniger zu ermöglichen. Diese Dissertation trägt zur Erreichung höherer Beschleunigungsgradienten und verbesserter Qualitätsfaktoren bei, indem SRF-Kavitäten gezielt angepasst werden. Der Schwerpunkt liegt auf der Synthese und Charakterisierung von SIS-Mehrschichtsystemen, um den Weg für SRF-Kavitäten auf Basis von Plasma-unterstützter Atomlagenabscheidung (PEALD) zu ebnen. Eine der größten Herausforderungen bei der Entwicklung von SIS-basierten SRF-Kavitäten ist die Herstellung konformer und gleichmäßiger Beschichtungen auf den komplexen Kavitätenformen. PEALD ist die vielversprechendste Technik, da sie konforme Beschichtungen auf hochstrukturierten, dreidimensionalen Substraten ohne Schatteneffekte und Präzision im sub-nm-Bereich ermöglicht. Darüber hinaus ist sie eine ausgereifte Technologie, die bereits in industriellen Prozessen etabliert ist. Die untersuchten SIS-Mehrschichtsysteme bestanden aus AlN-NbTiN, die auf planaren Substraten abgeschieden wurden: auf Nb, das kavitätsrelevante Bedingungen darstellt, und auf Si, um Einblicke in die intrinsischen Materialeigenschaften zu gewinnen. Die Optimierung der Synthese von SIS-Dünne Schichten mittels PEALD wurde durch die Untersuchung der supraleitenden Eigenschaften der NbTiN-Dünnschichten durchgeführt. Fundamentale Studien wurden unter Einsatz verschiedener Materialanalysetechniken durchgeführt, um die Mikrostruktur, Zusammensetzung, Kristallstruktur und supraleitenden Eigenschaften der Schichten zu untersuchen. Es wurde festgestellt, dass die durch PEALD abgeschiedenen Dünne Schichten glatt sind, was für die Aufrechterhaltung hoher Felder in SRF-Kavitäten essenziell ist, da Feldverstärkungen minimiert und frühes Quenching oder Verluste verhindert werden. Die Untersuchung legte einen Schwerpunkt auf die Grenzfläche zwischen den supraleitenden und isolierenden Schichten. Es wurde bestätigt, dass die NbTiN-Zusammensetzung (Verhältnis von Nb zu Ti im ternären System) durch den PEALD-Prozess präzise eingestellt werden kann. Die supraleitenden Eigenschaften von NbTiN-Schichten stehen in Zusammenhang mit der Zusammensetzung und Kristallstruktur der Schichten. Das Verhältnis von Nb zu Ti wurde auf 3:1 eingestellt, um eine verbesserte supraleitende Übergangstemperatur zu erreichen. Die mittels PEALD abgeschiedenen NbTiN-Schichten bildeten die relevante Phase δ-NbTiN. Nach der Abscheidung durchgeführte thermische Verfahren förderten das Kristallwachstum und die Ausgasung von Verunreinigungen, was die supraleitenden Eigenschaften der NbTiN-Dünne Schichten signifikant verbesserte. Der Prozess der Nachbehandlungsanwärmung wurde optimiert, wobei höhere Temperaturen zu größeren Verbesserungen führten. Der Einfluss des Glühens auf die Mikrostruktur, Morphologie, Zusammensetzung, Kristallstruktur und supraleitenden Eigenschaften der SIS-Mehrschichten wurde ausgewertet. Die durch PEALD hergestellten SIS-Mehrschichten erfüllten die notwendigen Kriterien für eine potenzielle Implementierung in SRF-Kavitäten und zeigten ihre Eignung für Vorbereitungsprozesse von Kavitäten. Dennoch sind HF-Leistungstests erforderlich, um die Wirksamkeit der SIS-Film-Beschichtungen zu bewerten.

Contents

List of Figures

10

List of Tables

1. Introduction to Superconducting-Insulating-Superconducting (SIS) multilayers for superconducting radio frequency (SRF) cavities

This section aims to provide a general view of the implementation of Superconductor-Insulator-Superconductor (SIS) multilayers in the potential next-generation of tailored superconducting radio frequency (SRF) cavities. First, a brief introduction to SRF cavities and RF superconductivity is given. For a deeper understanding of superconductivity, it is recommended to refer to [1–3]. Similarly, for a detailed look into SRF cavities Padamsee et al. [4] and Gurevich [5] should be consulted. Lastly, the innovative approach with SIS multilayers and their potential impact on SRF cavities are presented.

1.1. Basics of superconductivity and superconducting radio frequency (SRF) cavities

In particle accelerators, radio frequency (RF) cavities are structures responsible for accelerating the beam. Cavities are designed to resonate the electromagnetic waves at a radio frequency. Thus, the beam sees the electric field pointing towards its travelling direction and the magnetic field parallel to the cavity surface. Cavity efficiency is crucial for reducing the cost impact on large accelerator projects. It is determined by the quality factor (Q_0), which quantifies the energy efficiency as the ratio of the energy stored in the cavity to the energy lost in the cavity wall and can be expressed as:

$$Q_0 = \frac{G}{R_s} \tag{1.1}$$

where G is a geometrical factor that accounts for the field distribution and R_s is the surface resistance as a consequence of the electromagnetic field penetrating into the cavity surface. On account of minimising surface losses, cavities progressed from normal conducting to superconducting materials. Typically superconducting radio frequency (SRF) cavities have a Q_0 of five orders of magnitude higher than the normal conducting copper cavities [4]. Additionally, SRF cavities enable higher accelerating fields. The underlying reasons are addressed next, starting with a short introduction to the crucial aspects of RF superconductivity to then cover the main aspects for the SRF cavity performance.

First, superconductors are materials which exhibit zero direct current (DC) electrical resistance below a certain temperature. This temperature, known as critical temperature (T_c), sets the transition point between the normal conducting (NC) and the superconducting (SC) states. According to the Bardeen–Cooper–Schrieffer (BCS) theory [1], in the SC state pairs of electrons named Cooper pairs are formed by the mediation of the electron-phonon interaction. Thus, two electrons are bonded in a Cooper pair described by a single

wavefunction. To break a Cooper pair, the energy transferred to it must be higher than 2Δ, where Δ is the superconducting gap. This energy threshold can be achieved by increasing temperature, magnetic field, or electrical current. Due to the collective nature of Cooper pairs, which condense into a coherent quantum state with an effective total momentum of zero, they flow in coherence and unperturbed, hence without resistance. A simple approach is given by the two-fluid model, that divides the current flow in a superconductor into normal currents carried by unpaired electrons and supercurrents carried by Cooper pairs. Thus, the total density of charge carriers (n_t) can be expressed as:

$$n_t = n_{NC} \text{ (for T>T}_c\text{) ; } n_t = n_{NC} + n_{SC} \text{ (for T<T}_c\text{) ; } n_t = n_{SC} \text{ (for T=0)} \qquad (1.2)$$

Since Cooper pairs move frictionless, the whole DC current flows with no resistance through the supercurrents, shielding the normal conducting electrons from the applied field. In addition, superconductors present the feature of expelling magnetic field. This phenomenon is known as Meissner effect. As the material enters the superconducting state, screening currents circulate at the surface of the superconductor. These currents, which are indeed the Cooper pairs, generate a magnetic field opposite to the external applied magnetic field, counteracting and cancelling it out from the superconductor. The frictionless nature of the Cooper pairs ensures the permanent expulsion of the magnetic field. Nevertheless, even if supercurrents shield the bulk material, the magnetic field can penetrate a certain distance near the superconductor surface, through which it decays exponentially following:

$$H(x) = H_0 \exp\left(\frac{-x}{\lambda_L}\right); \qquad (1.3)$$

where λ_L is the London penetration depth and corresponds to the region where supercurrents are confined and where the magnetic field decays. Therefore λ_L is related to the density of supercurrent carriers (n_{SC}) by:

$$\lambda_L{}^2 \propto \frac{1}{n_{SC}}; \qquad (1.4)$$

making evident that the larger the density of Cooper pairs the more effectively the magnetic field is expelled and its temperature dependence as pointed by Equation 1.2. However, if a strong enough magnetic field is applied the screening effect is overcome and the field penetrates into the superconductor. The way this occurs determines the two types of superconductors: type I and type II superconductors. This is dictated by the Ginzburg-Landau (GL) parameter κ_{GL}:

$$\kappa_{GL} = \frac{\lambda_{GL}}{\xi_{GL}}$$

$$\text{type I: } \kappa_{GL} < \frac{1}{\sqrt{2}} \text{ ; } \xi_{GL} > \lambda_{GL} \qquad (1.5)$$

$$\text{type II: } \kappa_{GL} \geq \frac{1}{\sqrt{2}} \text{ ; } \xi_{GL} < \lambda_{GL};$$

where λ_{GL} is the GL penetration depth, which has the same meaning as the λ_L but takes into consideration the presence of defects, and ξ_{GL} is the GL coherence length which is defined as the distance over which the superconducting order parameter varies significantly. The distinction between type I and type II superconductors is that they behave differently

in their transition from the SC to the NC state under applied magnetic field. A visual representation is presented in Figure 1.1. On one hand, type I superconductors shift from the Meissner state to the NC state with a single phase transition upon a critical magnetic field (H_c), which is temperature dependent. This implies that the superconducting transition takes place at $T = T_c$ in the absence of magnetic field; while in the presence of magnetic field the transition would take place at $T < T_c$. On the other hand, type II superconductors, likewise temperature dependent, transit three different states: Meissner state, mixed state known as Schubnikov phase, and NC state. Therefore, type II superconductors present two critical fields: the lower critical field (H_{c1}) and the upper critical field (H_{c2}). The mixed state is delimited by $H_{c1} < H < H_{c2}$ and indicates the field range which is energetically favourable to the entry of quantified magnetic field flux while maintaining superconductivity in the rest of the regions. Each enter magnetic flux is named vortex and consists of a normal conducting core surrounded by superconducting currents that keep the rest of the material superconducting. Further, each vortex carries the quantified minimum field possible, thus the density of vortices increases with the applied magnetic field until it reaches H_{c2} and becomes energetically favourable for the material transition to its NC state. However, it is possible to maintain the Meissner state above H_{c1}, delaying the onset of vortex nucleation upon the metastable thermodynamic limit characterised by the superheating field (H_{sh}), where $H_{c1} < H_{sh} < H_{c2}$. The H_{sh} is explained by an energy barrier at the superconductor surface, known as Bean-Livingstone surface barrier, which vortices must overcome to penetrate the superconductor.

Although DC accelerators are feasible their accelerating energy is limited ~ 100 MeV [6] by the voltage breakdown, triggered by steady strong electric fields. Consequently, alternating current (AC) is used in cavities. However, unlike for DC, AC fields prevent the superconductor resistance to drop to zero. The reason for this is that while in DC all current is carried by Cooper pairs and the unpaired electrons are shielded from the applied field, in AC both paired and unpaired electrons carry current. This is because by applying an alternating field Cooper pairs are forced to constantly change their direction. In consequence, they are accelerated and decelerated within every cycle of the oscillating field. And although Cooper pairs move frictionless. However, they have higher inertia than
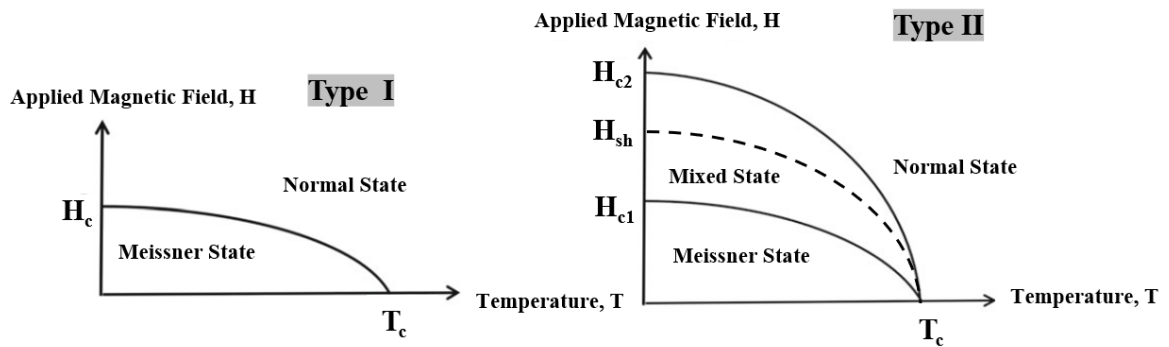
Figure 1.1: Applied magnetic field versus temperature for type I and type II superconductors. Image adapted from [7].

unpaired electrons thus, Cooper pairs take more time and energy to swap their direction. Unpaired electrons, which react faster to the change of direction of the AC field, see the electric fields leading to dissipation. The power dissipation is proportional to the frequency squared, resulting from the applied and induced fields. The BCS theory describes this power dissipation as:

$$R_{BCS} = A(\sqrt{\rho_{nc}}, \lambda_L{}^4, \xi_0, l) \frac{\omega^2}{T} \exp\left(\frac{-\Delta(T)}{\kappa T}\right) \tag{1.6}$$

where A is a constant which depends on intrinsic characteristics of the material: resistivity in the normal state (ρ_{nc}), London penetration depth (λ_L), Pippard coherence length of Cooper pairs (ξ_0), and the electron mean free path (l); ω is the RF frequency and Δ the superconducting gap. The exponential factor describes the probability of some Cooper pairs splitting by thermal excitation. This equation is valid at low temperatures $T < T_c/2$ where $\Delta(0) \approx \Delta(T)$. According to the BCS theory at $T = 0K$ all charge carriers condense into Cooper pairs; therefore the measured RF surface resistance of a cavity should tend to zero at low temperatures, since it follows R_{BCS}. However, experiments show a different behaviour as is shown in Figure 1.2. Thus, the surface resistance is the sum of the BCS resistance and a residual term thermal independent:

$$R_s = R_{BCS}(T) + R_{res}(\cancel{T}). \tag{1.7}$$
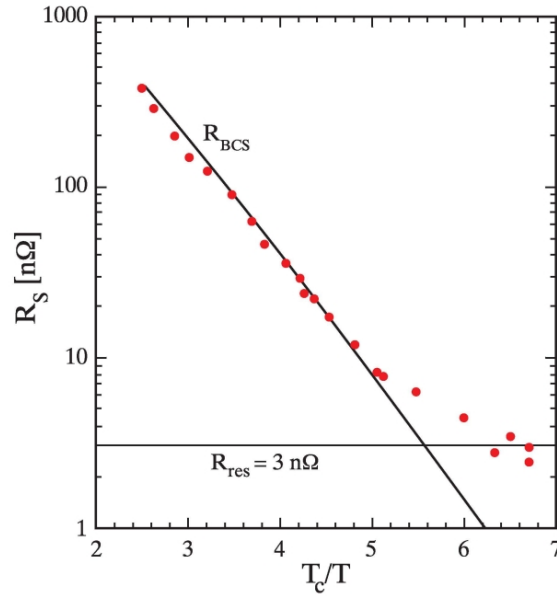
Figure 1.2: Measured RF surface resistance in a 9-cell SRF Nb cavity at DESY [8].

The residual resistance however is not fully understood although it is presumed to be field dependent and a sum of various factors [4]. In some cases its source can be unrelated to the superconducting surface, e.g. excessive losses in a coupler [4]. Although the most relevant and discussed here are surface-related sources e.g., trapped flux. In an ideal situation, when

a superconductor is cooled down in the presence of an external magnetic field (lower than H_{c1}), the flux lines will be expelled once $T < T_c$. However, real superconductors present lattice defects—interstitials, dislocations, and grain boundaries—and other inhomogeneities that act as pinning centres that trap magnetic flux or cause early entry [9]. The trapped and the early entry of flux vortices remain normal conducting in the Meissner region and result in dissipation under the RF field:

$$R_{flux}(\omega) = \frac{H_{ext}}{2H_{c2}}R_{NC}. \qquad (1.8)$$

It was observed that SRF cavities trap all the field present during its cool down [4]. Hence, it is crucial to minimise flux vortices by: shielding earth's or any other magnetic field, reducing the sensitivity to trapped magnetic flux affected by the cool down procedure—cool down velocity and the spatial temperature gradient [10]— and the pinning centres. Nevertheless, the pinning behaviour of crystalline defects and their role on RF dissipation is complex and will not be discussed in detail here. Antoine [9] is recommended for a more comprehensive understanding.

Concretely, SRF cavities are made of niobium (Nb) because of its good superconducting properties—among the pure metals, Nb presents the highest lower critical field (H_{c1}) and T_c. In addition, Nb has a high thermal conductivity necessary to dissipate RF loses. Besides, its mechanical and chemical properties make cavity manufacturing and treatments feasible. The shape and size of the cavity would depend on the type of particles to be accelerated and their velocity. For high accelerating gradients, as is the case for the European XFEL at DESY ($E_{acc} = 23.6$ MV/m and $Q_0 \geq 10^{10}$ [11]), the SRF cavities are 9-cell TESLA shape and operate at 1.3 GHz and 2 K. A visual representation is given in Figure 1.3. Although for R&D 1-cell TESLA cavities are employed.

Figure 1.3: SRF 1.3 GHz 9-cell TESLA cavity made of Nb. Image taken from [12].

1.2. Limitations of Nb SRF cavities

The performance of a cavity is often given by its Q_0 vs E_{acc} curve; where E_{acc} is the accelerating gradient that represents the energy gained by the beam along the cavity length. Exemplary Q_0 vs E_{acc} curves for different cavity treatments are presented in Figure 1.4.
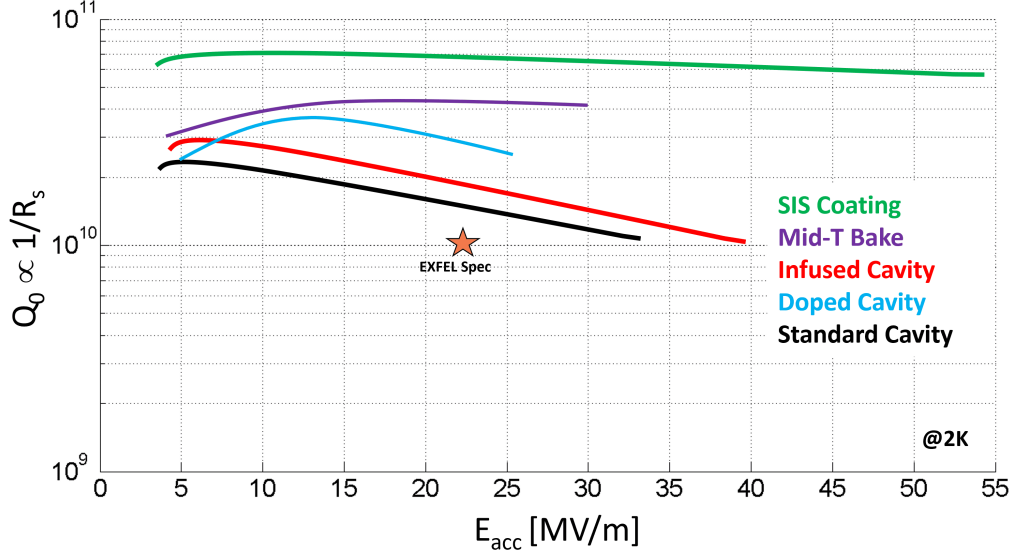
Figure 1.4: Comparison between SRF Nb cavity performance for different surface treatments: Standard [13], doped [14], infused [15], mid-T baked [16], and predicted SIS coated [17] cavities. The start represents the European XFEL specifications [18]. Courtesy of Marc Wenskat.

On one hand, the limit for E_{acc} is set by the magnetic field on the cavity surface. For a TESLA cavity the relation is given by $H_{peak}/E_{acc} = 4.26\,\mathrm{mT\,MV^{-1}\,m^{-1}}$ [19]. Therefore, for Nb with $H_{sh} = 228$ mT the maximum accelerating gradient possible would be $E_{acc} \approx 55\,\mathrm{MV\,m^{-1}}$. However, reaching such a limit is not viable. The superheating field is based on the premise of defect-free superconductors. But in reality, defects affect the supercurrents and hence the surface barrier, fostering vortex nucleation [6]. Moreover, the time necessary for vortex nucleation in the presence of defects is $1 \times 10^{-13}\,\mathrm{s}$, smaller than the RF period [6]. Thus, Nb SRF cavities are limited to values lower than $55\,\mathrm{MV\,m^{-1}}$. Therefore, to achieve higher accelerating gradients new routes must be explored.

On the other hand, the Q_0 is set by the RF surface dissipation, sum of R_{BCS} and R_{res} (Equation 1.7). Hence, minimising both resistances is crucial, although, at the operating temperature (2 K), losses are dominated by the R_{res}. The approach to minimise R_{res} is already mentioned in the section above. Conversely, the R_{BCS} depends among other factors (see Equation 1.6) on the electron mean free path, l. For a dirty superconductor ($l \ll \xi$), R_{Bcs} decreases with increasing l, reaching a minimum value at $l \sim \xi_0/2$ [20]. Beyond this point, a further increase in l rises R_{BCS}, saturating as the clean limit ($l \gg \xi$) is approached. For Nb cavities R_{BCS} has its limit at $l \sim 10$ nm, which corresponds to a residual resistance ratio (RRR) of ~ 4; while the Nb used for SRF cavities has RRR $= 300$ [21]. Therefore, the R_{BCS}, and in turn the Q_0, can be adjusted by impurity management. Hence the crucial role of the Nb surface and, in consequence, the importance of cavity surface treatments that modify the structural and chemical composition of the surface (see Figures 1.4 and 1.5). Various Nb oxides—Nb_2O_5, NbO_2, and NbO— form the native surface layer whose thickness varies with material characteristics and oxidation conditions [22]. For Nb SRF
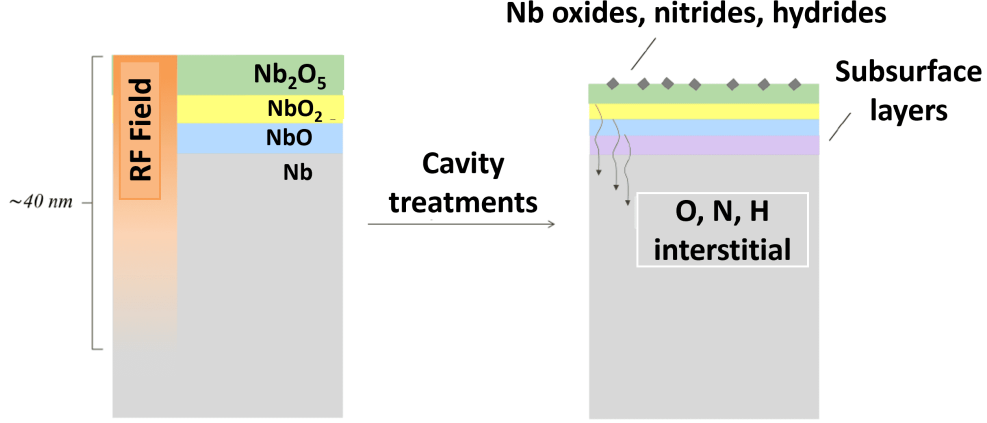
Figure 1.5: Schematic view of the RF surface: Nb native oxides and their prospective change with cavity treatments. The $\lambda_L^{Nb} \sim 40\,$nm; however, the RF field penetrates up to 100-200 nm. Sketch source: [23].

cavities, native oxides are $\sim 5\,$nm thick. However, the RF field penetrates the first 100-200 nm into the Nb surface. Hence, interstitials are also relevant for the cavity performance.

Several decades of research efforts have pushed Nb SRF technology near the limit of its capabilities, achieving an exceptional operating performance with Q_0 of 10^{10} and E_{acc} up to $40\,$MV$\,$m^{-1}. However, to further increase the accelerating gradient is necessary to break the Nb monopoly and pursue new strategies for SRF cavities.

1.3. Next-generation tailored SRF cavities

On account of RF superconductivity being a surface phenomenon, the proposal for the next generation of SRF cavities is to replace the bulk Nb with new tailored-designed cavities. These new cavities would merge a bulk material—serving as a support structure and heat dissipater—with various thin films addressing each of the specific requirements for SRF cavities. Thus, one could decouple the SRF surface from the support structure. A schematic view of the next-generation SRF cavity concept is presented in Figure 1.6. This new approach for SRF cavities would allow using as bulk materials with higher thermal conductivity, e.g. Cu, what could reduce significantly the cooling operational costs. An example of this are the Nb/Cu cavities, which are already implemented by CERN [24]. Among the various proposed layers for the next-generation of tailored SRF cavities, this thesis focuses on the R&D of the Superconducting-Insulating-Superconducting (SIS) multilayers.
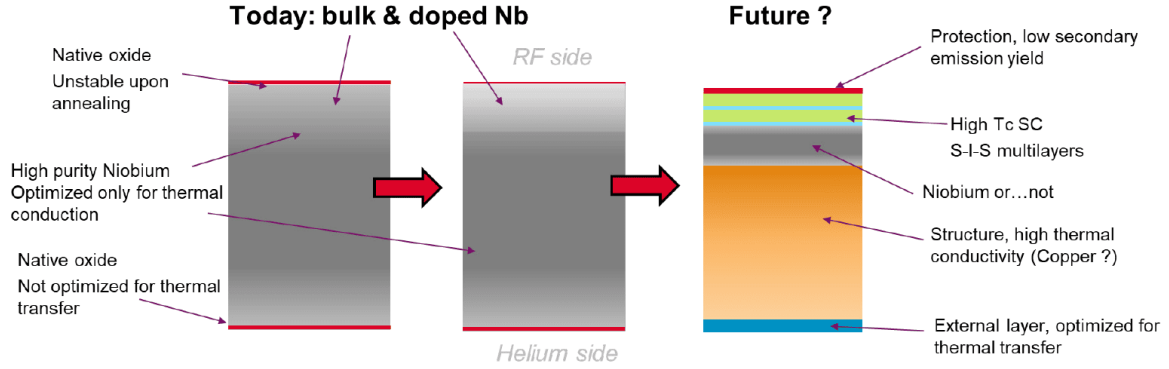
Figure 1.6: Comparison between the present SRF cavities and their potential path toward more efficient and with higher gradients SRF cavities. Sketch source: [25]

1.3.1. Superconductor-Insulator-Superconductor (SIS) structures

The approach of further improving SRF Nb cavities by tailoring the inner RF surface by coating Superconducting-Insulating-Superconducting (SIS) multilayers was proposed by Gurevich [17]. This idea can be understood as building on a shielding structure which enables to operate accelerating gradients greater than those tolerated by the Nb cavity and, moreover, significantly increases the quality factor. Specifically, it was predicted to achieve through SIS multilayers Q_0 of two orders of magnitude higher and double the accelerating gradients compared with bulk Nb cavities [26] (see Figure 1.4). In addition, the cryogenic costs could significantly decrease, as SIS SRF cavities would potentially raise the operating temperature to $4.2\,\mathrm{K}$. The following details this new concept that can be visualised in Figure 1.7.
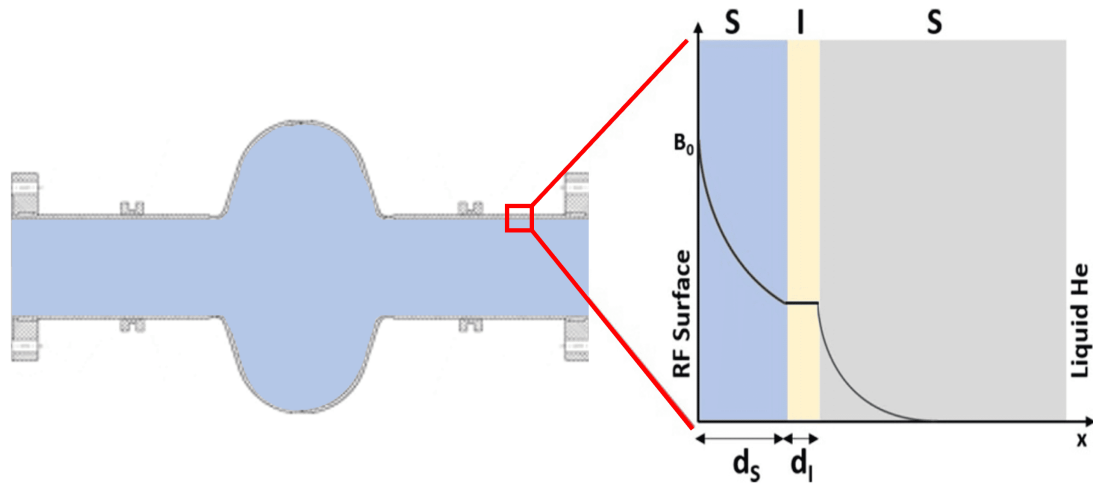
Figure 1.7: Schematic view of the SIS multilayer concept. It represents the SIS deposited on the inner surface of a 1.3 GHz Nb cavity and the field decay through the multilayers. Illustration adapted from [27].

On one hand, the top superconducting S-layer is chosen to benefit of a lower R_{BCS}. As indicated by Equation 1.6, this would be the case for superconductors with larger Δ, and thus high T_c, and low ρ_{nc} at low temperatures. Moreover, it has been empirically found that the $R_{res} \propto \sqrt{\rho_{nc}}$ [26]. Therefore one would expect the S-layer to exhibit also lower R_{res}. Although the latter cannot be generalised as many other factors play a role in the residual resistance. Conversely, superconductors with high T_c usually exhibit the disadvantage of larger λ and therefore lower H_{c1}, limiting the accelerating gradient. However, a thin film superconductor exhibits higher H_{c1} than its bulk form, as long as d $< \lambda$, where d is the film thickness. This is because the magnetic field penetrates easier in a thin film; thus, vortices are energetically unfavourable. For them to form the magnetic field must be stronger, hence the H_{c1} enhancement, which is given by [17, 28]:

$$H_{c1}^* = \frac{2\phi_0}{\pi d^2} \ln\left(\frac{d}{1.07\xi}\right) \tag{1.9}$$

where ϕ_0 is the magnetic flux quantum. This lower critical magnetic field enhancement, owing to the thin-film S-layer, would enable higher accelerating gradients. Further, the RF magnetic field penetrates the superconductor surface and decays exponentially through the S-layer. Hence, upon reaching the Nb interface the field has been attenuated down to a value that the bulk Nb can withstand without forming vortices. This way, through SIS multilayers, the bulk cavity is kept in the Meissner state at accelerating gradients greater than Nb can tolerate.

On the other hand, the insulating I-layer plays two important roles. First, it protects from vortex avalanche. By intercepting the vortices propagation, the I-layer confines dissipation to the S-layer. And second, it must exclude Josephson tunnelling and ensure that the superconductors behave independently.

The shielding effect of the SIS multilayer structure would enhance with the number of SI layers, according to:

$$H_{Nb} = H_0 \exp\left(\frac{-Nd_S}{\lambda}\right) \tag{1.10}$$

where N is the number of SI layers, d_S the S-layers thickness, and H_{Nb} the magnetic field strength at the Nb interface. The number of SI layers must be chosen to find a compromise between reducing vortex dissipation and dissipation caused by the suppression of superconductivity at the interfaces [26]. Further, there is an optimal thickness for the SI layers. The S-layer must balance being thin enough to enhance H_{c1}, but thick enough to still effectively shield the underlying bulk Nb. While the I-layer should be thick enough to avoid Josephson junction while limiting the handicap of low thermal conductivity. The achievable accelerating gradient by the SIS multilayers would be limited by the superheating field. For a multilayer structure consisting of a single S-layer and I-layer, vortex-penetration field, $H_{vp}^{ML}(d_S, \lambda_S, \xi_S, d_I, \lambda_{Nb})$, depends on the S-layer material and thickness, I-layer thickness, and material of the bulk superconductor [29] (Figure 1.8 top). Nevertheless, this field can be exceed, allowing vortices to form in the S-layer, as long as the field reaching the Nb interface is below the threshold that would cause vortex penetration [29]. The magnetic field limit has been recalculated considering the effect of surface defects by the suppression factor η [30] (see Figure 1.8 bottom). Figure 1.8 presents a visualisation of the optimal thicknesses

and the magnetic field limit provided calculated for a NbN-I-Nb multilayer structure. The latest model covers the thickness dependence of the thermodynamic critical field and the penetration depth [31]. However, so far the theoretical models do not take into account the I-layer dielectric losses or any perpendicular component of the magnetic field [26].

For a superconducting material to be a good candidate for SIS multilayers for SRF cavities it must fulfil the following [26]: higher T_c than Nb; low ρ_{nc} (at low temperatures); high
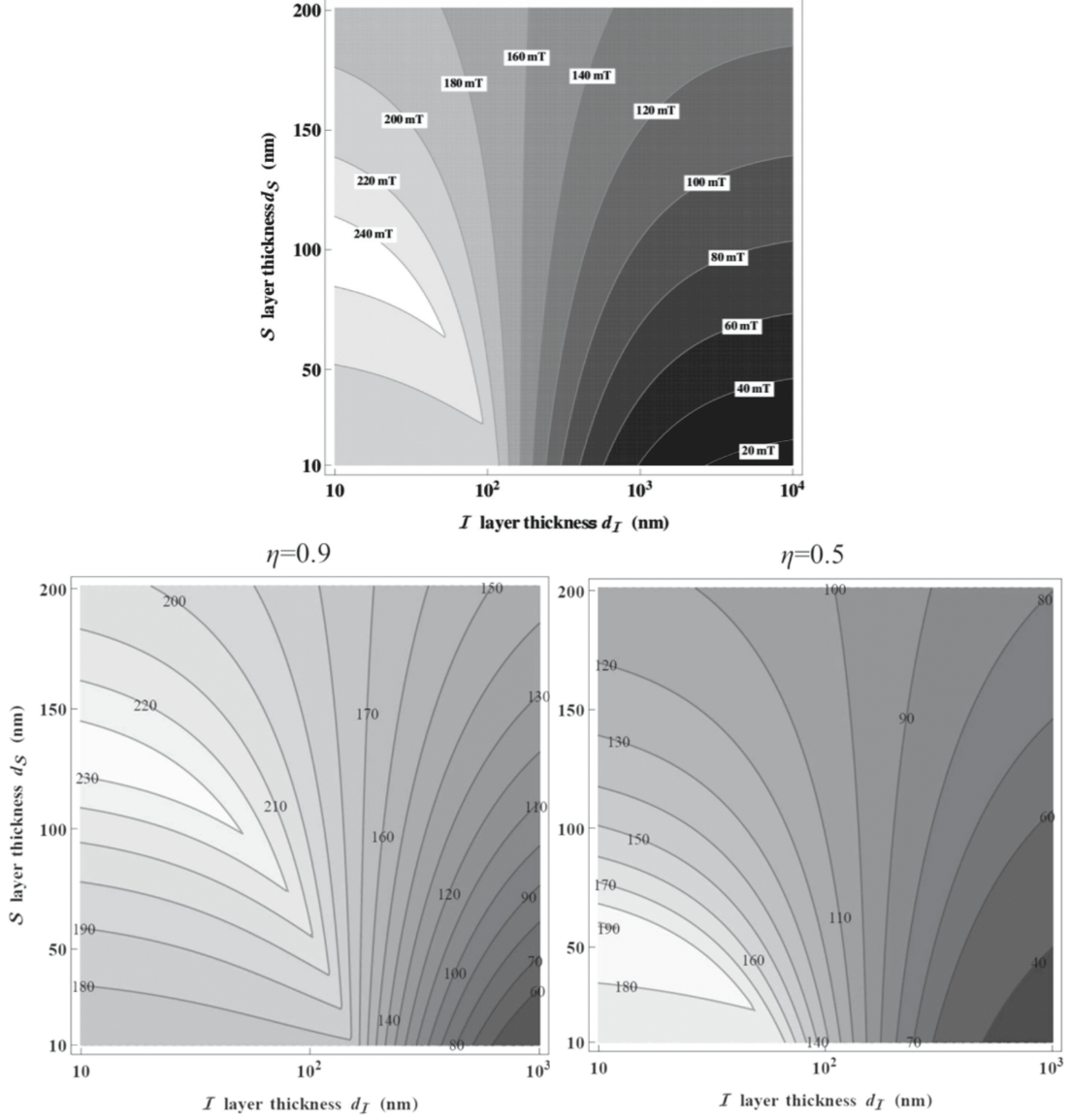
Figure 1.8: Magnetic field limit dependence on S- and I-layer thickness in SIS multilayers. The calculations correspond to a NbN-I-Nb: NbN ($\lambda = 200$ nm and $\xi = 5$ nm) and Nb ($\lambda = 40$ nm and $H_c = 200$ mT). Top graph: achievable peak surface-field without vortex dissipations [29]. Bottom graphs: achievable peak surface-field accounting for field attenuation in the S-layer and defects effects including a suppression factor η [30].

critical fields, H_{c1} and H_{c2} (this is achieved with $d < \lambda$); absence of nodes in its gap symmetry; not sensitive to radiation damage; and low secondary electron emission coefficient. Considering these requirements, the most commonly considered superconductors for the S-layer would be: Nb_3Sn, MgB_2, NbN, and NbTiN. However, among these superconductors the most favourable is NbTiN. Conversely, the others are discarded due to diverse reasons. On one side, Nb_3Sn is an A15 compound, and so it presents a peak in the density of states near the Fermi energy that makes Nb_3Sn very sensitive to crystalline disorder and radiation damage [32]. Further, Nb_3Sn is brittle, which demands novel tuning methods for cavity operation [33]. For MgB_2 the disadvantage is its band structure, consisting of two gaps. The developed SIS theory does not consider this aspect, so it is still unknown if such a type of superconductors can be favourable or not. Moreover, MgB_2 film properties degrade with exposure to moisture [33], what would be incompatible with the standard cavity cleaning procedures. Lastly, NbN weakness is that it presents much higher ρ_{nc} than NbTiN. In addition to its RF features, NbTiN presents further beneficial characteristics such as hardness, high melting point, thermal stability, and resistance to corrosion and oxidation [34]. The most considered materials for the I-layer are: Al_2O_3, AlN, Ta_2O_5, and MgO. Among them, the selected one is AlN. First, AlN is beneficial for the S-layer. It has been shown that AlN as a buffer layer promotes higher T_c values for NbN and NbTiN [35]. And further, it can act as oxygen diffusion barrier preventing oxygen diffusion from the native oxide into the S-layer, what can potentially degrade the superconducting properties of NbTiN. But also, AlN is favourable owing to its own features, such as high-temperature stability, hardness and high thermal conductivity [36].

Additionally, SIS multilayers present further requirements that may entail technological challenges. The deposited thin films must exhibit high-quality, good homogeneity, high density, and reduced surface and interface roughness for thicknesses on the order of few tens to hundred nanometers. Further, it is also required to have a fine thickness control while being able of uniformly coat the RF cavity surface. In particular, the latter represents a challenge for line-of-sight deposition techniques. Among the existing deposition techniques, atomic layer deposition (ALD) stands as the most promising choice. ALD is based on a sequence of self-limiting gas-solid surface reactions, that allows for a conformal and smooth deposition. Thus, ALD is capable of coating highly structured, three-dimensional substrates without shadowing effect and with sub-nanometer thickness resolution. Furthermore, because of its sequential working principle, it enables the deposition of alternating layers. All this together renders ALD particularly promising for depositing SIS multilayers on the internal surface of SRF cavities. A preliminary demonstration of the ALD potential, has been given by the successful deposition of Al_2O_3 on a 1.3 GHz single-cell TESLA cavity by thermal ALD [27]. Additionally, ALD is a mature technology already established in industrial processes, e.g. semiconductor and microelectronic industries.

This thesis focuses on mastering the deposition of SIS multilayers using plasma-enhanced ALD (PEALD) and investigating their properties, primarily those of the NbTiN S-layer, as it is the most relevant for SRF applications. The ultimate goal of this research—beyond this thesis—is to scale up SIS multilayers from samples to SRF cavities for RF testing.

2. Plasma-enhanced atomic layer deposition (PEALD) for SRF cavities

This section aims to provide a general knowledge of plasma-enhanced atomic layer deposition (PEALD), covering its fundamentals, capabilities, and suitability for SIS SRF cavities integration.

2.1. Introduction to atomic layer deposition (ALD)

The origin of atomic layer deposition (ALD) dates back to the 1960's-1970's, under the name of atomic layer epitaxy (ALE) [37] and molecular layering (ML) [38]. ALD emerged as a technology for crystalline films for electroluminescent displays. However, its most significant breakthrough was driven by the semiconductor industry during the 1990's. Until then, ALE was the most popular term to reference this technique. However, due to the amorphous and polycrystalline nature of the deposited films, this term became obsolete and was replaced by ALD. Nowadays, the term ALE corresponds to the abbreviation for atomic layer etching.

With the demand for smaller devices requiring conformal coatings and thickness control, ALD has gained increasing popularity. Nowadays, it is used in many applications, e.g., energy storage, sensor fabrication, biocompatible coatings, and nanoscale devices; while it has been implemented in industrial production lines such as semiconductors and solar cells. The interest in ALD continues to grow, driven, among other factors, by its conformality and uniformity in highly structured geometries. Among the vapour phase deposition techniques—physical vapour deposition (PVD), chemical vapour deposition (CVD), and ALD—what sets PVD and CVD apart from ALD is that they are flux-controlled processes, leading to challenges in obtaining controlled, uniform, and conformal coatings. Conversely, ALD is a surface-controlled process, governed by the self-limiting chemical reactions between volatile precursors and the substrate surface, allowing for conformal and uniform coatings even on complex or large-area substrates. ALD growth rate does not depend on the flux, although the flux determines how fast the saturation is reached. Thus, ALD ensures precise film growth [39]. All this is summed up in Figure 2.1, which contrasts ALD advantages with the limitations in uniformity, conformality and thickness control presented by line-of-sight deposition techniques such as PVD and CVD. Hence, ALD, being a non-line-of-sight deposition technique, not only presents a promising approach for next-generation of SRF cavities, based on tailored thin films, but also proves its maturity as a technology suitable for industrial application, as demonstrated in other industries when ALD developed from a niche technology to an establish method to finally its industrial application.
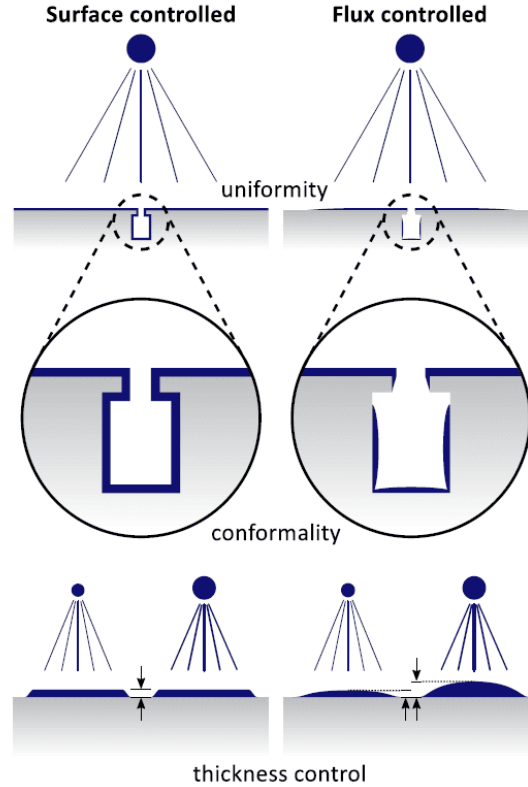
Figure 2.1: Surface controlled vs flux controlled processes and their effect on uniformity, conformality, and thickness control in a three-dimensional substrate. Sketch source: [40].

2.1.1. Fundamental principle of ALD

The deposition technique ALD relies on a sequential process of alternating, separated and self-limiting gas-solid reactions. The gases, referred to as precursors, are volatile molecules containing the element required for the desired thin film, generally at a central position surrounded by ligands. The solids are the reactive sites available on the substrate surface. Therefore, precursors must react only with surface groups, avoiding reactions with themselves, by-products, adsorbed species, or other precursors. Thus, precursor doses must be separated by a purge and/or pump step. Additionally, after the reaction of the first precursor, the new reactive surface groups must allow the next precursor to react. Moreover, for ALD, the surface reactions must be self-limiting. This means that reactions occur as long as the reactive sites are present or available for the precursor molecules. And it naturally stops when the reactive sites are already saturated. This prevents further precursor-surface reactions, despite any excess of precursor. As a result, ALD produces films that are extremely conformal and uniform in thickness, insofar as sufficient precursor flux reaches the surface sites.

Details of an ALD cycle

An ALD cycle is sketched at Figure 2.2 and made up of the following steps:
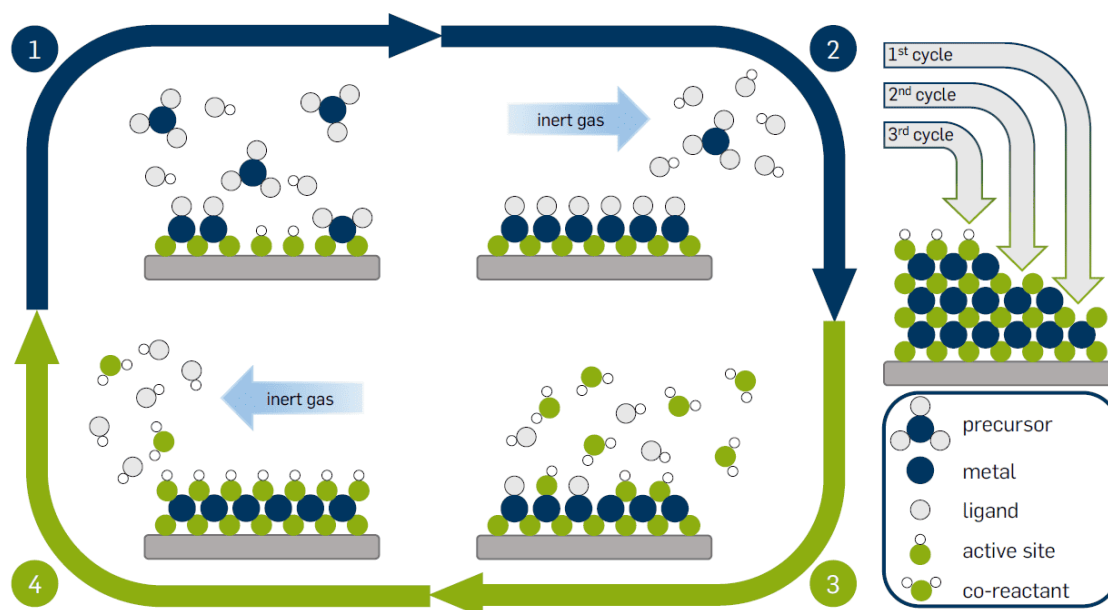
Figure 2.2: Schematic view of an ALD cycle. Sketch source: [41].

1. **Precursor dose:** initial precursor is pulsed into the reaction chamber—kept at the desired temperature for the complete process. The precursor chemically reacts with the substrate surface in a self-limiting manner. Once saturation occurs, no additional precursor is adsorbed, as all surface reactive sites are occupied. As a result, the atoms adsorbed onto the surface give rise to newly formed surface groups that must enable the next precursor to react.

2. **Purging:** deposition chamber is purged with inert gas and/or pumped out to remove all unreacted precursor and any by-products before the next precursor dose. This step has to be long enough to remove all the molecules but without exceeding the limit when the adsorbed material may start to desorb from the surface.

3. **Second precursor or co-reactant dose:** second precursor, often called co-reactant, undergoes self-limiting chemisorption with the previously adsorbed atoms, forming a monolayer of the desired material on the substrate and releasing by-products.

4. **Purging:** The chamber is once again evacuated, and a new cycle can be started as the first precursor can react with the surface groups on the deposited layer.

An ALD cycle produces a monolayer of the desired material and the total deposited thickness is controlled by the number of times the cycle is repeated. However, in ALD, the layer deposited with each precursor dose is not yet a monolayer of the final material. With each dose, only fragments of the precursor adsorb onto the surface; a complete monolayer of the target material forms only after the cycle is completed. To avoid confusion, it is more accurate to say that an ALD cycle produces an atomic layer of the target material.
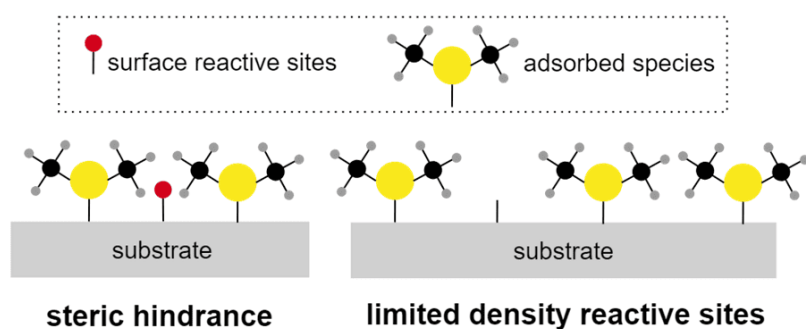
Figure 2.3: Schematich illustration of the two factors which determine chemisorption self-saturation: steric hindrance and limited density of reactive sites. Left: there is a physical obstruction of the reactive site which impedes the reaction with the precursor molecules. Right: there is a lack of reactive sites which prevent the precursor molecules to react and being chemisorbed. This is an adapted image from [42].

On another note, although an ALD cycle is intended to form a complete atomic layer, this is not always achieved in practice, particularly during the initial cycles. Factors such as steric hindrance, which blocks reactive sites and limits interactions with precursor molecules, as well as the limited density of reactive groups, can affect monolayer formation (see Figure 2.3). Note that this does not affect the ability to grow closed and dense films [39].

The thickness deposited onto the surface after a cycle is called growth per cycle (GPC). The GPC is constant as long as the gas-surface reactions are irreversible and self-limited. To this effect process parameters should be optimised. On one hand, the cycle steps above enumerated are adjusted over time. This is sketched in Figure 2.4. It is crucial to guarantee surface saturation in the case of the precursor dose and to avoid CVD within the purging step. Also, the cycle steps should not exceed the irreversibility threshold at which the adsorbed species desorb from the surface. On the other hand, temperature influences the surface reactions, and therefore the GPC, based on the number and type of reactive sites and the type of reaction mechanisms taking place [43]. This relationship is depicted in Figure 2.5. Thus, it is fundamental to operate in a temperature range that ensures self-saturating
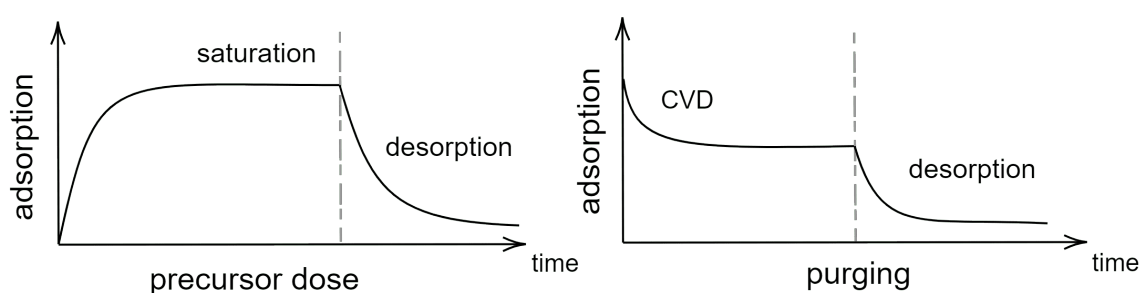
Figure 2.4: Cycle steps optimisation to guarantee ALD deposition. For the precursor dose three different scenarios: insufficient time turns into undersaturation; optimized time leads to saturation; and overtime gives rise to desorption. In the same way, for the purging step: insufficient time results in CVD deposition, while overtime results in desorption.

27
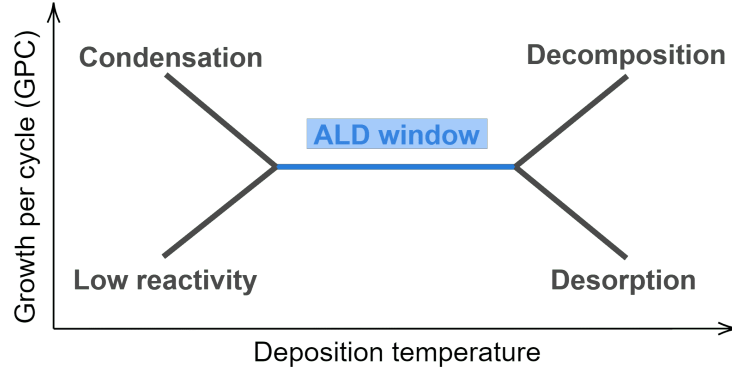
Figure 2.5: GPC as a function of temperature. ALD growth is ensured by the temperature range, i.e., the ALD window, which preserves the self-saturation. Often, within the ALD window, the GPC is constant but this is not necessarily always the case [44].

reactions. This temperature range is often referred to as ALD window. In contrast, outside the ALD window, the GPC may increase or decrease based on the dominant phenomena. At higher temperatures, precursor decomposition may induce CVD growth, increasing the GPC, or cause desorption of the film or adsorbed species, lowering the GPC. Similarly, at lower temperatures, precursors may condense and physisorb on the surface, increasing GPC, or insufficient thermal energy reduces precursor-surface reactions and thus decreases the GPC. For this last scenario, plasma-enhanced atomic layer deposition (PEALD) becomes particularly relevant, providing an alternative approach to address the low-reactivity problem.

2.2. Plasma-enhanced atomic layer deposition (PEALD)

Plasma-enhanced ALD (PEALD), also known as plasma-assisted ALD or radical-enhanced ALD, is a variation of the classical thermal ALD process, where plasma is used as a co-reactant during one of the dosing steps during the ALD cycle. An illustration of the PEALD cycle is given in Figure 2.6. While PEALD may offer advantages over thermal ALD processes, it also introduces additional complexity. For this reason, it may be employed only when the benefits exceed the challenges.
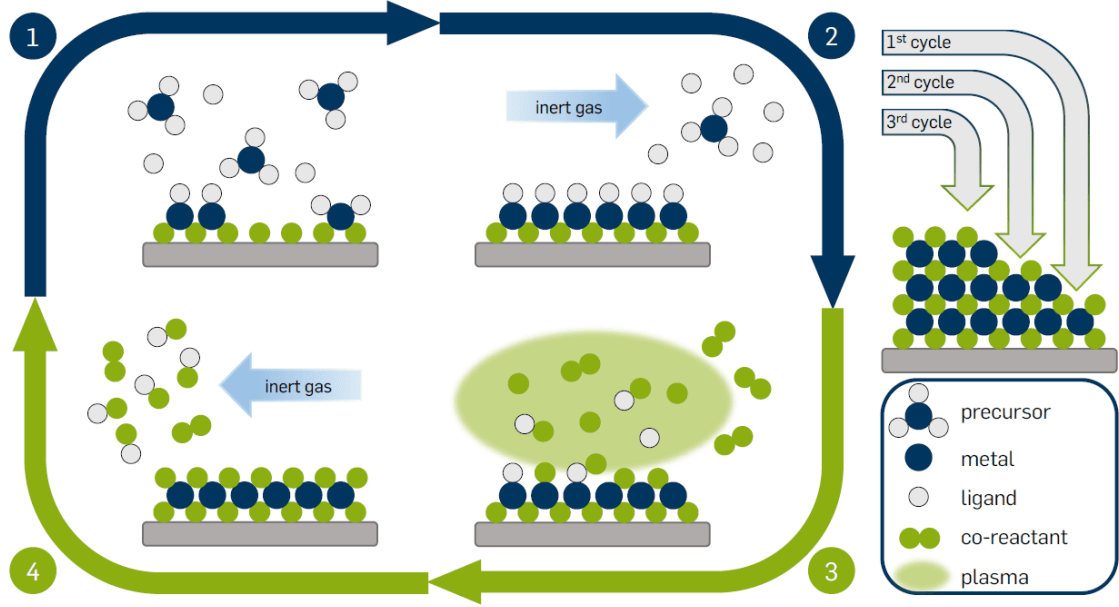
Figure 2.6: Schematic view of a PEALD cycle. Sketch source: [41].

2.2.1. Fundamentals of PEALD: role of plasma species, merits, and limitations

The plasma is a gas with free charged particles—electrons and positive ions—along with neutral excited and reactive atoms, molecules or fractions of molecules, known as radicals. At the macroscopic scale (beyond 1 mm) it stays quasi-neutral. The way plasma takes part in the ALD process is the following. On one hand, the reactive radicals contribute to surface chemical reactions. On the other hand, ions strike the surface and can lead to material modifications. Therefore, PEALD represents an energy-enhanced ALD process, resulting in higher-quality films [45].

To enable these interactions effectively, PEALD operates in non-equilibrium conditions or, in other words, PEALD uses cold plasma. This means that the electrons temperature is way higher than the gas temperature; which is achieved by keeping a low plasma pressure. The aim is to use electrical fields to heat the electrons enough to dissociate, ionize, and excite the gas while keeping the gas at a low temperature to prevent substrate heating. In this way, PEALD offers considerably greater reactivity than thermal ALD. Thus, PEALD enables reduced deposition temperatures and expands the options for precursors, deposited materials, and substrates. Meanwhile, PEALD may benefit from the ions-surface interaction by enhancing atomic ordering and facilitating impurity removal. Additionally, plasma cleaning becomes an option with PEALD as well. Overall, PEALD offers greater versatility than thermal ALD. However, it also presents certain disadvantages that must be considered: plasma-induced damage, limited conformality, and additional complexity. These challenges are addressed next.

Understanding the risk of plasma-induced damage requires insight into the role of ions in PEALD processes. Initially, ions in the plasma are at low temperatures. As they approach the substrate, the potential difference in the plasma sheath accelerates them towards the

29

surface. As a result, the ions become energetic and directional upon striking the substrate. In Figure 2.7 it is represented the formation and the influence of the plasma sheath. Note that the plasma sheath is not affected by microscopic features on the substrate. Therefore, the accelerated ions hit mostly the horizontal surfaces—top and bottom of the trenches—and less the lateral sides. This is important, as it may affect the film deposition. However, since surface reactions—and thus deposition—are driven by radicals, the shape of the plasma sheath generally does not impact conformality, although it can influence material properties.
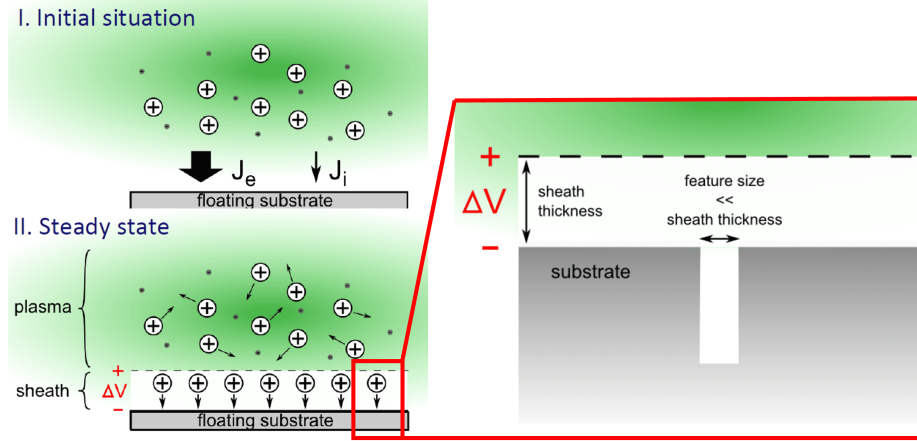
Figure 2.7: The illustration represents the formation and the influence of the plasma sheath. Electrons, with higher velocity than ions, reach the substrate faster, establishing a potential difference known as plasma sheath. With a thickness $d_{sheath} \sim 1$ mm, the plasma sheath remains unaffected by microscopic features on the substrate. Sketch source: [44] (modified version).

An overview of the influence of ions in relation to their energy is given by Figure 2.8. In PEALD, the ion energy can be reduced—by increasing the plasma pressure—or increased—by substrate biasing [46, 47]. Without biasing, the ions energy is on the order of 10^1 eV—too low for implantation/sputtering, high enough for desorption/adatom migration (See Figure 2.8). Thus, low energy ions may cause densification and improved crystallinity [48]. Further, electrons accelerated by substrate biasing have greater influence on the deposited films—the energy range of 25-75 eV might be the most interesting [44]. An example of this is given by Faraz et al. [47] that reported improved TiN film properties with increasing the bias voltage. In particular, the TiN film conductivity improves with ion-driven oxygen removal [44]. Therefore, as illustrated in Figure 2.9 C2, moderate ion energies can be beneficial, enhancing the atomic ordering and contributing to impurities removal [47, 48]. However, when ions are too energetic (Figure 2.9 C3) can lead to implantation or sputtering. The more energetic the ions or the higher their flux, the stronger their influence. This would depend on the plasma system and the process conditions. Therefore, the ion energy dose, i.e., plasma time × ion flux × mean ion energy [49], may be used to universally quantify the influence of ions in PEALD, regardless the setup conditions.
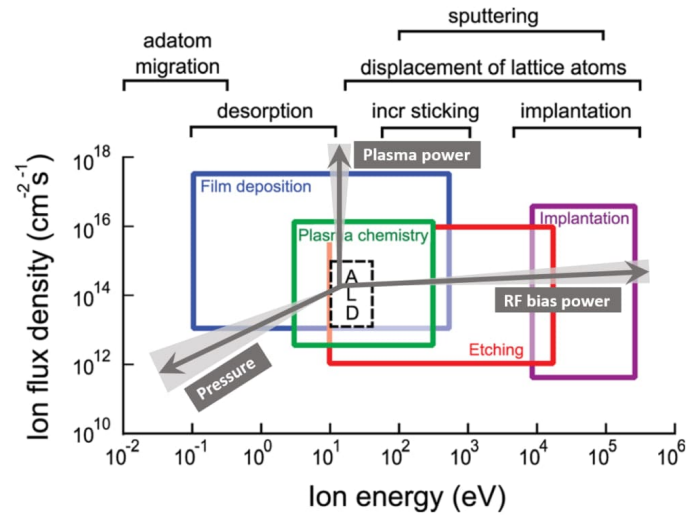
Figure 2.8: Influence of ion energy on plasma-based processes. In PEALD, the ion energy can be reduced by increasing the plasma pressure or increased by substrate biasing. The ion density increases with the plasma power. Sketch source: [44].
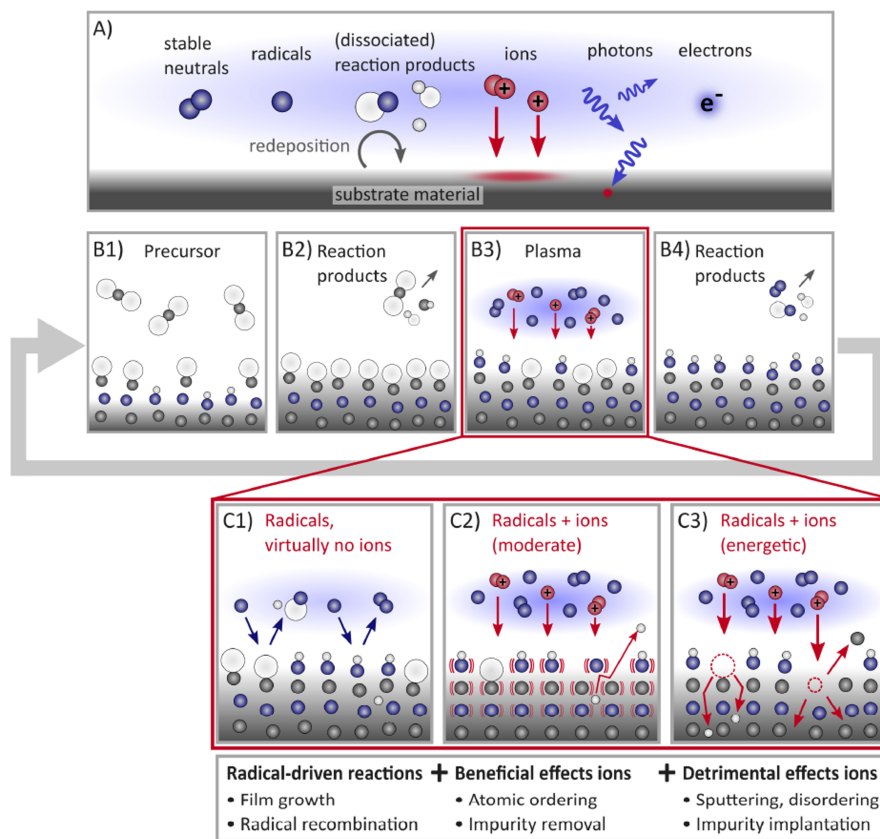
Figure 2.9: Overview: A) plasma species; B) PEALD cycle and C) the impact of ions according to their energy. Sketch source: [40].

31

Another factor that may contribute to the plasma-induced damage is radiation. The excited atoms in the plasma emit light in the visible and ultraviolet range, whose energy can reach up to 10 eV [50, 51], leading to surface damage. Indeed, in PEALD, radiation damage can be even more detrimental than ion damage. As an example, radiation can can break some of the bonds at the interface—often hydrogen bonds Si-H and Al-H [50, 51]. Thus, the radiation damage can be reduced by tuning the gas pressure and plasma power [50], and by the use of a quartz filter to block the UV radiation [44].

Lastly, in PEALD there is a potential limitation in conformality due to the recombination of plasma species. All plasma species are subject to recombination, however, due to its high reactivity radicals are the most prone. Recombination may occur to plasma species when striking the substrate surface—even if saturated—or the reactor walls. Recombination through gas-phase collisions is less likely since PEALD operates with cold plasma. Therefore, after collision with another surface atom, a more stable and non-reactive molecule forms. This phenomenon have two detrimental implications in PEALD. On one hand, reaction products—from surface and reactor walls—can dissociated again by the plasma and re-deposit, incorporating impurities into the film. This can be reduced by pumping out faster, using purging gas, and heating the reactor walls. On the other hand, as illustrated in Figure 2.10, radicals flux decreases with $(1-r)^N$, where r is the recombination probability and N the number of collisions. Since radicals are the specie that contributes the most to surface chemistry, and thus to deposition, the reduced flux of radicals caused by recombination can limit the conformality of PEALD. Although the recombination probability depends on each process and the specific deposition conditions. Generally speaking, PEALD films are more conformal at higher temperatures and pressures (r is lower), and at longer plasma doses (sufficient radical flux). Moreover, it has been demonstrated that PEALD can ensure high conformal deposition [52], up to an extremely high aspect ratio of ∼900 [53]. Therefore, for most of the applications and in particular for the one investigated here (a single-cell TESLA SRF cavity has an aspect ratio ∼5) PEALD may provide a conformal deposition.
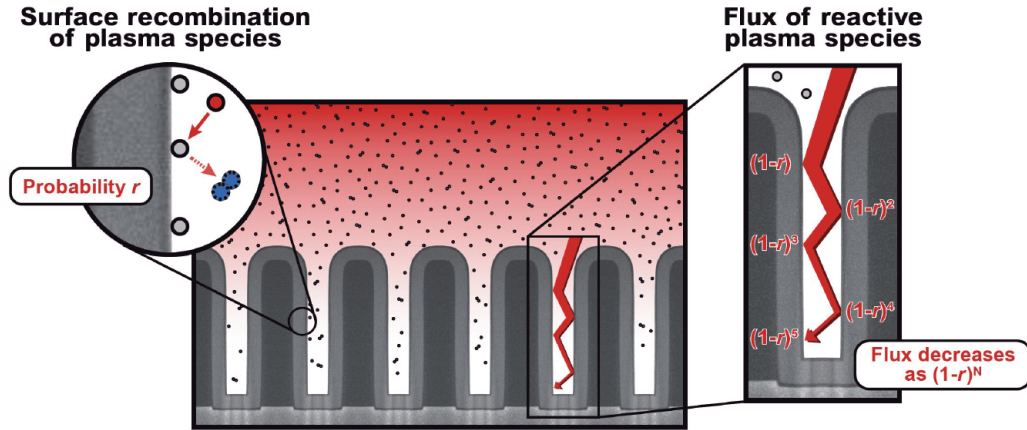
Figure 2.10: Illustration of the plasma species recombination and how can affect the flux of species inside of trenches. Sketch source: [44].

2.3. Alternative cycles: deposition of ternary compounds

The deposition cycle—whether ALD or PEALD—above described correspond to the simplest sequence. Generally, this process involves two surface reactions and results in a binary compound film. Although, choosing the right chemistry, single-element films, e.g. Ti, Ag or Pt, can also be deposited. For the deposition of ternary compounds different deposition sequences are possible. These are shown in Figure 2.11. On one hand, one can stick to the regular ALD deposition sequence, sketched in Figure 2.11 a), which alternates two precursors and their corresponding purging steps, and it is normally expressed as $(AB)^m$. In this case, one must use precursors or co-reactants which supply two of the three components into the film, e.g. bimetallic precursors which incorporate two metals into the film [54]. On the other hand, it is possible to alternate more than two precursors within a cycle. This sequence model is often known as multistep process. It is sketched in 2.11 b) and expressed as $(ABC)^m$. Lastly, the so-called supercycle approach expressed as $((A_1B_1)^m(A_2B_2)^n)^p$ and sketched at 2.11 c). It merges separate binary sequences, hence its name. In such a way, stoichiometry can be easily tailored by adjusting the number of times that each individual binary cycle is repeated.
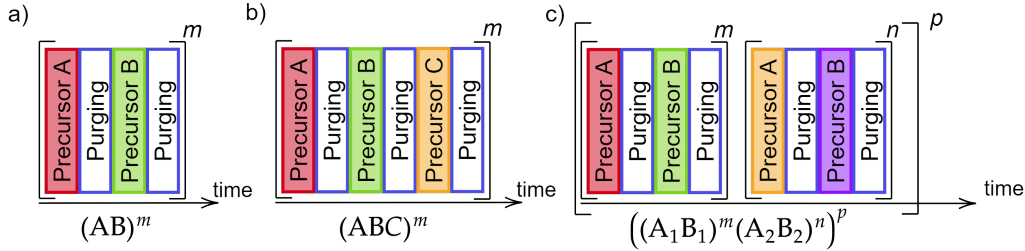
Figure 2.11: Schematic illustration of different ALD cycles: a) representation of the most basic ALD cycle where two precursors (A and B) are alternated. The variable m refers to the times this cycle is repeated; b) multistep cycle constituted of three precursors (A, B, and C). This process often results in a ternary compound; c) merge of two regular cycles into one supercycle. This approach is often used for depositing ternary compounds or doped films. By adjusting the variables m and n one can achieve the targeted composition and structure for the deposited films. This sketch is an adaptation from [39].

Additionally, ALD allows for the deposition of multilayers by performing different process sequences. The thickness of each layer is precisely controlled by adjusting the number of cycle repetitions. This feature is of particular interest for tailored SIS SRF cavities.

2.4. Materials achievable via thermal ALD and PEALD

The first PEALD process reported dates back to 1991 and involved GaAs deposition using a multistep cycle $(ABC)^m$ with three precursors: $GaMe_3$, AsH_3, and hydrogen radicals generated by a remote microwave-induced plasma source in a quartz tube [55]. Using radicals in ALD was patented in 1996 [56]. Since then, the interest in PEALD has been growing, boosted by new ALD applications emerging within and outside the semiconductor industry, and the rising desire towards crystalline materials—one of the PEALD assets. The yearly number of publications highlights its ascending trend (see Figure 2.12).
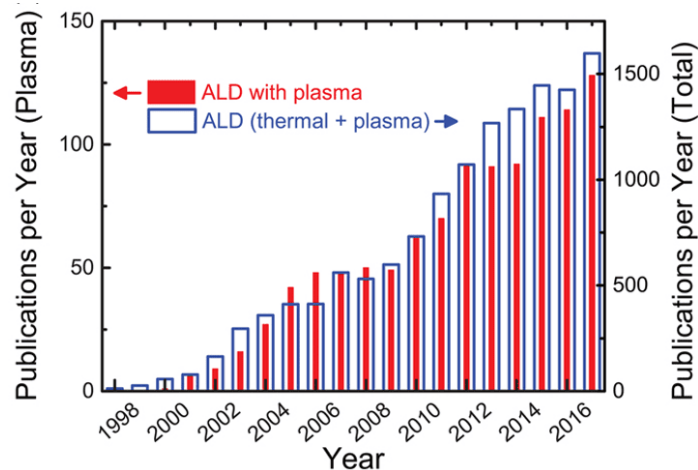
Figure 2.12: Number of publications per year about PEALD and ALD up to 2017. At a glance, one can discern the upward trend in the number of publications per year for both rankings over the last two decades. This graph is obtained from [57].

Moreover, PEALD has been integrated into high-volume manufacturing processes. In particular, PEALD has been of particular interest for applications that desire high-quality and conformal deposition on temperature-sensitive substrates. An example of this is PEALD of SiO_2 for self-alignment patterning, which has proven to be an effective method and is applied on an industrial scale [57].

In addition, a wide range of materials have been synthesised, as PEALD offers higher reactivity at lower temperatures, expanding the options for process chemistry. Figure 2.13 presents an overview contrasting the deposited films using thermal ALD, PEALD, or both. The deposition of oxides is the most commonly studied, in particular binary metal oxides such as Al_2O_3, TiO_2, ZnO, and Ta_2O_5, among others. Here, PEALD offers advantages in achieving lower deposition temperatures and shorter cycle times [54]. Besides oxides, various metal nitrides such as TiN, TaN, and NbN have been synthesised. Notably, PEALD nitrides have attracted considerable interest, with nearly all nitrides deposited by thermal ALD also achievable via PEALD, as shown in Figure 2.13 (b). Additionally, PEALD paved the way for the deposition of pure metals—Au deposition was achieved prior by PEALD than by thermal ALD [58]. Deposition of pure metals with thermal ALD may be sometimes challenging due to the lack of suitable chemistry [59], e.g. Ti or Ta. In these cases, the high reactivity of PEALD is beneficial [59]. Further, for single-element deposition a multistep process $(ABC)^m$ is preferable. Among the sulphides, fluorides, and phosphates thermal ALD prevails over PEALD. Generally speaking—and excluding radioactive and gaseous elements—compounds for all elements have been deposited by thermal ALD and PEALD, with only Cs and Tl as exceptions [57]. In conclusion, it has been proven that the stepwise approach of ALD/PEALD is suitable for the deposition of multi-compounds, mainly binary, but also ternary and quaternary compounds, and single-elements.

34
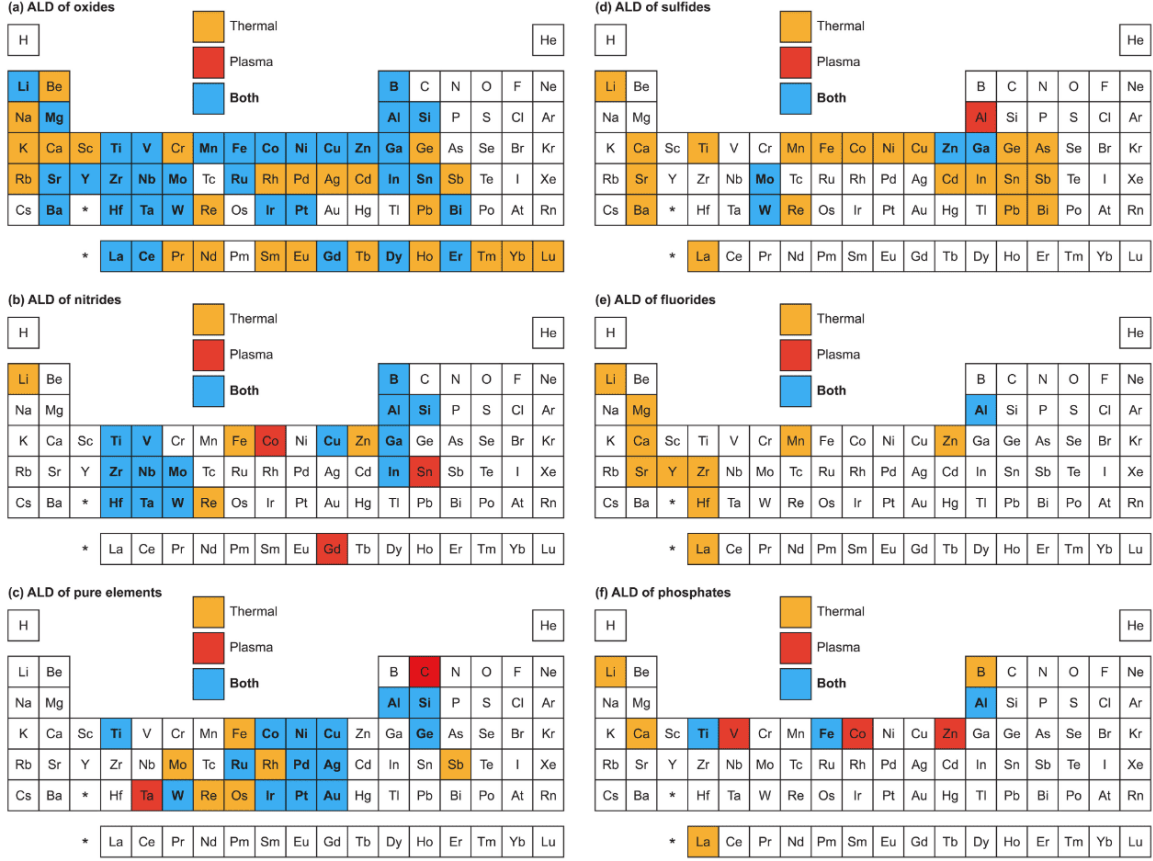
Figure 2.13: Periodic tables showing materials synthesised by thermal ALD and/or PEALD. The materials are clustered in groups: oxides, nitrides, pure elements, sulphides, fluorides, and phosphates. This figure belongs to Knoops et al. [57] and covers up to 2019.

2.5. State of art of SIS multilayers for SRF cavities by thermal ALD and PEALD

Nowadays, the R&D of the next-generation thin-film SIS-based SRF cavities with ALD is been developed at the pioneered CEA Paris-Saclay, and at Deutsches Elektronen-Synchrotron (DESY) together with Universität Hamburg. Given the potential of ALD over other deposition methods, an ALD reactor for SRF cavities is currently being commissioned at Fermilab [60]. Below, an overview of the studies conducted is presented.

2.5.1. Overview of the advancements on 1.3 GHz SRF cavities

The first studies of ALD-coated SRF cavities were conducted by Proslier et al. [61]. Specifically, two approaches were investigated. On the one hand, thermal ALD of Al_2O_3 and Nb_2O_5 with different thicknesses at 200 °C. Unfortunately, the deposition resulted in significant field emission which was assumed to be due to defective ALD layers or dust from the deposition process. High pressure rinsing (HPR) was conducted to clean the coated cavity, although the next cavity test showed field emission again, indicating ALD layers as the field

emission source and not the poor cleanliness. Only after a second coating, that buried the defective layers underneath, the cavity performance could be recovered. The other approach investigated is the removal of the Nb oxides at the interface of bulk Nb and the thermal ALD Al_2O_3 layer through high-temperature baking. This was previously investigated on samples [62], and then incorporated into cavities [61, 63]. However, two cavities showed multipacting and field emission ~ 20 MV/m. Therefore, it was deduced that defects and cracks on the Al_2O_3 layer could lead to field emission points. Moreover, these cracks would disable the barrier layer function enabling oxygen (e.g. from HPR) to diffuse. To know the cause of these defects would require further investigation, but hypotheses include the baking temperature and its cooldown, or changes due to oxygen diffusion.

The next experiments were conducted by Eremeev et al. [64] depositing Al_2O_3 at $120\,°C$. However, the films deposited were non-uniform and presented discolouration areas, which was assumed to be due to temperature variations across the cavity surface combined with an unoptimized process. Therefore, the performance of the cavity degraded.

The next investigation was performed by Kato and Hayano [65] at High Energy Accelerator Research Organization (KEK), using PEALD in a single-cell coupon cavity reactor. This investigation focused on SIS multilayers, with NbN and Al_2O_3. However, this investigation was interrupted and only PEALD NbN films were reported. Nevertheless, homogeneous and smooth films were achieved, although with carbon and oxygen contaminations, and poor nitrogen content. Further process optimisation and RF performance tests were required.

A new attempt to achieve an Al_2O_3 ALD SRF cavity was conducted by Kalboussi [66]. The ALD process was performed at $250\,°C$. After deposition, the cavity was annealed at $650\,°C$ for 4 hours. Once more, it resulted in multipacting at $18\,MV\,m^{-1}$. The cavity was chemically reset and the coating was repeated. Still, the cavity showed multipacting at $18\,MV\,m^{-1}$. Later, this process was repeated in a new cavity with an additional TiN layer and subsequent annealing step [67]. The TiN layer suppressed multipacting—although multipacting onset started $\sim 20\,MV\,m^{-1}$, RF processing allowed to increase fields—but the quality factor significantly degraded. Moreover, Kalboussi [67] investigated SIS multilayers—NbTiN and AlN—by thermal ALD. The deposition was carried at $450\,°C$ and uniform thicknesses along the cavity were ensured. During the subsequent annealing at $900\,°C$ there was vacuum degradation [68]; likely because the outgassing step between the initial cavity surface treatment and the ALD coating missed. This resulted in film delamination and degraded cavity performance—both quality factor and accelerating gradient [67, 68].

Finally, the goal of coating an Al_2O_3 layer without deteriorating the cavity performance was achieved by Wenskat et al. [69] at Universität Hamburg. Specifically, two TESLA single-cell SRF cavities, with baseline maximum accelerating gradients (before coating) of $\sim 20\,MV\,m^{-1}$ and $\sim 40\,MV\,m^{-1}$, were coated without detrimental effect on the cavities' performance—neither in the accelerating gradient nor in the quality factor. The deposition of Al_2O_3 of various thicknesses was conducted by thermal ALD at $120\,°C$.

2.5.2. Deposition of nitrides: thermal ALD vs PEALD

The deposition of the nitrides of interest—NbTiN and AlN—is feasible with both, thermal ALD and PEALD (see Figure 2.13 b). A short overview of the differences between the two methods is provided below, along with the reasons for selecting PEALD for this work.

Thermal ALD

The most common thermal ALD process of NbTiN is through metal chlorides—$NbCl_5$ and $TiCl_4$—precursors alternated with NH_3 as co-reactant [54]. The thermal ALD reaction for NbTiN is:

$$3NbCl_5 + 5NH_3 \rightarrow 3NbN(s) + 15HCl(g) + N_2(g) \tag{2.1}$$

$$2TiCl_4 + 2NH_3 \rightarrow 2TiN(s) + 6HCl(g) + Cl_2(g) \tag{2.2}$$
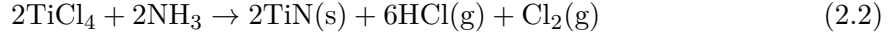
although the metal fluoride precursor NbF_5 would be also an option [70]. However, these processes present the following disadvantages. First, they may introduce small chlorine and fluorine contaminations in the deposited films [61, 70, 71]. Furthermore, the reaction by-products HCl and HF are highly corrosive and detrimental, which has been found to corrode the reactor walls, leading to the inclusion of iron impurities in the deposited films [72]. In addition, the thermally driven surface reactions require high process temperatures ($>400\,°C$ [54, 68]). Despite the high temperature, the reducing power of NH_3 is insufficient [71, 73]. This might degrade the superconducting properties of the nitride, which are highly sensitive to variations in stoichiometry and contaminations [61, 74–77]. Therefore, especially with chlorides, an additional Zn pulse as a reducing agent is needed to obtain high-quality films [71, 73], which has the drawback of incorporating a source of Zn contaminants. Lastly, the stoichiometric control over film composition is limited by the $NbCl_5$ etching nature [68, 71]. Conversely, an alternative ALD process using metalorganic alkylamide-based precursors avoids halogen residues [78]. However, these precursors have low decomposition temperatures [54] which can result in CVD growth for thermal ALD.

The most common thermal ALD process of ALN is:

$$AlCl_3 + NH_3 \rightarrow AlN(s) + 3HCl(g) \tag{2.3}$$
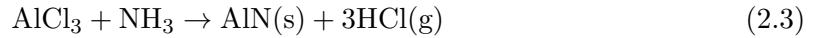
which requires high deposition temperatures ($450\,°C$ [68]), as thermal ALD of AlN does not lead to good quality at low temperatures [57].

PEALD

The most common PEALD process for NbTiN employs metalorganic alkylamide-based precursors—tetrakis(dimethylamino)titanium(IV) (TDMAT) [78–83] and (t-butylimido)tris (diethylamino)niobium(V) (TBTDEN)[79, 84–91]—and H_2/N_2 plasma. Although others metalorganic precursors such as tetrakis(ethylmethylamido)titanium(IV) (TEMAT) [92] and tert-butylimidotris(ethylmethylamido)niobium(V) (TBTMEN) [93], or metal chlorides precursors [89, 94, 95], and plasma gases, Ar and NH_3, can also be used. Next is the PEALD reaction for NbTiN, although less comprehensive than for thermal ALD, since plasma acts as a "black box" and the whole reactions are unknown.

$$Nb(NtBu)(NEt_2)_3(TBTDEN) + plasma\ H_2/N_2 \rightarrow NbN(s) + by\text{-}products(g) \tag{2.4}$$

$$Ti(NMe_2)_4(TDMAT) + plasma\ H_2/N_2 \rightarrow TiN(s) + by\text{-}products(g) \tag{2.5}$$
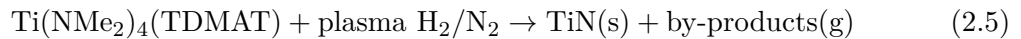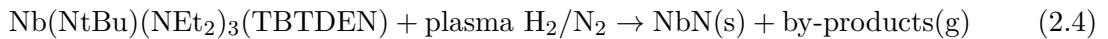
where, for simplification, Me represents the methyl group ($-CH_3$), Et represents the ethyl group ($-C_2H_5$), and tBu represents the tert-butyl group ($-C(CH_3)_3$).

Among the benefits of using PEALD over thermal ALD is replacing chloride precursors with metalorganic alkylamide-based precursors. This prevents undesired contaminations and by-products. Further, nitrogen from alkylamide reactants often becomes part of the film, sometimes acting as the main nitrogen source [54]. This is feasible because PEALD offers reduced deposition temperatures, preventing precursor decomposition, with higher reactivity. See Appendix A.1.3 for further details on metalorganic alkylamide-based precursors decomposition. In general, the additional energy from the ions improves crystallinity, results in denser films, and reduces the impurity levels. This is crucial for the NbTiN superconducting properties. Thus, high-quality nitrides can be achieved with PEALD at temperatures $<300\,°\mathrm{C}$.

On the other hand, AlN can also be deposited with PEALD. The deposition process alternates trimethylaluminum (TMA) and H_2/N_2 plasma:

$$\mathrm{Al(Me)_3(TMA) + plasma\ H_2/N_2 \rightarrow AlN(s) + by\text{-}products(g)} \tag{2.6}$$

Thus, PEALD offers for AlN films higher quality at lower temperatures [57, 96]. In particular, PEALD AlN results in smooth, continuous and pinhole-free films [59]. These characteristics are crucial for good dielectric films and its implementation into SIS multilayers in SRF cavities.

3. Fabrication process: deposition of AlN–NbTiN multilayers by PEALD and post-deposition annealing procedures

This section details the fabrication process of SIS multilayers on planar substrates for its use in SRF cavities, including the PEALD deposition process and post-deposition annealing procedures. It includes information on the PEALD setup, the substrate preparation, and the specifics of the deposition and annealing processes.

3.1. Overview of PEALD system

The PEALD system used in this thesis is the GEMStar XT-DP^{TM} from ARRADIANCE. The deposition reactor is shown in Figure 3.1, with more in detail in Figure 3.2. This system extends the capabilities of the thermal system GEMStar XT^{TM} by incorporating a plasma processing, enabling both thermal and plasma-enhanced ALD.

The additional components for plasma generation are: the RF power supply (SEREN R301 RF generator), the matching network, and the plasma head, which includes an inductive plasma coil and four plasma gas inputs. The RF power supply delivers up to 300 W at an operating frequency of 13.56 MHz into a 50 Ω load. This field ignites the plasma as gas flows through the coil. The coil, made of silver-plated copper, surrounds an air-cooled 20 mm quartz tube, which confines the plasma within a stable and controlled environment. This setup allows the use of up to four gases—argon, hydrogen, nitrogen, and oxygen—for
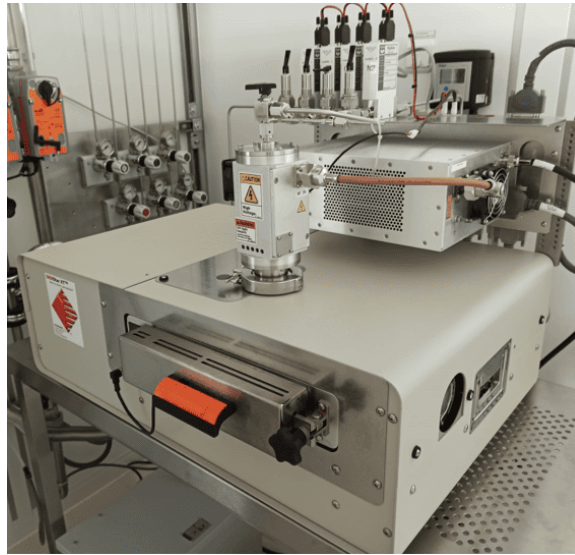
Figure 3.1: General visualization of the GEMStar XT-DP^{TM} system from ARRADIANCE, utilized in the present thesis. This device enables both thermal and plasma-enhanced ALD.
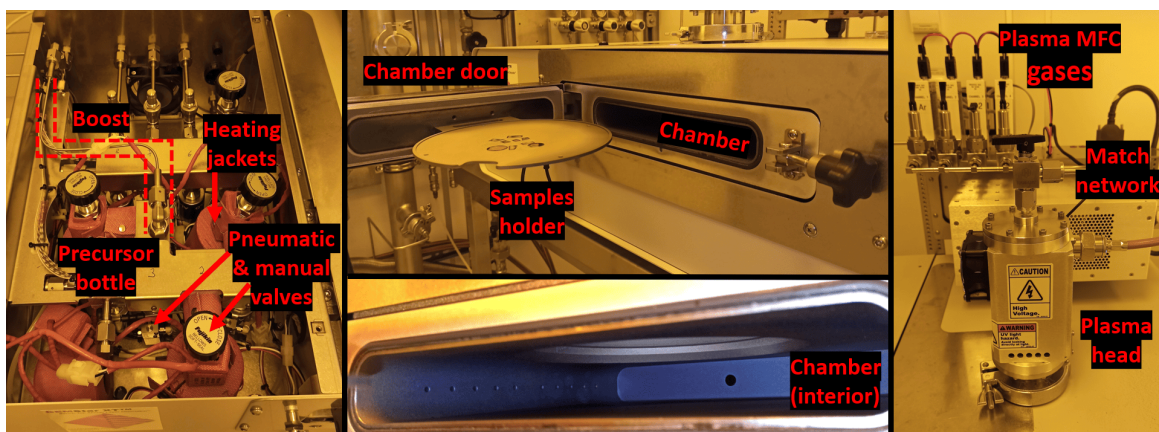
Figure 3.2: Overview of the GEMStar XT-DP$^{\text{TM}}$ reactor with the key components highlighted. Visualisation of the gas manifold assembly (left), deposition chamber (centre), and plasma generation components (right).

plasma processing. The reactor includes two gas manifolds, with capacity for up to eight precursor bottles. One of the precursor ports is equipped with a boost system, also known as pulsed vapour push. This system introduces inert gas into the precursor bottle through an additional valve, enhancing the delivery of the precursor. This is often used for precursors with low vapour pressure. The GEMStar precursor containers are cylinders made of stainless steel with a filling capacity of 125 mL and a heating temperature of up to 150 °C (see Figure A.3 in Appendix A.1).

Argon is used as the carrier gas due to its inert nature. The gas flow goes from right to left while the plasma species move downward from the plasma head (see Figure 3.2). The operating pressure is in the 50-500 mTorr range, which is equivalent to 10^{-1} mbar. The reactor—including walls to prevent condensation—can be heated up to 300 °C. Moreover, the reactor accommodates substrates up to 200 mm in diameter and 17 mm in height (using the sample holder) or 39 mm (without sample holder). However, one must consider potential plasma-induced side effects—such as etching, see Appendix A.1—when using large-dimension substrates.

3.2. Substrate selection and pre-deposition preparation

This subsection provides details on substrate selection and preparation process prior to deposition. It presents the criteria for choosing the substrates and describes the pre-deposition preparation methods applied to each substrate.

Two different substrates were used: silicon and niobium. The substrates were selected based on their compatibility with the characterisation technique used to analyse the thin film properties. For instance, Nb roughness limits the effectiveness of characterisation techniques that rely on reflection and scattering interactions. Therefore, silicon was used for studies with ellipsometry, X-ray reflectivity (XRR), and X-ray diffraction (XRD). Moreover, silicon was chosen for electrical transport measurements because it allows for the necessary electrical contacts, which is challenging with niobium due to its soft, ductile, and malleable nature. In this work, using niobium was found to lead to deformation and breakage of the

thin films as a consequence of electrical contact integration. For contactless inductive measurements, both substrates were used; although in some cases Nb may overshadow the thin film properties. Another factor to consider is the degree of impact that the substrate may have on the properties under investigation. Thus, both substrates were employed for surface morphology analysis, e.g., when assessing thin film interfaces. Conversely, the price, time, effort, and resources involved in the substrate preparation, were also considered. Thus, silicon was chosen for surface compositional analysis, such as X-ray photoelectron spectroscopy (XPS).

The silicon substrate is a wafer of 100 mm diameter, 525 µm thickness and (100) orientation. It is single-sided polished and has a native silicon dioxide layer, a few nanometers thick. Before deposition, the wafer was cut and cleaned in an ultrasonic bath in isopropanol for 2 minutes. Conversely, various niobium substrates were used: foils and sheet substrates (with conical and rectangular shapes). The Nb foils, were purchased from HMW Hauner, are $0.1 \times 40 \times 40 \, \text{mm}^3$ and have a RRR of 10-25. The Nb sheets were cut from leftovers from the European XFEL cavity production (RRR > 300, grain size ~50 µm). The conical-shaped substrates are 2.8 mm thick, 13.23 mm bottom outer diameter, and 10 mm top inner diameter. While the rectangular-shaped substrates are $11 \times 35 \times 1 \times \text{mm}^3$. Before deposition, the niobium substrates were treated following the standard cavity procedure, described below.

3.2.1. Niobium surface treatments

Niobium substrates were treated as closely as possible to cavities. This is important to grow the thin films in comparable conditions and mimic the cavity environment. A smooth and clean inner surface cavity is critical to reach high accelerating fields and quality factors. Therefore, the European XFEL recipe [97] has been followed, using an established setup designed for samples to ensure identical treatment to that experienced by the surface of cavities.

The first step is surface polishing, which removes machining-induced damage and the native Nb_2O_5 oxide layer—although this oxide will later regrow upon exposure to air. It consists of a coarse electropolishing (EP) which aims to remove ~140 µm. The EP acid is a mixture of hydrofluoric acid (HF, concentration 48%) and sulphuric acid (H_2SO_4, concentration 96%), with a volume ratio of 1 to 9 parts, respectively. The EP operates at 14 V and the acid is kept at 20-25 °C. After the coarse EP, the Nb surface looks smoother and shinier as shown in Figure 3.3. To remove acid residues ethanol rinsing is conducted. The next step is 800 °C annealing in ultra-high vacuum (UHV) for two hours because the HF acid introduces hydrogen into the niobium. Degassing the hydrogen is essential; otherwise, cooling to cryogenic temperatures causes hydride precipitation, which has been proven to cause a characteristic Q-drop [98]. In addition, mechanical stress is relieved. However, based on the annealing environment, the niobium surface is susceptible to re-incorporating interstitial impurities. Thus, a fine EP is performed, which removes 10-40 µm. Finally, the niobium undergoes a 48-hour annealing at 120 °C in UHV to mitigate the Q-slope at high-field [99].

In the case of the rectangular-shaped niobium substrates, the chemical surface treatment faced modifications since the sample geometry did not fit into the EP setup (see Figure 3.3). Therefore, the EP is replaced by another standard polishing procedure known as buffered
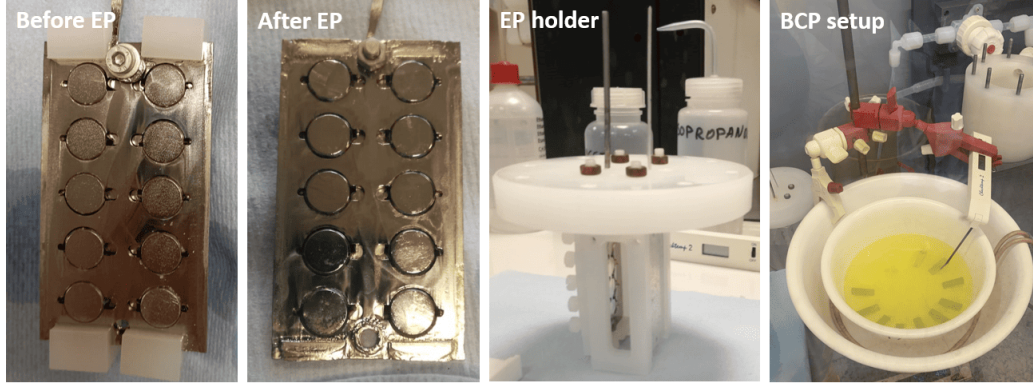
Figure 3.3: Photographs of the substrate chemical process: (from left to right) Nb conical-shaped substrates before and after EP; EP sample holder made of polytetrafluoroethylene to support conical-shaped substrates inside the acid; and BCP for rectangular-shaped substrates. Both EP and BCP are conducted inside a fume hood.

chemical polishing (BCP). This chemical treatment is also qualified for Nb based SRF cavities, as half of the XFEL cavities have been treated with BCP, and the other half with EP. Nonetheless, the preferred cavity surface treatment is EP, since it has been demonstrated that EP cavities can achieve higher accelerating fields than BCP cavities [100]. BCP uses an acid mixture with a volume ratio of 1 part HF(48%), 1 part nitric acid (HNO$_3$, 85%), and 2 parts phosphoric acid (H$_3$PO$_4$, 96%). The acid is kept at 15 °C. The two annealing steps were carried out as described above.

The final step of Nb SRF niobium cavity preparation, and thus for the Nb substrates as well, is an ultra pure high-pressure water rinse, known as HPR [97]. It aims to further enhance surface cleanliness by removing any remaining dust, particles, and chemical residues. For an optimal result, this step is conducted in a cleanroom class ISO 4 at DESY facilities. The HPR is performed in a vertical orientation with a specific sample holder, shown in Figure 3.4. A lance at a distance of 60 mm from the substrates ejects the ultra pure water with a pressure of about 100 bar onto the niobium surface. The water temperature should be above 18 °C, but must not exceed 60 °C. For the conical-shaped niobium substrates seven rinse cycles are repeated.
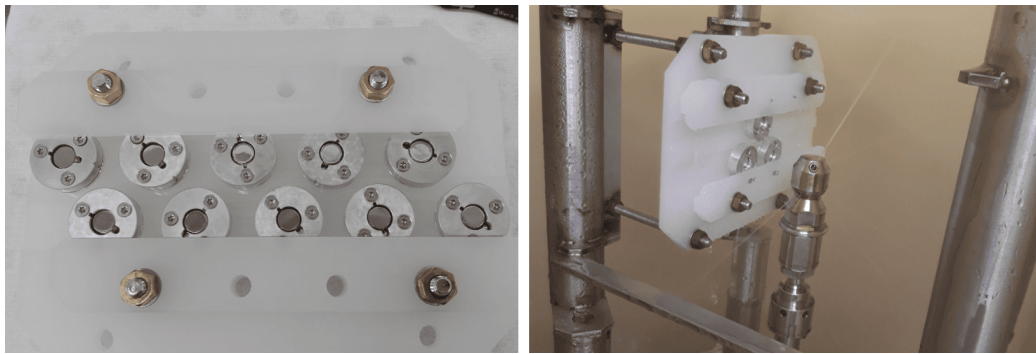
Figure 3.4: Adapting the high-pressure rinse (HPR) to the conical-shaped niobium substrates.

3.3. Experimental details of the SIS multilayer deposition process by PEALD

The following subsection introduces the PEALD deposition process for the SIS multilayers. Note that the PEALD working principle is explained in Section 2; here, only the experimental details are provided. It starts with the deposition details of the individual layers, followed by the multilayer deposition process.

3.3.1. Depositing NbTiN thin films

To deposit NbTiN by PEALD the supercycle approach—detailed in Section 2—is used. A supercycle combines two binary ALD cycles—in this case, PEALD cycles—alternating them within an outer loop, hence the name. A visual representation of a supercycle is given in Figure 2.11 c) and expressed by $((A_1B_1)^m(A_2B_2)^n)^p$, where A_i and B_i represent the exposure plus purge for each precursor, and m, n, and p the number of times each loop is repeated. For NbTiN, the alternating ALD sequences within the supercycle correspond to TiN and NbN. In this way, the ratio of Ti to Nb within the ternary compound can be tailored by adjusting the ratio of the individual ALD processes, or in other words, the ratio of m to n. Therefore, thermal ALD and PEALD provide a level of control on the composition of NbTiN that exceeds other deposition techniques. Below, the separate PEALD sequences, as well as the entire supercycle sequence, are elaborated.

The TiN sequence follows $(A_1B_1)^m$, where A_1 and B_1 represent respectively the precursor and plasma exposure, both including purge. The Ti precursor used is tetrakis(dimethylamino)titanium(IV) (TDMAT). It is a metal-organic precursor and was purchased in liquid form from Strem Chemicals. TDMAT exhibits a yellowish colour. The plasma gas is a mixture of hydrogen and nitrogen. The NbN deposition follows the same sequence structure. The precursor used is (t-butylimido)tris(diethylamino)niobium(V) (TBTDEN) purchased from Strem Chemicals as well. TBTDEN is also a metal-organic and liquid precursor, of brownish colour. During this study, differences in the colour of the TBTDEN precursor were apparent across various bottles—see Figure A.4 at Appendix A.1—despite the 98% purity stated by the manufacturer. It was observed that this could have an impact on the T_c of the NbTiN films ($<0.5\,\mathrm{K}$). Furthermore, TBTDEN exhibits low vapour pressure and low decomposition temperature [54]. Hence, it has been connected to a vapour push port or boost to enhance the transport from the precursor cylinder into the reactor. Similarly to TiN, the plasma gas for NbN deposition is a mixture of hydrogen and nitrogen. A NbTiN supercycle alternates m-times the TiN cycle and n-times the NbN cycle. The p-times supercycle repetition controls the total NbTiN deposited thickness. More specifics of the PEALD sequence are detailed below.

Optimising the deposition parameters for improved NbTiN film characteristics

Process parameters can significantly affect the properties of the deposited films, including the deposition rate, composition, crystallinity, and electrical properties. In particular, the PEALD process parameters have to do with the plasma, such as plasma power or flow of gases, or with the precursor, e.g., dosing time or precursor temperature, or with the reactor conditions, such as deposition temperature. During this study, the deposition parameters

43

for the NbTiN PEALD process were optimised concerning the electrical properties of the films and their application into SRF cavities. Below, are given the optimised recipe values.

The deposition is carried out at 250°C, which is the highest temperature recommended for the GEMStar XT-DP$^{\text{TM}}$, although, this high deposition temperatures result in fast o-ring degradation (see Appendix A.1.1). The substrates are kept at this temperature for 20 minutes before deposition starts, to ensure that they match the reactor's temperature. The precursors are also heated, TDMAT to 70 °C and TBTDEN to 90 °C. An argon flow of 10 sccm circulates continuously through the precursor manifold and the deposition chamber during the entire deposition process. Before the deposition begins, the plasma is ignited to further clean the substrate surface. Afterwards, the supercycle for depositing a "monolayer" of NbTiN is started, commencing with the TiN cycle. The TiN sequence was previously optimised [101]. Furthermore, the precursor manifold is also heated to prevent precursor condensation in its path into the reactor. The TDMAT dose is a 500 ms pulse, followed by a 40 s purge. Note that, during each precursor dose, an argon flow of 70 sccm passes through the plasma head to prevent the accumulation of precursor on the quartz tube. The plasma gas is a mixture of hydrogen and nitrogen, with respective flow rates of 45 sccm and 20 sccm, and a power of 300 W. The plasma is exposed for 60 s and followed by 120 s purge. Then, the supercycle continues with the NbN cycle. A boost of argon for 20 ms precedes the 500 ms of TBTDEN, followed by a 40 s purge. The plasma gas uses flow rates of 45 sccm for hydrogen and 12 sccm for nitrogen, a power of 300 W, and a duration of 90 s. It is followed by a 120 s purge. The supercycle closes with the NbN cycle being rerun three times. These supercycle parameters are listed in Table 3.1.

3.3.2. Depositing AlN thin films

The AlN PEALD process also follows the layout (AB)[1]. The precursor used is trymethylalu minum (TMA), also purchased from Strem Chemicals. TMA is a metal-organic precursor, colourless, and liquid, widely used in the ALD community. It is kept at room temperature during the process. The TMA dose is of 21 ms followed by a 30 s purge. After purging, the plasma is ignited for 10 s. The plasma gas is also a mixture of hydrogen and nitrogen, in this case with flow rates of 30 sccm and 30 sccm, respectively. The plasma power is again 300 W. Then, a 100 s purge concludes the cycle. The AlN PEALD process parameters are also listed in Table 3.1.

The AlN deposition is conducted at 250 °C. However, it was observed that depending on the film thickness, AlN films occasionally suffer from blistering. To overcome this problem the AlN deposition has been investigated at different deposition temperatures. The results of such an investigation are shown in Section 6.

3.3.3. Depositing AlN-NbTiN multilayers

In a similar fashion that a supercycle alternates separate ALD cycles to deposit ternary compounds, the deposition of multilayers follows the same procedure. Figure 3.5 illustrates the PEALD sequence for depositing AlN-Nb$_{\text{x}}$Ti$_{\text{1-x}}$N multilayers. The details of the individual AlN and NbTiN PEALD processes are given above and summarised in Table 3.1. The process starts with the AlN cycle which is repeated l-times to reach the desired thickness. Subsequently, the PEALD supercycle of Nb$_{\text{x}}$Ti$_{1-\text{x}}$N is conducted. The cycle ratio m to n
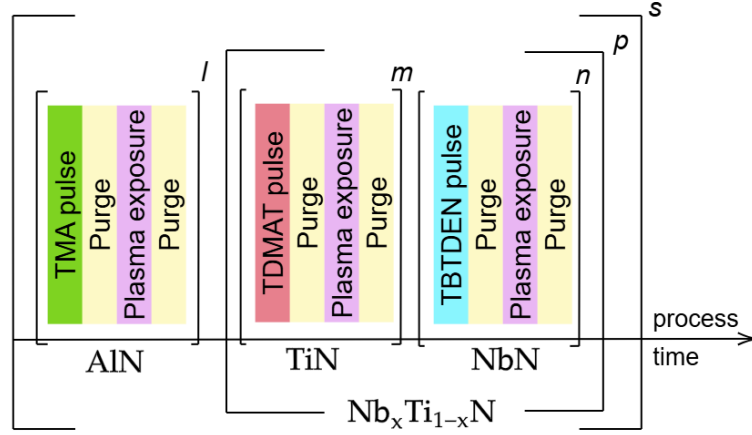
Figure 3.5: Schematic illustration of the PEALD sequence for depositing AlN-$Nb_xTi_{1-x}N$ multilayers. The films thicknesses is controlled by the supercycle l and p. The ratio of Ti to Nb is controlled by the ratio of m to n. The outer loop number s dictates the number of multilayers deposited. The colours are meaningless, their purpose is purely visual guidance.

for TiN to NbN, respectively, is adjusted to the targeted composition. The NbTiN film thickness is controlled by the *p-times* the supercycle is repeated. Finally, the number of AlN-$Nb_xTi_{1-x}N$ multilayers deposited is defined by the number s of the outer loop. The total deposition time depends on the selected film thicknesses, $Nb_xTi_{1-x}N$ composition, and number of multilayers deposited. To provide insight, the deposition of AlN-NbTiN multilayers, with thicknesses of 15 nm and 60 nm, takes approximately 100 h.

Table 3.1: PEALD process parameters for AlN, TiN, NbN, and NbTiN deposition

Process parameters	AlN	TiN	NbN	NbTiN
Precursor dose (ms)	21	500	(with pre-boost) 500	—
Purge (s)	30	40	40	—
Plasma dose (s)	10	60	90	—
Purge (s)	100	120	120	—
Plasma power (W)	300	300	300	—
Plasma gases: H_2/N_2 (sccm)	30/10	45/20	45/12	—
Precursor	TMA	TDMAT	TBTDEN	—
Supercycle ratio m:n	—	—	—	1:3

3.4. Post-deposition annealing procedures

It has been demonstrated that SIS multilayers deposited by PEALD, following the process described above, do not meet the SRF demands [102, 103]. This section will not delve into those requirements but will instead describe the post-deposition annealing procedures shown to enhance the multilayers sufficiently to still consider them as candidates for next-generation SRF cavities based on tailored thin films. Various annealing procedures have been investigated, including different annealing durations, temperatures, ramping and cool-

ing rates, and annealing atmospheres. Moreover, three different furnaces were employed. In the following, the technical characteristics of the furnaces are presented along with the annealing procedures undertaken, which are listed in Table 3.2.

Firstly, the MC-050 system by Annealsys has been employed for post-deposition annealing processes. Its halogen lamps provide fast management of the process temperature reaching up to $1100\,°C$. Therefore, high ramping rates for annealing processes were conducted within this furnace, compared to the other two furnaces presented below, which had slower ramping times. As a result, the processes performed were classified as rapid thermal annealing (RTA) or slow thermal annealing (STA). Apart from that, the MC-050 offers a vacuum of $1 \times 10^{-3}\,mbar$ and supports various annealing atmospheres, including nitrogen, a mixture of hydrogen and nitrogen, and a mixture of hydrogen and argon. Its relatively poor vacuum level—compared to the SRF requirements—and the annealing duration constraints imposed by the halogen lamps, made this furnace suited exclusively for early-stage material assessments.

Secondly, a ceramic tube furnace by Carbolite Gero GmbH & Co. KG is entirely dedicated to SRF sample R&D. Hence it is referred as sample furnace, enabling treatments under vacuum and nitrogen atmosphere. Among other treatments, this furnace is used in the annealing steps of the Nb surface preparation, Nb nitrogen infusion treatments, and the annealing of SIS multilayers on Nb and Si substrates. In order to accomplish the cleanliness prerequisite essential in this area, the sample furnace was subject to modifications, improving the base pressure down to $2 \times 10^{-8}\,mbar$ [21]. A residual gas analyzer examines gas constituents and ensures the cleanliness. A vacuum pump-stand by Edwards, consisting of a nEXT240D turbomolecular pump and a nXDS6i scroll pump, is used. Besides, the sample furnace features a ceramic tube Pythagoras Type C 610, with a length of 1000 mm, and an outer and inner diameter of 90 mm and 80 mm, respectively. It has three heating zones that provide a temperature gradient along the tube length. A temperature control system by GERO consisting of a CrFeAl heating coil is used for heating up to $1350\,°C$.

Lastly, another furnace, the so-called single-cell furnace [104], due to its capability of fitting a 1.3 GHz TESLA single-cell cavity inside, was also employed for SIS multilayers investigation. This furnace was manufactured by Xerion Berlin Laboratories GmbH. It is also dedicated to SRF cavity and sample R&D and is located in an ISO 5 cleanroom to minimise particle contamination. Featuring three heating zones, the single-cell is capable of reaching a maximum temperature of $1100\,°C$. Furthermore, it is equipped with a vacuum system that combines a turbomolecular and a cryopump, achieving a base pressure of $2 \times 10^{-8}\,mbar$ at room temperature after 8 h of pumping. Additional information on this furnace is given here [104].

In all cases, the substrate cooled down naturally without any additional cooling. Generally speaking, whenever in the present thesis a post-deposition thermal treatment is referred to exclusively as annealing it means STA, either inside the sample furnace or the single-cell furnace.

Table 3.2: Details of post-deposition annealing procedures for the various furnaces.

Furnace details	MC-050 furnace	Sample furnace	Single-cell furnace
Temperature range (°C)	$800 - 1000$	$1000 - 1100$	$700 - 1100$
Heating rate (°C/min)	60	3.3	3
Cooling rate (°C/min)	20	1	$1.5 - 2$
Duration (h)	$5 - 50$ (*min)	1	$1 - 5$
Base pressure (mbar)	$e - 3$	$10^{-6} - 10^{-8}$	10^{-8}
Annealing atmosphere	$H_2/N_2 - H_2/Ar - N_2$	$N_2 -$ vacuum	vacuum
Annealing procedure	RTA	STA	STA

4. Characterisation methods: experimental details

This section presents the experimental setups and procedures employed for each of the characterization techniques used for the investigation of the SIS multilayers grown by PEALD. The aim is not to delve into the operating principles of each characterization method but instead to provide information about the measurements and analyses performed. The characterizations were performed at the Center for Hybrid Nanostructures (CHyN) Universität Hamburg, unless mentioned otherwise.

4.1. Thickness evaluation

4.1.1. X-ray reflectivity (XRR)

X-ray reflectivity (XRR) is a surface-sensitive, non-destructive technique utilised for characterising thin films and multilayers, which can be amorphous, single-crystalline, and polycrystalline [105]. It gives information on film thickness, surface and interfacial roughness, and density, relying on X-ray elastic scatter off electrons. The measured curves show the variation of reflected X-ray intensity as a function of the incident angle (θ) relative to the surface. These curves display characteristic oscillations, known as Kiessig fringes [106], caused by interference effects when X-rays reflect off interfaces with different electron densities.

The XRR measurements were conducted at NanoLab (DESY Hamburg, Germany) [107], in a 6-circle diffractometer with Cu X-ray source under ambient conditions with the primary objective of assessing film thickness. Various layers and multilayers (AlN, NbN, TiN, NbTiN, AlN-NbTiN) deposited on silicon substrate were investigated. The results of the characterization are presented in Section 3. Additionally, multilayers of AlN-NbN and AlN-NbTiN in their as-deposited and annealed states were studied. The results are presented in Appendix B.1. No XRR measurements were performed using Nb as the substrate, as its surface roughness is rather large, which comprises the feasibility of XRR measurements since diffuse reflections increase the background noise.

Film thickness from XRR curves was determined by fitting the rocking curves to a model using the GenX software and by the analysis of the period of the Kiessig fringes, for single-layer systems. The intensity oscillations are caused by constructive and destructive interference between X-rays reflected from the top surface of the film and those reflected from the interface the film and the substrate. Thus, the change in the scattering vector in the specular direction can be related to the path difference for the X-rays reflected from the top and the bottom of the film by

$$\Delta Q \approx \frac{2\pi}{d} \tag{4.1}$$

where Q is the scattering vector in the specular direction defined by

$$Q = \frac{4\pi}{\lambda} \sin \theta \tag{4.2}$$

Therefore, the film thickness is given by

$$d \approx \frac{\lambda}{\Delta 2\theta} \tag{4.3}$$

4.1.2. Spectroscopic ellipsometry (SE)

Spectroscopic ellipsometry (SE) was also employed to evaluate the film thickness. It is an optical technique widely used due to its non-destructive nature, rapidity and ease of use. Unlike XRR, SE does not measure the intensity of light instead, it measures the relative phase and amplitude change of reflected polarized light [108]. The measured data is fitted by a model that includes the sample's layer structure (single films and multilayer stacks) and dispersion formulas to evaluate the material's optical properties and thickness.

The ellipsometer employed is a SENpro from Sentech Instruments GmbH. It measures in the wavelength range of 370-1050nm. All data were recorded at a fix incident angle. The software SpectraRay was utilized for data acquisition, modelling, fitting and reporting data. The sample structure model accounts for the silicon substrate, the SiO_2 native layer of fixed thickness, and the layer or layers under examination. Generally, all parameter except thickness were fixed. The dispersion model chosen for the fit depends on the type of material under investigation: a Cauchy model for SiO_2, Lorentz for the AlN, and Drude-Lorentz using two Lorentz oscillators for TiN. The results are given in Section 3.

Transition metal nitrides, which combine metallic and ceramic properties, present a complex electronic structure which leads to strong changes in their optical properties, i.e. dielectric function, absorption, reflectivity, etc., at low-energy or high-energy regions [109]. Additionally, the optical properties of transition metal nitrides can be highly sensitive to factors like film thickness, composition, and microstructure, making SE on NbN and NbTiN specially challenging [110].

4.2. Morphology

4.2.1. Scanning and transmission electron microscopes (SEM and TEM)

Scanning electron microscope (SEM) and transmission electron microscope (TEM) were used for high-resolution imaging of the multilayer surface and cross-section, respectively. Scanning transmission electron microscopy (STEM) was also used. Single layers and multilayers deposited on Si and Nb were examined. Various of the acquired images are shown in Section 6. It is possible to distinguish between SEM/STEM images and TEM images by the contrast between the layers. SEM and STEM, when using backscattered electrons, provides contrast based on the atomic number, with heavier elements resulting in brighter regions.

The SEM systems used were the Crossbeam 550 by Zeiss (at Universität Hamburg) and the Nova NanoSEM 450 by FEI [107]. While the TEM systems used were the Talos F200X by Thermo Fisher at Technische Universität Hamburg (TUHH) and the Tecnai Spirit 120 kV by FEI at École polytechnique fédérale de Lausanne (EPFL).

For TEM analysis, it is necessary to prepare lamellas. *Lamella* refers to a thin slice or layer of material, as the electron beam must pass through the sample to ensure adequate transmission and resolution. The lamellas were fabricated by focused ion beam (FIB) milling, with a top protection layer of Pt or Ga, using the Helios Nanolab G3 UC by Thermo Fisher at Technische Universität Hamburg and the FIB-SEM XB 540 by Zeiss at CERN (EN-MME-MM).

4.2.2. Atomic force microscope (AFM)

Atomic force microscope (AFM) was used to examine the surface topography of single layers and multilayers grown on Si and Nb. The sample surface is scanned by a tip mounted on a cantilever. Interaction forces between the tip and the sample surface cause the cantilever to detect, which is detected to create the surface map.

The AFM study was performed using the Dimension 3100 AFM by Veeco. Scan size varies from $2{\times}2\,\mu m$ to $20{\times}20\,\mu m$, scan rate was kept $<1\,Hz$, and the pixel resolution was $512{\times}512$ and $1024{\times}1024$. WSxM software was used for image processing and surface roughness analysis.

4.3. Composition

4.3.1. Energy dispersive X-ray spectroscopy (EDX)

Energy-dispersive X-ray spectroscopy (EDX) is a quick and non-destructive technique used in chemical analysis that enables both the identification and the quantification of the elemental composition of a sample [111, 112]. EDX is often coupled with electron microscopes since a high-energy electron beam is needed for both. The electron beam impacts the atoms, it ionizes them. Subsequently, an electron transition from a higher to a lower energy level results in the emission of an X-ray whose energy is unique to each element, allowing for their identification. Note, detection of light elements is limited in EDX.

Elemental identification and quantification was conducted by the EDX coupled to the Crossbeam 550 by Zeiss (at Universität Hamburg). The results are shown in Section 7. While elemental maps were taken with the Talos F200X by Thermo Fisher at Technische Universität Hamburg (TUHH) and by the Tecnai Spirit 120 kV by FEI at École polytechnique fédérale de Lausanne (EPFL), for AlN-NbTiN multilayers deposited on Si and Nb, respectively. The elemental maps are present in Section 6.

4.3.2. X-ray photoelectron spectroscopy (XPS)

X-ray photoelectron spectroscopy (XPS) is used to determine the elemental composition and chemical state of materials. Monochromatic X-rays irradiate the sample, and the photoelectrons emitted are detected. By analysing their energy, the elements and their chemical state can be determined. The XPS spectrum shows the number of detected electrons per energy interval versus their kinetic energy. The peaks in the spectrum correspond to the electrons from the top tens of angstroms; electrons generated deeper in the material contribute to the background signal. Therefore, XPS is surface-sensitive; although combined with ion bombardment or angle-resolved XPS (ARXPS) measurements, it enables depth studies.

XPS measurements were performed at Nanolab (DESY) [107] using the SPECS™ spectrometer shown in Figure 4.1. XPS spectra were recorded in fixed transmission mode in a vacuum of $1 \times 10^{-10}\,mbar$. As-deposited and annealed AlN-NbTiN multilayers deposited on Si were evaluated at their surface and after 40 min 40 minutes of argon ion bombardment (energy 1 keV, emission 6 mA, and Ar pressure $5 \times 10^{-6}\,mbar$). The thickness etched remains unknown. XPS sputtered analysis is presented in Section 7, while surface analysis is included in Appendix B.4. For element identification, an initial survey (pass energy 50 eV
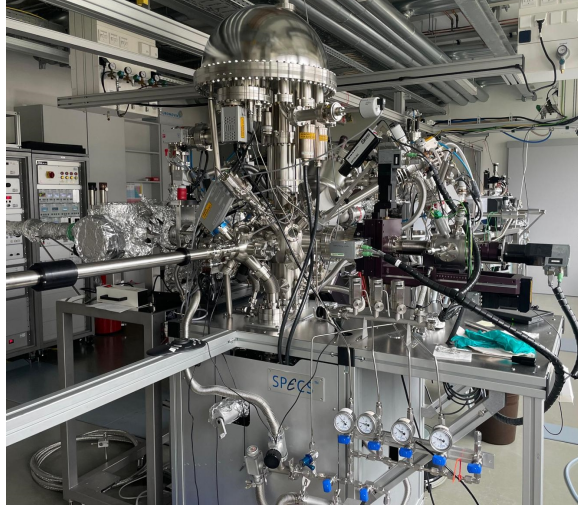
Figure 4.1: XPS spectrometer at NanoLab [107]. The system consists of the X-ray source and monochromator, the energy analyser, the ion gun, a micromanipulator stage, and the vacuum chamber.

and step size 0.5 eV) was conducted for the binding energy (BE) range 0-1200 eV. High-resolution scans (pass energy 30 eV and step size 0.1 eV) were taken for each of the detected peaks.

The deconvolution of the spectra was performed using the CasaXPS software. The deconvolution of each peak considers the contributions of other peaks. The background was subtracted using a Shirley background. The O 1s, C 1s, and N 1s peaks were fitted using a Gaussian/Lorentzian (G/L) peak shape with a 30% G/L mixing ratio, typically used for symmetrical spectra. The Ti 2p peak for TiN is challenging to fit [113–115]. The width of the spin-orbit components is different, being much broader for the $2p_{1/2}$ than the $2p_{3/2}$. Shake-up satellites—additional peaks that appear near the main peak as result from an energy-loss process during the photoemission of electrons—are visible. To reduce its complexity, only the $2p_{3/2}$ peak was fitted. Ti 2p spectrum has different peak shapes: Ti metal is asymmetric, TiO_2 is symmetric, and TiN has a complex peak shape. Consequently, the Ti 2p spectra were satisfactorily fitted by using a 70% G/L, along with a term for asymmetry or tailing T(2). For the Nb 3d line the two spin-orbit peaks were fitted. The model used to fit the peak shapes were: 50% G/L for symmetric Nb oxides and 70% G/L along with a tailing T(2) for asymmetric conducting Nb components [116, 117]. The area ratio for the spin-orbit doublets was fixed to 1.5 and the energy distance to 2.7 eV. For Nb oxides the full width half maximum (FWHM) of the doublets is the same; while for Nb nitrides and oxynitrides, the Nb $3d_{3/2}$ peak is much broader than the Nb $3d_{5/2}$ peak [117]. Additionally, Nb oxide peaks were kept broader than the rest of the contributions.

4.4. Crystallinity:X-ray diffraction (XRD)

X-ray diffraction (XRD) is a non-destructive technique used to investigate the crystallographic structure of materials (e.g., identifying the crystalline phases or estimating the average grain size) by measuring the intensity of the diffracted X-rays as a function of 2θ,

where θ is the incident angle. In XRD measurements using the Bragg-Brentano geometry, the sample stays fixed while the X-ray source and detector rotate. The diffraction pattern is obtained by scanning θ. Peaks result from the constructive interference of X-rays, which occurs when the Bragg's law:

$$n\lambda = 2dsin\theta \tag{4.4}$$

where n is an integer, λ is the X-ray wavelength, d is the lattice plane spacing, and θ the incidence angle at which X-rays are diffracted, is satisfied.

The PANalytical Empyrean diffractometer at Universität Siegen with a Cu k_α source in the Bragg–Brentano geometry was used. The intensity of the diffraction peaks produced by the thin films is weak, due to their reduced thickness, compared to the high intensity substrate contribution. Grazing-incidence XRD (GIXRD) offers a solution by increasing the X-ray interaction with the thin film, enhancing its diffraction signal. The evaluated samples consist of thin-film AlN-NbTiN and AlN-NbN multilayers grown on Si, as-deposited and annealed (for both, RTA and STA treated). The scans sweep 2θ from 25° to 95°. Peak identification was performed by comparing the measured peak angle to reference data from the inorganic crystal structure database (ICSD). The lattice constant (a) was derived from the lattice plane spacing and the Miller indices (hkl) of the lattice planes, using the relation for the cubic phase is:

$$d_{hkl} = \frac{a}{\sqrt{h^2 + k^2 + l^2}} \tag{4.5}$$

The average grain size (D) in the direction perpendicular to the lattice plane (hkl) is given by the Scherrer equation:

$$D_{hkl} = \frac{K\lambda}{\beta_{hkl}\ cos\theta} \tag{4.6}$$

where K is the Scherrer constant shape related, λ is the X-rays wavelength, β_{hkl} is the FWHM of the diffraction peak, and θ is the Bragg angle.

4.5. Cryogenic characterisation

4.5.1. Four-probe points electro- and magneto-transport measurements

Electro- and magneto-transport measurements were conducted in a physical property measurement system (PPMS) DynaCool from Quantum Design, using the electrical transport option (ETO). Figure 4.2 provides an image of this setup which holds temperatures from 1.8 to 400 K and magnetic fields up to ± 9 T. The measurements were performed in AC standard four-probe configuration.
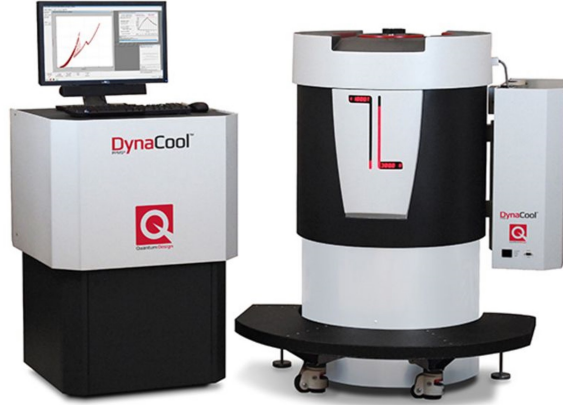
Figure 4.2: PPMS Dynacool. Image taken from Quantum Design Europe [118]

For the measurements the electrical current was set to 0.01 mA and the frequency to 6.1 Hz. On one hand, the electrical resistance was measured as a function of temperature: from 300 to 20 K in 0.5 K steps and from 20 to 2 K in 0.05 K steps. On the other hand, the resistance was measured as a function of perpendicular (out-of-plane) magnetic field from -9 to 9 T in 5 mT steps. The scope of these measurements was to determine the temperature T_c and width ΔT_c of the superconducting transition, the residual resistance ratio (RRR) and the upper critical field H_{c2}. The T_c was defined as the peak position of the derivative of resistance as a function of temperature and ΔT_c as the peak width. The RRR was defined as the ratio of the resistance at 300 to 20 K. It is useful since allows for a direct comparison of the structural quality and purity level between films. The H_{c2} was determined analogously to the critical temperature from the resistance vs magnetic field measurements.

4.5.2. Contactless inductive measurements

There are cases where having electrical contacts is not feasible. This would be the case when evaluating SIS multilayers grown on Nb. Using Nb as a substrate, which is softer and more malleable than Si, causes the thin multilayers to break. Therefore, contactless methods for evaluating the superconducting transition of NbTiN films are required. Two different methods were used depending on the Nb substrate dimensions. In the following, their details are given.

For Nb foils: Vibrating sample magnetometer (VSM)

Magnetometry was conducted using the vibrating sample magnetometer (VSM) option for the PPMS Dynacool (see Figure 4.3). This technique enables to study the magnetic moment of the sample in relation to temperature and applied magnetic field. Thus, for type II superconductors as it is the case of Nb and NbTiN, it is possible to explore the SC—Meissner and mixed—and NC states.
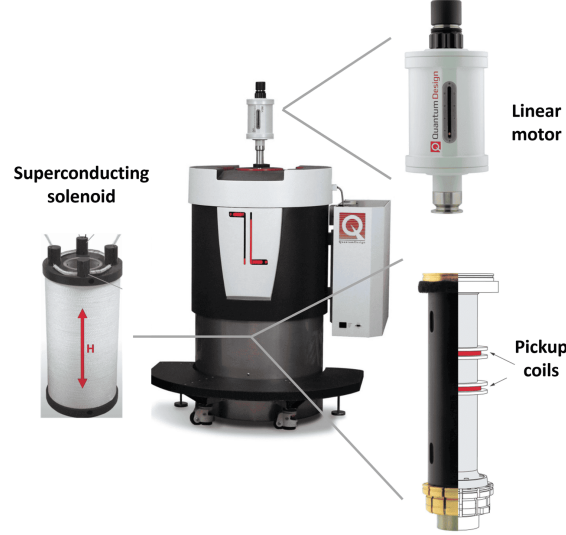
Figure 4.3: Parts of the VSM option for the PPMS Dynacool: superconducting solenoid, linear motor, and pickup coils. Image adapted from Quantum Design Europe [118]

The working principle of VSM relies on the Faraday's law induction. A superconducting solenoid generates a vertical magnetic field. The sample is mounted in a sample holder placed inside the solenoid and connected to a linear motor that makes the sample oscillate. This creates an oscillating field which induces a voltage in the pickup coils which can be linked to the magnetic moment of the sample (m) and the amplitude (A) and frequency (ω) of the oscillations by:

$$V_{coil} = -\frac{d\Phi}{dt} = -\left(\frac{d\Phi}{dz}\right)\left(\frac{dz}{dt}\right) = CmA\omega sin(\omega t) \tag{4.7}$$

Thick Nb substrates are not feasible for this measurement option; thus, Nb foils were employed. To emulate the environment of a SRF cavity, the samples were placed with the applied magnetic field orientated parallel to the sample surface (in-plane). Despite this, experimental limitations rule out the applied field from being entirely parallel to the sample surface. Additionally, to prevent trapped flux the samples were cooled down below T_c without an externally applied field, named zero field cooling (ZFC). In addition, a warming-up procedure, above T_c, was also executed to release the trapped flux between each measurement. Moreover, the VSM operates at an oscillation amplitude of 2 mm and a frequency of 40 Hz.

Magnetic moment measurements were conducted in two ways: as a function of temperature under a constant magnetic field, and the opposite, as a function of the applied field at a fixed temperature. On one hand, the m(T) curves were taken from 4.5 to 20 K in steps of 0.5 K in an applied field of 50 Oe. The T_c was defined as the onset of the magnetic moment change. On the other hand, for the m(H) curves the magnetic field was increased from 0 to 1500 Oe in steps of 50 Oe at six different constant temperatures. Because of the defects, the m(H) curve shows a rounded rather than a sharp maximum, which makes H_{c1} difficult to identify. Instead, the first penetration field (H_{fp}) was determined. The H_{fp} represents the magnetic field at which the first magnetic flux penetrates the superconductor. In the

m(H) curve the H_{fp} corresponds to the field at which the magnetic moment deviates from the linearity characteristic of the Meissner state. Thus, H_{fp} was defined using the criterion $\Delta m = 1.8 \times 10^{-5}$ emu, being Δm the magnetisation curve after subtracting the Meissner line [119, 120]. Moreover, demagnetisation effects caused by the sample geometry [121], which lead to early flux penetration, were considered. Thus, an approximation of H_{c1} was obtained.

For bulk Nb

SIS multilayers grown on bulk Nb samples of size $11 \times 35 \times 1\,\mathrm{mm}^3$ were evaluated at the central cryogenic laboratory at CERN. The measurement station consists of a contactless two-coil system operated in a cryostat. Its measurement principle is based on an inductive technique that detects the magnetic field expulsion as the sample turns superconducting, a result of the Meissner effect.

A schematic of the measurement setup is given in Figure 4.4. The two coils are parallel with opposite orientations. The sample to be measured is placed between the two coils with its faces parallel to the coil planes. The coated side faces the so-called drive coil, through which an AC current is driven, generating an alternating magnetic field which induces a voltage in the pickup coil, at the opposite sample side. The measure starts at $4.5\,\mathrm{K}$ to prevent flux trapping while cooling down. Later the drive coil is turned on. Because the sample is in SC state, the screening currents prevent the magnetic field from penetrating it, so the pickup coil detects only a base background noise sum of the external noise and the
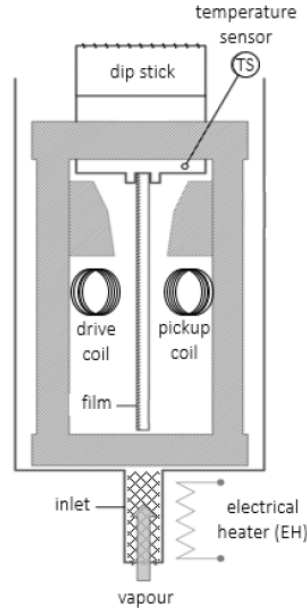
Figure 4.4: Schematics of the contactless inductive station for measuring the superconducting transition of films at CERN for SRF applications. The schematic of the complete experimental setup is given by Fonnesu et al. [122]. The measurements were conducted by Lea Preece (UHH) and Daniel Turner (CERN).

field leaking around the sample. The temperature then is ramped up. When temperature achieves T_c the transition from SC to NC state causes a jump in the detected signal, as a result of the magnetic field entering the sample and reaching the pickup coil.

One limitation of this method is that it is not possible to detect a film T_c below the T_c of Nb. The substrate, still in its SC state, blocks the field lines from reaching the pickup coil, screening the film SC to NC transition.

5. Determination of film thickness

This section explores the thickness determination of PEALD-grown films, whose deposition process has been detailed in section 3. The discussion extends to the analysis and assessment of film thickness. Moreover, the evaluation of various film thicknesses, i.e., different numbers of PEALD cycles performed, enables GPC determination. The investigation covered various films: NbN, TiN, NbTiN, and AlN, along with multilayers, before and after post-deposition annealing.

5.1. Transition metal nitrides: NbN, TiN, and NbTiN thin films

This section introduces the thickness studies conducted on NbN, TiN, and NbTiN thin films. The results presented here are based on measurements performed on thin films deposited on silicon substrates, rather than niobium substrates. This is due to the significant surface roughness of our Nb conical substrates after the surface preparation process detailed in Section 3, which limits XRR analysis.

5.1.1. Evaluating NbN thin films: thickness and GPC determination

Four different NbN thin films were measured by XRR. These films were deposited under identical conditions with the only difference being the number of cycles conducted, resulting in different film thicknesses. The evaluated films correspond to 200, 300, 400, and 1000 PEALD cycles deposited on different silicon substrates; therefore, different samples. As observed, a greater number of cycles implies increased thickness evidenced by shorter periods of oscillations—demonstration in Equation 4.3. The thickness of the films was evaluated using two different approaches: Analysis of the Kiessig fringe period and fitting of the reflectivity curves. For the fitting, the elements considered were: The Si substrate, the native SiO_2, and the layer under examination. Neither Nb surface oxides nor oxynitrides, additional interface, and hydration layers were contemplated. Thus, the analysis is simplified, although it limits its accuracy. Note, the aim here is to deduce the GPC of the NbN PEALD process. Hence, the investigated samples are as-deposited.

The reflectivity curves at low angles for the four NbN samples are shown in Figure 5.1. It is noticeable that the 400 cycles sample reveals a larger critical angle in comparison to the other three samples. The critical angle, which establishes the limit to X-rays from total reflection to penetrate the material undergoing refraction, can be written using Snell's law as

$$\theta_c \approx \sqrt{2\delta} \tag{5.1}$$

where the real part of the refractive index is related to the scattering properties by

$$\delta = \frac{\lambda^2}{2\pi} r_e \rho_e \tag{5.2}$$

with ρ_e the electron density of the material. Hence, a larger critical angle indicates higher electron density. Therefore, the 400 cycles sample exhibits a different film structure and/or

composition, just as uniform critical angles across the other samples—200, 300, and 1000 cycles—suggest that these samples are consistent with each other. The analysis software GenX uses the density of each layer expressed in units formula per cubic angstrom (FU Å^{-3}). As a result, the fitted mass density is between 4.9 and 5.4 g cm^{-3} for all samples except the 400 cycles sample, which is 7.8 g cm^{-3}. The bulk NbN density is 8.47 g cm^{-3} [123]; however, for NbN thin films, it varies with the deposition technique and conditions. For PEALD-films grown at 250 °C the reported densities are: 6.5 g cm^{-3} [90], 7.6 g cm^{-3} [87], and 7.9 g cm^{-3} [79], while for thermal ALD (deposition temperature is 450 °C), is 7.5 g cm^{-3} [68]. In the case of reactive magnetron sputtering is 6.8 g cm^{-3} [124]. Compared to these values, the densities obtained in the current study—except for the value corresponding to the 400 cycles sample—are notably lower. Indeed, the values are more consistent with the densities of Nb oxides (Nb$_2$O$_5$=4.6 g cm^{-3} [125] and NbO$_2$=5.9 g cm^{-3} [126]) rather than with NbN. It is well known that NbN oxidises when exposed to air, with nitrogen being replaced by oxygen to form Nb oxides at its surface [113]. Considering this, incorporating additional layers of Nb oxides, oxynitrides, or both into the XRR fitting model is beneficial for more comprehensive results. The distinct behaviour of the 400 cycles sample may be attributed to a reduced interval between deposition and XRR analysis; however, since it has not been systematically investigated, it remains speculative. Additionally, as shown in Figure 5.2, the 400 cycles curve exhibits larger amplitude oscillations at low angles. It indicates that the 400 cycles film may have not only a higher electron density but also smoother interfaces or greater homogeneity, than the other samples. Rougher interfaces cause X-rays to scatter in various directions, leading to a reduction of the amplitude of oscillations. This observation aligns with the assumption of the 400 cycles film having none or less oxidation compared to the other measured samples.
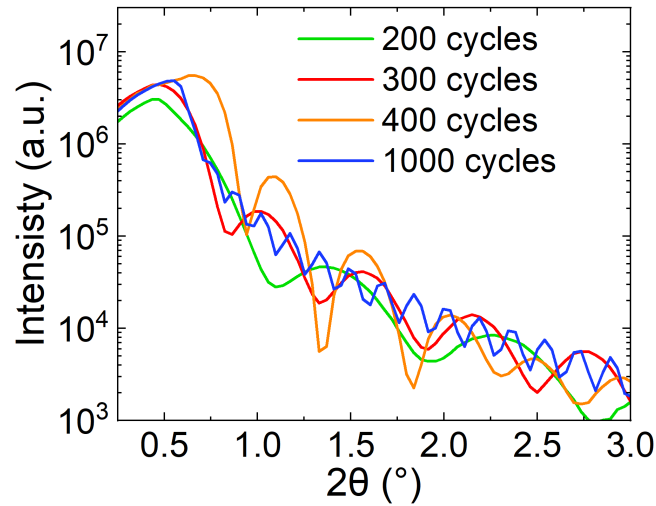
Figure 5.1: Reflectivity curves at low angles for four different NbN films. Notably, the orange curve which corresponds to 400 cycles, exhibits a shifted critical angle and a larger amplitude. It suggests a notable difference in electron density relative to the other films.
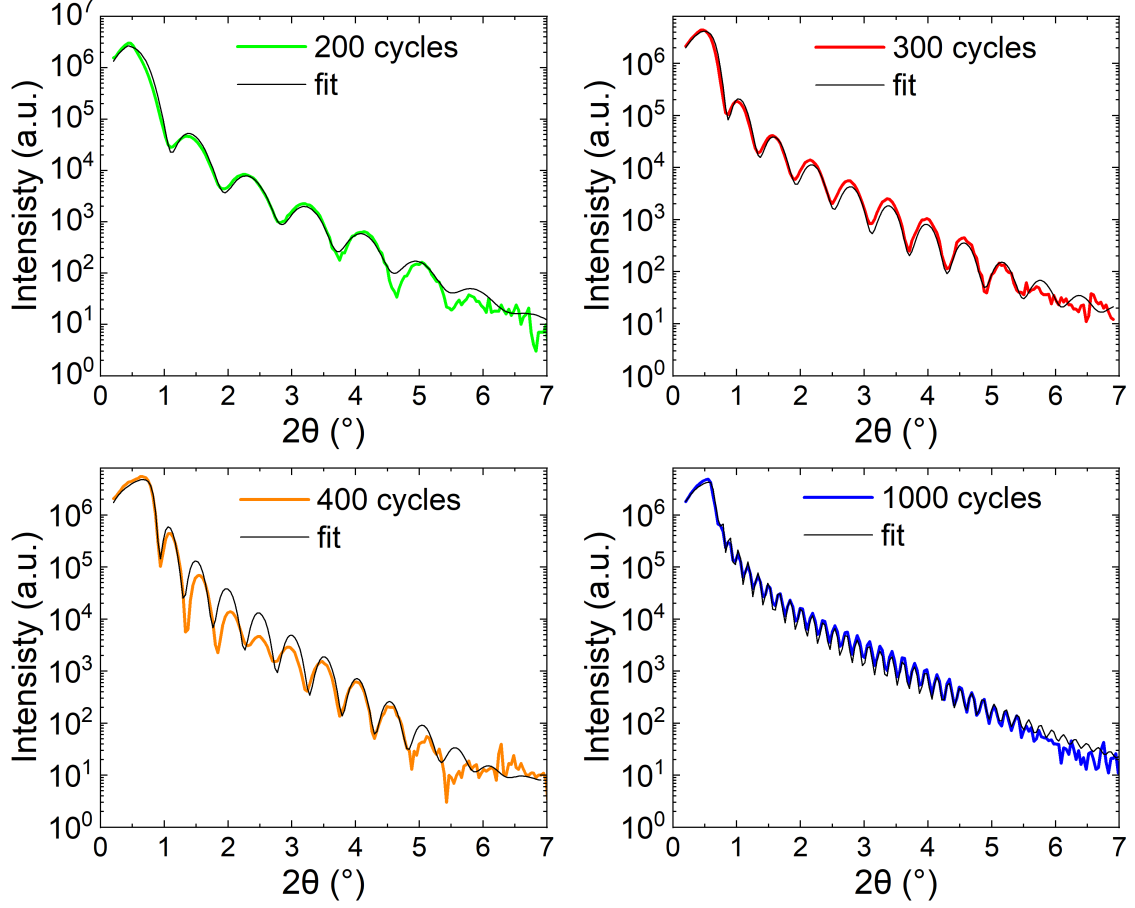
Figure 5.2: X-ray reflectivity profiles for four NbN films with different thicknesses, corresponding to deposition cycles of 200, 300, 400, and 1000. Film thickness increases with the number of cycles as evidenced by the shorter period of oscillations. The colour solid lines represent the experimental data while the black solid lines are the fits. To improve the fit, more layers may be added to the model. This change would primarily impact oscillation amplitude, driven by roughness and electron density, with only slight effects on thickness, which depends on fringe spacing.

The thicknesses of the NbN films were determined from the four rocking curves shown in Figure 5.2, through both fitting and analysis of the Kiessig fringes. The obtained values are presented in Figure 5.3 as a function of the number of cycles. There are small deviations between thicknesses obtained from both methods, turning slightly more pronounced when increasing the number of cycles. The result for 400 cycles deviates from linearity towards lower thickness, indicative of a reduction in its GPC, suggesting a denser film. This observation aligns with the film densities mentioned above, obtained from fitting. The obtained average—excluding the 400 cycles sample—GPC_{NbN} is $0.050 \pm 0.001\,nm/cycle$, which is slightly lower than our estimate of $0.06\,nm/cycle$ [102, 103]. This prior estimate was derived from the composition ratio of Nb to Ti in $Nb_xTi_{1-x}N$ films (measured by EDX) and the supercycle ratio m:n (see Table 3.1), using the known GPC for TiN. An explanation for the variance in the GPC_{NbN} could be the influenced growth within the supercycle vs the
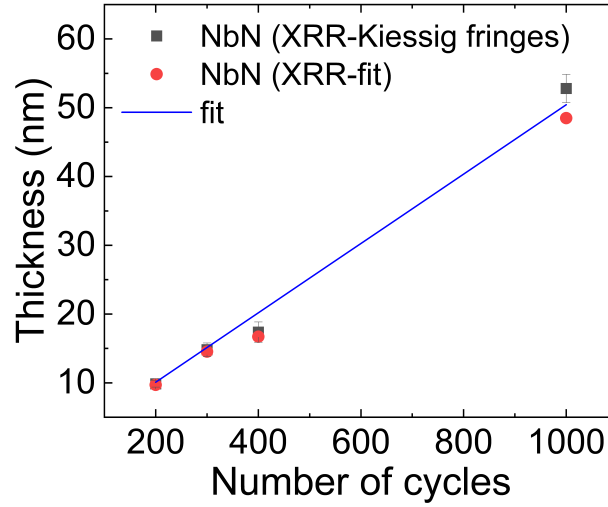
Figure 5.3: Linear relationship between NbN film thickness and the number of PEALD cycles completed. Data points extracted from XRR curves: Kiessig fringes analysis (black squares) and fitting (red circles). The blue line fits y = mx with $R^2 = 0.998$. The slope is 0.050 ± 0.001 nm/cycle and represents the GPC_{NbN}. The values corresponding to the 400 cycles sample were excluded from the fit due to the deviation from linearity. This deviation suggests a decrease in GPC, suggesting a denser film.

NbN cycle. Furthermore, the obtained GPC_{NbN} is consistent with PEALD films deposited at the same temperature [87, 91] and at 300 °C [79]. Although, other studies report higher GPC values of $0.064 - 0.069$ nm/cycle [84, 85, 87, 88] and lower values $0.015 - 0.04$ nm/cycle [89, 90] GPC_{NbN} using also TBTDEN as the precursor. Conversely, a GPC of 0.025 nm/cycle is reported for thermal ALD using chlorine precursor at 450 °C [68]. Hence, the GPC strongly depends on the chemistry and deposition conditions.

5.1.2. Evaluating TiN thin films: thickness and GPC determination

The study comprised the analysis of six different samples which exclusively differ in the number of TiN PEALD cycles conducted, ranging from 100 to 300 cycles. The film thickness was assessed using XRR—only for the films with 200 and 300 cycles—and spectroscopic ellipsometry (SE). Two rocking curves—corresponding to 200 and 300 cycles—are shown in Figure 5.4. It is visible that the period of the oscillations shortens when increasing the number of cycles. The film thickness was derived from the analysis of the Kiessig fringes. These reflectivity profiles show well-defined oscillations at lower angles, but a pronounced damping as the incident angle increases. The strong attenuation suggests a low electron density contrast between the TiN layer and the substrate, indicating a poorly defined and less sharp interface. This observation suggests the presence of an interfacial layer between the TiN and the native SiO_2. Previous studies have shown that plasma can cause the formation of an interfacial layer between the PEALD deposited layer and the substrate. An analysis of this effect for the various layers under investigation—NbN, TiN, NbTiN, and
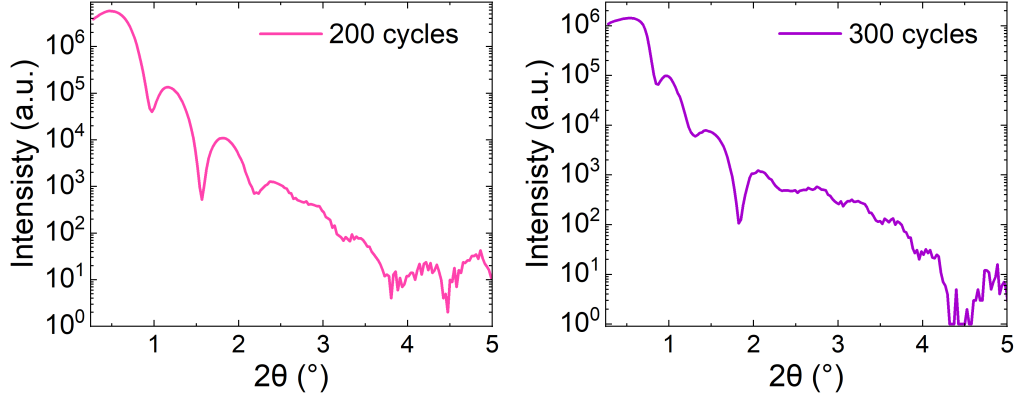
Figure 5.4: X-ray reflectivity profiles corresponding to two TiN films with 200 and 300 cycles. Film thickness increases with the number of cycles as evidenced by the shorter period of oscillations.

AlN—is given in the conclusions of this section. On another note, a closer look at the low-angle regions in Figure 5.4 indicates increased roughness for the 300 cycles film relative to the 200 cycles film, evident in the blurred oscillations caused by the rougher surface. As films grow thicker, i.e., with more cycles, the surface can become rougher due to the accumulation of growth imperfections.

The GPC for TiN deposited by PEALD at $250\,°\mathrm{C}$ is given by the slope of the fit in Figure 5.5. The obtained value is $0.069 \pm 0.001\,\mathrm{nm/cycle}$. For comparison, literature values for $\mathrm{GPC_{TiN}}$ using TDMAT are in the range of $0.035 - 0.077\,\mathrm{nm/cycle}$ [78–80, 82, 127], since
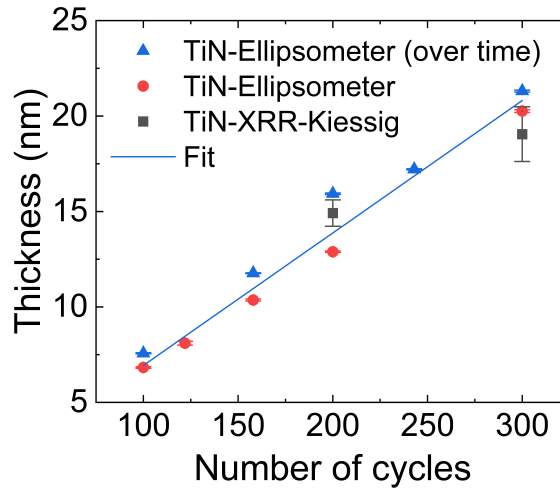
Figure 5.5: Relationship between TiN film thickness and the number of PEALD cycles completed. Six different samples were studied.. The thickness was evaluated via SE, after deposition and over time, and with X-ray reflectivity, derived from the analysis of the Kiessig fringes. The blue line fits all data points by a linear relationship which intercepts at the origin. The slope, which gives the $\mathrm{GPC_{TiN}}$, is $0.069 \pm 0.001\,\mathrm{nm/cycle}$ and $R^2 = 0.995$.

the GPC is influenced by the deposition conditions. For TiCl$_4$ as alternative precursor, lower GPC is obtained, ranging from 0.026 - 0.06 nm/cycle for PEALD [94, 95], and of 0.019 nm/cycle for thermal ALD [68].

5.1.3. Evaluating NbTiN thin films: thickness and GPC determination

Six NbTiN films were measured by XRR: three corresponding to 100 supercycles and three to 243 supercycles. Two XRR profiles—one for 100 supercycles, the other for 243—are compared in Figure 5.6. The increase in thickness and surface roughness with the number of supercycles is indicated by shorter periods and damped oscillations. Furthermore, these curves exhibit a pronounced flattening when increasing 2θ above 2 ° (see Figure 5.2 for comparison). It is due to diffuse scattering and low electron density contrast, resulting from a non-sharp interface between NbTiN layer and substrate, a behaviour also observed for TiN but not for NbN. Formation of interfacial layers between NbTiN and substrate can be the origin of flattening. Another hypothesis could be the presence of non-uniformities or voids at the bottom of the PEALD deposited layer. Indeed, PEALD, at the early stages of the nucleating phase, is associated with island growth before coalescing into a continuous film. However, this hypothesis is dismissed, as the observed flattening is too pronounced to result from minor anomalies. Moreover, it would also occur for NbN, which is not the case (see Figure 5.2). Given the significant degree of flattening observed the previous explanation is more plausible.
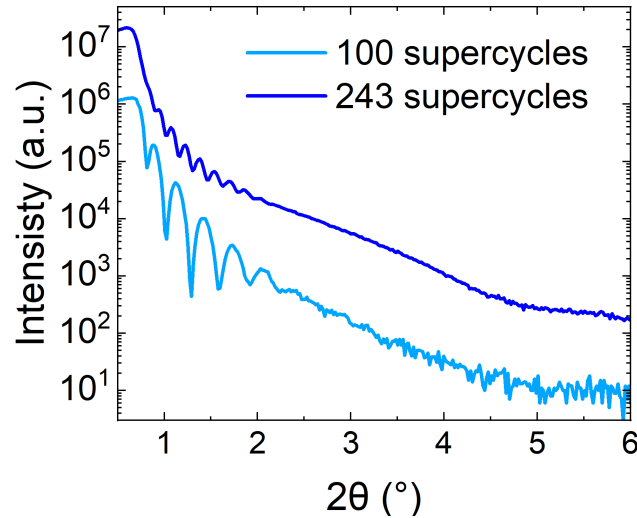
Figure 5.6: Comparison of XRR profiles for NbTiN films with 100 and 243 supercycles. Film thickness increases with the number of cycles as evidenced by the shorter period of oscillations. Surface roughness also increases with the number of cycles, indicated by dampened oscillations at low angles. Both curves exhibit significant flattening at angles above 2 °, indicating interfacial roughness or non-sharp electron density boundaries.
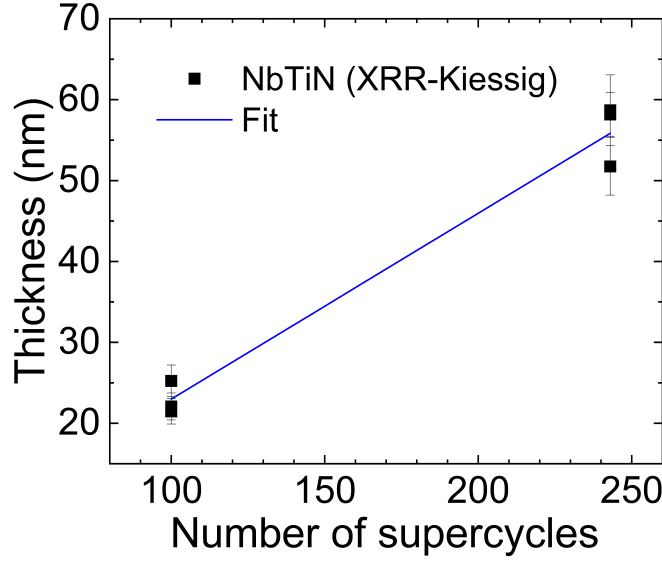
Figure 5.7: NbTiN film thickness versus the number of PEALD supercycles. Data points are obtained from the Kiessig fringe of the XRR curves. The slope of the blue fit gives the GPC_{NbTiN} of a supercycle, which is 0.229 ± 0.006 nm/supercycle. $R^2 = 0.996$.

The film thickness was derived from the analysis of the Kiessig fringes in Figure 5.6. The obtained values, plotted as a function of the number of cycles, are shown in Figure 5.7. The derived GPC_{NbTiN} is 0.229 ± 0.006 nm/supercycle. It is worth noting that the optimised NbTiN supercycle includes 1 TiN cycle and 3 NbN cycles. By comparison, the calculated GPC_{NbTiN} from the growth rates of the individual PEALD processes, i.e., $1 \times GPC_{TiN} + 3 \times GPC_{NbN}$, is 0.219 ± 0.004 nm/supercycle.

5.2. Investigating thickness of AlN thin films

This subsection presents the thickness evaluation of the other layer of interest for SIS multilayers, i.e., the AlN. The AlN films were examined via XRR and SE. Six different samples—with the number of PEALD cycles ranging from 150 to 350—were examined, of which only one was studied with XRR. SE was chosen for its more rapid execution over XRR. Figure 5.8 shows the reflectivity curve where the Kiessig fringes, particularly at low angles, appear blurred. It suggests irregularities at the surface and interface such as roughness and intermixing material, as discussed before. The fringe period was examined, yielding to a GPC_{AlN} of 0.070 ± 0.001 nm/cycle. Conversely, thicknesses obtained via SE are displayed in Figure 5.9 as a function of the number of PEALD cycles, resulting in a GPC_{AlN} of 0.069 ± 0.001 nm/cycle. Both results are consistent with each other and align with literature values [128].
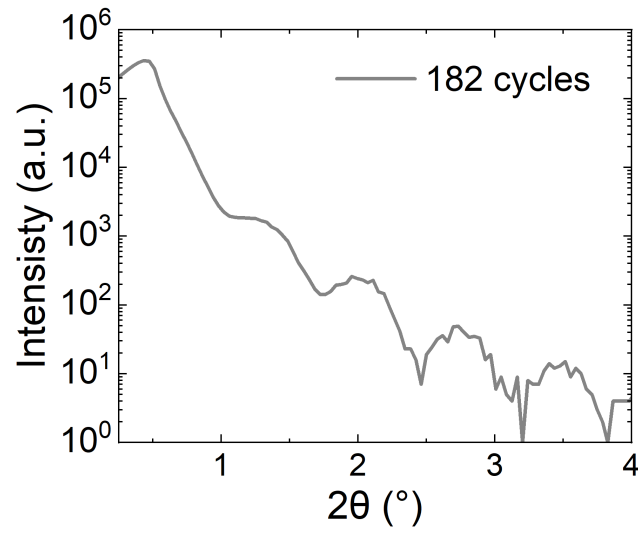
Figure 5.8: XRR curve for 182 PEALD cycles of AlN film grown at 250 °C. Blurred oscillations suggest a low electron density contrast at the interface with the substrate and surface roughness.
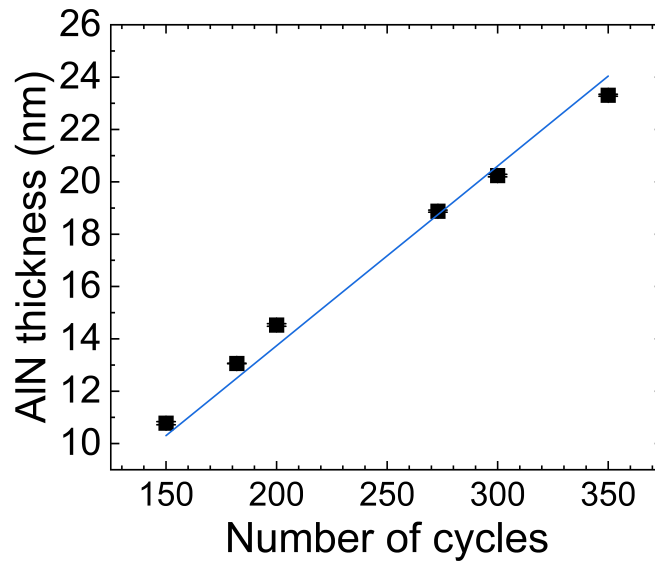
Figure 5.9: AlN film thickness, measured through ellipsometer, as a function of the number of PEALD cycles, ranging from 150 to 350. Films deposition was at 250 °C. The blue line represents y = mx, with the slope 0.069 ± 0.001 nm/cycle representing the GPC_{AlN} and $R^2 = 0.997$.

5.2.1. Impact of deposition temperature on AlN thin film thickness

As earlier mentioned in Section 3, PEALD of AlN was studied at different temperatures to overcome blistering. Additional information can be found in Section 6. Here, the focus is the thickness evaluation of AlN films deposited at temperatures between 80 °C and 250 °C. The deposition temperature plays a significant role in the film growth. It influences both surface chemistry and the kinetics of surface reactions; hence, its impacts on the growth rate [87]. Typically, higher deposition temperatures result in denser films, hence reduced thickness and lower GPC, as revealed in Figure 5.10. Conversely, a dramatic thickness increase at high deposition temperatures would be a sign of precursor decomposition, resulting in CVD growth. However, it is not the case here, as TMA starts to decompose around 370 °C [129]. On the other hand, a prominent increase in thickness at low deposition temperatures would indicate either precursor condensation or deposition of chemically non-inert films which can drastically oxidise [96].
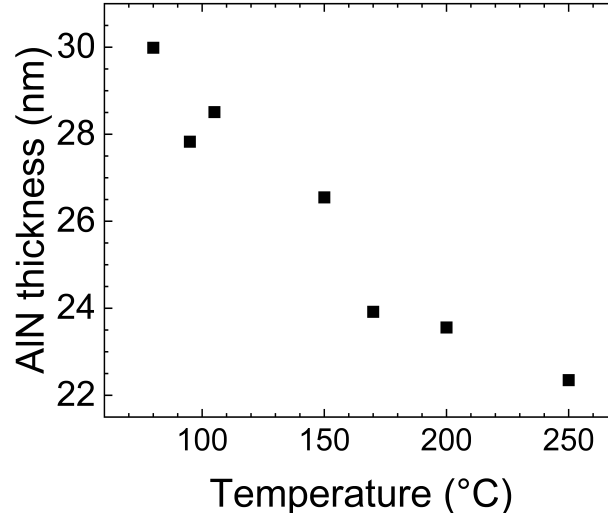
Figure 5.10: Thickness as a function of deposition temperature for AlN films deposited by PEALD. Thickness was determined via SE.

5.3. Impact of post-deposition thermal annealing on AlN-NbTiN multilayers

The final part of this section is dedicated to a brief analysis of the target multilayers through XRR. In particular, the samples investigated consist of AlN-NbTiN and AlN-NbN multilayers, deposited in vacuo, with the dielectric first, followed immediately by the superconductor. The multilayers are comprised of 200 cycles of AlN and 100 supercycles of NbTiN or 400 cycles of NbN, resulting in a stack with two layers of roughly 15 nm and 25 nm, respectively. The samples were investigated as-deposited and after the two post-deposition thermal treatments namely RTA and STA—described in Section 3. The goal is to see the effect of post-deposition annealing on the multilayers. This investigation proved complex
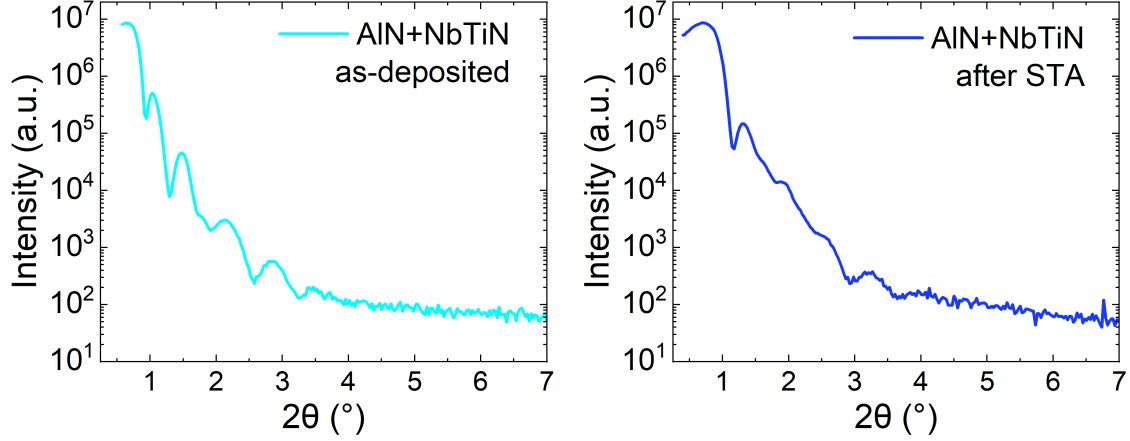
Figure 5.11: Comparative of XRR profiles for AlN-NbTiN multilayers: as-deposited (left) and after STA (right). Strong damping occurs due to STA, suggesting poor electron density contrast at the interfaces, indicating interface mixing.

due to several factors. On one hand, unknown oxidation layers on the surface and limited knowledge of interfacial layers on the substrate and between layers limited fitting accuracy. On the other hand, the XRR profiles revealed blurred Kiessig fringe, making fitting essential for film thickness analysis. Finally, silicon substrates introduced interface variations relative to niobium, which is the relevant substrate for multilayer applications on SRF cavities. Hence, considering the fitting complexity and the used of silicon as substrate, an elaborate analysis was not conducted. Consequently, the study is a qualitative examination of multilayer XRR profiles before and after annealing, while addressing potential reasons for the observed changes.

For AlN-NbTiN, Figure 5.11 includes the rocking curves from the multilayers as-deposited and annealed (STA). On one hand, for the multilayers as-deposited, the profile shows pronounced oscillations, indicating uniformity and distinction between the NbTiN and AlN layers. Although, the flattening at angles above $3°$ suggests blurred substrate-AlN interface, as discussed before. On the other hand, after annealing, the oscillations are damped and blurred, indicating substantial interfacial changes and reduced smoothness. This observation is validated by cross-sectional TEM studies, which show layers intermixing (see Section 6). Intermixing between AlN-NbTiN multilayers due to high temperature ($>600\,°C$) was also observed by Valente-Feliciano et al. [130]. This effect, however, seems to be more significant for AlN-NbTiN than AlN-NbN multilayers (see Figure B.1 in Appendix B.1). This could be explained by the higher affinity of Ti for the multilayers components over Nb. Lastly, a shift to larger angles in the critical angle after annealing suggests an increase in density which agrees with Sowa et al. [87], and indicates changes in the surface oxides.

5.4. Summary and conclusions

The conducted survey allowed the thickness determination for each of the layers under study, essential for deriving the GPC for each PEALD process. The obtained values are listed in Table 5.1. Moreover, XRR has proven to be a powerful tool for investigating the layers and

Table 5.1: Values of growth per cycle (GPC) obtained for each PEALD process at 250 °C. *Growth per supercycle, where the supercycle comprises $1 \times$ TiN + $3 \times$ NbN cycles.

PEALD Layer	AlN	TiN	NbN	NbTiN*
GPC (nm/cycle)	0.069 ± 0.001	0.069 ± 0.001	0.050 ± 0.001	0.219 ± 0.004

multilayers. It provides valuable information on thickness, surface roughness, and interfacial properties.

The potential appearance of interfacial layer between the deposited layer and the substrate can be attributed to a plasma-induced effect. The ions may transfer their kinetic energy to the surface at impact, inducing surface modification. The increased energy can enhance diffusion at the interface, resulting in interface layer formation. Furthermore, the reactive radicals can diffuse beneath the surface, possibly affecting the bonding structure. The presence of interfacial layer between the deposited layer and the substrate is suggested for the XRR profiles of AlN, TiN, and NbTiN, although not for NbN layers. For AlN, the presence of interfacial layers is confirmed by complementary cross-sectional EDX analysis presented in section 6. Figures 6.2 and 6.4 point to the presence of three layers: AlN, Al_xO_y or $Al_xO_yN_z$, and Si_xN_y or $Si_xO_yN_z$. Previous studies of AlN deposited by PEALD have shown the high affinity of AlN for oxygen and the appearance of interfacial layers—oxidation of PEALD layer or nitridation of silicon—when using silicon substrates [131–133]. For TiN, NbTiN, and NbN complementary analysis are still required. Previous studies for TiN PEALD have shown the formation of SiN_x, SiO_xN_y, TiO_2, or TiO_xN_y depending on the experimental conditions [94, 95, 134]. However, for the interface between the NbN PEALD layer and Si, higher oxygen concentrations are reported, but no evidence of interfacial layer formation has been found in the literature.

To understand why interfacial layer forms at the TiN/SiO_2 interface but would not at the NbN/SiO_2 interface, various potential explanations are addressed. First, from thermodynamic point of view. The Gibbs free energies were not calculated, as the plasma introduces complexities that make the precise chemical reactions unknown. However, comparing heats of formation provides valuable insights into the relative stability of each compound. The values—obtained from [135, 136]—are sorted from most negative to least negative:

ΔH_f^0 (heat of formation)
$Nb_2O_5 < Al_2O_3 < TiO_2 < SiO_2 < NbO_2 < Si_3N_4 < NbTiN < NbO < TiN < AlN < NbN$

The ΔH_f^0 indicates that from the Nb oxides only Nb_2O_5 would be more stable than SiO_2. While for Al_2O_3 and TiO_2 both are more stable than SiO_2. However, since the exact interfacial compounds are unknown, this remains speculative. Another hypothesis could consider differences in oxygen solubility between TiN and NbN; however, this has been dismissed due to the amorphous nature of the films during the initial ALD cycles, i.e., at the interface. The next assumption account on the affinity with oxygen. Oxygen shows stronger affinity with TiN than with NbN [137]. Hence, it would tend to form TiO_2 at the SiO_2 interface, which would act as an oxygen barrier. While for NbN, Nb oxide species could still form, although they would not be capable of stopping oxygen diffusion, preventing a defined layer from forming. This hypothesis would be support by the observation of TiO_2

acting as a better diffusion barrier than Nb oxides [138, 139]. However, further studies, e.g., XPS depth profiling or synchrotron-based XRR, are need to shed more light at interfaces.

Lastly, XRR profiles for post-deposition annealed multilayers point to layers intermixing—more prominent for NbTiN than NbN—and rough interfaces. See Appendix B.1 for further details.

6. Microscopic analysis of thin films and multilayers morphology

Understanding the specifics of the morphology of PEALD coated thin films and multilayers is crucial for assessing their potential for SRF cavity applications. Surface roughness and localised defects have been shown to cause degradation of SRF cavity performance [4, 140, 141]. This section explores the study of cross-section and surface morphology. It includes the evaluation of the layers of interest—individual layers and multilayers—as well as the influence of Si or Nb as substrates. Furthermore, the impact of the post-deposition annealing on the sample morphology is also investigated. Scanning electron microscopy (SEM) and transmission electron microscopy (TEM) combined with energy dispersive X-ray spectroscopy (EDX), as well as atomic force microscopy (AFM) were utilised.

6.1. Interfaces examination through cross-section view

The purpose of this analysis is to shed light on the interfaces of the multilayer systems studied. Cross-sections of AlN-NbTiN multilayers grown on Si and Nb have been examined, before and after annealing. Lamellas were fabricated using a focus ion beam (FIB) and analysed through SEM and TEM at the Technische Universität Hamburg, using the systems Talos F200X and Helios Nanolab G3 UC, both from Thermo Fisher. The fabrication of the lamella includes depositing ${\sim}2\,\mu\mathrm{m}$ of a Pt layer to avoid any multilayer damage, for improved cross-section view, and easier welding and transfer of the lamella to the TEM grid. Before imaging, the Pt layer was milled to a thickness of ${\sim}200\,\mathrm{nm}$. Subsequently, elemental mapping via EDX was performed.

6.1.1. Multilayers grown on Si substrate

The images in Figure 6.1 show the cross-sectional view of the multilayers in their as-deposited state and after annealing. For the as-deposited multilayer (Figure 6.1 a), a crystalline and well-adhered NbTiN film is observable. However, in the case of AlN, multiple layers are observed instead of a single AlN film. At the AlN-NbTiN interface, a pronounced layer is visible; while at the AlN-Si interface, another layer or intermixing of layers is suggested. This observation is consistent with the XRR analysis (see Section 5). A potential explanation for this behaviour is the diffusion of oxygen from the native silicon oxide present on the silicon surface. To investigate this further, elemental analysis was performed using EDX. As for the annealed multilayers (Figure 6.1 b), darker areas within the AlN film suggest intermixing and a blurred NbTiN/AlN interface as a consequence of the high temperature. The XRR analysis in Section 5 supports this observation. Elemental mapping was also performed for the annealed multilayers. The elemental mappings are shown in Figures 6.2 and 6.3 for the as-deposited and annealed multilayers, respectively. The measured elements are: Nb, Ti, Al, N, O, and Si.
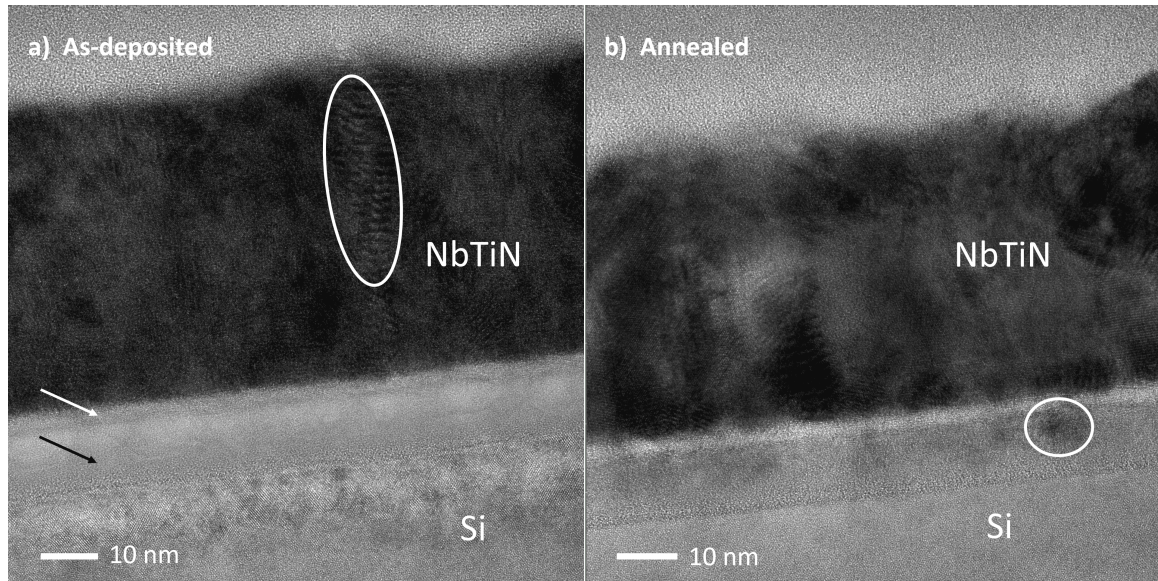
Figure 6.1: Cross-sectional view of Si-AlN-NbTiN multilayers: a) as-deposited and b) annealed. a) Crystal grains and planes reveal the crystalline nature of NbTiN. In place of AlN film, various layers are visible. b) Annealing results in blurred AlN-NbTiN interface and intermixing, evidenced by the darker areas within the AlN film. Markers serve as guides to eye.

The observations derived from Figure 6.2 for the as-deposited Si-AlN-NbTiN multilayers are as follows. The presence of a NbTiN film is obvious. It shows a native oxide layer on its surface and some oxygen traces within. The interface AlN-NbTiN is observed to be sharp. In addition, the pronounced layer at the AlN-NbTiN interface—also visible in Figure 6.1—is identified as AlN; while aluminium oxide may form beneath it. Furthermore, nitrogen and silicon signals suggest the nitridation of the substrate. Both phenomena—formation of interfacial oxide and nitridation of the substrate—may be plasma-induced as earlier explained (see summary and conclusions in Section 5). Previous studies of PEALD AlN have shown the appearance of an oxide interfacial layer and nitridation of silicon [131–133]. Lastly, Figure 6.2 suggests good adhesion between the deposited layers and the substrate, as no voids are visible at the interfaces.

For annealed multilayers, Figure 6.3 displays the elemental mapping. The oxygen signal indicates that the native oxide persists with annealing. XPS studies suggested increased surface oxidation caused by annealing (see surface XPS analysis in Appendix B.4). The oxygen within the NbTiN film persists despite the high-temperature annealing. In place of the AlN layer, the elemental mapping confirm the presence of Al, O and N, presumably forming AlO_xN_y. Furthermore, Figure 6.3 reveals that the dark areas seen in Figure 6.1 are Ti, suggesting that annealing causes Ti diffusion into the AlN film. Moreover, Al diffusion into the overlying layer. The finding aligns with the observations extracted from the XRR analysis (see Section 5) and agrees with the work done by Valente-Feliciano et al. [130], which indicates AlN-NbTiN intermixing at high temperatures (>600 °C). Lastly, annealed multilayers exhibit partial delamination, presumably due to different thermal expansion coefficients between the substrate and thin films. This observation is demonstrated for mul-
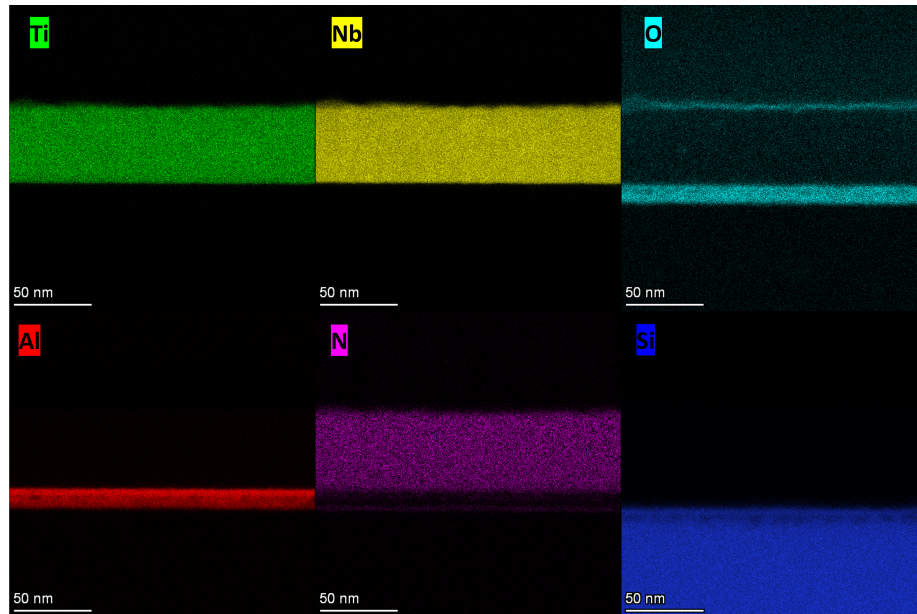
Figure 6.2: EDX elemental mapping: Cross-sectional view of **as-deposited** AlN-NbTiN multilayers grown on Si. The O signal reveals the formation of a native oxide layer on the NbTiN surface. In place of AlN, Al, O, and N are present; with higher Al concentration at the interface with NbTiN. A close look at N and Si signals suggests substrate nitridation and lower densification of the substrate.
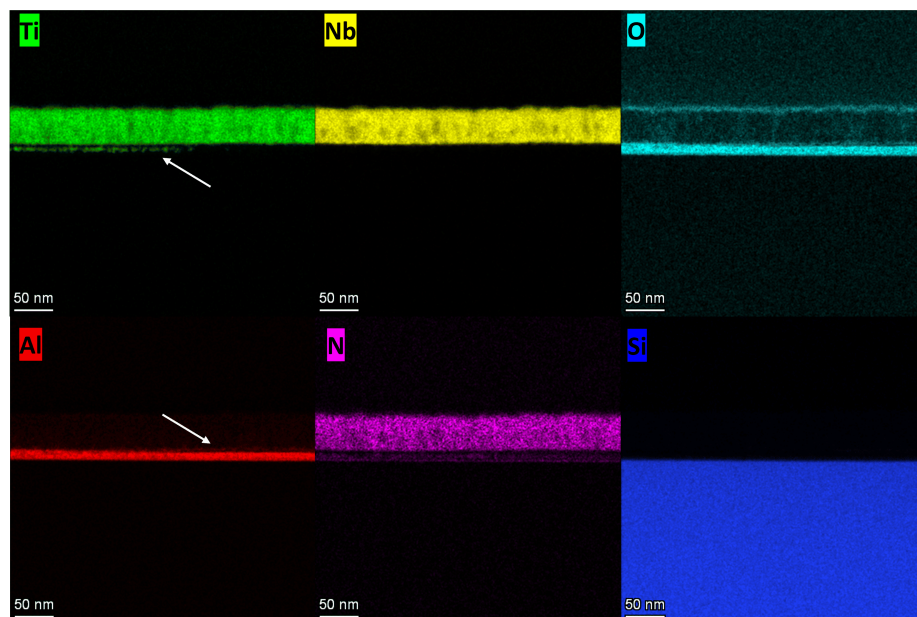
Figure 6.3: EDX elemental mapping: Cross-sectional view of **annealed** AlN-NbTiN multilayers grown on Si. Native NbTiN oxides are present. The arrows indicate Ti and Al diffusion into the other layer. Al, O, and N signals suggest the formation of AlO_xN_y.
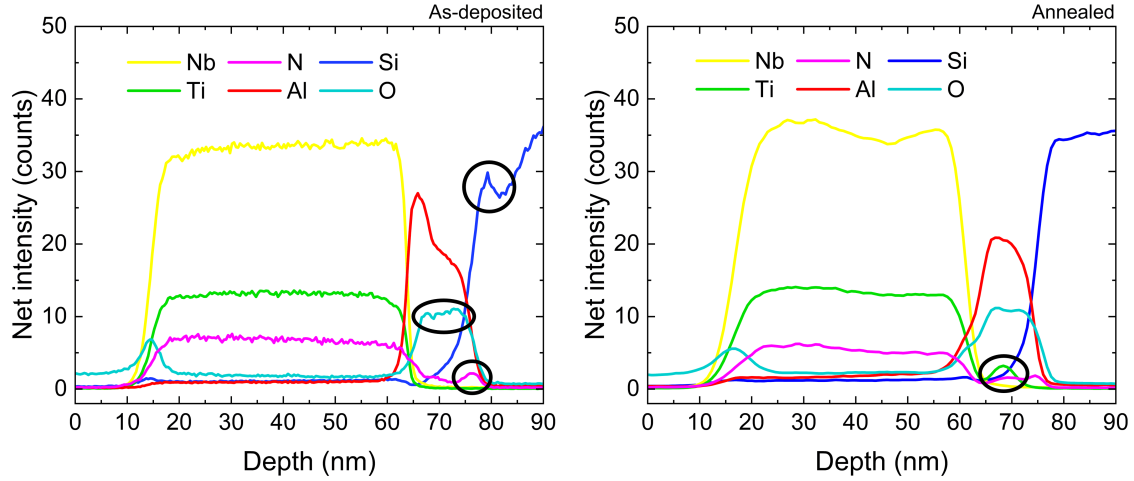
Figure 6.4: EDX depth profile for Si-AlN-NbTiN: as-deposited (left) and annealed (right). **As-deposited:** AlN is present at the interface with NbTiN; while aluminium oxide forms beneath it. The Al, O, N, and Si signals indicate a diffuse interface with the substrate. The N peak points to substrate nitridation. The drop in the Si signal (also visible in Figure 6.2) indicates reduced densification of the substrate surface. **Annealed:** Surface NbTiN oxides become more pronounced. The overlapping Nb, Ti, N, Al, and O signals indicate a burred interface between NbTiN and the underlying layer. The Ti peak confirms Ti diffusion into the layer beneath it. The colour code is consistent with the elemental mappings. Markers serve as guides to the eye.

tilayer deposited on Si (see Figure 6.17 and 6.15) and will be further discussed later in this Section.

Figure 6.4 contrasts the EDX depth profile for Si-AlN-NbTiN multilayers in their as-deposited and annealed states. It corroborates the observations derived from Figures 6.2 and 6.3. Further, it aligns with the observation extracted from the XRR analysis, demonstrating that annealing causes a blurred interface between NbTiN and the underlying layer, as indicated by the overlapping signals. In addition, the elemental depth profile corroborates the film thicknesses; although, it is not the most suitable technique for this purpose. By examining the x-axis of Figure 6.4, film thicknesses of 15.5 nm for AlN and 52.9 nm for NbTiN are determined. These values are consistent with the calculated thicknesses—derived from the number of PEALD cycles and the corresponding GPC—for AlN and NbTiN respectively 12.6 nm and 53.2 nm. After annealing, film thicknesses vary respectively to 16.6 nm and 50.7 nm, supporting the observation of Ti diffusion into the underlying layer.

6.1.2. Multilayers grown on Nb substrate

Multilayers grown on Nb were examined, aiming to contrast them with those deposited on Si, particularly regarding AlN. Figure 6.5 displays cross-sectional view of as-deposited Nb-AlN-NbTiN multilayer. It can be noted the crystalline character of both deposited films by the presence of planes differently oriented. Moreover, the films exhibit good adhesion to the adjacent layer and the Nb substrate with smooth interfaces. The mild interface roughness is attributed to the original substrate Nb surface. Contrary to Figure 6.1 a, a
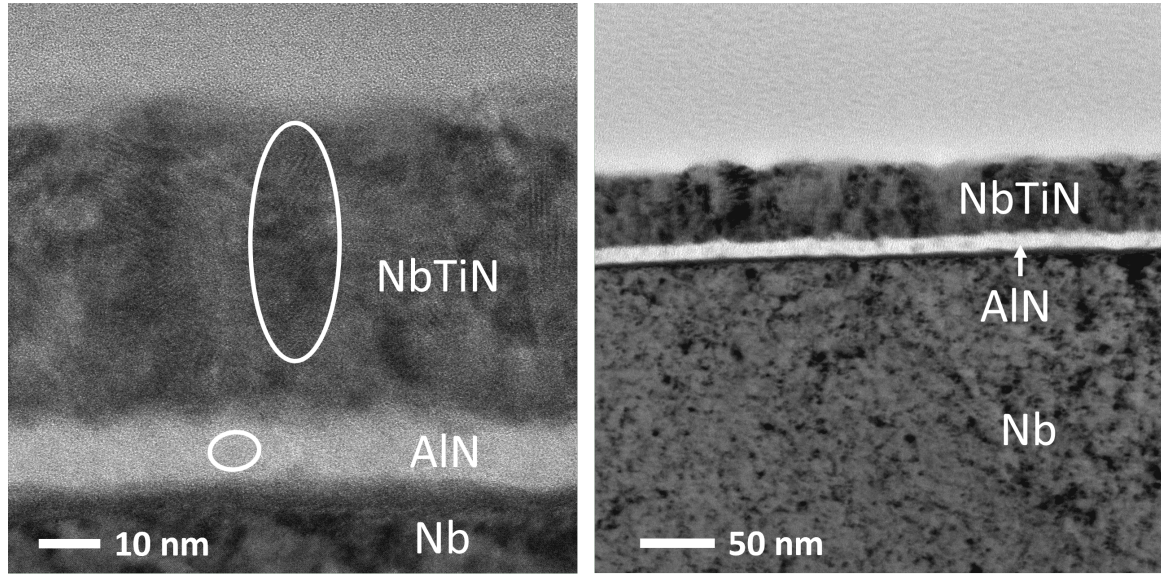
Figure 6.5: Cross-sectional view of as-deposited Nb-AlN-NbTiN multilayers. The interface roughness is attributed to the mimic substrate roughness. The deposited layers are crystalline (see grains and planes) and exhibit good adhesion. Furthermore, unlike to deposition on Si, only a single layer is discernible at place of AlN. On top of NbTiN, there is the protective Pt layer. Markers serve as guides to the eye.

single layer seems to form in place of the insulating layer. Figure 6.6 shows the elemental mapping of as-deposited Nb-AlN-NbTiN multilayers. As for multilayers grown on Si, oxygen is present in the AlN layer when grown on Nb. It is assumed that O diffuses from native Nb oxides, potentially forming aluminium oxides or oxynitrides. Further, the layers appear well-defined with no signs of intermixing. Nitrogen is detected in both the AlN and NbTiN layers, although its concentration is lower in the AlN layer. Conversely, Figure 6.7 shows the elemental mapping of annealed Nb-AlN-NbTiN multilayers. Annealing causes Al to diffuse into NbTiN layer. This observation aligns with the findings for multilayers grown on Si and with previous studies [130]. However, unlike for annealed multilayers grown on Si (see Figure 6.3), no signs of Ti diffusion into AlN are visible. Lastly, Figure 6.7 suggests a reduction in nitrogen content in the AlN layer due to annealing.
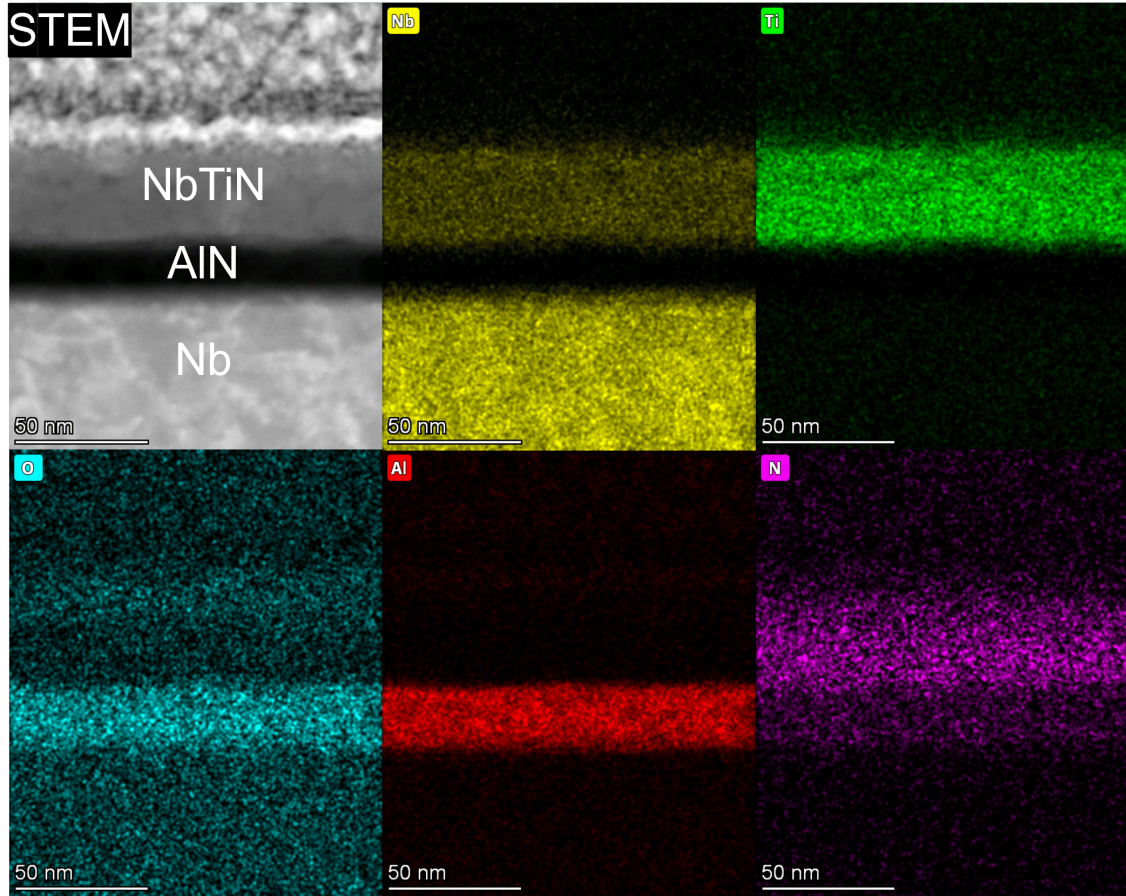
Figure 6.6: EDX elemental mapping of as-deposited Nb-AlN-NbTiN multilayers. The interfaces are well-delineated, with no signs of intermixing, and smooth. The roughness is attributed to the Nb substrate. Nitrogen is detected in both layers, although at a lower concentration in the AlN layer. Oxygen potentially diffuses from Nb oxides into the AlN, suggesting the formation of aluminium oxide or oxynitride. The analysis was conducted at EPFL in collaboration with CERN. Credits go to Stephan Pfeifer (CERN) for the Nb-AlN-NbTiN as-deposited and annealed lamellas fabrication and Daniel Turner (CERN), Alice Moros (CERN), and David Reyes (EPFL) for the STEM-EDX elemental maps.
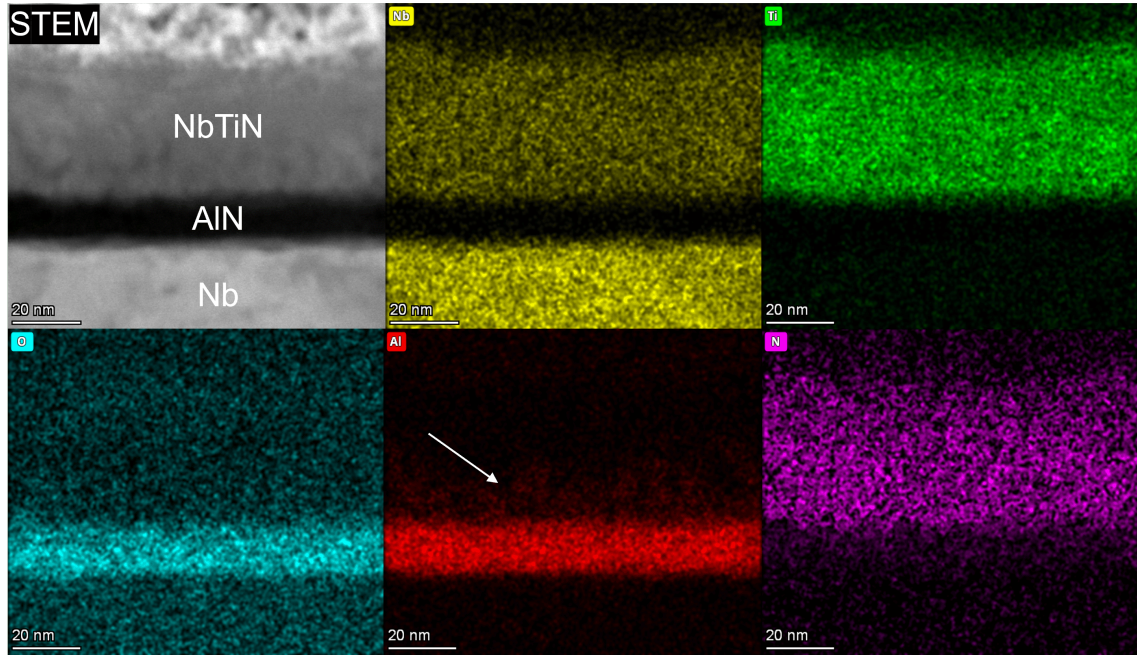
Figure 6.7: EDX elemental mapping of annealed Nb-AlN-NbTiN multilayers. Annealing causes Al to diffuse into the NbTiN layer. Nitrogen is detected in both layers but at an even lower concentration in the AlN layer after annealing. Oxygen is still present in the AlN layer. The analysis was conducted at EPFL in collaboration with CERN. Credits go to Stephan Pfeifer (CERN) for the Nb-AlN-NbTiN as-deposited and annealed lamellas fabrication and Daniel Turner (CERN), Alice Moros (CERN), and David Reyes (EPFL) for the STEM-EDX elemental maps.
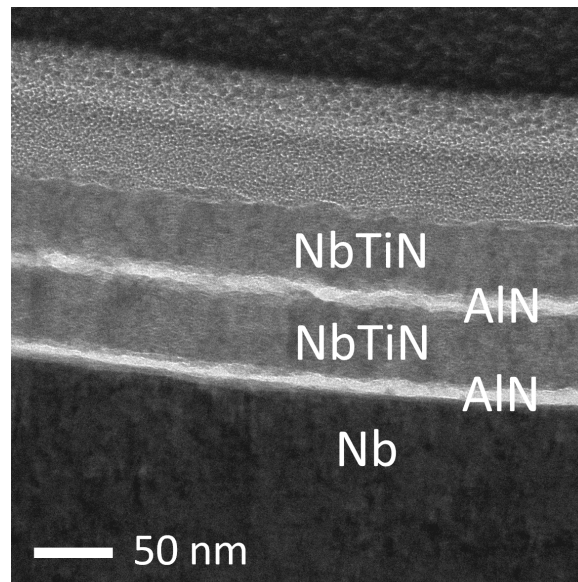
Figure 6.8: Cross-sectional view of Nb-(AlN-NbTiN)^2 multilayers in their as-deposited state.

Lastly, Figure 6.8 shows the cross-sectional view of Nb-(AlN-NbTiN)^2 multilayers in the as-deposited state. The multilayers seem to be well limited. The interface roughness is attributed to the mimic Nb substrate roughness. In Figure 6.8 the structure exhibits good adhesion between films and substrate. However, as discussed later in this Section, that is not always the case—see Figure 6.11. Additionally, Figure 6.9 presents the elemental mapping for Nb-(AlN-NbTiN)^2. It reaffirms the level of layering achieved via PEALD. No voids are visible between layers; which appear well-defined and delimited. However, Nb and Ti signals suggest a potential diffusion into the sandwiched AlN layer at certain spots. EDX depth profile is necessary in order to confirm such observation. Unfortunately, no oxygen signal has been recorded. The cross-section analysis after the post-deposition thermal treatment of such a multilayer is missing.
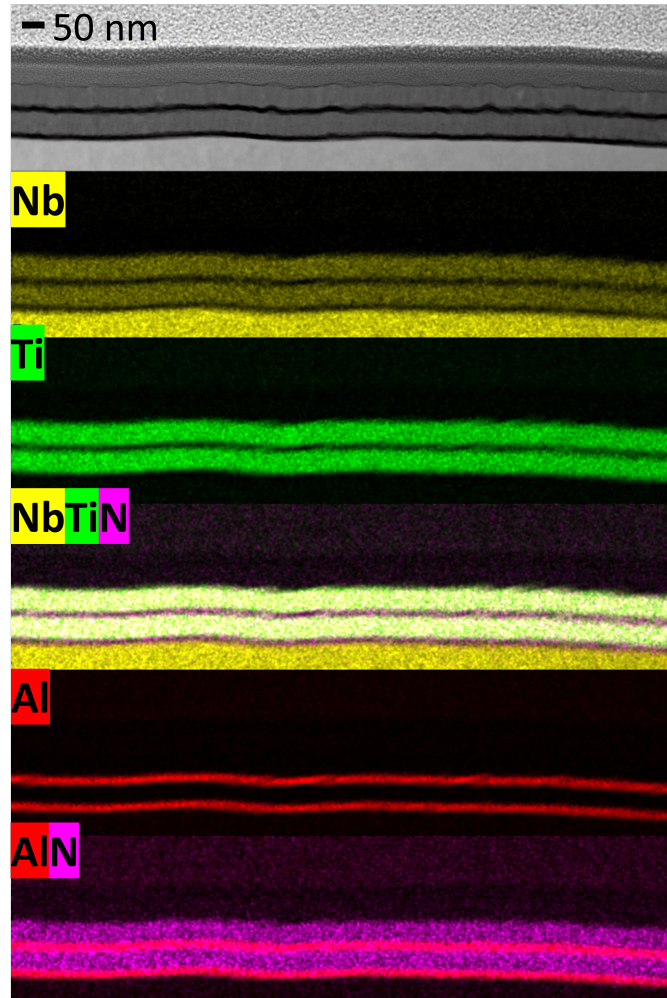
Figure 6.9: Elemental mapping of Nb-(AlN-NbTiN)^2 as-deposited multilayers. The multilayers are well-defined and delimited. The interface roughness can be attributed to the Nb roughness. Nb and Ti signals suggest a potential diffusion into the sandwiched AlN.

6.2. Investigating blister formation

Topography evaluation of thin films and multilayers reveals the arbitrary presence of blisters across the surface. The term *blister* defines a circular protrusion, with a smooth and rounded top and a base connected to the film, resembling a half-sphere. The blisters emerge on as-deposited thin films and multilayers. Figure 6.10 shows various examples of blisters and a cross-section view, which reveals local buckle-delamination. *Buckling* refers to the detachment of a film from the substrate or an adjacent layer, typically caused by excessive stress at the interface [142]. Its circular shape suggests that the stress distribution is the same around the central axis of the blister. Moreover, blisters exhibit a distinctive dot—not always centred—which can be distinguished via SEM and AFM as shown in 6.10 b. The nature of the dot remains unknown, but it is speculated to represent either a defect involved in blister formation or a region of stress accumulation in the blistered film. The size and distribution of the blisters are often arbitrary—see Figure 6.10 a and c. Nonetheless, there seems to be a relation between the size, the density, and the substrate which will be further elaborated below.
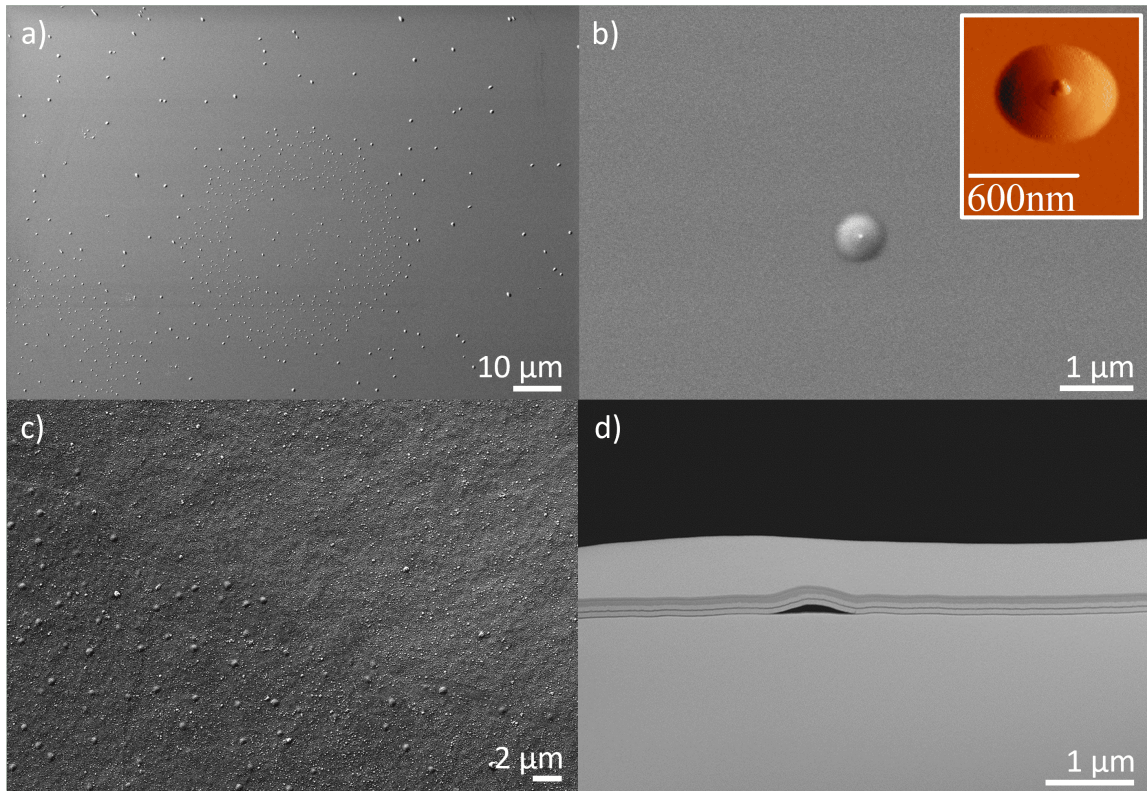
Figure 6.10: Blister characteristics: a) and c) show the random distribution and size; b) a zoom-in reveals its distinctive dot; d) shows a cross-section of a single blister. Note, blisters emerge on thin films and multilayers in their as-deposited state.
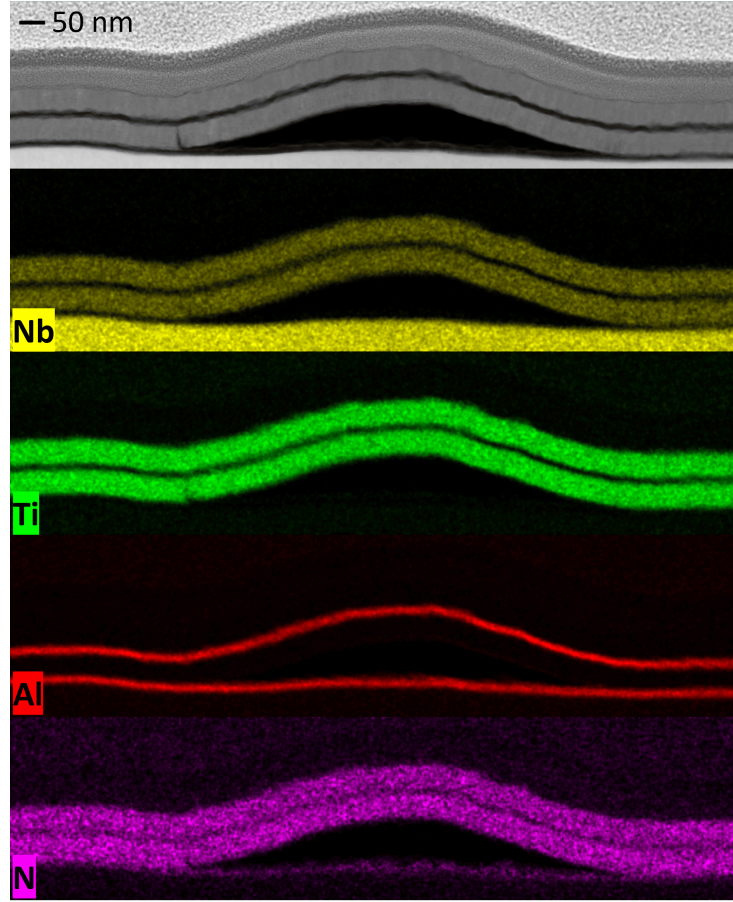
Figure 6.11: EDX elemental mapping for a blister. The samples, also shown in Figure6.9, consists of Nb-(AlN-NbTiN)^2 in its as-deposited state. The initial AlN layer is adhered to the Nb. The successive NbTiN suffers from detachment, resulting in a blister. The layer exhibits a rupture at the spot where detachment starts. Detachment do not occur for the successive AlN-NbTiN layers, which are well attached, do not present any anomaly and mirror the blister geometry. Unfortunately, no oxygen signal has been recorded.

According to EDX (Figure 6.11), for Nb-(AlN-NbTiN)^2, the blister appears to be voids. The detachment appears to occur at the NbTiN film while the AlN film remains adhered to the Nb substrate surface. However, this would not be always the case as blisters are alike present when a single layer of AlN is deposited

The formation of blisters is a long-known issue in thin-film multilayers [143–145]. In PEALD, ions and radiation from the plasma can damage the films [50] (see details in Section 2). Two distinct plasma-induced blistering processes may occur. On the one hand, ion bombardment may develop compressive stress on the film, resulting in blistering [146–149]. It potentially could be mitigated by reducing the ions energy through increasing the plasma gas pressure [147] or by reducing the ion flux density using lower plasma power [95, 96]. Another alternative to tune the ions energy would be through substrate biasing [46]. On the other hand, the formation of blisters can be linked to the accumulation of gas

desorbed [148–151]. Ions and radiation can break hydrogen bonds [50, 51, 149]. Trapped hydrogen desorbs in the form of H_2 and H_2O gas. The films acting as barriers may prevent the gas from diffusing out, leading to blister formation. This hypothesis may account for the difference between Nb and Si substrates, as hydrogen likely diffuses more readily into Nb than Si. Unfortunately, EDX is not suitable for detecting light elements; therefore, it cannot be ruled out from Figure 6.11 that the blisters may potentially be filled with hydrogen gas.

Various scenarios have been investigated, including different layers and multilayers (AlN, NbN, TiN, NbTiN, AlN-NbN, AlN-NbTiN, and $(AlN-NbTiN)^2$) deposited on Si and Nb substrates. Furthermore, other factors such as the film thickness, the deposition temperature, the plasma parameters (gases and exposure time), and the substrate position inside the deposition reactor were examined (see Appendix B.2). However, the occurrence of blisters remains inconsistent, making it challenging to determine the precise conditions under which they form and thus, their underlying cause.

Nonetheless, there are relevant conclusions that can be drawn from this investigation. Firstly, there are variations in blister size and density, based on the substrate. For Nb, blisters exhibit a height and diameter in the order of 300 nm and 1 μm, respectively; in contrast to 60 nm and 500 nm when it comes to Si. Furthermore, greater blister density is observed for Nb than for Si. However, blistering is more likely to occur when using Si as the substrate than Nb. At a deposition temperature of 250 °C, for Nb substrates, blistering is observed only in samples consisting of Nb-AlN-NbN and Nb-$(AlN-NbTiN)^2$. While for Si substrates, the only combination that does not show blistering is Si-NbTiN. To determine whether blistering is plasma-driven or thermally driven (thicker film results in extended exposure to the deposition temperature), the number of deposition cycles was reduced while maintaining the same total deposition heating time. The observation was that blistering would be plasma-induced. Thicker films exhibit more blisters, supporting the hypothesis of ion-bombardment causing blistering, since compressive stress increases with thickness [142]. Mitigation of ion-induced blistering has been reported by raising [149] and decreasing [128] the temperature. Deposition temperatures ranging from 80 °C to 250 °C were examined, however, inconsistencies make it challenging to draw definitive conclusions about the optimal deposition temperature (see details in Appendix B.2).

6.3. Impact of post-deposition thermal annealing on the morphology of thin films and multilayers

The impact of post-deposition thermal annealing on the morphology of thin films and multilayers was examined. The sample surface was examined under various considerations: the substrate, the thin film or multilayers deposited, the presence of blisters, the type of annealing conducted, the furnace used, and the annealing temperatures.

6.3.1. Evaluating the impact of RTA and STA on surface morphology

The morphology changes resulted from the two post-deposition thermal treatments described in Section 3—RTA and STA—are contrasted. Multilayers deposited on Nb and Si were examined. Figure 6.12 shows the surface of AlN-NbTiN and AlN-NbN multilayers deposited on Nb: as-deposited, and after conducting RTA and STA. In their as-deposited state, the multilayers' surface is smooth—corresponding to Figure 6.12 a and d. The grain

size is quite small, suggesting fine-grain or amorphous structure representative of ALD [152]. By contrast, both post-deposition annealing procedures induce surface morphology changes. As evidenced in Figure 6.12 b, c, e and f, the surface becomes rougher and textured, with more distinct grains that seem to have increased in size. This observation suggests annealing induced grain growth and recrystallization; which is discussed further in Section 8. A consistent behaviour is observed for multilayers of AlN-NbTiN deposited on Si. Figure 6.13 compares AFM scans of the multilayers in their as-deposited state and after RTA and STA treatments. The root mean square (RMS) surface roughness increases with the post-deposition treatments. The values are 0.92 nm, 2.42 nm, and 1.19 nm for as-deposited, RTA-, and STA-treated multilayers, respectively; while for the plain silicon wafer is 0.5 nm. The analyses suggest that RTA has a greater effect on surface roughness, regardless of the substrate. This may be attributed to the higher stress experienced by the multilayers during RTA, likely caused by the faster ramping and cooling rates.
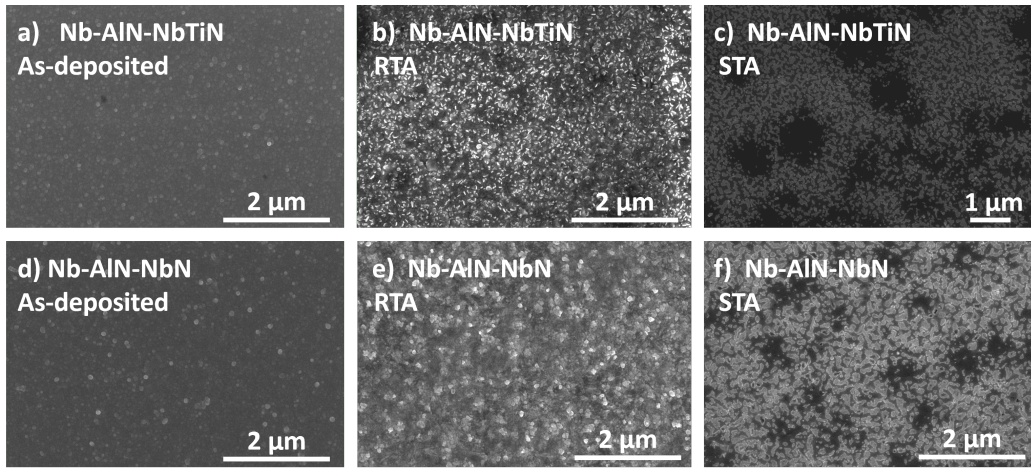
Figure 6.12: SEM images of the surface morphology of multilayers—AlN-NbTiN and AlN-NbN—deposited on Nb: as-deposited, and after RTA and STA treatments. Post-deposition treatments lead to greater textured surfaces and grain growth.
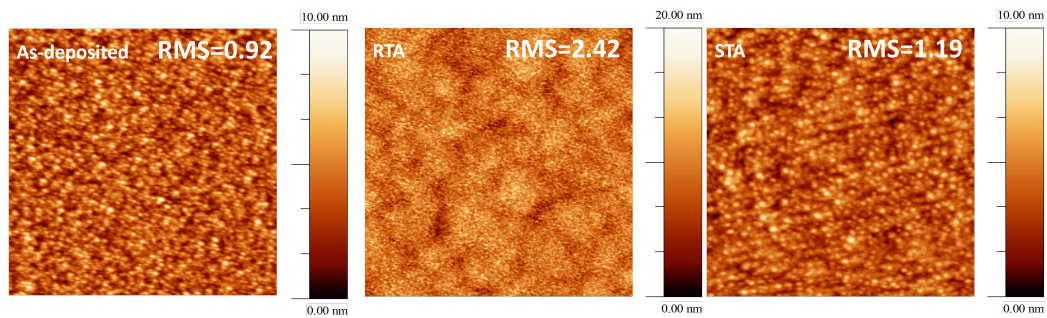
Figure 6.13: Surface evaluation of AlN-NbTiN multilayers deposited on silicon: as-deposited state and after RTA and STA treatments. AFM scan size is $2 \times 2\,\mu$m. Both thermal treatments lead to increased surface roughness. The bare substrate has a RMS of 0.5 nm.

6.3.2. Assessing annealing-induced defects

After annealing, various features or annealing-induced defects can be observed on the sample surface. Here, annealing refers to STA (see Section 3 for further details).

Firstly, circular bumps—distinct from blisters—of varying sizes form across the surface, often resulting in film cracks. An example of this defect is shown in Figure 6.14 a and b, where cracks are also visible. Additionally, a blister and delamination or peel-off—discussed later—are also evident in Figure 6.14. Bump formation is observed across the entire temperature range examined ($700\,°C$ to $1100\,°C$), with higher annealing temperatures leading to a greater number of bumps. Various scenarios were examined, including Nb and Si substrates, single layers of NbTiN and NbN, and multilayers of AlN-NbTiN with varying thicknesses. The findings reveal that bumps occur for multilayers grown on Si, with thicker layers resulting in a greater number of bumps. In contrast, bumps do not form on single layers or multilayers grown on Nb (see Figures 6.16 and 6.17 a). Elemental mapping for a cross-sectional view of a bump is shown in Figure 6.15, revealing partial buckle-delamination of the NbTiN layer from the AlN layer. Here, buckling is a consequence of annealing, driven by mismatches in thermal expansion across the multilayer structure, which result in compressive stress [142, 153]. Compressive stress occurs when a film tends to shrink more than the substrate or the adjacent layer during cooling but is constrained. When the stress exceeds the adhesion strength of the interface, partial buckle-delamination occurs. The coefficient of thermal expansion (CTE or α) describes the fractional change in size per degree of temperature change for a material. A higher CTE indicates that a material shrinks more during cooling. The CTE values for the materials under examination are listed in Table 6.1, with values for Al_2O_3 included because EDX elemental mapping revealed high oxygen concentrations within the AlN film. The greater thermal expansion mismatch with Si compared to Nb may explain why buckling occurs with Si substrates. Moreover, the relative stress ($\sigma \propto E \cdot \alpha_{mismatch} \cdot \Delta T$) of NbTiN is approximately 2.3 times the stress of AlN, to their underlying material, suggesting, as shown in Figure 6.15, that buckle-delamination occurs in the NbTiN film. Finally, film thickness strongly influences buckling, with thicker films exhibiting more buckling [142]. In conclusion, annealing-induced bumps are assumed to be buckling, caused by thermal expansion mismatches across the multilayer system grown on Si. Consequently, buckling can be excluded as a concern for SIS SRF cavities.

Table 6.1: Material properties obtained from [154, 155] *Calculated for a ratio of Ti to Nb=1/3.

Material	Si	Nb	AlN	Al_2O_3	NbTiN*
CTE ($\mu m\,m^{-1}\,K^{-1}$)	2.6-4.2	7.3	5.7	8.4	9.9
E modulus (GPa)	130-185	105	350	400	513
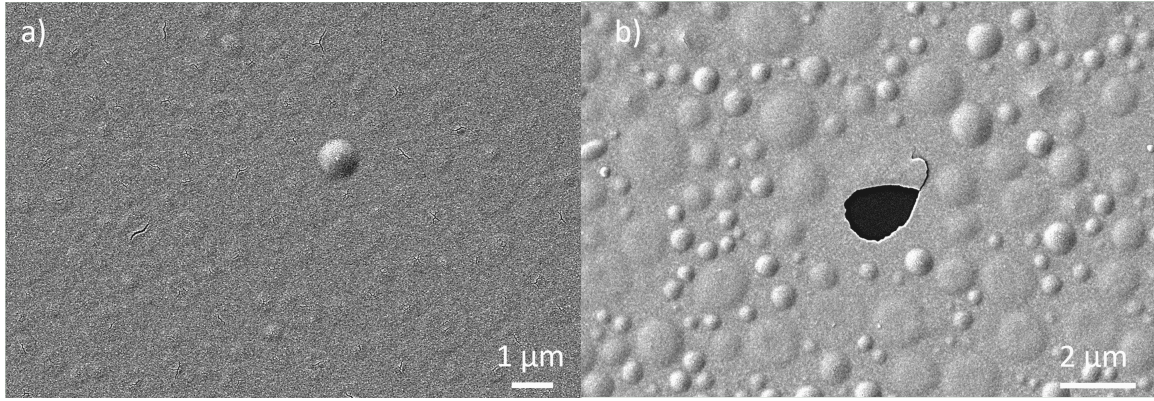
Figure 6.14: Annealed Si-AlN-NbTiN in a) sample furnace and b) single-cell furnace. See details in Section 3. Buckling, resulting in film cracks, is evident for both SEM images. Different cooling rates may be the reason for blisters to a) be unaffected or b) lead to peel-off.
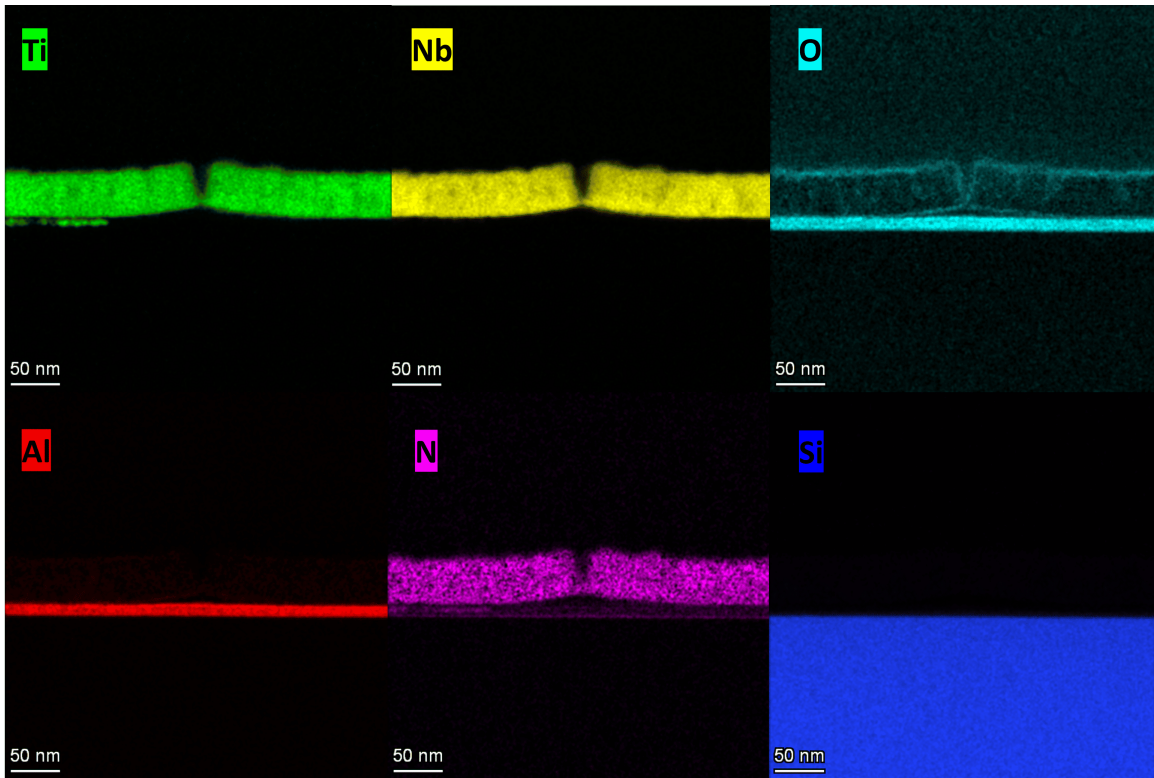
Figure 6.15: Elemental mapping for buckle-delamination resulting in film crack. The NbTiN film partially detaches from the AlN layer.
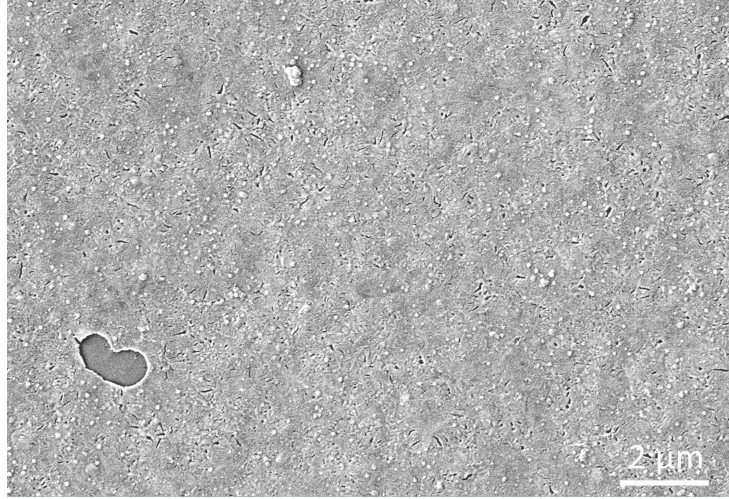
Figure 6.16: Annealed Nb-AlN-NbN surface. The annealing was performed in the single-cell furnace. With annealing, blisters lead to peel-off. No annealing-induced buckling is visible. Minor cracks are due to recrystallization.

Another annealing-induced defect is film peel-off, as shown in Figures 6.14 b), 6.16, and 6.17. Peel-off has been observed exclusively for samples that exhibit blisters in their as-deposited state. Elemental analysis through EDX (see Figure 6.17) confirms that peel-off occurs for NbN and NbTiN, while the AlN layer remains intact. It is assumed that the annealing-induced stress, together with the stress already present in the film due to the blister [144], exceeds a critical threshold, resulting in peel-off. This hypothesis is consistent with Figure 6.11, which shows that in a blister the detachment occurs for NbTiN. Additionally, it was demonstrated that annealing conditions play a role in peel-off. Figure 6.14 shows that blisters can a) be unaffected or b) lead to peel-off, under different annealing conditions.
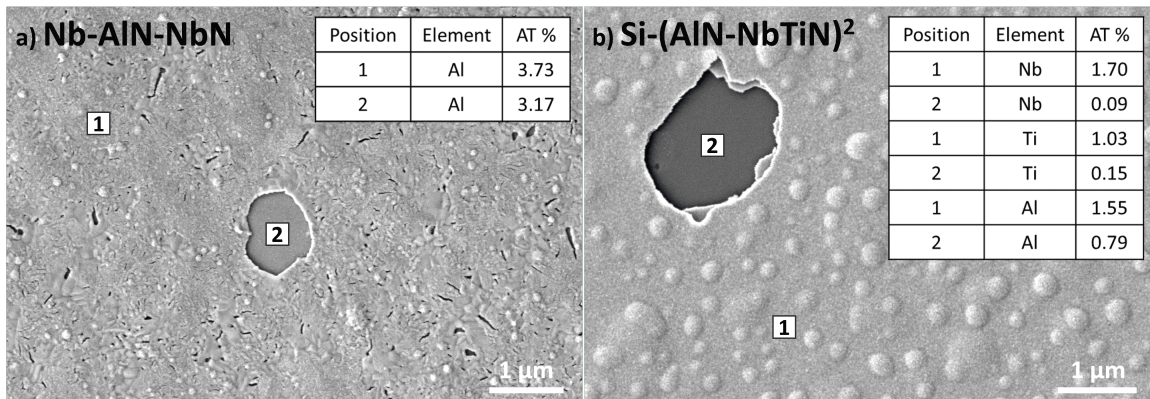
Figure 6.17: EDX analysis within and out of the peel-off. a) Nb-AlN-NbN: Al EDX signal confirms that AlN layer remains intact. Peel-off occurs for the NbN layer; b) $Si - (AlN\text{-}NbTiN)^2$: Peel-off occurs for one of AlN and both NbTiN layers. The initial AlN layer remains intact.

83

6.4. Summary and conclusions

Cross-section evaluation:

Firstly, elemental mapping reveals the presence of Al, N and O at the AlN layer, suggesting the formation of aluminium nitride and aluminium oxide, or aluminium oxynitrides. It occurs regardless of whether Si or Nb is used as the substrate. It is assumed that oxygen is absorbed from the native oxides of the substrate. For the Si substrate, the hypothesis is that a certain number of AlN PEALD cycles are required to consume all oxygen species from the substrate before the growth of AlN begins. This idea is supported by Figure 6.1 a, which suggests the formation of two layers in place of AlN, and by Figure 6.4 a, which shows lower oxygen content at the AlN and NbTiN interface. Conversely, for the Nb substrate, Figure 6.8 indicates the formation of a single layer. Unfortunately, an EDX depth profile to confirm this observation has not been conducted.

Moreover, the elemental mappings show the presence of oxygen within the NbTiN film; although in a lower amount than for AlN films. For NbTiN, oxygen impurities may originate from: the deposition environment (note that the base pressure is not low), the quartz tube ion-induced erosion, the plasma-reactor wall interactions, the impurities in precursors or process gases, and post-deposition oxidation [44, 156]. Hence, ultra-high purity conditions are suggested to reduce oxygen contaminations [157, 158].

Lastly, post-deposition annealing causes intermixing between AlN and NbTiN layers. The studies show that Al diffuses into NbTiN in multilayers grown on both Si and Nb substrates. However, Ti diffusion into AlN is only visible in the multilayers deposited on Si. Ti diffusion is not homogeneous; instead, it appears locally. Thus, it cannot be excluded that this phenomenon may be an artefact caused by lamella fabrication. Moreover, the EDX depth profile indicates that annealing reduces interface sharpness. The finding aligns with the observations from the XRR analysis (see Section 5) and agrees with previous reports [130].

Surface morphology evaluation:

Firstly, as-deposited and annealed multilayers exhibit smooth surfaces, a characteristic feature of PEALD. Surface roughness is known to degrade the SRF cavity performance potentially causing loss of superconductivity due to field enhancement and early magnetic flux penetration. Surface roughness is the limiting factor for Nb_3Sn coated SRF cavities, which quench at fields $\approx 20\,\mathrm{MV\,m^{-1}}$ [159]. Therefore, achieving a smooth surface is crucial for SIS-based SRF cavities to reach high accelerating gradients.

Two buckle-delamination defects were observed: blisters and bumps. Blisters arise on thin films and multilayers in their as-deposited state. Their formation is plasma-induced. Differences in blistering between Nb and Si substrates could be attributed to the potential influence of grain boundaries, surface roughness, or surface species. The inconsistencies in blister formation, which make it challenging to determine the deposition conditions to prevent it, could be attributed to the plasma jitter noted during the experiments. Conversely, bumps arise due to the post-deposition thermal annealing; thus, they are thermally-induced. Bumps may be attributed to thermal expansion mismatches across the multilayers. It occurs for multilayers grown on Si, not on Nb. Therefore, bumps annealing-induced are not a concern for SIS SRF cavities. Lastly, annealing may lead to peel-off for samples exhibiting blistering in their as-deposited state. It is assumed to result from excessive accumulated stress in the blistered films.

7. Compositional analysis

This section explores the chemical composition of NbTiN PEALD-grown films, evaluating various Nb to Ti ratios and the potential impact of post-deposition annealing.

7.1. Various compositions of NbTiN

Thin films with eight different compositions of $Nb_xTi_{1-x}N$ were deposited. The ratio of Nb to Ti within the ternary compound can be tailored by adjusting the ratio of the individual PEALD processes inside the supercycle, or in other words, the ratio of n to m. Note the PEALD supercycle for NbTiN can be expressed by $((A_1B_1)^m(A_2B_2)^n)^p$, where A_i and B_i represent the exposure plus purge for each precursor/plasma, and m, n, and p the number of times each loop is repeated (see more details in Section 3). The $Nb_xTi_{1-x}N$ films, varying composition from Ti-rich to Nb-rich, exhibit a gold-yellowish colour characteristic of the nitride cubic δ-phase [77, 160]. The greater the Ti content, the more yellow. Figure 7.1 shows the ratio of Nb to Ti measured by EDX as a function of the ratio in the PEALD supercycle. The linear relationship indicates the precise control PEALD offers over the elemental composition, using the minimum number of cycles. By contrast, due to the etching nature of the $NbCl_5$ precursor, thermal ALD does not provide a linear relationship between composition and ALD ratio [68, 71]. Thus, using $NbCl_5$ requires more TiN cycles to achieve Ti-rich $Nb_xTi_{1-x}N$ films. Lastly, EDX analysis revealed no differences in Ti and Nb content between as-deposited and post-deposition annealed films.
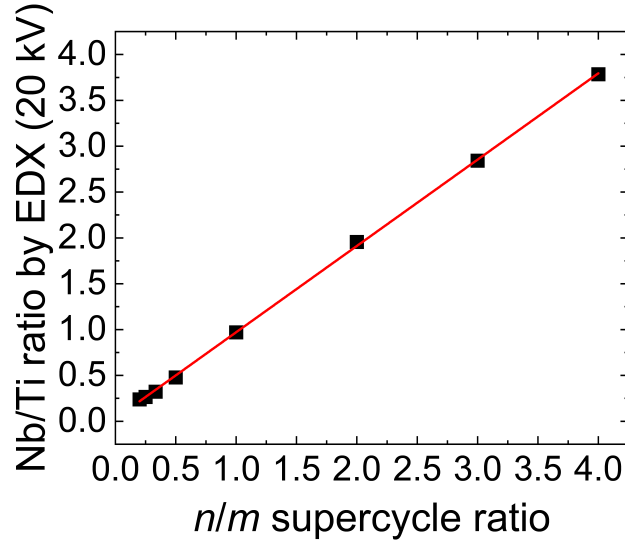
Figure 7.1: Ratio of Nb to Ti measured by EDX as a function of the ratio in the PEALD supercycle, for $Nb_xTi_{1-x}N$ films with eight different compositions. The red line represents the linear relationship between the elemental composition and the PEALD supercycle with a slope of 0.941 and R^2 of 0.999.

7.2. X-ray photoelectron spectroscopy (XPS)

To explore potential compositional changes in NbTiN films due to the post-deposition thermal treatment, *ex-situ* XPS was performed on AlN-NbTiN multilayers in their as-deposited and annealed states. The XPS measurements were conducted on the surface (these results are presented in Appendix B.4) and after argon ion bombardment. The sputtered thickness is unknown. A preliminary survey was conducted to identify the elements in the sample (see Appendix B.4), revealing the presence of Nb, Ti, N, C, and O. The absence of Al or Si peaks indicates that the sputtering depth remained within the NbTiN layer, without reaching the AlN interface. High-resolution scans of each peak were taken and deconvoluted by simultaneously fitting all elemental lines for a more comprehensive analysis. The XPS spectra were analysed qualitatively—identifying elemental composition and chemical states based on peak positions and separations—and quantitatively—determining elemental concentrations from peak heights or areas. The samples evaluated are AlN-NbTiN multilayers (10 nm and 60 nm thick, deposited in that order on Si by PEALD), in their as-deposited and annealed states.

7.2.1. Qualitative evaluation of XPS peaks after depth etching

Surface oxidation of NbTiN films occurs when exposed to air. A continuous substitution of nitrogen by oxygen from the inner to the surface results in a mixture of Nb and Ti oxides and oxynitrides, with TiO_2 at the outer surface and oxynitrides sandwiched beneath [113, 116, 161]. Surface XPS spectra of Ti 2p, Nb 3d, and O 1s confirm the presence of Ti and Nb oxides and oxynitrides (see Figures B.7 and B.6 in Appendix B.4). After etching, both Ti 2p and Nb 3d peaks (respectively *left* and *right* column in Figure 7.2) shift from an oxidised surface to a more pronounced nitride character of the films. Contributions of nitrides, which increase with annealing, and oxynitrides are observed in both Ti and Nb spectra. The deconvolution of the as-deposited and annealed Ti 2p spectra (Figure 7.2 c and e) shows no evidence of TiO_2. TiN [113, 114, 162], TiN_xO_y [162], and a shake-up satellite [115] are visible. No contributions from metal [113, 162] or carbide [163] were detected, as there is no peak at 454.0 eV. The deconvolution of the as-deposited and annealed Nb 3d spectra (Figure 7.2 d and f) indicates the presence of NbN [113, 116, 164, 165], two different oxynitride NbN_xO_y [113] and $NbN_{x'}O_{y'}$ [116, 165], and Nb_2O_5 [113, 117, 164, 166]. The presence of Nb_2O_5 in the spectra of the sputtered films may indicate that the etching depth was insufficient to remove the native oxides entirely. Note, no metal [165] or carbide [116] signals are detected.

Figure 7.3 shows the N 1s, O 1s, and C 1s peaks after etching. The *left* column highlights the contrast between the as-deposited and annealed samples, while the *right* column the deconvolution of the peaks after annealing. The rise in the annealed N 1s peak, suggests that annealing enhances the nitride character of the NbTiN films. This observation is consistent with the annealed Ti 2p and Nb 3d peaks. Its deconvolution (Figure 7.3 b) indicates nitride (NbN [113, 115] and TiN [162]) and oxynitride (NbN_xO_y [113]) contributions. Figure 7.3 c shows no major changes in the O 1s peaks due to the annealing. Two oxynitrides are identified: NbN_xO_y at lower binding energy [90] and TiN_xO_y at higher binding energy, based on the apparent binding energy difference between Ti 2p and O 1s [162]. Lastly, C 1s peaks (see Figure 7.3 e and f) point that the etching has successfully removed the surface
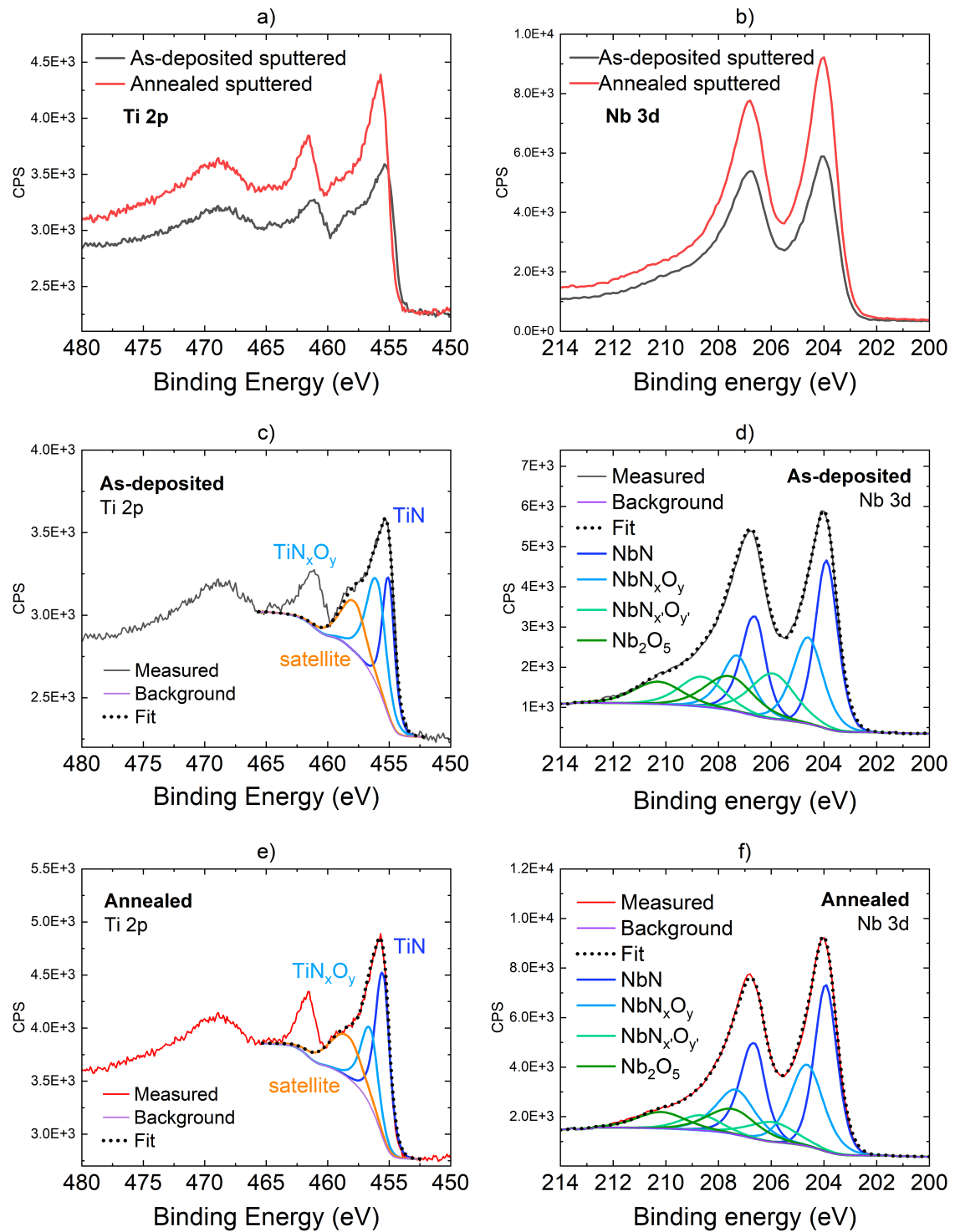
Figure 7.2: High-resolution XPS spectra for the binding energy regions of Ti 2p (*left*) and Nb 3d (*right*) after etching. The first row contrasts the as-deposited with the annealed sample. In contrast, the second and third rows show the deconvolution of the peaks for the as-deposited and annealed samples, respectively.
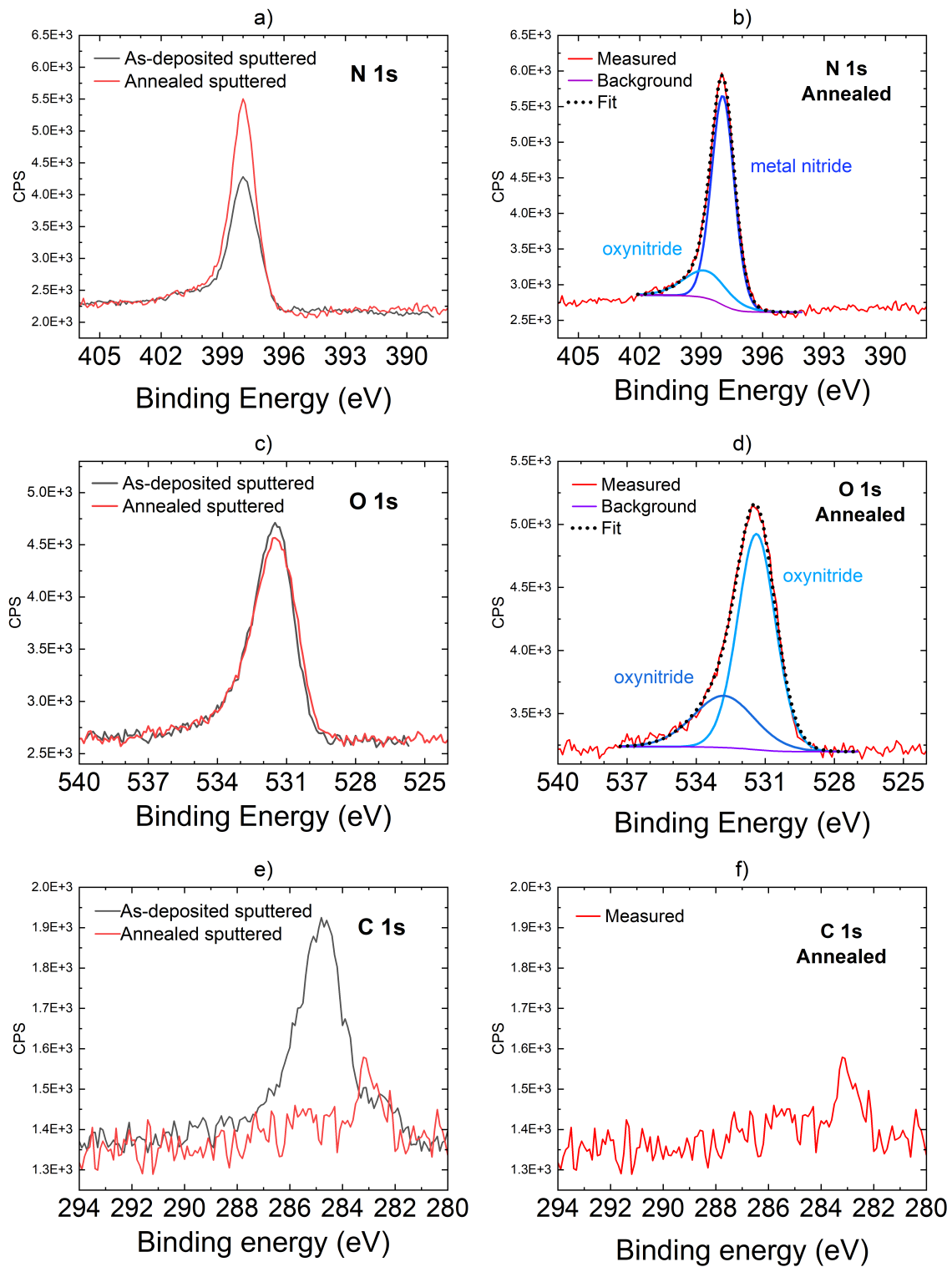
Figure 7.3: Sputtered high-resolution XPS spectra for the binding energy regions of N 1s, O 1s, and C 1s peaks. *Left*: as-deposited vs annealed; *Right*: deconvolution of the annealed peaks.

adventitious pollution [117, 167] (see surface C 1s peak analysis in Appendix B.4). Carbon may still be present in the as-deposited NbTiN film in low amounts, as indicated by the weak peak intensity. This carbon likely originates from unreacted or decomposed precursor fragments [90, 168] or from the vacuum during deposition. Annealing may result in carbon outgassing, as suggested by the significant decrease in the C 1s signal. While a metal carbide signal could be present, its weak intensity makes it indistinguishable from the background, and no carbide contributions are observed in the high-resolution Ti 2p or Nb 3d spectra.

7.2.2. Quantitative evaluation of XPS peaks after depth etching

The XPS quantitative analysis gives the relative concentrations derived from the relative peak areas. For the elemental quantification, the area considered is the one under the major core-level line for each element high-resolution spectrum—including shake-up lines [169]. For a more accurate analysis, one could employ each deconvoluted peak area; however, since there are some contributions, e.g. metal oxide or metal nitride, that could be attributed to both Ti and Nb it was not realised. Nevertheless, the relative concentrations for the contributions identified in each high-resolution peak are given in Table B.2 in Appendix B.4. Moreover, the XPS raw signal intensities do not directly represent the elemental concentrations due to various factors such as the excitation source, photoionization cross-section, electron mean free path, spectrometer settings, and more. Atomic sensitivity factors, which relate the measured signal intensity to the actual concentration of an element in the sample, were applied to correct for these influences [170].

The element concentrations are listed in Table 7.1 for as-deposited and annealed samples after depth etching (the surface analysis is given in Table B.3 in Appendix B.4). The most significant observation is the substantial reduction in carbon concentration within the NbTiN film due to the annealing. It decreases from 15.5% to near the detection limit, indicating that the presence of carbon in annealed NbTiN films is negligible. By contrast, no evidence of oxygen degassing is observed, with a concentration around 20%. The nitride character of the film may be enhanced with the annealing. Moreover, the relative concentrations of Nb and Ti maintain the compositional ratio of niobium to titanium established by the chosen PEALD process (3:1), supporting the observations derived from the EDX analysis and demonstrating the precise control over the composition of NbTiN films offered by PEALD. Note, the slight ratio deviation is attributed the use of the element peak areas instead of the areas of the deconvoluted peak contributions.

Table 7.1: Quantitative analysis of the elemental composition after depth etching for as-deposited and annealed samples.

% Atomic	As-deposited	Annealed
Oxygen	22.7	21.2
Carbon	15.5	1.2
Nitrogen	28.9	34.7
Titanium	6.7	9.2
Niobium	26.2	33.6

Note, for an adequate XPS quantitative analysis all spectra must be recorded under identical instrument settings. In addition, the quantification depends on relative peak areas, which are affected by the choice of background function and endpoints; thus, its accuracy is $\pm 5\%$ [170]. Lastly, ion bombardment may produce chemical reduction, atomic mixing, preferential sputtering, and other effects that modify the surface [162]. Consequently, the sputtered surface may not necessarily reflect the true composition of the original layer. For instance, preferential sputtering during etching as well as mixing effects of the compounds present due to backscattering are found, especially, in the case of alloys [114], which may provide misleading information. This could be one explanation why niobium oxides are visible at Nb 3d peaks after etching. Thus, angle-resolved XPS (ARXPS) would offer a more accurate analysis.

7.3. Summary and conclusions

EDX analysis shows that PEALD offers a precise control of the the Nb to Ti ratio in $Nb_x Ti_{1-x} N$ films, with no changes caused by the post-deposition annealing.

XPS analysis revealed the presence of the elements: Nb, Ti, N, O, and C. No Al or Si lines are visible for any of the samples investigated. However, in the additional XPS study presented in Appendix B.4, F—likely from the O-ring used for sealing the PEALD chamber—was detected. The most significant finding is that annealing result in C degassing for the NbTiN films, reducing its signal till the negligible level. Additionally, the deconvolution of peaks indicates NbTiN oxidation forms oxides and oxynitrides, whose thickness may be less than 10 nm, since the nitride lines are visible at the surface spectra. After depth etching, the absence of Ti oxide, while Nb oxide and oxynitrides remain present, suggests Ti oxide may be outer layer—which agrees with literature—and insufficient material removal. It could explain the high oxygen content, 20% for NbTiN films after sputtering, and the lack of Al peak, despite evidence of Al diffusion into NbTiN caused by the annealing (see cross-section studies in Section 6). Thus, the removed thickness remains unknown. Additionally, annealing may lead to greater surface oxidation—more pronounced for Ti—and enhance the nitride character within the NbTiN film, as indicated by the increase of the contributions relative areas.

8. Crystal structure analysis

This section explores the structural properties of the PEALD-deposited films under investigation, with a particular focus on NbTiN. The crystallinity of niobium nitrides plays a pivotal role in their superconducting properties [74]. Thus, in the context of SIS multilayers for enhancing the performance of SRF cavities, the analysis of the crystallinity of NbTiN films is essential. Besides NbTiN, NbN films were also examined. The AlN films were briefly examined, as the insulating layer in SIS multilayers is less critical to SRF cavity performance, and the importance of highly crystalline AlN in this context is still unclear. Furthermore, films produced by thermal ALD and PEALD are often amorphous or have a nanopolycrystalline character. To counter this, post-deposition thermal treatments are commonly used to enhance their crystallinity. The impact of post-deposition annealing procedures on the films was also studied.

Various characterisation techniques were utilised for this analysis. First, TEM and EBSD confirmed the presence of well-ordered crystalline domains in the films. Lastly, the crystalline phases were identified through an XRD analysis. Together, these techniques offer a comprehensive understanding of the structural quality of NbTiN, which is crucial for advancing the development of SIS multilayers for SRF cavities. The results of these analyses are presented in the following sub-sections.

8.1. Evidence of crystalline nature

Figure 8.1 a) presents a cross-sectional view of SIS multilayers, where the crystalline nature of the as-deposited NbTiN thin film of about 60 nm thick becomes apparent. The inset shows the electron diffraction ring pattern characteristic of polycrystalline structures with different orientations [74], generated by the NbTiN structure. For NbTiN films, as part of SIS multilayers, grown on Si (see Figure 6.1) crystal grains and planes are also visible. Conversely, for AlN films small grains are noticeable when deposited on Nb. It was discussed in Section 6 that AlN behaves differently when deposited on Si compared to Nb, and that surface oxides of the substrates may have a relevant impact on the deposited film. From the crystallinity point of view, it seems that Nb would be a more favourable substrate. The minimum size required for obtaining a TEM diffraction pattern limits the evaluation of the AlN layer. Figure 8.1 b) contrats the EBSD patterns for multilayers in their as-deposited and annealed states, revealing more prominent Kikuchi lines for the annealed sample. It demonstrates the effectiveness of post-deposition thermal treatments in promoting crystallinity and grain growth of the PEALD-deposited films. This will be discussed in the sub-section 8.3.2.

91
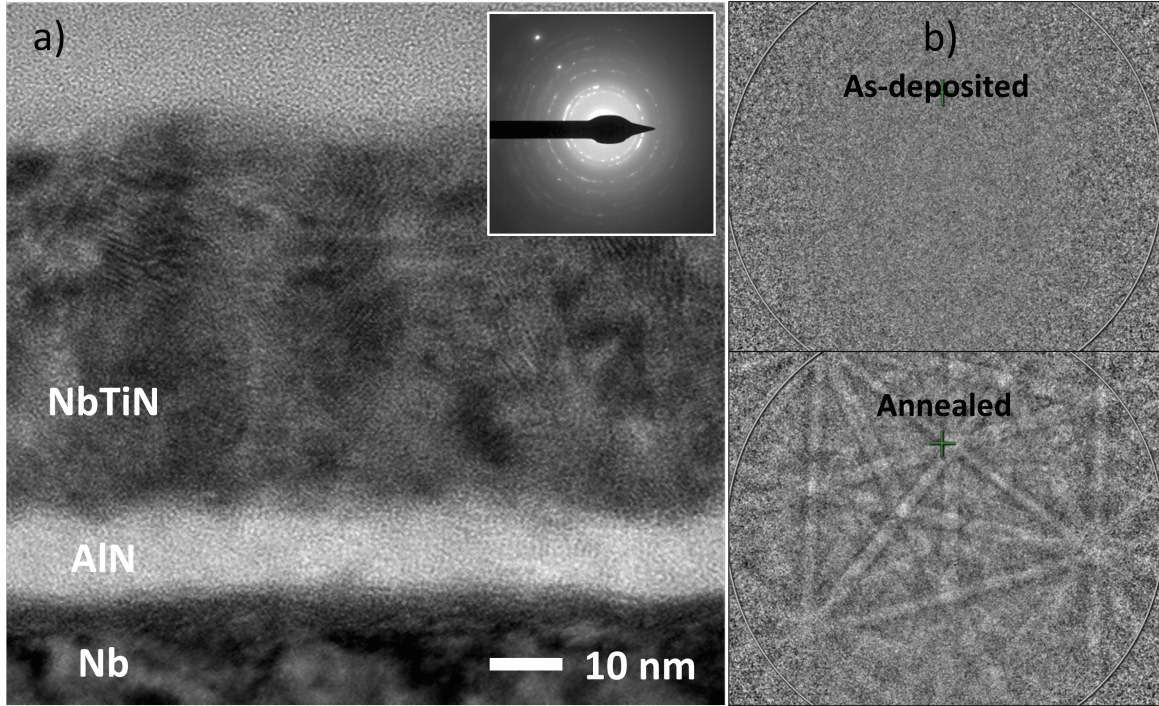
Figure 8.1: a) Cross-sectional view of a SIS multilayer. Randomly oriented grains and their planes are visible. The inset displays the electron diffraction diagram. The ring pattern reveals the polycrystalline nature of the films. b) Kikuchi lines observed through EBSD. The observation of prominent lines—which were assigned to NbTiN—for annealed Nb-AlN-NbTiN, supports the idea of annealing enhancing the NbTiN crystallinity and grain growth. In the as-deposited state, Kikuchi lines are not discernible, presumably because small grain sizes lead to insufficient signal for detection.

8.2. Overview of crystalline phases for the materials under study

An overview of the various crystalline phases of the films being analysed in this study is given. It serves as a foundation for phase identification during the upcoming analysis. Understanding these phases is crucial for accurate phase identification during subsequent analysis, as it directly impacts the evaluation of their structural and superconducting properties.

Niobium nitrides

A crucial aspect when investigating the crystallinity of PEALD NbN thin films is to consider the existence of the various NbN crystalline structures. Indeed, Nb-N presents a complex system and although a lot of effort has been undertaken for its clarification [34, 74, 171–174], the various proposed phase diagrams are often contradictory [175]. An example of this discrepancy between diagrams is observable in Figure 8.2. The main reasons for the inconsistency between the proposed diagrams are the fast phase transformation requiring
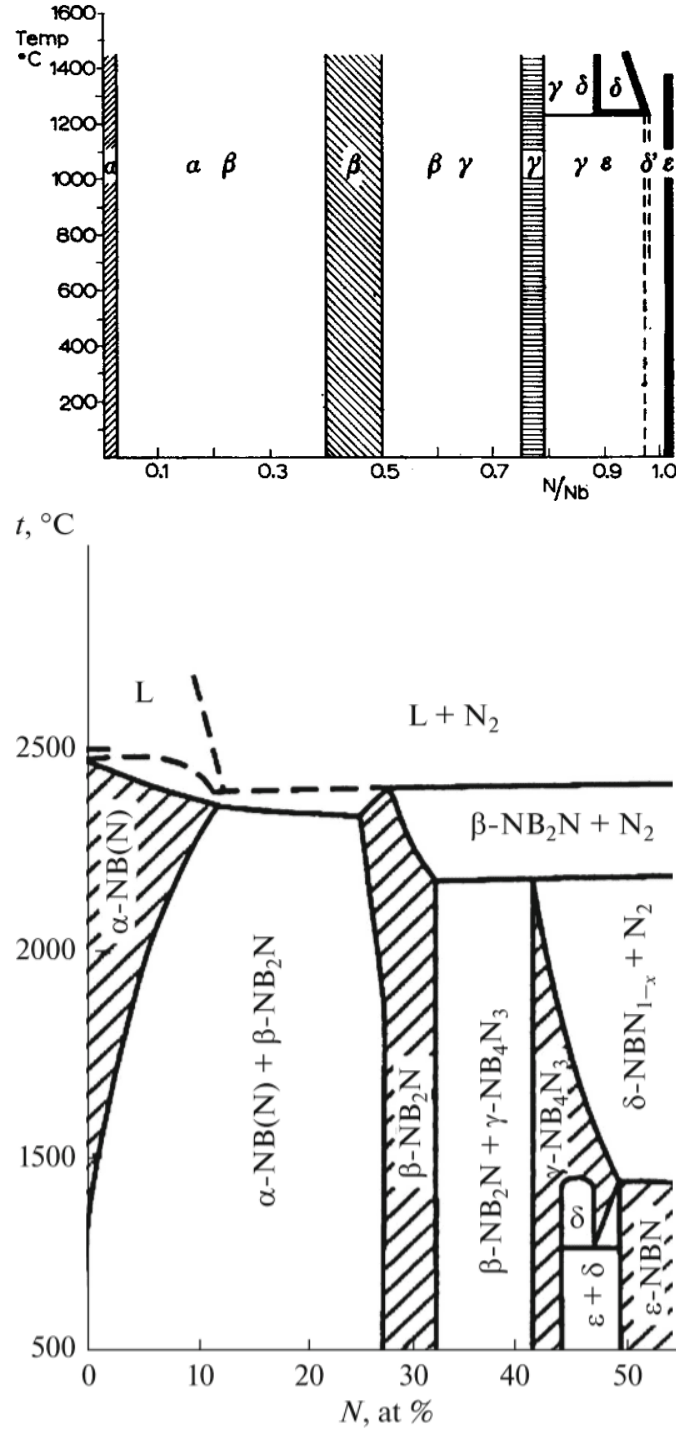
Figure 8.2: Phase diagrams most commonly accepted of the Nb-N system proposed by Brauer [171] (upper) and Holleck [172] (bottom).

in-situ investigations [175] and errors in phase identification caused by diffraction peaks being located at the same positions [176, 177]. Despite this, the following niobium nitride

crystal structures are generally accepted (see Figure 8.3): Nb-rich phases (i) α-NbN a solid solution of N in a Nb cubic lattice, (ii) β-Nb$_2$N hexagonal, and (iii) γ-Nb$_4$N$_3$ tetragonal; nearly stoichiometric phases (iv) δ-NbN cubic, (v) δ'-NbN hexagonal, and (vi) ϵ-NbN hexagonal; and N-rich phases (vii) Nb$_5$N$_6$ hexagonal, and (viii) Nb$_4$N$_5$ tetragonal.

A first indication of crystalline phase of NbN films can often be inferred from their colour, which serves as a visual cue to the specific crystal structure formed. A golden colour indicates cubic or tetragonal phases, while a silver colour indicates a hexagonal phase [178, 179]. This relationship between colour and type of crystal structure also applies to Nb oxynitrides [171]. Moreover, it must be considered that the superconductivity of NbN strongly depends on both the crystal structure and the Nb to N ratio [74]. Among the NbN phases the δ-phase posses the highest superconducting critical temperature with T$_c$ =17.3 K [180]. The δ-phase has been reported to form at high temperatures, above 1370 °C according to [181], 1270 °C to Oya and Onodera [173], 1230 °C to Brauer [171], and between 1070 and 1225 °C to Lengauer et al. [175]. Nonetheless, δ-NbN has been prepared at low temperatures: at 200 °C by magnetron sputtering without [182] and with substrate biasing [183], and at 350 °C by PEALD [86]. Lengauer et al. [175] showed that the temperature for phase transformation varies with the nitrogen content (see phase diagrams in Figure 8.2). Furthermore, the NbN$_x$ phases exist for different Nb to N ratios. In the case of cubic δ-NbN, it exists at compositions near stoichiometry, with x $= 0.88 - 0.98$ and x $= 1.015 - 1.062$ [178]. However, with a nearly stoichiometric composition, it becomes an unstable structure because it presents a large number of vacancies, both metal and non-metal [74, 173], resulting in δ' hexagonal phase [74]. Thus, δ-NbN is limited by its instability, which can be mitigated by introducing impurities which stabilise the NaCl type structure [74, 183]. One example is the cubic δ-NbTiN. The addition of Ti to NbN—Ti is a good nitrogen getter [160, 184]—reduces both types of vacancies and enhances phase stability. Among the NbN
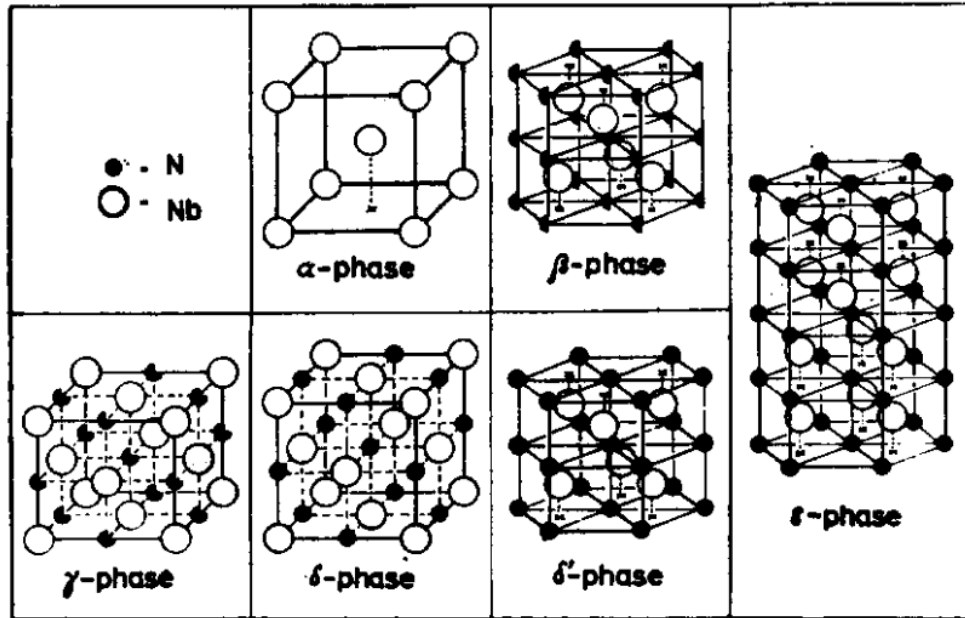
Figure 8.3: NbN crystal structures, excluding N-rich phases. Image taken from [171].

phases, the next highest T_c is associated with the tetragonal phases γ-Nb_4N_3 and Nb_4N_5, though there is a lack of consensus in the literature regarding the T_c values. For γ-Nb_4N_3, Buscaglia et al. [181] reported $12 - 15$ K, while Babu and Guo [34] gave 8.5 K. Similarly, for Nb_4N_5, Babu and Guo [34] reported 15.3 K, Motohashi et al. [185] reported $8 - 10$ K, and Patel et al. [75] reported up to 7 K. The lowest T_c corresponds to the hexagonal phases β-Nb_2N and Nb_5N_6. For the β-Nb_2N phase contradicting findings have been reported; either a wide range of T_c or the absence of superconductivity up to 2 K [186]. However, Babu and Guo [34] clarified this, demonstrating that the single β-Nb_2N was actually composed of four different structures; all of them are found to be superconductors with T_c ranging from 0.6 K to 6.1 K. Similarly with the Nb_5N_6 phase, which was reported to be non-superconducting by Terao [186] and to exhibit a T_c up to 9.7 K by Patel et al. [75]. Lastly, the hexagonal δ' and ϵ phases are reported to be non-superconducting [74, 175, 178]. An important final point is that the NbN phases can transform into one another by adding or removing nitrogen during high-temperature (above $1000\,°C$) annealing [74, 171, 172, 175, 186, 187]. Annealing N-rich phases under vacuum leads to nitrogen loss, whereas Nb-rich phases gain nitrogen when annealed in a nitrogen atmosphere. The exact composition depends on the nitrogen pressure [171]. Both scenarios involve Nb and N atoms rearrangement. Moreover, the temperature for phase transformation depends on the nitrogen composition, and the temperature rates in cases involving lattice distortion during the transformation [175]. Finally, it must be noted, NbN is prone to accumulating oxygen, which can replace a portion of nitrogen [183]. Oya and Onodera [74] observed that Nb oxynitrides, usually referred to as Nb(N,O), form for the α-, β-, γ-, and δ-phase. Additionally, Brauer [171] reported the existence of the oxynitride phase ϵ-Nb(N,O). Furthermore, similar to nitrides, the δ-Nb(N,O) phase exhibits superconductivity, with a T_c ranging from 9.6 K to 14.7 K, depending on its composition [188].

Niobium titanium nitride

In the case of the Nb-Ti-N ternary system only an isothermal section of the phase diagram is available [172]; this is given in Figure 8.4 for $1200\,°C$ and 1 bar N_2 pressure. Under these conditions the equilibrium phase of the ternary nitride allows any Ti and Nb content. The two nitrides, δ-NbN and δ-TiN, are completely miscible resulting in a ternary compound with a cubic phase stable at room temperature [172, 189] and an intermediate lattice constant [190]. Its lattice constant follows the linear relationship given by Vegard's law, with a larger value for the higher Nb concentration and on the contrary, a smaller value for the higher Ti concentration [160, 172]. Furthermore, NbTiN seems to exist only in the rocksalt δ-phase [161, 172, 189]. A practical conclusion is therefore that the presence of titanium stabilises the phase of interest. Moreover, NbTiN features a yellow colour characteristic of the nitride cubic δ-phase [77, 160]. All NbTiN films deposited studied here show a gold-yellowish colour. It was noted that the higher the Ti content, the more yellowish the films become. Lastly, NbTiN is superconducting with a Tc up to 17-18 K [160]. In particular, a Tc $=17.5$ K was reported by Pessall and Hulm [190], $T_c = 17.8$ K by Benvenuti et al. [189] and Tc $=17.9$ K by Buscaglia et al. [77]. Furthermore, as NbN does, NbTiN T_c shows a dependency upon the nitrogen content as well as on the Nb to Ti ratio [32, 160, 190, 191].
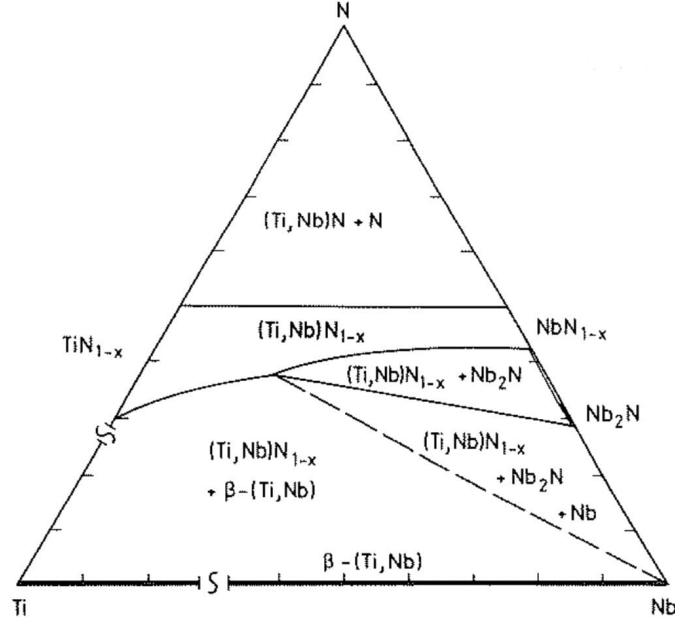
Figure 8.4: Phase diagram for the Nb-Ti-N system [172]. The β-(Ti, Nb) alloy undergoes a nitridation process at 1200 °C and 1 bar N_2 pressure. The cubic δ-NbTiN phase is formed at any Ti and Nb content.

8.3. Crystalline phase identification via XRD analysis

This subsection presents the results of the XRD analysis, including phase identification and the evaluation of the impact of post-deposition annealing on the crystalline structure. The examined samples are multilayers of AlN-NbTiN and AlN-NbN in their as-deposited and annealed states. The multilayers were grown on Si substrate, as the roughness of the fine grain Nb hinders its use. For the examination of SIS multilayers grown on Nb, the use of a synchrotron beamline is recommended to obtain better signal-to-noise ratios. At the end of this section, Table 8.1 summarises the results. Any mention of annealing defaults to the STA procedure, unless stated otherwise.

8.3.1. Influence of an AlN buffer layer on the crystallinity of NbTiN films

The impact of a 15 nm AlN buffer layer on the crystallinity of 60 nm NbTiN was evaluated. Both samples—with and without the AlN layer—were analysed as-deposited and after annealing. The details of the annealing procedure—in this thesis named STA—are given in Section 3.4.

The motivation for this study arises from reports indicating that an AlN buffer layer enhances the superconductivity of NbTiN and NbN [35, 161, 192, 193]. Generally, a buffer layer reduces the lattice mismatch between the substrate and the deposited layer and helps epitaxial growth. Ideally, both the buffer and the deposited layer should have the same structure and similar lattice constants. In the current case, cubic NbTiN (rocksalt) and hexagonal AlN (wurtzite) have different crystal structures. However, previous studies showed that

the improvement on T_c and the resistivity originates from the lattice matching between the planes (001) of AlN and the (111) of NbTiN or NbN, which promotes a better crystallisation [35, 161, 192, 193]. The atoms on the rocksalt (111) plane form an hexagonal arrangement and the distance between atoms closely matches the lattice constant of the AlN wurtzite structure (see Figure 8.5). Consequently, AlN not only would act as a good material for the insulating layer in SIS multilayers but also as an effective buffer layer that promotes NbTiN epitaxial growth. Additionally, AlN would also act as a diffusion barrier, preventing oxygen diffusion from the native oxide at the substrate surface into the NbTiN film.

The obtained XRD patterns are displayed in Figure 8.6. The highlighted diffraction peaks confirm the presence of the rocksalt cubic δ-NbTiN phase [194, 195]. The δ-NbTiN peaks lie between the cubic δ-NbN [196] (black dashed lines) and δ-TiN [197] (pink dashed lines) peaks. From lower to higher angles the marked peaks correspond to the planes (111), (200), (220), (222), and (400). Hence, the diffraction peaks are nearer to those of δ-NbN, except for the peak at 61.7° which is closer to that of δ-TiN. Such a peak shift could be caused by small variations in composition, presence or absence of impurities and vacancies, or strain [176, 198]. The splitting of $\sim$75° and $\sim$90° peaks suggests the presence of such irregularities. Furthermore, annealing results in XRD pattern variations. The peaks at 41.7° and $\sim$35° become narrower, indicating grain growth [176]. In addition, the peak at $\sim$35° shifts to higher angles, suggesting changes in the film's stoichiometry or in the impurities and vacancies. Both observations indicate that NbTiN crystallinity enhances upon annealing. Moreover, annealing also results in the crystallisation of AlN in a hexagonal wurtzite structure, as indicated by the peak at 33° corresponding to the (100) plane [199]. This peak is only visible for the AlN-NbTiN sample after annealing (dark blue). However,
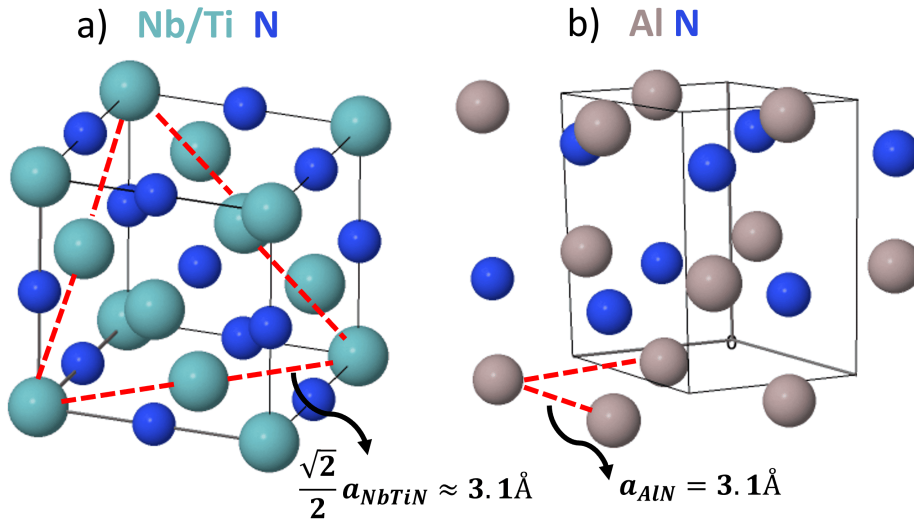
Figure 8.5: Crystal structures: a) Rocksalt NbTiN. The Nb and Ti atoms are non-differentiated; b) Wurtzite AlN. The red lines outline the (111) and (001) planes. Images modified from FIZ Karlsruhe - ICSD [200]
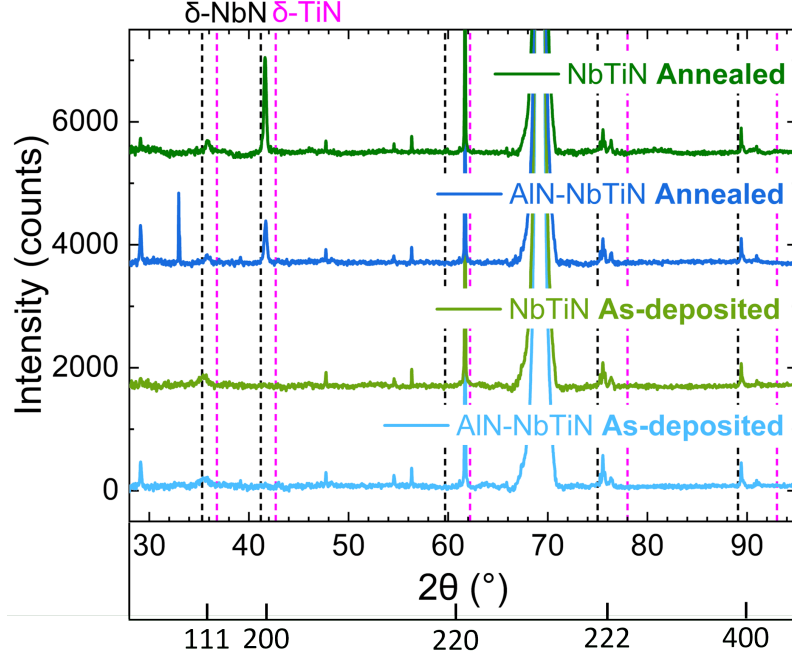
Figure 8.6: X-ray diffraction patterns of NbTiN films deposited with and without an AlN buffer layer, comparing both as-deposited and annealed states. Highlighted peaks demonstrated the presence of the ternary cubic δ-NbTiN. Its peaks lie between cubic δ-NbN (black dashed lines) and δ-TiN (pink dashed lines). The bottom x-axis indicates the corresponding planes.

the (002) AlN peaks at $\sim$35° is masked by the overlap with the (111) NbTiN peak. Besides NbTiN and AlN peaks, some additional peaks are visible. At low angle $\sim$29°, the AlN-NbTiN samples have a peak, both as-deposited and after annealing. This peak is slightly discernible for the single NbTiN film exclusively after annealing. The nature of this peak remains unclear. The current hypothesis is that it may arise from a compound formed at the interface with the Si substrate. This assumption is supported by cross-sectional studies referenced in Section 6.1, particularly Figure 6.4. Consistent with this observation, this peak position aligns with the diffraction peak of various compositions in the Al-O-N system [201] and Al-Si-O-N system [202]. In the case of annealed NbTiN, a cross-sectional analysis is needed to clarify and understand the types of compounds that might be forming at the interface, which could account for this peak. Lastly, note the silicon peaks located at 47.7°, 56.3°, 76.5° and 69.2° [203]. The nature of the peaks at 54.5° and 90.0° remains unidentified.

Furthermore, since the cubic δ-NbN and δ-TiN phases are miscible [172, 189], the lattice constant for $Nb_xTi_{1-x}N$ can be predicted by the Vegard's law:

$$a_{Nb_xTi_{1-x}N} = x\, a_{NbN} + (1 - x)\, a_{TiN} \qquad (8.1)$$

which relates the lattice constant to the ternary compound composition and the bulk lattice constants of NbN and TiN, 4.39 Å and 4.23 Å, respectively [204]. The ternary Nb-Ti-N

98

system has been shown to follow this linear relationship with a slight positive deviation from linearity [160, 172]. The predicted lattice constant in this study is 4.35 Å. The lattice constant obtained from the XRD analysis using equations 4.5 and 8.1, for the as-deposited NbTiN film is 4.37 ± 0.01 Å. Within uncertainties, it closely matches both the predicted value and the reported value for PEALD-films with similar Nb to Ti ratio, 4.36 Å [79]. Other deposition methods, like thermal ALD and sputtering—also for similar Nb to Ti ratios—obtained values of 4.29 Å [67] and 4.30-4.33 Å [205], respectively, below the predictable value. In addition, the conducted annealing reduces the lattice constant to 4.35 ± 0.02 Å, matching the predictable value.

No discernible differences were found in the crystallinity of the PEALD-deposited NbTiN films with or without AlN as a buffer layer, regardless of their state, i.e., as-deposited or annealed. The XRD patterns display the same NbTiN diffraction peaks, and the lattice constants are not influenced by the buffer layer. The main hypothesis is that the as-deposited AlN is amorphous, which prevents the epitaxial growth needed to NbTiN crystallinity. Nonetheless, T_c of NbTiN film was still enhanced by the presence of the AlN layer. Previous studies already showed increased T_c when depositing NbTiN on AlN [35, 161, 192]. Their hypothesis is that reduced lattice mismatch increases T_c. However, Krause et al. [193] observed a degradation of the superconducting properties for better lattice match when comparing various buffer layers. Thus, the NbTiN superconducting properties might also depend on other factors like strain [206] or AlN grain tilt and twist [192]. For the case studied samples in this work, the slight improvement of T_c is attributed to the AlN layer acting as a barrier layer [207], preventing oxygen diffusion from the native silicon oxide into the NbTiN.

8.3.2. Influence of different post-deposition thermal treatments on the crystallinity of AlN-NbTiN films

The previous subsection pointed out that post-deposition annealing, concretely STA, enhances the crystallinity of PEALD-deposited NbTiN films. This subsection further explores the effects of two annealing procedures: RTA and STA. The details of both annealing procedures are given in Section 3.4. The XRD patterns of AlN-NbTiN films as-deposited, and RTA- and STA-treated samples are given in Figure 8.7. The identified peaks, in line with Figure 8.6, correspond to hexagonal AlN and cubic NbTiN phases. Annealing may facilitate atomic mobility, leading to the annihilation of growth-induced defects and grain boundary migration [208], which results in impurities outgassing, stress release, and grain growth [176, 182, 187]. Upon annealing, the peak at $\sim35\,°$ shifts and notably reduces its FWHM, suggesting grain growth and changes in the film's stoichiometry or impurities and vacancies levels. The rise of the peak at $\sim33\,°$ is also visible, which corresponds to AlN, and the emergence of the peak $\sim41\,°$, which corresponds to δ-NbTiN. RTA and STA processes significantly enhance the crystallinity of the films. This observation aligns with the occurrence of Kikuchi patterns in the EBSD analysis and agrees with previous studies on NbN deposited by PEALD [90] and NbTiN deposited by thermal ALD [67], which reported improvement in film crystallinity after thermal treatments at $1000\,°C$ and $900\,°C$, respectively.
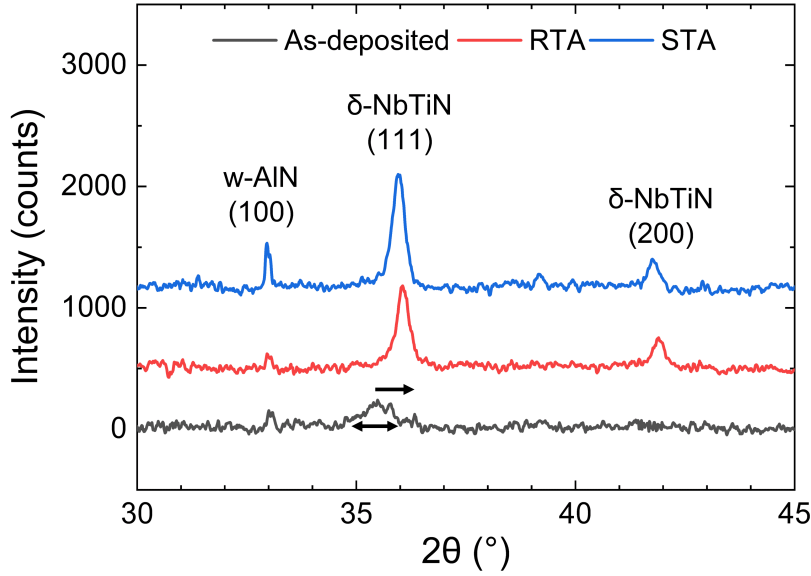
Figure 8.7: XRD patterns of NbTiN films deposited on AlN by PEALD in their as-deposited, after RTA, and after STA states. Both post-deposition processes enhance the crystallinity of the AlN and NbTiN films. The arrows highlight the peak shift and the reduction in FWHM.

The shift of the diffraction peaks towards higher angles translates into decreased lattice constants. Indeed, the as-deposited sample has a calculated lattice constant of 4.37±0.01 Å. However, the RTA- and STA-treated samples exhibit smaller values of 4.33±0.03 Å and 4.35±0.02 Å, respectively. These lattice constants are within uncertainties the same, although they suggest a slight downward trend upon annealing. Shifts in the diffraction peaks, and consequently the changes in lattice constant, result from strain due to the presence or absence of impurities and vacancies, offering information about the film stoichiometry. Hence, the lattice constants of δ-NbN and δ-TiN, and thus of δ-NbTiN, are often used as an indication of the stoichiometry and vacancy or impurity content of the films [160, 178]. The slightly higher value for the as-deposited NbTiN, can be an indicator of the presence of impurities, as larger lattice constants indicate a larger amount of oxygen and carbon in the nitride films [74, 76, 185]. The reduction of the lattice constant observed with both annealing procedures suggests the outgassing of impurities. This assumption aligns with the findings of the XPS analysis on the impact of annealing on NbTiN film composition. These results are presented in Section 7 and indicate annealing causing outgassing, primarily carbon. No direct correlation between the lattice constant obtained and the measured T_c was found for the NbTiN films in their as-deposited, RTA, and STA states. A detailed report on the T_c of the examined NbTiN films is given in Section 9. The same observation was made by Tian et al. [90] for NbN films, highlighting that factors such as strain [206], grain tilt and twist [192] may also play a role. The smaller lattice constant of RTA-treated samples compared to STA-treated can be explained by a larger nitrogen content in the film [68]. It is worth remembering that RTA is conducted under nitrogen atmosphere, while

STA is under vacuum. This would align with our findings which show that RTA-treated samples present lower T_c than STA-treated samples, given that T_c depends on both lattice constant and nitrogen content [209].

Lastly, NbTiN grain size has been calculated from Scherrer's equation (Equation 4.6) based on its diffraction peak at $\sim 35°$. The choice of a single peak is justified by the high variability in the mean grain size obtained from all peaks, a common issue in polycrystalline materials where grain orientation and size can vary significantly. Because the scope here is to reflect annealing induced grain growth, single peak values are enough. Thus, grain size increases from 8.5 nm for the as-deposited sample, to 24.4 nm and 24.4 nm with RTA and STA treatments, respectively.

In summary, it has been demonstrated that both annealing procedures promote the diffraction peaks indicating enhanced film crystallinity and grain growth. Lastly, the reduced lattice constant upon annealing sustains the notion that impurities are outgassed with the heat treatment.

8.3.3. Study of the crystallinity of as-deposited and annealed AlN-NbN films

In this section, the crystallinity of PEALD NbN films is briefly examined. To this end, 15 nm AlN and 60 nm NbN layers grown on Si were analysed in both their as-deposited and annealed states.

In contrast with NbTiN, whose stable crystalline configuration is the rocksalt cubic structure [161, 172], NbN holds eight different crystal structures (see its phase diagrams in Figure 8.2) including cubic, tetragonal and hexagonal structures. Moreover, it must be noted that the phase identification of NbN films requires special care. The individual assignment of the diffraction peaks is difficult due to the overlapping from different phases [176, 177]. Generally, for XRD patterns with angles below $90°$ the distinction between the different hexagonal NbN structures, and between the cubic and the tetragonal structures is not possible in most cases [176].

The XRD pattern, shown in Figure 8.8, reveals the absence of peaks at $41°$, ruling out the presence of cubic and tetragonal NbN phases. This observation aligns with the silver colour observed in the NbN film, which, as mentioned earlier, is a signature of its hexagonal structure. Furthermore, the position of the diffraction peaks matches the hexagonal structure although differentiation between the phases Nb_2N [210], δ'-NbN [211], ϵ-NbN [212], and Nb_5N_6 [213] is not achievable. This finding aligns with the poor superconductivity of the NbN films. A greater T_c is expected for the cubic and tetragonal NbN phases; while low T_c or even lack of superconductivity down to 2 K has been reported for the NbN hexagonal phases. No significant structural changes were observed in the NbN films due to annealing. Additionally, the peak located at $\sim 54°$ could be assigned to Nb oxynitrides [214, 215]. Lastly, as discussed earlier, the peak at $33°$ indicates AlN crystallisation and the peaks at $47.7°$, $56.3°$, and $69.2°$ belong to the silicon wafer [203].
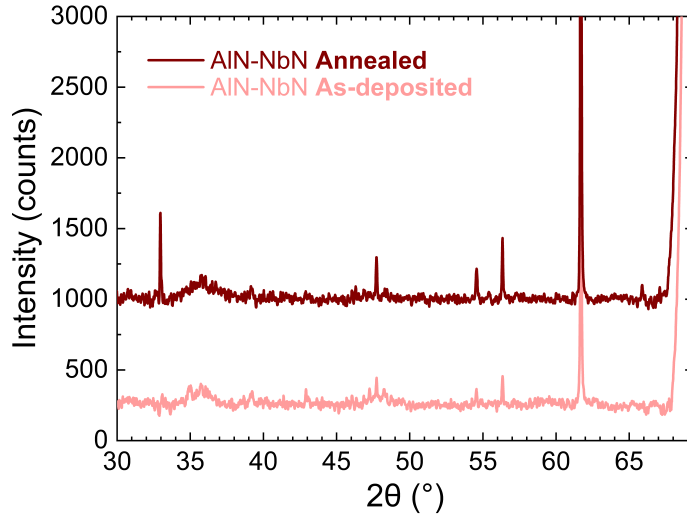
Figure 8.8: Diffraction peaks of AlN-NbN films deposited on silicon wafers. It presents a comparison between as-deposited and annealed samples. The x-axis displays angles ranging from 30° to 70° for a better view of the lack of peak at 41°.

8.4. Summary and conclusions

The findings of the crystal structure analysis are summarised in Table 8.1. It is worth to recall that this study was conducted using Si as substrate. Both as-deposited NbTiN and NbN thin films were found to be polycrystalline, exhibiting respectively rocksalt and hexagonal crystal structures. Although the phase of NbN remains unidentified, the grey colour and lack of a peak at 41° are indicative of a hexagonal structure. In contrast, as-deposited AlN is amorphous; however, with annealing, it crystallises into wurtzite structure. Furthermore, the presence or absence of AlN as a buffer layer does not alter the lattice constant of NbTiN. Moreover, post-deposition annealing was demonstrated to greatly enhance the crystallinity of NbTiN thin films by promoting crystal growth and reducing the lattice constant.

Table 8.1: Summary of crystallographic findings across the different samples and post-deposition treatments. Any mention of annealing defaults to STA unless stated otherwise

Sample	lattice constant (Å)	Structure	Phase
As-deposited:NbTiN	4.37 ± 0.01	rocksalt	δ
Annealed:NbTiN	4.35 ± 0.02	rocksalt	δ
As-deposited:AlN-NbTiN	4.37 ± 0.01	amorphous ; rocksalt	δ
Annealed:AlN-NbTiN	4.35 ± 0.02	wurtzite ; rocksalt	w ; δ
As-deposited:AlN-NbTiN	4.37 ± 0.01	amorphous ; rocksalt	$-$; δ
RTA:AlN-NbTiN	4.33 ± 0.03	wurtzite ; rocksalt	w ; δ
STA:AlN-NbTiN	4.35 ± 0.02	wurtzite ; rocksalt	w ; δ
As-deposited:AlN-NbN	$-$	amorphous ; hexagonal	$-$; unknown
Annealed:AlN-NbN	$-$	wurtzite ; hexagonal	w ; unknown

9. Evaluation of the superconducting properties

This section focus on the superconducting characterisation of the PEALD films, a crucial aspect for their potential integration into SRF cavities. The analysis is conducted through ETO and VSM in the PPMS Dynacool (see Section 4 for further information). A comparative analysis between NbN and NbTiN films is first conducted, underlining the advantage of the ternary over the binary nitride. Next, the role of the Nb to Ti ratio is explored to determine the optimal composition for enhancing superconducting properties. Given that initial measurements show relatively low transition temperatures (T_c), the study further investigates the effect of post-deposition thermal annealing on improving the T_c. Additional factors affecting the superconducting performance of NbTiN films, such as film thickness, deposition temperature, substrate type, and the use of an AlN buffer layer, are also analysed. Finally, magnetisation curves are presented, comparing the performance of AlN-NbTiN multilayers under different conditions and on different substrates. These evaluations offer valuable insights into optimising NbTiN films for SIS multilayers on SRF cavities. Some of the presented results were already reported [102, 103].

9.1. NbN vs NbTiN thin films deposited by PEALD

The earlier discussion addressed the benefits of partial substitution of Nb atoms with Ti atoms for stabilising the crystalline phase of interest. It was demonstrated that NbTiN films crystallise in the cubic δ-phase, whereas NbN films form in a hexagonal structure. Here, the discussion centres on the advantages that the incorporation of Ti offers in terms of electrical transport properties.

For the implementation of SIS multilayers in SRF cavities, NbN appears as a suitable option because of among other factors its high T_c= 17.3 K [181]. However, it has been widely reported that NbN exhibits high residual and room temperature resistance, a negative temperature coefficient of resistance and low RRR [216–220], resulting in high surface resistance and a low quality factor in SRF cavities. There are two reasons behind such anomalous resistance of NbN thin films. On one hand, the lack of long range order plus the presence of strong grain boundary scattering play a significant role. The NbN grains are separated by boundaries that consist of voids, normal conducting areas, and non-conductive areas, presumably oxides [184]. This issue is particularly pronounced in polycrystalline films. On the other hand, NbN exhibits a high density of N vacancies, along with Nb vacancies, contributing to its resistance [32, 184].

The resistance of NbN thin films as a function of temperature is displayed in Figure 9.1. In the as-deposited state, the NbN film exhibits a high negative temperature coefficient, which becomes positive after annealing, suggested to arise from a reduction on the amount of grain boundaries and impurities outgassing. The RRR improves with the annealing however, none of the films exhibit a superconducting transition. This observation is consistent with the above XRD analysis regarding PEALD-NbN films, both as-deposited and annealed, which exhibited hexagonal phase, which correlates with non-superconductivity or low T_c (see Section 8 for more details about XRD analysis and NbN T_c for its various structures).

103
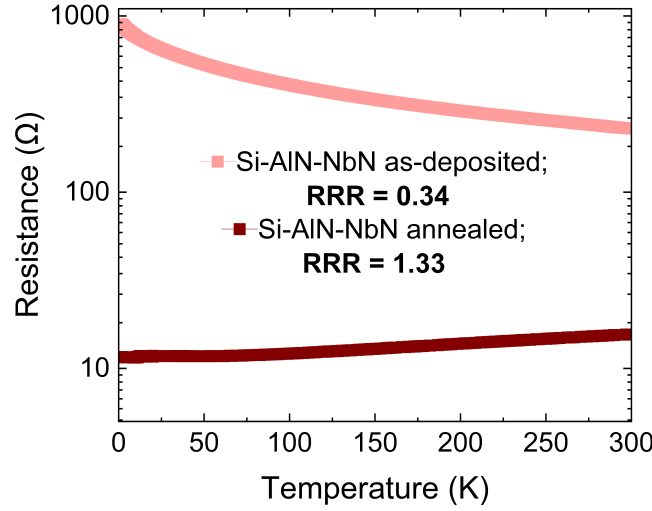
Figure 9.1: Temperature dependence of the electrical resistance of NbN thin films in their as-deposited and annealed states. Note the y-axis is plotted on a logarithmic scale. There is an important reduction in both the room temperature and the residual resistance with annealing; nonetheless, the films do not exhibit superconducting transition.

Alternatively, NbTiN emerges as an interesting substitute, since it combines the superconducting properties of NbN and the good metallic properties of TiN. Both nitrides are miscible and result in a ternary compound which offers higher T_c= 17.8 K [189], despite the low T_c= 5.4 K of TiN [32] and T_c= 9.5 K of the NbTi alloy [160], and lower resistance than NbN. The decrease in resistance is the consequence of two factors First, heat of formation is larger for TiN ($80\,\mathrm{kcal\,mol}^{-1}$) than for NbN ($56\,\mathrm{kcal\,mol}^{-1}$) [189], being less prone to react with impurities and thus limiting the formation of undesirable compounds at grain boundaries, reducing the strong grain boundary scattering issues. Second, Ti is a good nitrogen getter [26, 160, 184], reducing the effect of nitrogen and metal vacancies. It must be noted that since NbTiN is a ternary compound its properties are linked to its specific composition.

9.2. Exploring the role of NbTiN composition

The TiN and NbN systems are indeed miscible [77, 172], leading to the formation of a stable ternary compound, whose properties are influenced by the concentrations of Nb and Ti [190, 191, 221]. Basically, it forms the B1 structure with a partial substitution of Nb atoms with Ti atoms. In this study, the PEALD of $Nb_xTi_{1-x}N$ is performed in a supercycle fashion, the details of which are given in Section 3. By adjusting the cycle ratio m to n for TiN to NbN, respectively, the targeted composition can be tuned. Eight films with different compositions ranging from Ti-rich to Nb-rich were evaluated, with a fixed thickness of ~25 nm for all samples. It was shown above by EDX (see Section 7.1) that there is a linear relationship between the PEALD supercycle and the elemental composition, offering an advantage over thermal ALD for which this is not feasible [68, 71].

Table 9.1: List of the various $Nb_xTi_{1-x}N$ compositions under examination. The first row represents the PEALD supercycle ratio while the second is the Nb content.

Nb:Ti (n:m)	1:5	1:4	1:3	1:2	1:1	2:1	3:1	4:1
x Nb (in %)	16.7	20	25	33.3	50	66.7	75	80

The various $Nb_xTi_{1-x}N$ investigated compositions are listed in Table 9.1. Their electrical and magneto-transport evaluation is presented in Figure 9.2. The resistance as a function of temperature for three different NbTiN compositions is displayed in Figure 9.2 a). In particular, corresponding to 25% , 66.7% , and 75% of Nb content (represented from lighter to darker colour). It is evident the variation in the metallic nature of the films. As one would expect the more Nb content the higher the resistance at low temperatures. This is reflected in the RRR values, which decrease as the Nb content increases. Still, the eight NbTiN compositions exhibit superconducting transition. The resistivity at room temperature follows a similar trend. Taking a broad view it increases with the Nb content; however, it lowers for the NbTiN film with the highest Nb content. When comparing the resistivity of the NbTiN film with 75% Nb content to literature values, it is found to be significantly higher, specifically 2.5 times higher than films of similar thickness deposited by PEALD [79], suggesting lower films quality. In fact, the obtained T_c values do not exceed the 7 K, no matter the film composition. A possible reason could be the a high amount of impurities incorporated into NbTiN films during the PEALD-deposition process. XPS analysis supports this assumption (see Section 7). However, as anticipated, T_c shows a strong dependence upon the Nb content. It is visible in Figure 9.2 c) that when increasing the Nb content T_c first increases, reaching a maximum for 50% and 60% Nb content, but then decreases for higher Nb concentrations. Previous studies reported distinct trends between T_c and NbTiN composition [32, 68, 79, 160, 190, 221–223], with a broad range of compositions over which the maximum T_c is achieved. For example, T_c reaches its maximum at 50% [160, 221, 224], 60% [190], or the 70% [191] of Nb content. These variations can be attributed to factors beyond just the Nb/Ti ratio, such as nitrogen content, level of impurities, and strain in the lattice. Lastly, despite the low quality film indicated by the high resistivity and lower-than-expected T_c, the superconducting transition is sharp over the whole range of compositions. Thus, the low ΔT_c, less than 0.3 K over all the compositions range, indicates a good film homogeneity, as expected for PEALD. In addition, the resistance was measured as a function of the applied magnetic field at a constant temperature close to the T_c of the films. Figure 9.2 d) provides a visualisation for the same three different compositions, while Figure 9.2 e) shows the relationship of the derived H_{c2} with the film composition. The H_{c2} increases with the Nb content, following the trend reported by Yen et al. [191].
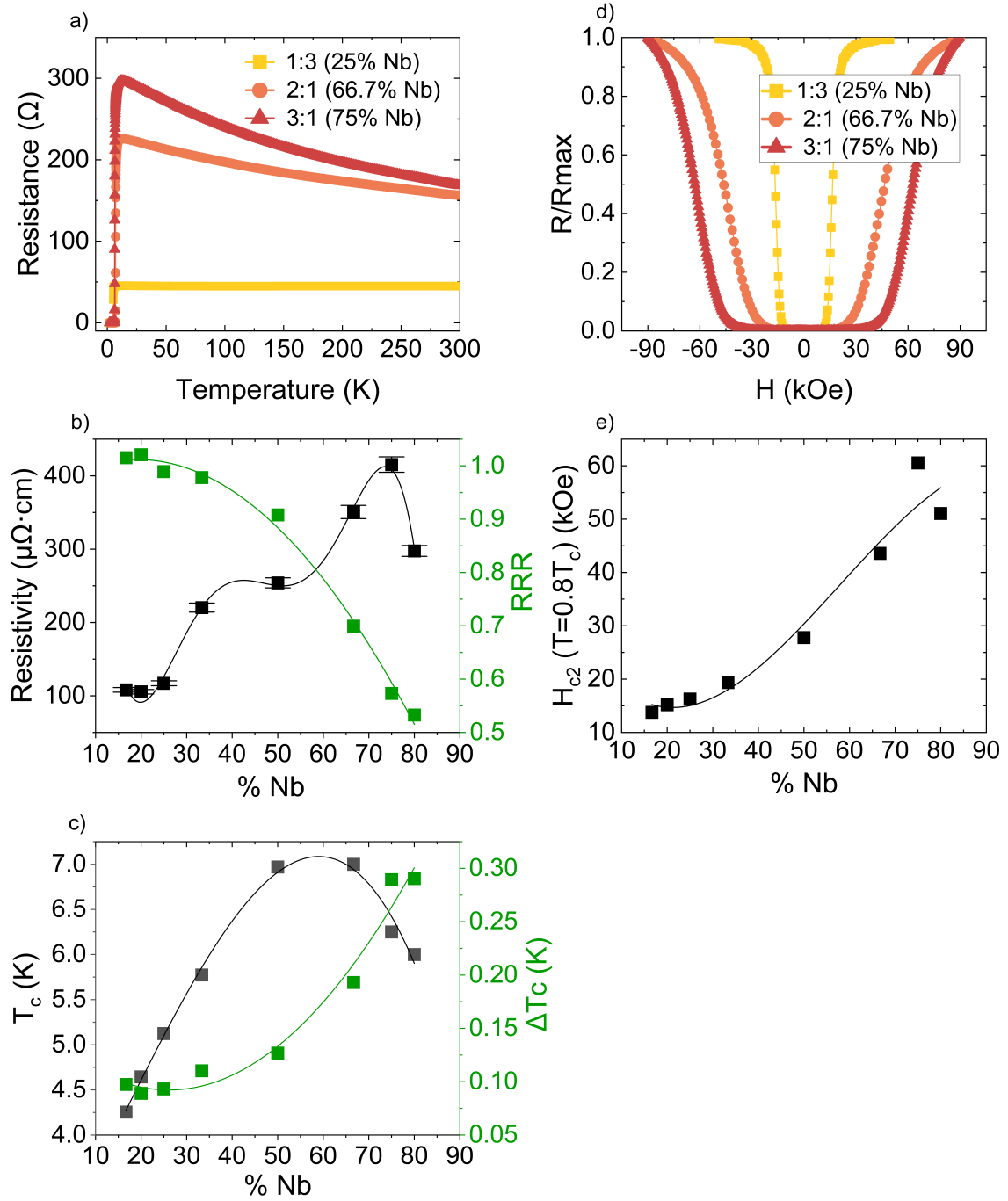
Figure 9.2: Electrical and magneto-transport properties as a function of the Nb content in the NbTiN film. a) Resistance as a function of temperature for three compositions; b) resistivity at room temperature and RRR and c) T_c and ΔT_c as a function of Nb content on NbTiN thin films for eight different compositions; d) normalised resistance as a function of applied magnetic field showing the superconducting transition for three compositions; and e) H_{c2}, determined at a temperature 80% of T_c, for the eight compositions. Solid lines serve as guides to the eye.
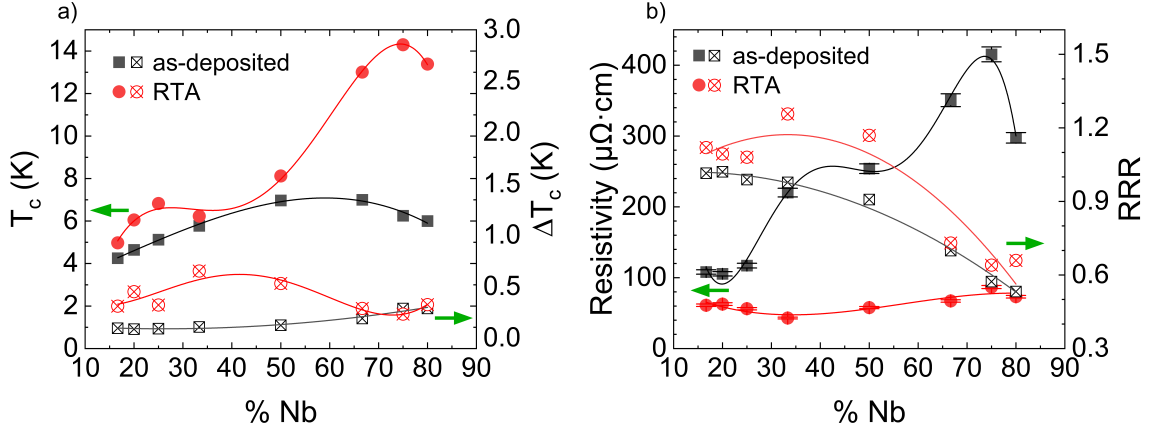
Figure 9.3: Contrast of the electrical-transport properties over the range of compositions for the as-deposited and after RTA films. RTA greatly improves the film properties, particularly for compositions above 50% of Nb content. a) T_c and T_c, and b) room temperature resistivity and RRR. Filled circle/square indicate T_c and resistivity data, while hollow circle/square represent ΔT_c and RRR. Green arrows and solid lines serve as guides to the eye.

In pursuit of a better performance of NbTiN films, various post-deposition thermal annealing procedures were investigated, whose details are given in Section 3. The results of RTA-treated NbTiN films with different compositions are presented in Figure 9.3. The higher the Nb content is the more favourable the RTA impact. In particular, for compositions above 50%, T_c approaches two times its as-deposited value and the resistivity decreases by a factor of 4 to 5. The optimal composition ratio was found to be 75% of Nb and 25% of Ti, resulting in $T_c =14.3\,\mathrm{K}$, $\Delta T_c =0.23\,\mathrm{K}$, $\rho_{300\mathrm{K}} =77.3\,\mu\Omega\,\mathrm{cm}$ and RRR = 0.64, after RTA treatment.

9.3. Impact of film thickness and different annealing procedures

The previous subsection identified the optimal composition for the NbTiN thin films: 75% of Nb versus 25% of Ti, or in other words a 3 to 1 ratio of Nb to Ti. Here, the impact of film thickness is evaluated, as well as various post-deposition annealing procedures. Although further details of both annealing procedures are given in Section 3, it is worth remembering that the labelling of RTA and STA comes from rapid and slow thermal annealing.

It is well known that the dimensional reduction from bulk to thin films alters the material electronic properties. For superconducting films with a thickness comparable or less than the coherence length, the formation and stability of Cooper pairs are affected, causing a reduction of T_c and an increase of the resistivity compared to the bulk values. For instance, for NbTiN thin layers of thickness below 10 nm, a dramatic variation in electrical properties occurred [209]. In extreme cases, superconductivity can be completely suppressed if the films are too thin to sustain coherent Cooper pairs. To investigate these effects on PEALD-NbTiN films, various film thicknesses ranging from 6 to 74 nm were analysed. The film thickness was controlled by the GPC and the number of PEALD supercycles conducted.

The resistance over temperature for the various thicknesses evaluated is given in Figure 9.4. The thinnest film does not exhibit a superconducting transition down to 2.5 K. The high disorder level is presumed to be the cause. However, as the film thickness increases, the films become superconducting and T_c increases. The observed thickness dependence of T_c is attributed to an increase in grain size, hence reduced grain boundaries. For films thicker than 12 nm, the transition gets sharper, with a transition width below 0.2 K. Nevertheless, although T_c raises with thickness, it does not improve enough for implementation in SIS multilayers for Nb SRF cavities, as the T_c remains bellow Nb T_c. Thus, post-deposition thermal annealing procedures—RTA and STA—at 1000 °C were applied to the entire range of thicknesses.

In this study, it has been demonstrated that both RTA and STA promote the grain growth and crystallisation of NbTiN film (see Section 8) and that STA results in carbon outgassing (see Section 7). Both events are presumed to positively impact the transport properties of NbTiN films by minimising scattering events. Figure 9.5 illustrates that both annealing procedures—RTA and STA—improve the electrical transport properties of NbTiN films across the entire range of thicknesses. Overall, the room temperature resistivity, Figure 9.5 b, is lowered over the entire range of thicknesses similarly for both treatments. However, at low temperatures, when electron scattering from lattice defects, such as grain boundaries and interstitial impurities, significantly affect resistivity [225], STA has proven more beneficial, particularly for thicker films, as indicated by higher RRR values (see Figure 9.5 c). The en-
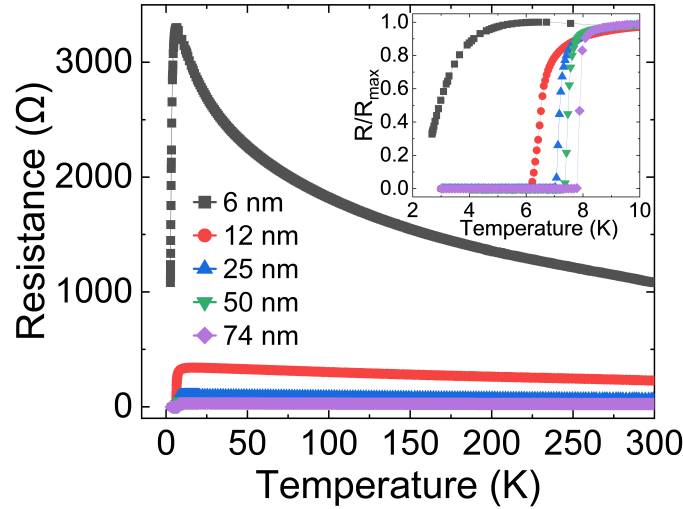
Figure 9.4: Resistance over temperature for the various film thicknesses: main from 300 to 2 K and inset zoom in for low temperatures (normalised). The 6 nm NbTiN layer does not exhibit superconducting transition down to 2.5 K.
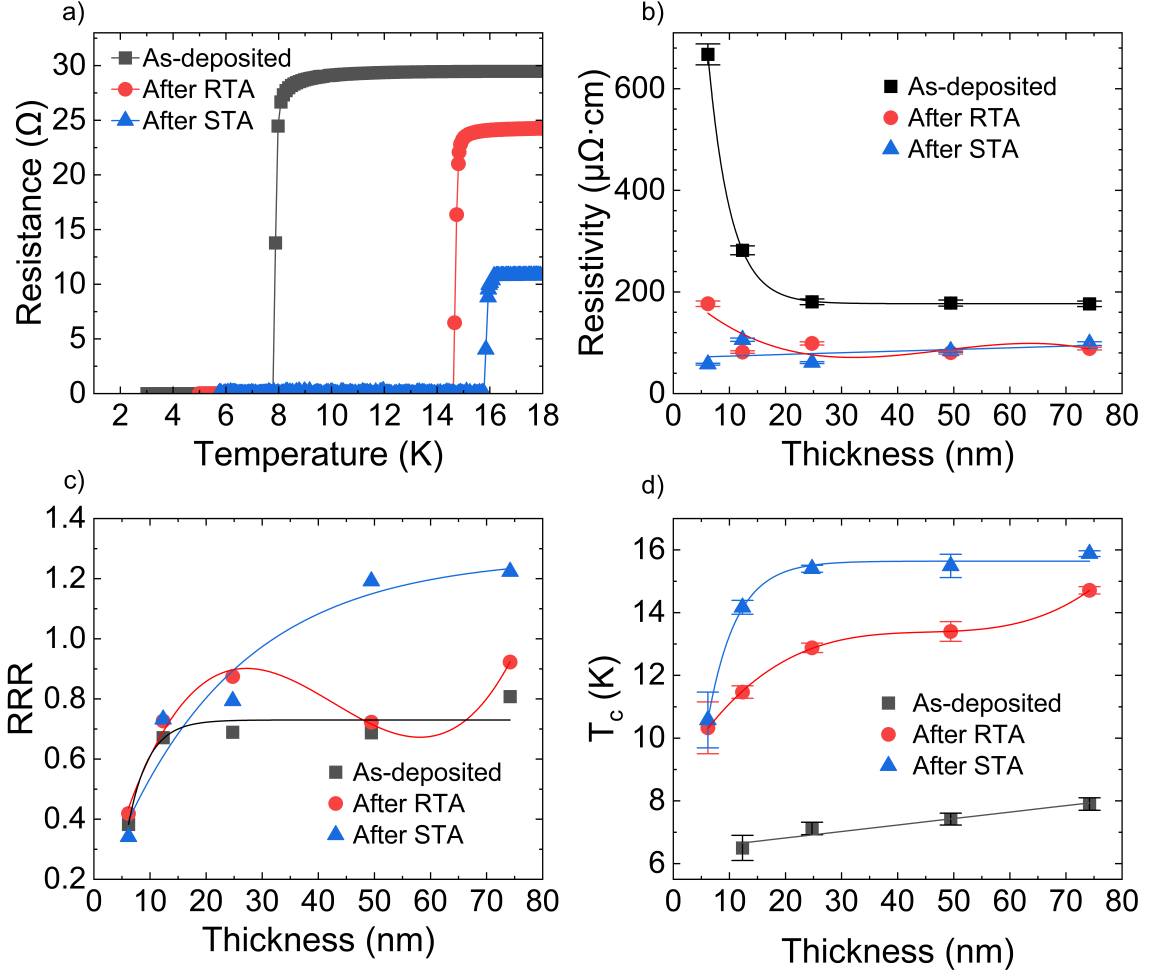
Figure 9.5: Comparing as-deposited and RTA- and STA-treated NbTiN films across the range of thicknesses. a) Resistance as a function of low temperature for the 74 nm thick film. The trend over the range of thicknesses in b) resistivity at 300 K, c) RRR, and d) T_c is shown in black for as-deposited, in red after RTA, and in blue after STA. Solid lines serve as guides to the eye.

hanced crystallinity of STA-treated films compared to RTA-treated films is assumed to be due to longer exposure to high temperatures. This hypothesis is supported by observing more pronounced Kikuchi patterns for STA- versus RTA-treated films. Interestingly, as seen in Figure 9.5 d, the thinnest film becomes superconducting after both thermal annealing procedures with T_c above 10 K. This finding could indicate that as-deposited NbTiN of 6 nm thick may be amorphous, becoming polycrystalline only after thermal treatment. Conversely, thicker films may be already polycrystalline in their as-deposited state, and exhibit superconducting transition. To conclude, both post-deposition thermal treatments have proven to significantly enhance T_c, although STA resulted in a better outcome with a maximum value of 15.9 K.

9.3.1. Impact of the annealing temperature

For the results shown above, the annealing temperature was kept at 1000 °C. However, a prior evaluation of the annealing temperature and duration was conducted. The results are presented here, first for RTA and then for STA. Note that the labelling of RTA and STA comes from rapid and slow thermal annealing. See Section 3 for more annealing details.

RTA

The Figure 9.6 shows the T_c of RTA-treated NbTiN thin films. These films have a thickness of around 25 nm. Moreover, it must be noted the NbTiN composition, with a ratio of Nb to Ti of 2 to 1. This composition differs from the rest of the films evaluated, which are 3 to 1. The annealing temperatures performed were 800, 900, and 1000 °C. While the annealing duration ranges from 5 to 50 minutes. Both process parameters were limited by the furnace capabilities. At 800 °C, there is no significant benefit in T_c after annealing, regardless of the duration. However, when increasing the annealing temperature, the films began to exhibit enhanced superconducting properties. At 900 °C, T_c oscillates between 9 and 12 K with inconsistent annealing durations. This suggests that the energy provided at this temperature, across the entire range of examined annealing durations, is insufficient for stable recrystallisation. Thus, small changes in the annealing parameters were observed to lead to significant changes. However, at 1000 °C, there is no significant difference in T_c for the various annealing durations, suggesting that this temperature provides enough energy for stable recrystallisation.
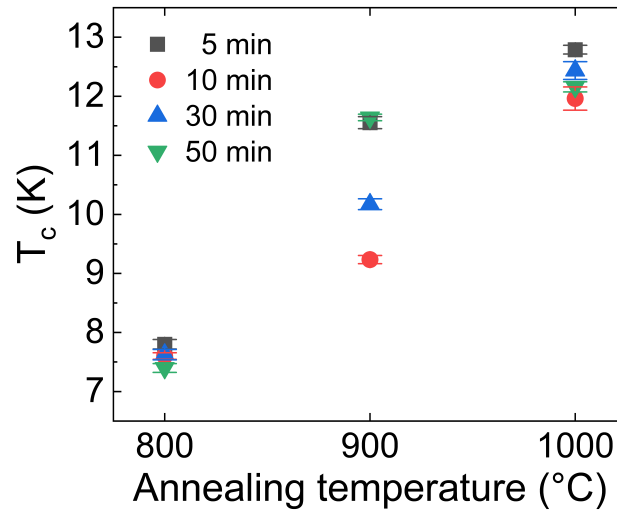
Figure 9.6: Critical temperature for NbTiN thin films RTA-treated at different temperatures and durations. The NbTiN films have a ratio of Nb to Ti of 2 to 1.

STA

NbTiN films with a thickness of 60 nm and compositional ratio of 75% Nb to 25% Ti were STA-treated. The examined annealing temperatures range from 700 to 1100 °C. Between 700 and 800 °C the annealing duration lasts 5 hours, whereas for higher temperatures it is 1 hour. The observations are summarised in Figure 9.7, a) for T_c and b) for resistivity at 300 K and RRR. The T_c and room temperature resistivity follow a similar enhancement trend across the different temperatures. At 700 °C, no remarkable benefit in the T_c is achieved through annealing. However, at 750 °C, T_c shows a notable enhancement and at 780 °C, it overcomes the T_c values obtained at 1000 °C for the RTA procedure. This indicates that a low temperature for a longer duration also provides the necessary thermal load to drive the crystallisation. Moreover, when comparing the same annealing temperatures and durations, i.e. 900 °C, one realises that the residual heat experienced during ramping and cooling down also plays an important role. It is worth remembering that the labelling of RTA and STA comes from rapid and slow thermal annealing. This points to a difference in the ramping rates, which is 20 times faster for RTA than STA. However, there would be a threshold in temperature at which the thermal energy provided into the system compensates for the duration factor. The examination of various ramping rates in both RTA and STA suggested this temperature to be 1000 °C. Additionally, 1100 °C is revealed to be unfavourable. This could be because this temperature was found to cause excessive morphology damage in the sample. Another assumption could be nitrogen outgas or ternary compound segregation. Further studies are required to clarify these observations.
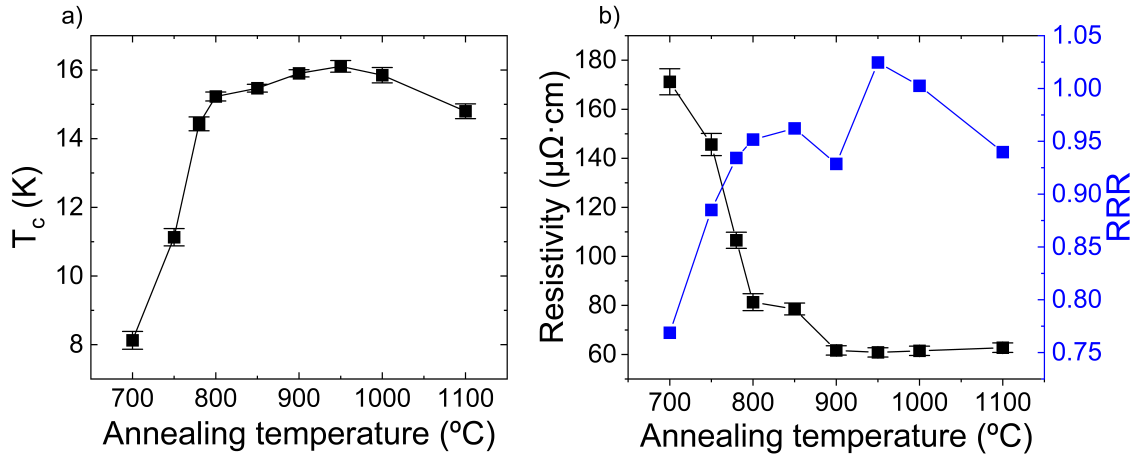
Figure 9.7: Effect of the annealing temperature on the electrical transport properties of STA-treated NbTiN thin films: a) T_c and b) resistivity at room temperature and RRR. The best performance is achieved for 950-1000 °C. Between 700 and 800 °C the annealing lasts 5 hours, whereas for higher temperatures it is 1 hour. Solid lines are guides to eyes.

9.4. Effect of deposition temperature

The deposition temperature is a factor that directly impacts the ALD chemistry and the crystallisation during film growth. In general, higher deposition temperatures result in denser films with larger grains. This means having fewer defects such as vacancies, more
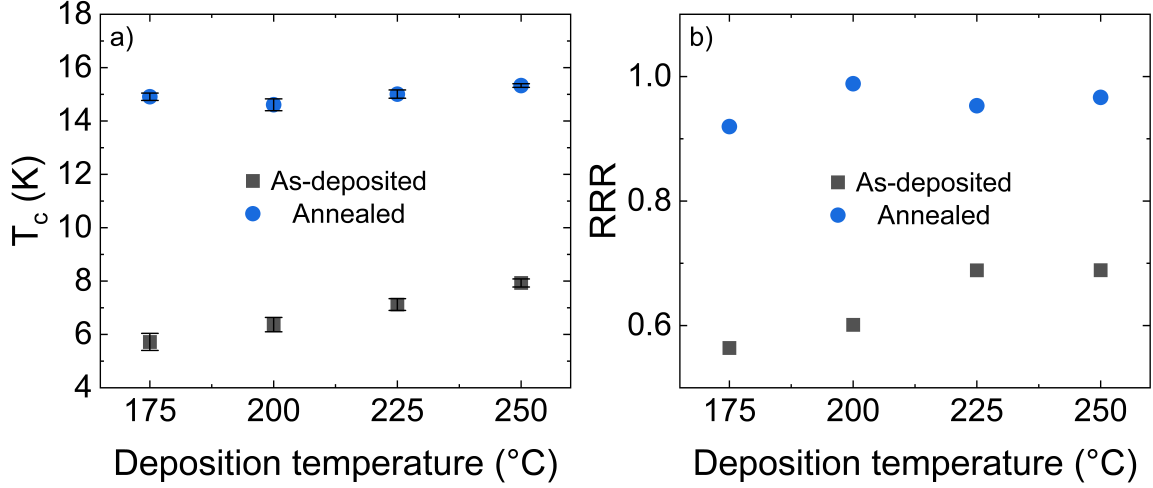
Figure 9.8: Evaluation of the impact of the deposition temperature on the low temperature conductivity. The black squares denote as-deposited values, while blue circles the annealed ones. a) For as-deposited films, T_c increases with deposition temperature. Upon annealing, this dependence disappears. b) RRR show a similar trend.

compact thin films, and a reduced number of grain boundaries. Higher deposition temperatures reduce the impurities within the film, improving the conduction.

Here, NbTiN films were deposited at temperatures ranging from 175 °C to 250 °C and examined. The results from their electro-transport measurements are given in Figure 9.8 (black squares), showing a) T_c and b) RRR. Then, the films were annealed and reevaluated. The results are also included in Figure 9.8 (blue circles). As expected, there is an increase in T_c and RRR with the deposition temperature. This suggests a less defective crystalline structure of the NbTiN films deposited at higher temperatures, resulting in less impurity scattering and hence, higher T_c and RRR values. Moreover, it was investigated whether post-deposition annealing could compensate for the impact of the deposition temperature. The results suggest that high-temperature annealing minimize the differences seen in as-deposited films grown at different temperatures.

9.5. Impact of the substrate and buffer layer on the superconductivity of NbTiN

Here, the superconducting transition of NbTiN was examined for thin films deposited on Si and Nb substrates. Moreover, the potential effect of AlN as a buffer layer as well as the impact of high temperature annealing on both substrates were assessed.

9.5.1. Silicon wafer as substrate

The NbTiN films deposited on silicon were characterised in a PPMS Dynacool from Quantum Design described in Section 4.

The films' resistance as a function of temperature is displayed in Figure 9.9. All films show a sharp superconducting transition, regardless AlN layer is present or not. In both

Table 9.2: Summary of NbTiN properties for the samples in Figure 9.9

Si-NbTiN	$T_c \pm \Delta T_c$ (K)	RRR	**Si-AlN-NbTiN**	$T_c \pm \Delta T_c$ (K)	RRR
As-deposited	7.7 ± 0.2	0.702	As-deposited	8.0 ± 0.2	0.732
Annealed	15.7 ± 0.2	0.829	Annealed	16.0 ± 0.2	1.033

cases, the transition shifts from near $8\,$K toward higher temperatures, near $16\,$K, as a result of post-deposition annealing. The T_c and RRR values are listed in Table 9.2. The obtained T_c values for the samples with and without the AlN layer are within uncertainties the same, independent of whether the films are as-deposited or annealed. This finding aligns with the XRD findings presented in Section 8, where it was demonstrated that there are no discernible differences between the samples with and without AlN as a buffer layer. In other words, regardless of the presence or absence of the AlN layer, NbTiN crystallises in its δ-phase and possesses the same lattice constant. Consequently, the slight increase in T_c should not be attributed to AlN enhancing the NbTiN crystallinity [35, 161, 192] but acting as a barrier layer [207], preventing oxygen diffusion from the native silicon oxide into the NbTiN. The impact of AlN acting as a diffusion barrier would be more significant on thinner NbTiN films (here the films are $60\,$nm thick) where T_c would be affected by the larger ratio of oxygen impurities.Under the annealing conditions, the thin native silicon oxide layer likely initiates or completes its sublimation process through the reaction $Si(s) + SiO_2(s) \rightarrow 2SiO(g)$ [226, 227]. In this scenario, the gas species could either diffuse into the NbTiN or escape through it. Nevertheless, despite the absence of an AlN layer, annealing still enhances the T_c of the NbTiN films. The RRR values for annealed samples, both with and without the AlN layer, support the hypothesis that AlN acts as a diffusion barrier layer.
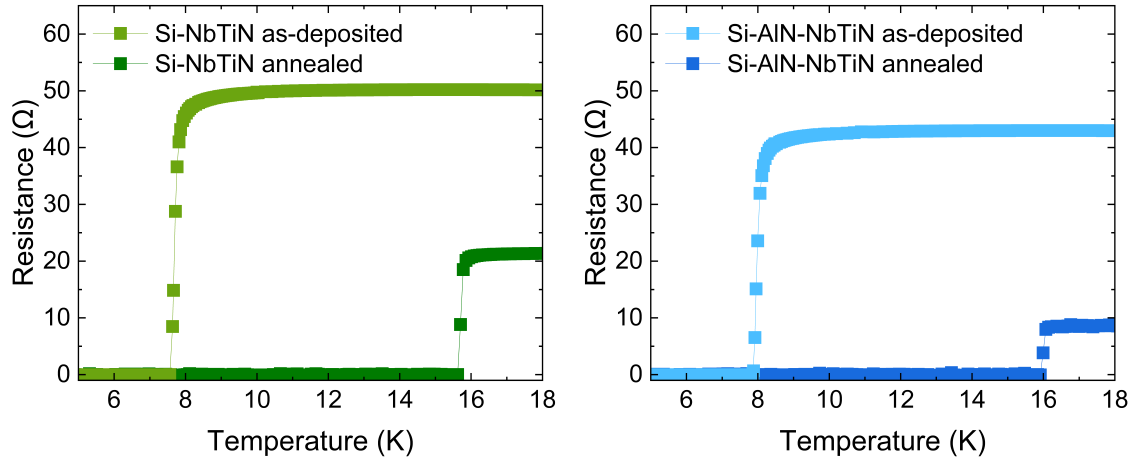
Figure 9.9: Film resistance as a function of low temperature. The superconducting transition occurs regardless of whether NbTiN is grown directly on silicon or with an AlN buffer layer. Post-deposition annealing likewise rises the T_c of both films.

9.5.2. Niobium as substrate

The S(I)S multilayers grown on bulk Nb were characterised in an inductive measurement station at CERN [122]. A contactless measurement method was found to be necessary during this study. Due to the soft and malleable nature of Nb, it was observed that applying electrical contacts damage the thin films. The details of this measurement technique are given in Section 4. In total, four samples were evaluated: Nb-NbTiN and Nb-AlN-NbTiN, both in their as-deposited and annealed states.

The superconducting transitions are displayed in Figure 9.10. It is worth noting that, in their as-deposited state, light green and light blue in Figure 9.10, the NbTiN superconducting transition cannot be detected since it occurs at a temperature below the T_c of Nb and the magnetic field is blocked by its screening currents. Thus, the observed transition at $9.5\,K$ corresponds to the Nb substrate. Annealing was expected to rise the T_c of NbTiN above that one of Nb, as occurs for multilayers grown on Si. For the annealed Nb-AlN-NbTiN (see Figure 9.10 dark blue) two transitions are visible: one at $9.5\,K$ corresponding to the Nb T_c and another at $1414.2\,K$ corresponding to the NbTiN film. However, annealing does not result in the emergence of a high-temperature superconducting transition of NbTiN in the absence of an AlN layer (see Figure 9.10 dark green). Nevertheless, as studied by Preece [228], the NbTiN film is still superconducting. There are two hypotheses for explaining this absence of enhanced T_c after annealing. One may be the decomposition of the native Nb oxides and the oxygen diffusion into the NbTiN thin film. This native oxide is indeed a system of three oxide layers: NbO, NbO_2, and Nb_2O_5, from the Nb-oxide interface to the surface [229]. During the PEALD process, conducted at $250\,°C$, the Nb_2O_5 could have started to reduce into NbO_2 [229, 230]. However, annealing at high temperature would dissolve completely the Nb_2O_5 and NbO_2 layers [229]. The NbO does not dissolve at temperatures below $1600\,°C$ [229, 231]. It is plausible that the oxygen partially diffuses into the NbTiN thin film resulting in significantly reduced T_c. Thus, in the absence of an AlN layer, a pre-deposition heat treatment would be essential for removing NbO_2 and Nb_2O_5 from the
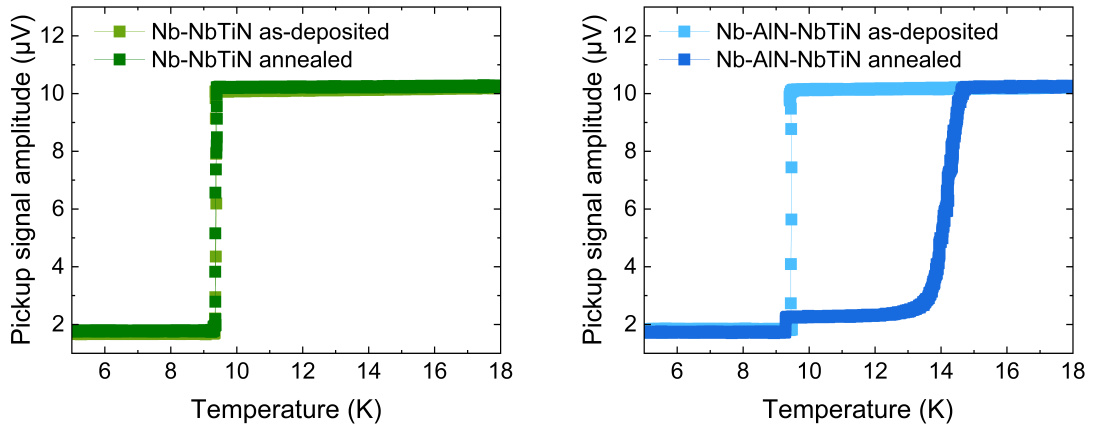
Figure 9.10: As-deposited and annealed multilayers grown on Nb substrates: Nb-NbTiN (left) and Nb-AlN-NbTiN (right). Light colours represent as-deposited states, while dark colours correspond to the annealed state.

Nb surface to achieve a high-Tc NbTiN layer. However, the hypothesis of element diffusion from the NbTiN film into the Nb substrate cannot be excluded. Further investigation is needed to address this event.

9.6. Magnetisation curves through VSM

Magnetometry and transport measurements allow for the detection of the transition of materials from normal conducting to superconducting state. However, unlike transport measurements—conducted by a four-probe method—which evaluate locally the response of the thin film, magnetometry monitors the behaviour of the entire sample. This means that not only the thin film deposited on the upper side of the substrate is captured, but also the partial coating on the bottom side of the substrate, characteristic of ALD, and the substrate. The magnetisation was studied as a function of temperature and the applied magnetic field. The findings of these studies are presented in the following subsections.

9.6.1. Curves m(T) for AlN-NbTiN multilayers grown on Si and Nb

First, the magnetic moment of samples consisting of AlN-NbTiN multilayers deposited on Si and Nb substrates is compared. Due to limitations in the experimental setup, direct measurements on bulk Nb substrates were not feasible, so Nb foils were used instead. The examined samples were deposited and annealed together with the ones analysed by ETO and an inductive measurement station at CERN [122], whose results are reported in the previous section 9.5.

The magnetic moment as a function of temperature is displayed in Figure 9.11: a) for Nb and b) for Si substrates. The large difference in magnitude of the magnetic moment between the Nb foil and the NbTiN thin film, because of the substantial contrast in thickness, masks the superconducting transition of the thin film. At a glance, the magnetic moment measured
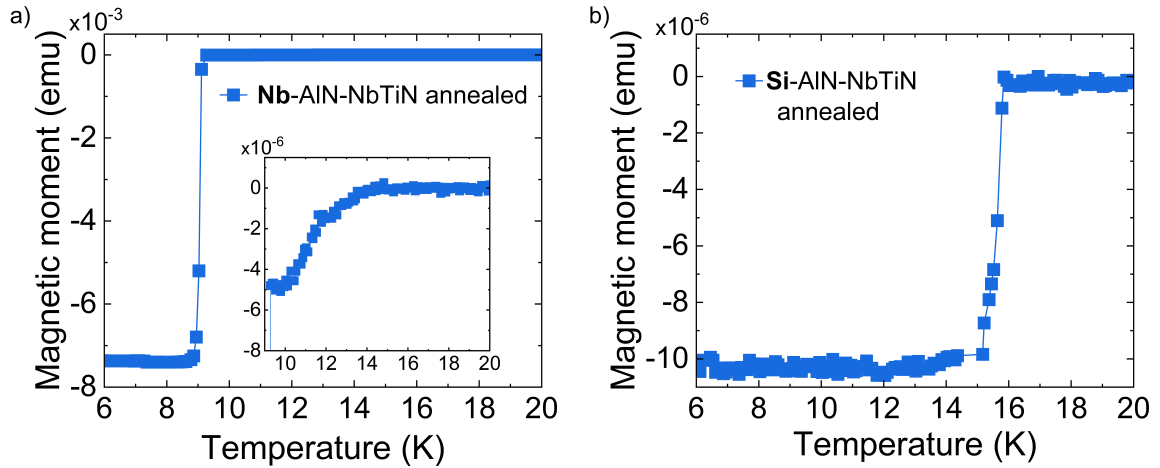
Figure 9.11: m(T) curves for AlN-NbTiN multilayers on a) Nb and b) Si substrates. The insert in a) shows a zoom-in which reveals the superconducting transition of the NbTiN thin film, otherwise indistinguishable in the total signal. The measure was taken at ZFC and 50 Oe.

115

originates from the Nb and only its superconducting transition is distinguishable at $T_c = 9.27\pm0.04\,K$. However, the transition of NbTiN is visible at $T_c = 14.2\pm0.1\,K$ by zooming in (see Figure 9.11 insert). Conversely, a single transition takes place at $T_c = 15.8\pm0.1\,K$ for the multilayers grown on Si. The fact that a single transition is observed for the NbTiN thin film, regardless of the substrate, confirms the existence of a single crystalline phase. The obtained results agree with those obtained for annealed AlN-NbTiN multilayers deposited on Si and Nb substrates in Section 9.5. Lastly, the small reduction in T_c for multilayers grown on Nb substrates compared to those on Si may be a consequence of the greater roughness of the substrate, which may affect the film's superconducting properties.

9.6.2. Curves m(T) for AlN-NbTiN: comparing as-deposited and after annealing

The comparison between as-deposited and thermally treated AlN-NbTiN multilayers on Si substrates reveals a clear distinction in their superconducting properties, as seen through the variation in their magnetic moments with temperature, presented in Figure 9.12. The idea is to cross-check the results obtained via ETO (and presented in Figure 9.5) using VSM.

The analysis shows a significant shift in T_c towards higher temperatures due to both thermal treatments, revealing T_c of $8.0\pm0.4\,K$, $14.5\pm0.3\,K$, and $15.5\pm0.3\,K$ for as-deposited, RTA-, and STA-treated samples, respectively. These findings are in agreement with the ones obtained via ETO. Moreover, the difference in the magnitude of the magnetic moments is remarkable. This is due to microstructural changes within the three samples. The measured magnetic moment is related to the amount of magnetic field expelled from the superconductor. This depends on the amount of pinning centers and the strength of their pinning force [9]. As-deposited films are expected to have a higher number of grain boundaries and interstitial defects, which can act as pinning centres. While thermal treatments were dem-
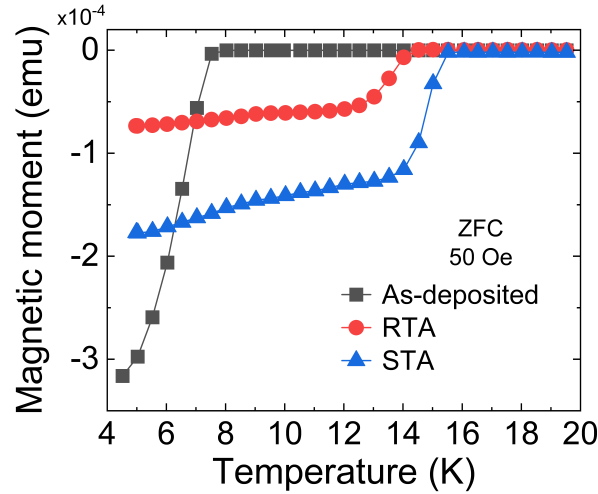
Figure 9.12: Magnetic moment as a function of temperature for a Si-AlN-NbTiN sample in the states: as-deposited and RTA- and STA-treated. The three curves show the superconducting transition. The measure was taken at ZFC and 50 Oe.

onstrated to induce significant surface defects, especially when using Si as substrate (see Section 6.3). Broadly speaking, the larger the dimension of the defect the stronger is the pinning center [9]. This may clarify why annealed films trap more flux. Lastly, the slight slope for the RTA and STA curves, points towards pinning weakening while increasing temperature, so that vortex-vortex repulsion may overcome the pinning force [232]. To gain a more comprehensive understanding of vortex dynamics in SIS multilayers, further investigations, specifically involving Nb substrates, are necessary. It will help clarify the role of substrate-induced defects and their influence on flux pinning and superconducting performance.

9.6.3. Curves m(H)

The evaluation of the magnetic moment as a function of the applied field at a fixed temperature is shown below.

Magnetisation loop: hysteresis

For a perfect type II superconductor, the negative magnetisation increases linearly with the applied magnetic field (Meissner state) till its maximum at H_{c1} when sharply starts decreasing (mixed state) until it becomes zero at H_{c2} (NC state). In addition, when the field is ramped down to zero the magnetisation curve follows its reverse path. However, for non-ideal superconductors, defects act as pinning centers that trap flux vortices, preventing them from moving freely. Additionally, in VSM measurements, applying a uniform and perfectly parallel magnetic field to the sample's surface is challenging, especially for samples that do not have an ellipsoidal shape, which can result in a perpendicular field component.

Lastly, a higher roughness increases flux pinning although because of the small roughness presented by thin films the surface pinning is diminished [9]. As a result, the magnetisation curve shows irreversibility, hysteresis, and a round maximum, as shown in Figure 9.13. The
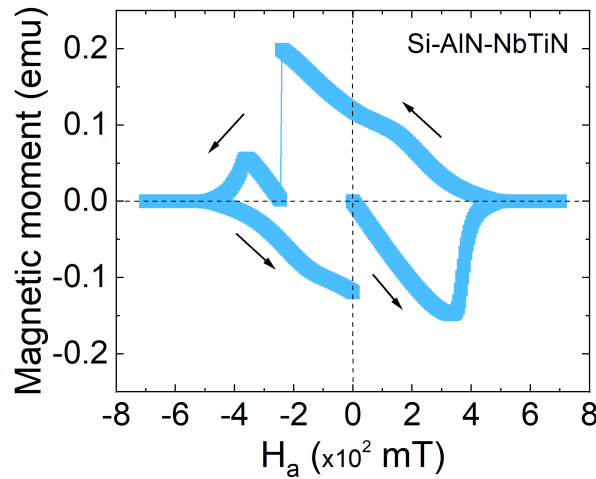
Figure 9.13: Magnetic moment vs applied magnetic field loop measured at 4.2 K.

magnetic moment must be reversed to the magnetic moment be zero again. However, at zero magnetic field, the existence of trapped flux is evident, since the magnetic moment is not zero. To release the trapped flux it is needed to warm up above T_c. Thus, a warming up procedure was applied between each measurement. Lastly, the jump observed in the magnetisation curve in Figure 9.13 is characteristic of strong pinning [9, 233].

Curves m(H) for AlN-NbTiN: comparing as-deposited and annealed (RTA and STA)

This subsection compares the magnetic properties of AlN-NbTiN multilayers on silicon substrates, specifically analysing the as-deposited, RTA-, and STA-treated samples. The focus is on the magnetic moment as a function of the applied magnetic field at a constant temperature, which helps to understand the flux penetration behaviour of these samples.

Virgin magnetisation curves, describing the initial response of the films to an increasing external magnetic field, were measured for each of the three samples at six different temperatures below T_c. Examples of virgin curves at different temperatures are displayed in Figure 9.14. The point at which the magnetic moment deviates from linear H_a dependence sets the field at which the first magnetic flux penetrates the superconductor, named first penetration field (H_{fp}). In an ideal case with a superconductor free of defects and an ellipsoid geometry, H_{fp} would be equal to H_{c1}. However, in practical conditions, the presence of defects within the material, along with contributions from non-uniform and non-parallel magnetic fields, results in flux penetrating the superconductor at lower fields than expected. This early flux penetration is typically influenced by factors such as the quality of the film, grain boundaries, impurities, and the sample's geometry. Therefore, demagnetisation effects caused by the sample geometry were taken into account.
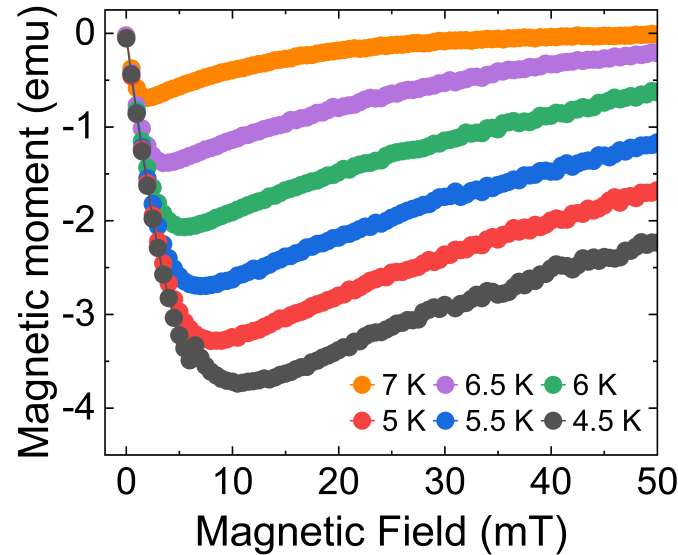
Figure 9.14: Virgin magnetisation curves recorded at different temperatures for the multilayers sample in its as-deposited state.
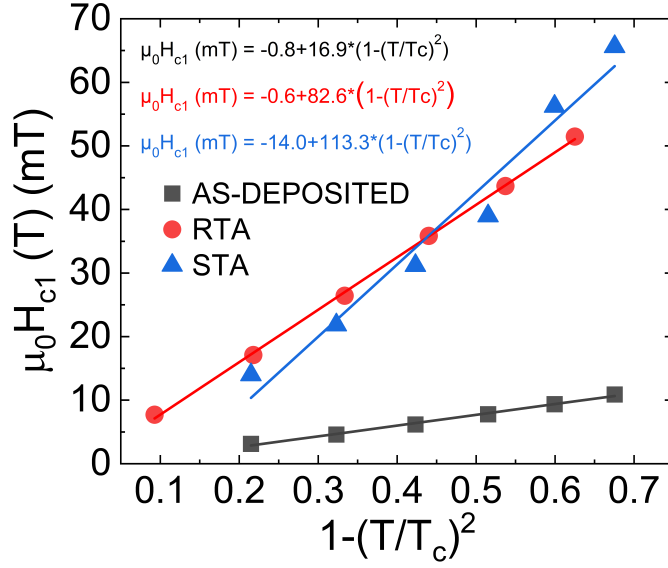
Figure 9.15: Variation of H_{c1} as a function of the reduced temperature $1 - (T/T_c)^2$ for the as-deposited, RTA, and STA. The linear fit functions are given in the same colour-code.

Performing the virgin curves at various temperatures allows to obtain the $H_{c1}(T)$ trend for the thin films as-deposited, after RTA, and after STA. Figure 9.15 depicts $\mu_0 H_{c1}$ as a function of the reduced temperature $1 - (T/T_c)^2$. The plot illustrates how the H_{c1} varies with temperature, approaching zero as the temperature gets closer to T_c. Through a linear fit, one can obtain the field value $\mu_0 H_{c1}$ at the SRF cavity operating temperature (2 K). The obtained values are respectively $15\,\mathrm{mT}$, $81\,\mathrm{mT}$, and $98\,\mathrm{mT}$ for as-deposited, after RTA and STA, respectively. It is demonstrated that the post-deposition annealing significantly elevates $\mu_0 H_{c1}$. In addition, these findings are close to the previously reported $\mu_0 H_{c1} = 120\,\mathrm{mT}$ for $\sim 35\,\mathrm{nm}$ thick NbTiN (Nb:Ti=3:1) films deposited by PEALD [79] and the values for sputtered films (thickness unknown) 83 and $200\,\mathrm{mT}$ for (Nb:Ti=3:1) and (Nb:Ti=4:1), respectively [234]. Furthermore, bulk NbTiN has a $\mu_0 H_{c1} \approx 30\,\mathrm{mT}$ [235]. Thus, it was confirmed the enhancement of $\mu_0 H_{c1}$ because of the film geometry.

9.7. Summary and conclusions

The evaluation of NbTiN films for SIS multilayers in SRF cavities highlighted their superior performance compared to NbN. Films of $Nb_x T_{1-x}N$ with different compositions were investigated, with a fixed thickness of $25\,\mathrm{nm}$. However, even for its optimised compositions (75% of Nb over Ti 25%), as-deposited NbTiN films exhibit a T_c below that one of Nb. Further, NbTiN films of various thicknesses were examined. It is assumed that as-deposited the films are polycrystalline—unless for 6 nm thick which is presumably amorphous. The highest T_c achieved (for NbTiN films in their as-deposited state) was $8\,\mathrm{K}$, far from $T_c^{NbTiN} = 17.8\,\mathrm{K}$. It is assumed that the low T_c obtained is mainly caused by the incorporation of impurities into the films during the PEALD deposition process. XPS analysis, presented in Section 7, supports this hypothesis. In fact, PEALD-NbTiN films with the same Nb to Ti ratio, similar

thickness, and the same chemistry (TDMAT, TBTDEN, and H_2/N_2 plasma 300 W) were reported to exhibit a T_c of 12.5 K [79]. However, Yemane et al. [79] prepared the films at a higher temperature (300 °C versus 250 °C) and under a better vacuum (two orders of magnitude lower [236]). A higher deposition temperature would grow denser films, resulting in a superior crystalline structure with fewer defects and more tightly packed grain boundaries. Thus, higher deposition temperatures are associated with higher T_c and lower residual resistance. Assuming a linear relationship between T_c and deposition temperature (as shown in Figure 9.8), NbTiN grown at 300 °C—not feasible due to reactor limitations—would have a T_c <9.5 K, still below the value reported by Yemane et al. [79]. Moreover, the experience gained from small leaks in the system emphasises the importance of a good vacuum level to prevent impurities in NbTiN films. Changes in the chemical composition affect the electrical and superconducting properties of NbTiN [188, 191, 206, 237, 238]. Moreover, NbTiN films deposited by thermal ALD at much higher temperatures (500 °C) revealed similar T_c values (7-8 K) [68], demonstrating that PEALD produces in general greater quality films. However, since $T_c^{NbTiN} < T_c^{Nb}$ it is excluded the use of these as-deposited NbTiN films for SIS multilayers for SRF cavities.

In pursuit of a better performance, post-deposition annealing was investigated. It was shown in Section 8, that post-deposition heat treatments improve the NbTiN crystallinity and, thus, its superconductivity. Indeed, in the present section, it was demonstrated that high-temperature annealing enhances the performance of NbTiN films, achieving T_c values of 14-16 K. Moreover, annealing resulted in grain growth and outgassing of impurities (see Sections 7 and 8), which would enhance the residual resistance. The obtained results confirmed the improvement in the residual resistance, especially for STA. These results agree with other studies [68, 74, 90, 187, 239, 240], demonstrating that annealing is essential to promote T_c and lower resistivity.

Moreover, it was demonstrated that using Nb as the substrate, as is the case for the goal application, requires an AlN layer acting as a diffusion barrier to achieve NbTiN with a high T_c. It is assumed that annealing dissolves the Nb oxides, Nb_2O_5 and NbO_2. Without an AlN layer, oxygen partially diffuses into the NbTiN thin film, preventing NbTiN from achieving a high T_c [238]. To address this issue, either an AlN barrier or pre-deposition heat treatment to remove surface oxides is needed.

Lastly, the evaluation through VSM of AlN-NbTiN multilayers confirms, in agreement with the XRD analysis in Section 8, the existence of a single NbTiN phase. Moreover, the T_c values obtained for Si and Nb substrates, align with the results obtained via ETO and the contactless inductive station at CERN. Slightly lower T_c values were obtained when using Nb as the substrate, which may be caused by its higher roughness. The evaluation of the H_{c1} was conducted using Si as the substrate because the film magnetic moment response was masked by the thicker Nb substrate. Finally, it was demonstrated that post-deposition thermal treatments notably increase H_{c1}. For a STA-treated multilayer the obtained value of $\mu_0 H_{c1}$ =98 mT is in line with previous literature [79, 234]. Moreover, it demonstrated the thin film enhancement in comparison to its bulk value.

10. Conclusions and future perspectives

The main purpose of this thesis has been to synthesise SIS multilayers via PEALD, and to evaluate their potential for use in SRF cavities in pursuit of improving their performance. Thermal ALD Al_2O_3-based cavities are proven feasible, achieving conformal coatings without degrading cavity performance [69], recognizing ALD as the most suitable technique for this application. For SIS multilayers, the superconducting performance of the thin film is crucial, for which PEALD outperforms thermal ALD. This work aims to pave the way for PEALD-based SRF cavities.

In this work, the synthesis of multilayers consisting of AlN and NbTiN was conducted at $250\,°C$ using the precursors TMA, TDMAT, and TBTDEN, and H_2/N_2 mixture as the plasma gas. Sequential deposition was performed without breaking vacuum on planar substrates. Surface roughness, non-uniformity, and porosity are identified as limiting factors for thin film-based SRF cavities grown via other deposition techniques [33, 159]. Here, the PEALD-deposited multilayers were found to be smooth, with surface roughness in the nanometer range. Additionally, the thin films were observed to be homogeneous and void-free. The XRR and cross-section analyses revealed a sharp and well-defined interface between AlN and NbTiN films. However, it was observed that during deposition, AlN incorporates oxygen from the native substrate oxides. A certain number of AlN PEALD cycles are required to fully consume the oxygen species. Moreover, it was shown that PEALD offers precise control of the Nb to Ti ratio, which can be tailored by adjusting the ratio of the individual PEALD processes inside the NbTiN supercycle. Various NbTiN compositions were evaluated. The Nb to Ti ratio was set to 3:1 to optimise the superconducting transition temperature. The superconducting performance of NbTiN films depends on the crystal structure, although less than for NbN [206], and on the composition. The PEALD-deposited NbTiN films formed the δ-NbTiN phase of interest. However, NbTiN films exhibited a $T_c{<}8\,K$, compromising its suitability for SIS. The low T_c observed in as-deposited NbTiN films is attributed to the incorporation of impurities during deposition, which affects the superconducting properties of NbTiN [188, 191, 206, 238]. Oxygen, carbon, and hydrogen impurities are known to be incorporated into nitride ALD films arising from the precursors, the process gases, plasma source erosion, and the deposition environment [57, 134, 158]. XPS analysis revealed that as-deposited NbTiN contains carbon ($\sim$16 at.%) and oxygen ($\sim$23 at.%).

Post-deposition annealing was proven necessary to obtain NbTiN films suitable for SIS applications in SRF cavities. XPS showed that annealing reduces carbon to the detection limit, while oxygen remains nearly unchanged ($\sim$21 at.%). Moreover, annealing was observed to improve film crystallinity, promoting grain growth—which increases the electron mean free path—and reducing the lattice constant. As a result, the superconducting properties of NbTiN films significantly enhanced, achieving a high $T_c{\sim}16\,K$. The resistivity (at room temperature) was reduced $<70\,\mu\Omega\,cm$. The entry field was significantly improved. A maximum of $98\,mT$ was achieved for NbTiN films, higher than the $30\,mT$ reported for bulk NbTiN [235], supporting the hypothesis that critical fields are enhanced when NbTiN is prepared as a thin film [241]. XRR and cross-section analysis showed, however, that an-

nealing results in faded interface between AlN and NbTiN, with Al diffusion into NbTiN. Additionally, for annealed NbTiN films grown on Nb, it was observed that an AlN layer acting as diffusion barrier is necessary to achieve high T_c. Various annealing procedures were evaluated. Higher annealing temperatures (900-1000 °C), slower thermal ramps, and lower base pressure were found to result in greater NbTiN film performance.

Moreover, PEALD-SIS multilayers grown on Nb underwent the standard cavity cleaning procedure, HPR. SEM and EDX analyses confirmed the presence of AlN and NbTiN after seven HPRs (see Appendix B.3), demonstrating the PEALD-SIS multilayer can withstand the cavity regular test preparation.

However, although PEALD-SIS multilayers showed promising results, the occurrence of surface defects, in addition to annealing-induced Al diffusion, could compromise their use for SRF cavities. Blister of arbitrary size and distribution were found. Their formation remains inconsistent, which made challenging to determine the conditions under which they form. Plasma-induced effects—ion bombardment causing compressive stress [146–149] or ions and radiation breaking hydrogen bonds resulting in gas accumulation [148–151, 242]—are thought to be the cause of blistering. With annealing, blisters resulted in peel-off, most likely due to accumulated stress, which would be particularly detrimental for SRF applications. Thus, preventing blister formation is crucial. It could be mitigated by reducing ions energy through increasing plasma gas pressure [147], reducing ion flux density using lower plasma power [95, 96], or tuning ions energy via substrate biasing [46]. Additionally, annealing induced other surface defects, when using Si as the substrate, caused by thermal expansion mismatches across the multilayers and the substrate.

This work was carried out with the PEALD GEMStar system using planar substrates. Further investigations could be conducted in the new PEALD system under commissioning, which aims to achieve SIS multilayers on 1.3 GHz SRF cavities. To achieve NbTiN films with a high T_c without requiring post-deposition annealing, established strategies could be applied. First, deposition temperature could be increased. It is known that higher deposition temperatures result in denser and more crystalline films, which would benefit T_c and normal conductivity. PEALD-NbTiN films deposited at 300 °C exhibit T_c =12.8 K [79]. In addition, based on the experience acquired, reducing the amount of impurities incorporated into the films during deposition should be addressed. Suggested strategies include improving the vacuum conditions [57, 157], replacing the plasma quartz tube with an alumina tube [156], increasing H_2 in the plasma gas mixture [131], ensuring homogeneous heating of the reactor walls, and using substrate biasing [47, 158]. Moreover, perfluorelastomer o-rings should be avoided to prevent contamination of the films with fluorine (see Appendix B.4). *In-situ* pre-deposition annealing should be investigated to dissolve Nb oxides, prior AlN deposition.

Additionally, to determine the optimal thicknesses of AlN and NbTiN thin films, third-harmonic measurements with local magnetometer are advised to evaluate H_{c1} on batches of samples with varying thicknesses for both layers.

Lastly, a comprehensive evaluation of how PEALD SIS multilayers perform under SRF cavity conditions is essential to determine their feasibility. Thermal dissipation is crucial to prevent the cavity to quench. The thermal conductance of SIS multilayers requires investigation, as the presence of the insulating layer and multiple interfaces may affect the heat dissipation. Experiments are ongoing at Universität Hamburg [243], with results to be

published soon. In addition, field emission is a concern for SRF, as it can result in power losses and limit the accelerating gradient. Preliminary secondary electron yield (SEY) measurements are ongoing at Universität Hamburg, revealing lower SEY values for SIS compared to bulk Nb, suggesting a reduced risk of field emission. The findings are shortly to be published. Finally, RF characterisation of PEALD-SIS multilayers is still required. PEALD of SIS multilayers on a $1.3\,\mathrm{GHz}$ SRF cavity or on a quadrupole resonator (QPR) samples would allow for RF tests. Thin film coated cavities are expected to reduce the R_{BCS} (even minimise it when the mean free path and the coherence length meet the condition $l \sim \xi_0/2$). Conversely, the R_{res} required assessment. PEALD thin films feature small grains and thereby, high density of grains boundaries, which are presumed to trap considerable flux. Additionally, since superconductivity experience weakening at the grain boundaries, it can be assumed that early field penetration occurs—a vortex typically interacts with either small clusters of pinning defects spaced around the coherence length or with a dense distribution of weak pinning centers [9]. Hence, any defect with depleted superconductivity promotes trap flux and early vortex entry. However, when the crystalline disorder around the grain boundary extends in the same order of magnitude as the coherence length, as it is the case for superconducting thin films, it serves as the most efficient trap mechanism. The R_{flux} results from vortex oscillation. Its minimum is determined by a compromise between the density of pinning centres and their pinning strength. Flux expulsion studies for PEALD SIS multilayers are in progress at CERN, with preliminary results already presented [244] and further results expected soon.

List of abbreviation

AFM Atomic force microscope.

ALD Atomic layer deposition.

ALE Atomic layer etching.

ARXPS Angle-resolved X-ray photoelectron spectroscopy.

BCP Buffered chemical polishing.

BE Binding energy.

CVD Chemical vapour deposition.

EDX Energy dispersive X-ray spectroscopy.

EP Electropolishing.

FFKM Perfluoroelastomer.

FIB Focus ion beam.

FWHM Full width half maximum.

GIXRD Grazing incidence X-Ray diffraction.

GPC Growth per cycle.

HIPIMS High power impulse magnetron sputtering.

HPR High pressure rinsing.

NC Normal conducting state.

PEALD Plasma-enhanced atomic layer deposition.

PPMS Physical property measurement system.

PVD Physical vapour deposition.

RMS Root mean square.

RRR Residual resistance ratio.

RTA Rapid thermal annealing.

SC Superconducting state.

SE Spectroscopic ellipsometry.

SEM Scanning electron microscope.

SIS Superconducting - insulating - superconducting.

SNSPD Superconducting nanowire single photon detectors.

SRF Superconducting radio frequency.

STA Slow thermal annealing.

STEM Scanning transmission electron microscope.

TDMAT Tetrakis(dimethylamido)titanium(IV).

TDTDEN Tris(diethylamido)(tert-butylimido)niobium(V).

TEM Transmission electron microscope.

TMA Trimethylaluminum.

UHV Ultra high vacuum.

VSM Vibrating sample magnetometer.

XPS X-ray photoelectron spectroscopy.

XRD X-ray photoelectron diffraction.

XRR X-ray reflectivity.

ZFC Zero field cooling.

References

[1] J. Bardeen, L. N. Cooper, and J. R. Schrieffer, "Theory of superconductivity", Physical Review **108**, 1175–1204 (1957).

[2] K. H. Bennemann and J. B. Ketterson, "Superconductivity: conventional and unconventional superconductors", in , Vol. 1, edited by K. H. Bennemann and J. B. Ketterson (Springer Berlin Heidelberg, 2008).

[3] S. Vonsovsky, Y. Izyumov, and E. Kurmaev, "Superconductivity of transition metals.", in Their alloys and compounds, Springer Series in Solid-State Sciences 27 (Springer-Verlag Berlin Heidelberg, 1982).

[4] H. Padamsee, J. Knobloch, and T. Hays, Rf superconductivity for accelerators, Wiley Series in Beam Physics and Accelerator Technology (Wiley, 2008).

[5] A. Gurevich, "Theory of rf superconductivity for resonant cavities", Superconductor Science and Technology **30**, 034004 (2017).

[6] C Antoine, Materials and surface aspects in the development of srf niobium cavities, 2012.

[7] Y. Slimani and E. Hannachi, "Superconducting materials: fundamentals, synthesis and applications", Superconducting Materials: Fundamentals, Synthesis and Applications, 1–399 (2022).

[8] DESY, Photon science web page, `https://photon-science.desy.de/e58/e186104/e186305/e186344/e186398/PIF_eng.html?preview=preview`.

[9] C. Z. Antoine, "Influence of crystalline structure on rf dissipation in superconducting niobium", Physical Review Accelerators and Beams **22**, 034801 (2019).

[10] J. C. Wolff, J Eschke, A Goessel, K Kasprzak, D Reschke, L Steder, L Trelle, M Wiencek, and W. C. A. Hillert, "Impact of medium temperature heat treatments on the magnetic flux expulsion behavior of srf cavities *", in Proceedings of srf2023 (2023), pp. 731–735.

[11] N Walker, D Reschke, J Schaffran, L Steder, and M Wenskat, "Performance analysis of the european xfel srf cavities, from vertical test to operation in modules", in Proceedings of linac2016, east lansing, mi, usa (2017).

[12] C. Adolphsen, "The international linear collider technical design report - volume 3.i: accelerator in the technical design phase", Fermi National Accelerator Laboratory (FNAL), `10.2172/1347941` (2013).

[13] D. Reschke, V. Gubarev, J. Schaffran, L. Steder, N. Walker, M. Wenskat, and L. Monaco, "Performance in the vertical test of the 832 nine-cell 1.3 ghz cavities for the european x-ray free electron laser performance in the vertical test d. reschke et al.", Physical Review Accelerators and Beams **20**, 042004 (2017).

[14]A. Grassellino, A. Romanenko, O. Melnychuk, Y. Trenikhina, A. Crawford, A. Rowe, M. Wong, D. Sergatskov, T. Khabiboulline, and F. Barkov, "Nitrogen and argon doping of niobium for superconducting radio frequency cavities: a pathway to highly efficient accelerating structures", Superconductor Science and Technology **26**, 10.1088/0953-2048/26/10/102001 (2013).

[15]A. Grassellino, A. Romanenko, Y. Trenikhina, M. Checchin, M. Martinello, O. S. Melnychuk, S. Chandrasekaran, D. A. Sergatskov, S. Posen, A. C. Crawford, S. Aderhold, and D. Bice, "Unprecedented quality factors at accelerating gradients up to 45 mvm1 in niobium superconducting resonators via low temperature nitrogen infusion", Superconductor Science and Technology **30**, 094004 (2017).

[16]S. Posen, A. Romanenko, A. Grassellino, O. S. Melnychuk, and D. A. Sergatskov, "Ultralow surface resistance via vacuum heat treatment of superconducting radio-frequency cavities", Physical Review Applied **13**, 014024 (2020).

[17]A. Gurevich, "Enhancement of rf breakdown field of superconductors by multilayer coating", Applied Physics Letters **88**, 12511 (2006).

[18]H Weise, "The tesla xfel project", in Proceedings of epac of 2004 (2004).

[19]B. Aune, R. Bandelmann, D. Bloess, B. Bonin, A. Bosotti, M. Champion, C. Crawford, G. Deppe, B. Dwersteg, D. A. Edwards, H. T. Edwards, M. Ferrario, M. Fouaidy, P. D. Gall, A. Gamp, A. Gössel, J. Graber, D. Hubert, M. Hüning, M. Juillard, T. Junquera, H. Kaiser, G. Kreps, M. Kuchnir, R. Lange, M. Leenen, M. Liepe, L. Lilje, A. Matheisen, W. D. Möller, A. Mosnier, H. Padamsee, C. Pagani, M. Pekeler, H. B. Peters, O. Peters, D. Proch, K. Rehlich, D. Reschke, H. Safa, T. Schilcher, P. Schmüser, J. Sekutowicz, S. Simrock, W. Singer, M. Tigner, D. Trines, K. Twarowski, G. Weichert, J. Weisend, J. Wojtkiewicz, S. Wolff, and K. Zapfe, "Superconducting tesla cavities", Physical Review Special Topics - Accelerators and Beams **3**, 092001 (2000).

[20]G. T. J. Ciovati, "Basic principles of rf superconductivity", presented at the Tutorials of 19th International Conference on RF Superconductivity (SRF201) (2019).

[21]C. Bate, "Study of nitrogen-enriched niobium and its influence on the performance on superconducting rf cavities", PhD thesis (Universität Hamburg, 2022).

[22]C. Nico, T. Monteiro, and M. P. Graça, "Niobium oxides and niobates physical properties: review and prospects", Progress in Materials Science **80**, 1–37 (2016).

[23]G. D. L. Semione, "Niobium near surface composition relevant for superconducting radio-frequency cavities", PhD thesis (Universität Hamburg, 2020).

[24]L. V. Cid, A Bianchi, G Bellini, L. A. Ferreira, S Leith, C. P. Carlos, G Rosaz, W. V. Delsolaro, and G. Switzerland, "Results of the rd rf testing campaign of 1.3 ghz nb/cu cavities", in 21th int. conf. rf supercond. srf23 (2023).

[25]A.-M. Valente-Feliciano, "Materials for superconducting accelerators: beyond bulk nb", in 21st international conference on rf superconductivity - tutorials (2023).

[26]A.-M. Valente-Feliciano, "Superconducting RF materials other than bulk niobium: a review", Superconductor Science and Technology **29**, Publisher: IOP Publishing, 113002 (2016).

[27] M. Wenskat, G. K. Deyu, I. G. Díaz-Palacio, R. H. Blick, R. Zierold, and W. Hillert, "Successful al2o3 coating of superconducting niobium cavities with thermal ald", Superconductor Science and Technology **36**, 015010 (2022).

[28] A. A. Abrikosov, "On the lower critical field of thin layers of superconductors of the second group", J. Exptl. Theoret. Phys. (U.S.S.R.) **19**, 1464–1469 (1964).

[29] T. Kubo, Y. Iwashita, and T. Saeki, "Radio-frequency electromagnetic field and vortex penetration in multilayered superconductors", Applied Physics Letters **104**, 54 (2014).

[30] T. Kubo, "Multilayer coating for higher accelerating fields in superconducting radio-frequency cavities: a review of theoretical aspects", Superconductor Science and Technology **30**, 10.1088/1361-6668/30/2/023001 (2017).

[31] T. Kubo, "Optimum multilayer coating of superconducting particle accelerator cavities and effects of thickness dependent material properties of thin films", Japanese Journal of Applied Physics **58**, 088001 (2019).

[32] R. D. Leo, A. Nigro, G. Nobile, and R. Vaglio, "Niboium-titanium nitride thin films for superconducting rf accelerator cavities", Journal of Low Temperature Physics **78**, 41–50 (1990).

[33] A.-M Valente-Feliciano1, C Antoine, S Anlage, G Ciovati, J Delayen, F Gerigk, A Gurevich, T Junginger, S Keckert, G Keppel, J Knobloch, T Kubo, O Kugeler, D Manos, C Pira, T Proslier, U Pudasaini, C. E. Reece, R. A. Rimmer, G. J. Rosaz, T Saeki, R Vaglio, R Valizadeh, H Vennekate, W. V. Delsolaro, M Vogel, P. B. Welander, M Wenskat, and T. Jefferson, "Next-generation superconducting rf technology based on advanced thin film
technologies and innovative materials for accelerator enhanced performance and energy reach", (2022).

[34] K. R. Babu and G. Y. Guo, "Structure- and composition-tunable superconductivity, band topology, and elastic response of hard binary niobium nitrides nb2 n, nb4 n3 and nb4 n5", Physical Review B **108**, 064505 (2023).

[35] T. Shiino, S. Shiba, N. Sakai, T. Yamakura, L. Jiang, Y. Uzawa, H. Maezawa, and S. Yamamoto, "Improvement of the critical temperature of superconducting nbtin and nbn thin films using the aln buffer layer", Superconductor Science and Technology **23**, 10.1088/0953-2048/23/4/045004 (2010).

[36] X. W. Chen, C. H. Jia, Y. H. Chen, H. T. Wang, and W. F. Zhang, "Epitaxial growth and optical properties of al- and n-polar aln films by laser molecular beam epitaxy", Journal of Physics D: Applied Physics **47**, 125303 (2014).

[37] T. Suntola and J. Antson, U.S. Patent No. 4,058,430 (1977).

[38] V. B. Aleskovskii, "Some aspects of molecular layering reactions (in Russian)", in Abstract of Scientific and Technical Conference, Goskhi-mizdat, Leningrad (1965).

[39] H. C. Knoops, S. E. Potts, A. A. Bol, and W. M. Kessels, "Atomic layer deposition", in , Vol. 3 (North-Holland, Jan. 2015), pp. 1101–1134.

[40] K. Arts, "Conformality and the role of ions during plasma-assisted atomic layer deposition", (2021).

[41] L. Mai and A. Devi, "Investigation of amino-alkyl coordinated complexes as new precursor class for atomic layer deposition of aluminum, tin and zinc oxide thin films and their application", `10.13154/294-7658` (2020).

[42] H. C. Guo, E. Ye, Z. Li, M.-Y. Han, and X. J. Loh, "Recent progress of atomic layer deposition on polymeric materials", Materials Science and Engineering: C **70**, Recent Advances in Biomedical Materials, 1182–1191 (2017).

[43] R. L. Puurunen, "Surface chemistry of atomic layer deposition: a case study for the trimethylaluminum/water process", Journal of Applied Physics **97**, 121301 (2005).

[44] E. Kessels, Plasma-assisted atomic layer deposition: basics, equipment, applications, AVS Webinar, 2023.

[45] D. R. Boris, V. D. Wheeler, N. Nepal, S. B. Qadri, S. G. Walton, and C. C. R. Eddy, "The role of plasma in plasma-enhanced atomic layer deposition of crystalline films", Journal of Vacuum Science Technology A: Vacuum, Surfaces, and Films **38**, 40801 (2020).

[46] H. B. Profijt, M. C. M. van de Sanden, and W. M. M. Kessels, "Substrate-biasing during plasma-assisted atomic layer deposition to tailor metal-oxide thin film growth", Journal of Vacuum Science Technology A: Vacuum, Surfaces, and Films **31**, `10.1116/1.4756906/246140` (2013).

[47] T. Faraz, H. C. Knoops, M. A. Verheijen, C. A. V. Helvoirt, S. Karwal, A. Sharma, V. Beladiya, A. Szeghalmi, D. M. Hausmann, J. Henri, M. Creatore, and W. M. Kessels, "Tuning material properties of oxides and nitrides by substrate biasing during plasma-enhanced atomic layer deposition on planar and 3d substrate topographies", ACS Applied Materials and Interfaces **10**, 13158–13180 (2018).

[48] K. Arts, J. H. Deijkers, T. Faraz, R. L. Puurunen, W. M. Kessels, and H. C. Knoops, "Evidence for low-energy ions influencing plasma-assisted atomic layer deposition of sio2: impact on the growth per cycle and wet etch rate", Applied Physics Letters **117**, 31602 (2020).

[49] T. Faraz, K. Arts, S. Karwal, H. C. M. Knoops, and W. M. M. Kessels, "Energetic ions during plasma-enhanced atomic layer deposition and their role in tailoring material properties", Plasma Sources Science and Technology **28**, 024002 (2019).

[50] H. B. Profijt, P. Kudlacek, M. C. M. van de Sanden, and W. M. M. Kessels, "Ion and photon surface interaction during remote plasma ald of metal oxides", Journal of The Electrochemical Society **158**, G88 (2011).

[51] H. B. Profijt, S. E. Potts, M. C. M. van de Sanden, and W. M. M. Kessels, "Plasma-assisted atomic layer deposition: basics, opportunities, and challenges", Journal of Vacuum Science Technology A: Vacuum, Surfaces, and Films **29**, `10.1116/1.3609974/244582` (2011).

[52] G. Dingemans, C. A. A. van Helvoirt, D. Pierreux, W. Keuning, and W. M. M. Kessels, "Plasma-assisted ald for the conformal deposition of sio2: process, material and electronic properties", Journal of The Electrochemical Society **159**, H277 (2012).

[53] K. Arts, M. Utriainen, R. L. Puurunen, W. M. Kessels, and H. C. Knoops, "Film conformality and extracted recombination probabilities of o atoms during plasma-assisted atomic layer deposition of sio2, tio2, al2o3, and hfo2", Journal of Physical Chemistry C **123**, 27030–27035 (2019).

[54] V. Miikkulainen, M. Leskelä, M. Ritala, and R. L. Puurunen, "Crystallinity of inorganic films grown by atomic layer deposition: overview and general trends", Journal of Applied Physics **113**, 21301 (2013).

[55] M. D. Keijser and C. V. Opdorp, "Atomic layer epitaxy of gallium arsenide with the use of atomic hydrogen", Applied Physics Letters **58**, 1187–1189 (1991).

[56] A. Sherman, U.S. Patent No. 5,916,365 (Filed in 1996).

[57] H. C. M. Knoops, T. Faraz, K. Arts, and W. M. M. E. Kessels, "Status and prospects of plasma-assisted atomic layer deposition", Journal of Vacuum Science Technology A **37**, 030902 (2019).

[58] M. B. E. Griffiths, P. J. Pallister, D. J. Mandia, and S. T. Barry, "Atomic layer deposition of gold metal", Chemistry of Materials **28**, 44–46 (2016).

[59] S. M. George, "Atomic layer deposition: an overview", Chemical Reviews **110**, 111–131 (2010).

[60] L. Grassellino, M. Checchin, S. Posen, G. Eremeev, A. Romanenko, and A. Grassellino, "Commissioning of new cvd/ald furnace at fermilab", in Proceedings of the 21st international conference on rf superconductivity (Aug. 2023).

[61] T. Proslier, J Norem, J Elam, and M Pellin, "Results from point contact tunneling spectroscopy and atomic layer deposition*", in Proceedings of srf2009 (2009).

[62] T. Proslier, J. Zasadzinski, J. Moore, M. Pellin, J. Elam, L. Cooley, C. Antoine, J. Norem, and K. E. Gray, "Improvement and protection of niobium surface superconductivity by atomic layer deposition and heat treatment", Applied Physics Letters **93**, `10.1063/1.2995996/336152` (2008).

[63] T. Proslier, Y. Ha, J. Zasadzinski, G. Ciovati, P. Kneisel, C. Reece, R. Rimmer, A. Gurevich, L. Cooley, G. Wu, M. Pellin, J. Norem, J. Elam, and C. Antoine, "Atomic layer deposition for srf cavities", in Proceedings of pac09 (2009).

[64] G Eremeev, A. T. Wu, A.-M Valente-Feliciano, and D Gu, "Exploring the effect of al 2 o 3 ald coating on a high gradient ilc single-cell cavity *", in Proceedings of ipac2012 (2012).

[65] S Kato and H Hayano, "Plasma-enhanced ald system for srf cavity; plasma-enhanced ald system for srf cavity", in 18th international conference on rf superconductivity: srf2017 (2017).

[66] Y. Kalboussi, "Material engineering of ALD- deposited multilayer to improve the superconducting performances of RF cavities under intense RF fields", in IPAC conference (2021).

[67] Y. Kalboussi, "ALD-deposited multilayer to improve the superconducting performances of RF cavities", 10th International workshop on thin films and new ideas for pushing the timits of RF superconductivity, 2022.

[68] Y. Kalboussi, "Nano hetero-structures for improving performances of superconductors under high fields", PhD thesis (Université Paris-Saclay, 2023).

[69] M. Wenskat, G. K. Deyu, I. G. Díaz-Palacio, R. H. Blick, R. Zierold, and W. Hillert, "Successful al2o3 coating of superconducting niobium cavities with thermal ALD", Superconductor Science and Technology **36**, Publisher: IOP Publishing, 015010 (2022).

[70] T. Proslier, "Atomic layer deposition of thin superconducting films and multilayers: coupons and cavity tests", 16th International Conference on RF Superconductivity, 2013.

[71] T. Proslier, J. Klug, N. C. Becker, J. W. Elam, and M. Pellin, "(invited) atomic layer deposition of superconductors", ECS Transactions **41**, Publisher: IOP Publishing, 237 (2011).

[72] P. Pizzol, "Superconductive thin films for rf applications", Doctoral dissertation, PhD thesis (University of Liverpool, 2018).

[73] M. Ritala, P. Kalsi, D. Riihelä, K. Kukli, M. Leskelä, and J. Jokinen, "Controlled growth of TaN, ta3n5, and TaOxNy thin films by atomic layer deposition", Chemistry of Materials **11**, Publisher: American Chemical Society, 1712–1718 (1999).

[74] G. I. Oya and Y. Onodera, "Transition temperatures and crystal structures of single-crystal and polycrystalline nbnx films", Journal of Applied Physics **45**, 1389–1397 (1974).

[75] U. Patel, S. Avci, Z. L. Xiao, J. Hua, S. H. Yu, Y. Ito, R. Divan, L. E. Ocola, C. Zheng, H. Claus, J. Hiller, U. Welp, D. J. Miller, and W. K. Kwok, "Synthesis and superconducting properties of niobium nitride nanowires and nanoribbons", Applied Physics Letters **91**, 162508 (2007).

[76] P. Duwez and F. Odell, "Phase relationships in the binary systems of nitrides and carbides of zirconium, columbium, titanium, and vanadium", Journal of The Electrochemical Society **97**, 299 (1950).

[77] V. Buscaglia, C. Bottino, R. Musenich, P. Fabbricatore, G. Gemme, R. Parodi, B. Zhang, and P. Parodi, "Nitridation of niobium-46 wt.1300 °c", Journal of Alloys and Compounds **226**, 232–241 (1995).

[78] L. Assaud, K. Pitzschel, M. Hanbücken, and L. Santinacci, "Highly-conformal tin thin films grown by thermal and plasma-enhanced atomic layer deposition", ECS Journal of Solid State Science and Technology **3**, P253–P258 (2014).

[79] Y. T. Yemane, M. J. Sowa, J. Zhang, L. Ju, E. W. Deguns, N. C. Strandwitz, F. B. Prinz, and J. Provine, "Superconducting niobium titanium nitride thin films deposited by plasma-enhanced atomic layer deposition", Superconductor Science and Technology **30**, 095010 (2017).

[80] I. Krylov, E. Zoubenko, K. Weinfeld, Y. Kauffmann, X. Xu, D. Ritter, and M. Eizenberg, "Obtaining low resistivity (100 cm) tin films by plasma enhanced atomic layer deposition using a metalorganic precursor", Journal of Vacuum Science Technology A: Vacuum, Surfaces, and Films **36**, 51505 (2018).

[81] C. Badie, H. Tissot, B. Sciacca, M. K. Barr, J. Bachmann, C. Vallée, G. Gautier, T. Defforge, V. Astie, J.-M. Decams, M. Bechelany, and L. Santinacci, "Conductive tin thin films grown by plasma-enhanced atomic layer deposition: effects of n-sources and thermal treatments", Journal of Vacuum Science Technology A **41**, 32401 (2023).

[82]N. Samal, H. Du, R. Luberoff, K. Chetry, R. Bubber, A. Hayes, and A. Devasahayam, "Low-temperature (200 ° c) plasma enhanced atomic layer deposition of dense titanium nitride thin films", Journal of Vacuum Science Technology A: Vacuum, Surfaces, and Films **31**, 1–137 (2013).

[83]J. Elam, M Schuisky, J. Ferguson, and S. George, "Surface chemistry and film growth during tin atomic layer deposition using tdmat and nh3", Thin Solid Films **436**, 145–156 (2003).

[84]E. Deguns, M. J. Sowa, M. J. Dalberth, R. Bhatia, R. Kanjolia, D. Moser, G. M. Sundaram, and J. S. Becker, "Plasma-enabled ald of niobium nitride using an organometallic nb precursor", ECS Transactions **33**, 177–182 (2010).

[85]M. Ziegler, L. Fritzsch, J. Day, S. Linzen, S. Anders, J. Toussaint, and H. G. Meyer, "Superconducting niobium nitride thin films deposited by metal organic plasma-enhanced atomic layer deposition", Superconductor Science and Technology **26**, 025008 (2012).

[86]M. Ziegler, S. Linzen, S. Goerke, U. Bruckner, J. Plentz, J. Dellith, A. Himmerlich, M. Himmerlich, U. Hubner, S. Krischok, and H. G. Meyer, "Effects of plasma parameter on morphological and electrical properties of superconducting nb-n deposited by mo-peald", IEEE Transactions on Applied Superconductivity **27**, `10.1109/TASC.2017.2744326` (2017).

[87]M. J. Sowa, Y. Yemane, J. Zhang, J. C. Palmstrom, L. Ju, N. C. Strandwitz, F. B. Prinz, and J. Provine, "Plasma-enhanced atomic layer deposition of superconducting niobium nitride", Journal of Vacuum Science Technology A: Vacuum, Surfaces, and Films **35**, 1–143 (2017).

[88]M. Ukibe and G. Fujii, "Superconducting characteristics of nbn films deposited by atomic layer deposition", IEEE Transactions on Applied Superconductivity **27**, `10.1109/TASC.2017.2655719` (2017).

[89]P Pizzol, J. W. Roberts, J Wrench, O. B. Malyshev, R Valizadeh, and P. R. Chalker, "Atomic layer deposition of niobium nitride from different precursors", (2017).

[90]L. Tian, I. Bottala-Gambetta, V. Marchetto, M. Jacquemin, A. Crisci, R. Reboud, A. Mantoux, G. Berthomé, F. Mercier, A. Sulpice, L. Rapenne, F. Weiss, C. Jiménez, and E. Blanquet, "Improved critical temperature of superconducting plasma-enhanced atomic layer deposition of niobium nitride thin films by thermal annealing", Thin Solid Films **709**, 138232 (2020).

[91]C. Sheagren, P. Barry, E. Shirokoff, and Q. Y. Tang, "Atomic layer deposition niobium nitride films for high-q resonators", Journal of Low Temperature Physics **199**, 875–882 (2020).

[92]Z. X. Chen, X. Li, W. M. Li, and G. Q. Lo, "Plasma-enhanced atomic layer deposition (peald) of tin using the organic precursor tetrakis(ethylmethylamido)titanium (temat)", MATEC Web of Conferences **39**, 01010 (2016).

[93]J Hinz, A. J. Bauer, and L Frey, "Analysis of nbn thin film deposition by plasma-enhanced ald for gate electrode application", Semiconductor Science and Technology **25**, 075009 (2010).

[94] E. Langereis, S. B. Heil, M. C. V. D. Sanden, and W. M. Kessels, "In situ spectroscopic ellipsometry study on the growth of ultrathin tin films by plasma-assisted atomic layer deposition", Journal of Applied Physics **100**, 10.1063/1.2214438 (2006).

[95] S. B. S. Heil, E. Langereis, F. Roozeboom, M. C. M. van de Sanden, and W. M. M. Kessels, "Low-temperature deposition of tin by plasma-assisted atomic layer deposition", Journal of The Electrochemical Society **153**, G956 (2006).

[96] S. Goerke, M. Ziegler, A. Ihring, J. Dellith, A. Undisz, M. Diegel, S. Anders, U. Huebner, M. Rettenmayr, and H.-G. Meyer, "Atomic layer deposition of AlN for thin membranes using trimethylaluminum and h2/n2 plasma", Applied Surface Science **338**, 35–41 (2015).

[97] D. E. S. DESY, "Series surface and acceptance test preparation of superconducting cavities for the european xfel", XFel/A-D, Revision B (2009).

[98] B Bonin and R. W. Roth, "Q degradation of niobium cavities due to hydrogen contamination", Particle Accelerators **40**, 59–83 (1992).

[99] G. Ciovati, G. Myneni, F. Stevie, P. Maheshwari, and D. Griffis, "High field q slope and the baking effect: review of recent experimental results and new data on nb heat treatments", Physical Review Special Topics - Accelerators and Beams **13**, 022002 (2010).

[100] K. Saito, H. Inoue, E. Kako, T. Fujino, S. Noguchi, M. Ono, and T. Shishido, "Superiority of electropolishing over chemical polishing on high gradients", Particle Accelerators **60**, 193–217 (1998).

[101] L. F. Ehmcke, "Optimierung von tin-dünnfilmen abgeschieden mittels pe-ald", Bachelor's Thesis (Universität Hamburg, Universität Hamburg, 2019).

[102] I. González Díaz-Palacio, M. Wenskat, G. K. Deyu, W. Hillert, R. H. Blick, and R. Zierold, "Thermal annealing of superconducting niobium titanium nitride thin films deposited by plasma-enhanced atomic layer deposition", Journal of Applied Physics **134**, 035301 (2023).

[103] I. González Díaz-Palacio, M. Wenskat, G. K. Deyu, W. Hillert, R. H. Blick, and R. Zierold, "Erratum: "Thermal annealing of superconducting niobium titanium nitride thin films deposited by plasma-enhanced atomic layer deposition" [J. Appl. Phys. 134(3), 035301 (2023)]", Journal of Applied Physics **134**, 159902 (2023).

[104] M. Wenskat, C. Bate, R. Ghanbari, W. Hillert, and C. Martens, "A New Ultra-High Vacuum Furnace for SRF R&D", in Proc. 21th int. conf. rf supercond. (srf23) (2023), pp. 855–858.

[105] N. Ida and N. Meyendorf, eds., Handbook of advanced non-destructive evaluation (Springer Nature Switzerland AG, 2018).

[106] H. Kiessig, "Untersuchungen zur totalreflexion von röntgenstrahlen", Annalen der Physik **402**, 715–768 (1931).

[107] A. Stierle, T. F. Keller, H. Noei, V. Vonk, and R. Roehlsberger, "Desy nanolab", Journal of large-scale research facilities JLSRF **2**, A76–A76 (2016).

[108] H. Fujiwara, Spectroscopic ellipsometry: principles and applications (John Wiley and Sons, Oct. 2007), pp. 1–369.

[109] J. Humlíček, A. Nebojsa, J. Hora, M. Stráský, J. Spousta, and T. Šikola, "Ellipsometry and transport studies of thin-film metal nitrides", Thin Solid Films **332**, 25–29 (1998).

[110] R. Bower, D. A. Loch, E. Ware, A. Berenov, B. Zou, P. E. Hovsepian, A. P. Ehiasarian, and P. K. Petrov, "Complementary metal-oxide-semiconductor compatible deposition of nanoscale transition-metal nitride thin films for plasmonic applications", ACS Applied Materials and Interfaces **12**, 45444–45452 (2020).

[111] G. Friedbacher and H. Bubert, "Surface and thin film analysis: a compendium of principles, instrumentation, and applications, second edition", Surface and Thin Film Analysis: A Compendium of Principles, Instrumentation, and Applications, Second Edition, Chapter 18 EDXS, `10.1002/9783527636921` (2011).

[112] V. D. Hodoroaba, "Energy-dispersive x-ray spectroscopy (eds)", Characterization of Nanoparticles: Measurement Processes for Nanoparticles, 397–417 (2020).

[113] G. Jouve, C. Séverac, and S. Cantacuzène, "Xps study of nbn and (nbti)n superconducting coatings", Thin Solid Films **287**, 146–153 (1996).

[114] K. S. Robinson and P. M. Sherwood, "X-ray photoelectron spectroscopic studies of the surface of sputter ion plated films", Surface and Interface Analysis **6**, 261–266 (1984).

[115] G. Greczynski, D. Primetzhofer, J. Lu, and L. Hultman, "Core-level spectra and binding energies of transition metal nitrides by non-destructive x-ray photoelectron spectroscopy through capping layers", Applied Surface Science **396**, 347–358 (2017).

[116] A. Darlinski and J. Halbritter, "Angle-resolved xps studies of oxides at nbn, nbc, and nb surfaces", Surface and Interface Analysis **10**, 223–237 (1987).

[117] T. F. Scientific, Thermo fisher scientific: xps of atomic elements, `https : / / www . thermofisher . com/de/de/home/materials-science/learning-center/periodic-table.html`.

[118] Quantum Design Europe, Physical property measurements in a cryogen-free system, (2024)

[119] G. Balakrishnan, C. K. Subramaniam, D. M. K. Paul, S. Piñol, and R. Vijayaraghavan, "An upper limit on the lower critical field in single crystal nd1.85ce0.15cuo4y", Physica C: Superconductivity **177**, 310–314 (1991).

[120] C. S. Yadav and P. L. Paulose, "Upper critical field, lower critical field and critical current density of fete0.60se0.40 single crystals", New Journal of Physics **11**, 103046 (2009).

[121] E. H. Brandt, "Irreversible magnetization of pin-free type-ii superconductors", Physical Review B **60**, 11939 (1999).

[122] D. Fonnesu, J. Bremer, T. Koettig, L. L. Amador, C. P. Carlos, G. Rosaz, and A. Vaaranta, "CERN Based Tc Measurement Station for Thin-Film Coated Copper Samples and Results on Related Studies", in Proc. 20th Int. Conf. on RF Superconductivity (SRF'21) (2021), pp. 105–108.

[123] Inorganic Crystal Structure Database (ICSD), Collection Code 982: Preparation and Structure of Stoichiometric Delta NbN, DOI: 10.3891/acta.chem.scand.31a-0077, 1977.

[124] C. S. Sandu, M. Benkahoul, M. Parlinska-Wojtan, R. Sanjinés, and F. Lévy, "Morphological, structural and mechanical properties of nbn thin films deposited by reactive magnetron sputtering", Surface and Coatings Technology **200**, 6544–6548 (2006).

[125] K. Kato, "Structure refinement of h-nb2o5", Acta Crystallographica Section B: Structural Science, Crystal Engineering and Materials **32**, 764–767 (1976).

[126] H. J. Schweizer and R. Gruehn, "Zur darstellung und kristallstruktur von beta-nb o2", Zeitschrift fuer Naturforschung, Teil B: Anorganische Chemie, Organische Chemie **37**, Collection Code 35181, 1361–1368 (1982).

[127] P. Caubet, T. Blomberg, R. Benaboud, C. Wyon, E. Blanquet, J.-P. Gonchond, M. Juhel, P. Bouvet, M. Gros-Jean, J. Michailos, C. Richard, and B. Iteprat, "Low-temperature low-resistivity peald tin using tdmat under hydrogen reducing ambient", Journal of The Electrochemical Society **155**, H625 (2008).

[128] D. D. Fischer, M. Knaut, J. Reif, F. Nehm, M. Albert, and J. W. Bartha, "Direct plasma-enhanced atomic layer deposition of aluminum nitride for water permeation barriers", Journal of Vacuum Science Technology A: Vacuum, Surfaces, and Films **38**, 22419 (2020).

[129] M. Broas, H. Jiang, A. Graff, T. Sajavaara, V. Vuorinen, and M. Paulasto-Kröckel, "Blistering mechanisms of atomic-layer-deposited AlN and al2o3 films", Applied Physics Letters **111**, 141606 (2017).

[130] A.-M. Valente-Feliciano, J. K. Spradlin, G Eremeev, C. E. Reece, M. C. Burton, and R. A. Lukaszew, "Growth and characterization of multilayer nbtin films * fundamentals srf rd-other materials d04-multi-layer coatings", in Proceedings of srf2015 (2015).

[131] N. Gungor and M. Alevli, "Oxygen incorporation in aln films grown by plasma-enhanced atomic layer deposition", Journal of Vacuum Science Technology A **40**, 22404 (2022).

[132] M. Legallais, H. Mehdi, S. David, F. Bassani, S. Labau, B. Pelissier, T. Baron, E. Martinez, G. Ghibaudo, and B. Salem, "Improvement of aln film quality using plasma enhanced atomic layer deposition with substrate biasing", ACS Applied Materials and Interfaces **12**, 39870–39880 (2020).

[133] M. Broas, P. Sippola, T. Sajavaara, V. Vuorinen, A. P. Perros, H. Lipsanen, and M. Paulasto-Kröckel, "Structural and chemical analysis of annealed plasma-enhanced atomic layer deposition aluminum nitride films", Journal of Vacuum Science Technology A: Vacuum, Surfaces, and Films **34**, 10.1116/1.4953029/245817 (2016).

[134] E. I. Suvorova, O. V. Uvarov, K. V. Chizh, A. A. Klimenko, and P. A. Buffat, "Structure, oxygen content and electric properties of titanium nitride electrodes in tinx/la:hfo2/tinx stacks grown by peald on sio2/si", Nanomaterials 2022, Vol. 12, Page 3608 **12**, 3608 (2022).

[135] NIST Chemistry WebBook, NIST Chemistry WebBook, National Institute of Standards and Technology, 2024.

[136] G. K. Tirumalasetty, M. A. V. Huis, C. M. Fang, Q. Xu, F. D. Tichelaar, D. N. Hanlon, J. Sietsma, and H. W. Zandbergen, "Characterization of nbc and (nb, ti)n nanoprecipitates in trip assisted multiphase steels", Acta Materialia **59**, 7406–7415 (2011).

[137] J. Hinz, A. J. Bauer, T. Thiede, R. A. Fischer, and L. Frey, "Evaluation of nbn thin films grown by mocvd and plasma-enhanced ald for gate electrode application in high-k/sio2 gate stacks", Semiconductor Science and Technology **25**, 10.1088/0268-1242/25/4/045009 (2010).

[138] R. M. Oliveira, L. Hoshida, A. C. Oliveira, M. M. Silva, L. Pichon, and N. M. Santos, "Evaluation of the resistance to oxidation of niobium treated by high temperature nitrogen plasma based ion implantation", Surface and Coatings Technology **312**, 110–116 (2017).

[139] B. E. Tegner, L. Zhu, C. Siemers, K. Saksl, and G. J. Ackland, "High temperature oxidation resistance in titanium–niobium alloys", Journal of Alloys and Compounds **643**, 100–105 (2015).

[140] M. Wenskat, "Automated optical inspection and image analysis of superconducting radio-frequency cavities", Journal of Instrumentation **12**, P05016 (2017).

[141] B. Radjenović and M. Radmilović-Radjenović, "The effect of plasma etching on the surface topography of niobium superconducting radio frequency cavities", Electronic Materials Letters **10**, 1039–1043 (2014).

[142] H. Mei, R. Huang, J. Y. Chung, C. M. Stafford, and H. H. Yu, "Buckling modes of elastic thin films on elastic substrates", Applied Physics Letters **90**, `10.1063/1.2720759/166416` (2007).

[143] G. Abadias, E. Chason, J. Keckes, M. Sebastiani, G. B. Thompson, E. Barthel, G. L. Doll, C. E. Murray, C. H. Stoessel, and L. Martinu, "Review article: stress in thin films and coatings: current status, challenges, and prospects", Journal of Vacuum Science Technology A: Vacuum, Surfaces, and Films **36**, `10.1116/1.5011790/19749143/020801_1_ACCEPTED_MANUSCRIPT.PDF` (2018).

[144] A. G. Evans and J. W. Hutchinson, "On the mechanics of delamination and spalling in compressed films", International Journal of Solids and Structures **20**, 455–466 (1984).

[145] J. W. Hutchinson, M. D. Thouless, and E. G. Liniger, "Growth and configurational stability of circular, buckling-driven film delaminations", Acta Metallurgica et Materialia **40**, 295–308 (1992).

[146] R. A. V. D. Bos, C. J. Lee, J. P. Benschop, and F. Bijkerk, "Blister formation in mo/si multilayered structures induced by hydrogen ions", Journal of Physics D: Applied Physics **50**, 265302 (2017).

[147] A. Werbrouck, K. V. de Kerckhove, D. Depla, D. Poelman, P. F. Smet, J. Dendooven, and C. Detavernier, "Plasma-enhanced atomic layer deposition: correlating o2 plasma parameters and species to blister formation and conformal film growth", Journal of Vacuum Science Technology A: Vacuum, Surfaces, and Films **39**, 62402 (2021).

[148] M. Broas, H. Jiang, A. Graff, T. Sajavaara, V. Vuorinen, and M. Paulasto-Kröckel, "Blistering mechanisms of atomic-layer-deposited aln and al2o3 films", Applied Physics Letters **111**, 141606 (2017).

[149] A. S. Kuznetsov, M. A. Gleeson, and F. Bijkerk, "Temperature dependencies of hydrogen-induced blistering of thin film multilayers", Journal of Applied Physics **115**, `10.1063/1.4875484/905492` (2014).

[150] H. Liu, S. Guo, R. B. Yang, C. J. Lee, and L. Zhang, "Giant blistering of nanometer-thick al2o3/zno films grown by atomic layer deposition: mechanism and potential applications", ACS Applied Materials and Interfaces **9**, 26201–26209 (2017).

[151] B. Vermang, H. Goverde, V. Simons, I. De Wolf, J. Meersschaut, S. Tanaka, J. John, J. Poortmans, and R. Mertens, "A study of blister formation in ALD al2o3 grown on silicon", in 2012 38th IEEE photovoltaic specialists conference, ISSN: 0160-8371 (June 2012), pp. 001135–001138.

[152] O. Nilsen, O. B. Karlsen, A. Kjekshus, and H. Fjellvåg, "Simulation of growth dynamics in atomic layer deposition. part i. amorphous films", Thin Solid Films **515**, 4527–4537 (2007).

[153] S. Goyal, K. Srinivasan, G. Subbarayan, and T. Siegmund, "Buckling, wrinkling and debonding in thin film systems", IEEE International Reliability Physics Symposium Proceedings, 430–439 (2010).

[154] H. Holleck, "Material selection for hard coatings", Journal of Vacuum Science Technology A **4**, 2661–2669 (1986).

[155] Mse supplies llc, `https://www.msesupplies.com/`.

[156] I. Krylov, X. Xu, K. Weinfeld, V. Korchnoy, D. Ritter, and M. Eizenberg, "Properties of conductive nitride films prepared by plasma enhanced atomic layer deposition using quartz and sapphire plasma sources", Journal of Vacuum Science Technology A: Vacuum, Surfaces, and Films **37**, 32 (2019).

[157] G. B. Rayner, N. O'Toole, J. Shallenberger, and B. Johs, "Ultrahigh purity conditions for nitride growth with low oxygen content by plasma-enhanced atomic layer deposition", Journal of Vacuum Science Technology A: Vacuum, Surfaces, and Films **38**, 62408 (2020).

[158] S. Karwal, B. Karasulu, H. C. Knoops, V. Vandalon, W. M. Kessels, and M. Creatore, "Atomic insights into the oxygen incorporation in atomic layer deposited conductive nitrides and its mitigation by energetic ions", Nanoscale **13**, 10092–10099 (2021).

[159] S. Posen, "Nb3sn superconducting radiofrequency cavities:a maturing technology for particle accelerators and detectors", White Paper for Snowmass 2021 (2022).

[160] W. Mayr, W. Lengauer, V. Buscaglia, J. Bauer, M. Bohn, and M. Fialin, "Nitridation of ti/nb alloys and solid-state properties of -(ti,nb)n", Journal of Alloys and Compounds **262-263**, 521–528 (1997).

[161] H. Machhadani, J. Zichi, C. Bougerol, S. Lequien, J. L. Thomassin, N. Mollard, A. Mukhtarova, V. Zwiller, J. M. Gérard, and E. Monroy, "Improvement of the critical temperature of nbtin films on iii-nitride substrates", Superconductor Science and Technology **32**, `10.1088/1361-6668/aaf99d` (2019).

[162] P. Prieto and R. E. Kirby, "X-ray photoelectron spectroscopy study of the difference between reactively evaporated and direct sputter-deposited tin films and their oxidation properties", Journal of Vacuum Science Technology A **13**, 2819–2826 (1995).

[163] P. M. Korusenko, S. N. Nesov, S. N. Povoroznyuk, P. V. Orlov, D. N. Korotaev, K. N. Poleschenko, and E. E. Tarasov, "Data on the morphology and chemical state of coatings based on tin obtained by condensation with ion bombardment on various substrates", Data in Brief **27**, 104737 (2019).

[164] A. D. Pandey, G. D. L. Semione, A. Prudnikava, T. F. Keller, H. Noei, V. Vonk, Y. Tamashevich, E. Elsen, B. Foster, and A. Stierle, "Surface characterization of nitrogen-doped nb (100) large-grain superconducting rf cavity material", Journal of Materials Science **53**, 10411–10422 (2018).

[165] M. Ziegler, S. Linzen, S. Goerke, U. Bruckner, J. Plentz, J. Dellith, A. Himmerlich, M. Himmerlich, U. Hubner, S. Krischok, and H. G. Meyer, "Effects of plasma parameter on morphological and electrical properties of superconducting nb-n deposited by mo-peald", IEEE Transactions on Applied Superconductivity **27**, 10.1109/TASC.2017.2744326 (2017).

[166] L. Zhang, L. You, L. Ying, W. Peng, and Z. Wang, "Characterization of surface oxidation layers on ultrathin nbtin films", Physica C: Superconductivity and its Applications **545**, 1–4 (2018).

[167] M. Kot, J. Łobaza, F. Naumann, H. Gargouri, K. Henkel, and D. Schmeißer, "Long-term ambient surface oxidation of titanium oxynitride films prepared by plasma-enhanced atomic layer deposition: an xps study", Journal of Vacuum Science Technology A: Vacuum, Surfaces, and Films **36**, 1–114 (2018).

[168] M. J. Sowa, L. Ju, A. C. Kozen, N. C. Strandwitz, G. Zeng, T. F. Babuska, Z. Hsain, and B. A. Krick, "Plasma-enhanced atomic layer deposition of titanium vanadium nitride", Journal of Vacuum Science Technology A: Vacuum, Surfaces, and Films **36**, 6–103 (2018).

[169] F. M. John, F. S. William, E. Peter, and D. B. Kenneth, "Handbook of x-ray photoelectron spectroscopy", Perkin-Elmer Corporation, Physical Electronics Division **6509** (1992).

[170] G. Greczynski and L. Hultman, "A step-by-step guide to perform x-ray photoelectron spectroscopy", Journal of Applied Physics **132**, 11101 (2022).

[171] G. Brauer, "Nitrides, carbonitrides and oxynitrides of niobium", Journal of the Less Common Metals **2**, 131–137 (1960).

[172] H. Holleck, Binäre und ternäre carbid- und nitridsysteme der übergangsmetalle (Schweizerbart Science Publishers, Stuttgart, Germany, Sept. 1984).

[173] G. I. Oya and Y. Onodera, "Phase transformations in nearly stoichiometric nbx", Journal of Applied Physics **47**, 2833–2840 (1976).

[174] G. Brauer and W. Kern, "Zersetzungsdrücke und phasengrenzen von niobnitriden", Zeitschrift für anorganische und allgemeine Chemie **507**, 127–141 (1983).

[175] W. Lengauer, M. Bohn, B. Wollein, and K. Lisak, "Phase reactions in the nb–n system below 1400°c", Acta Materialia **48**, 2633–2638 (2000).

[176] M. Benkahoul, E. Martinez, A. Karimi, R. Sanjinés, and F. Lévy, "Structural and mechanical properties of sputtered cubic and hexagonal nbnx thin films", Surface and Coatings Technology **180-181**, 178–183 (2004).

[177] M. Fenker, M. Balzer, R. V. Büchi, H. A. Jehn, H. Kappl, and J. J. Lee, "Deposition of nbn thin films onto high-speed steel using reactive magnetron sputtering for corrosion protective applications", Surface and Coatings Technology **163-164**, 169–175 (2003).

[178]S. Leith, M. Vogel, J. Fan, E. Seiler, R. Ries, and X. Jiang, "Superconducting nbn thin films for use in superconducting radio frequency cavities", Superconductor Science and Technology **34**, 025006 (2021).

[179]F. Mercier, S. Coindeau, S. Lay, A. Crisci, M. Benz, T. Encinas, R. Boichot, A. Mantoux, C. Jimenez, F. Weiss, and E. Blanquet, "Niobium nitride thin films deposited by high temperature chemical vapor deposition", Surface Coatings Technology, `10.1016/j.surfcoat.2014.08.084` (2014).

[180]K. S. Keskar, T. Yamashita, and Y. Onodera, "Superconducting transition temperatures of r. f. sputtered nbn films", Japanese Journal of Applied Physics **10**, 370–374 (1971).

[181]V. Buscaglia, F. Caracciolo, M. Ferretti, M. Minguzzi, and R. Musenich, "Effect of pressure on the composition and superconducting tc value of nbn prepared by combustion synthesis", Journal of Alloys and Compounds **266**, 201–206 (1998).

[182]M. Wen, T. An, S. X. Du, X. Guo, C. Q. Hu, K. Zhang, and W. T. Zheng, "Thermal stability of microstructure and mechanical properties of nbnhard films", Materials Science Forum **817**, 137–142 (2015).

[183]A. D. Pogrebnjak, V. M. Rogoz, O. V. Bondar, N. K. Erdybaeva, and S. V. Plotnikov, "Structure and physicomechanical properties of nbn-based protective nanocomposite coatings: a review", Protection of Metals and Physical Chemistry of Surfaces **52**, 802–813 (2016).

[184]V. Palmieri, "New materials for superconducting radiofrequency cavities", in 10th workshop on rf superconductivity, edited by JACoW (2001), pp. 162–169.

[185]T. Motohashi, M. Ito, Y. Masubuchi, M. Wakeshima, and S. Kikkawa, "Crystal structure and superconducting properties of hexagonal lithium-niobium oxynitride", Inorganic Chemistry **51**, 11184–11189 (2012).

[186]N. Terao, "New phases of niobium nitride", Journal of the Less Common Metals **23**, 159–169 (1971).

[187]Y. Pei, Q. Fan, X. Ni, and X. Gu, "Controlling the superconducting critical temperature and resistance of nbn films through thin film deposition and annealing", Coatings 2024, Vol. 14, Page 496 **14**, 496 (2024).

[188]R. Roy, P. F. Carcia, R. Messier, and D. Rogowski, "The effect of composition on the superconducting transition temperature in nbnxoy", Materials Research Bulletin **10**, 379–382 (1975).

[189]C. Benvenuti, P. Chiggiato, L. Parrini, and R. Russo, "Production of niobium-titanium nitride coatings by reactive diffusion for superconducting cavity applications", Nuclear Instruments and Methods in Physics Research Section B: Beam Interactions with Materials and Atoms **124**, 106–111 (1997).

[190]N. Pessall and J. K. Hulm, "Superconducting alloys of interstitial compounds", Physics Physique Fizika **2**, 311 (1966).

[191]C. M. Yen, L. E. Toth, Y. M. Shy, D. E. Anderson, and L. G. Rosner, "Superconducting hc-jc and tc measurements in the nb–ti–n, nb–hf–n, and nb–v–n ternary systems", Journal of Applied Physics **38**, 2268–2271 (1967).

[192]R. Rhazi, H. Machhadani, C. Bougerol, S. Lequien, E. Robin, G. Rodriguez, R. Souil, J. L. Thomassin, N. Mollard, Y. Désieres, E. Monroy, S. Olivier, and J. M. Gérard, "Improvement of critical temperature of niobium nitride deposited on 8-inch silicon wafers thanks to an aln buffer layer", Superconductor Science and Technology **34**, 045002 (2021).

[193]S. Krause, D. Meledin, V. Desmaris, A. Pavolotsky, V. Belitsky, M. Rudziński, and E. Pippel, "Epitaxial growth of ultra-thin nbn films on alxga1xn buffer-layers", Superconductor Science and Technology **27**, 065009 (2014).

[194]FIZ Karlsruhe – Leibniz Institute for Information Infrastructure, Collection Code 644573, Retrieved from Inorganic Crystal Structure Database (ICSD).

[195]FIZ Karlsruhe – Leibniz Institute for Information Infrastructure, Collection Code 644572, Retrieved from Inorganic Crystal Structure Database (ICSD).

[196]FIZ Karlsruhe – Leibniz Institute for Information Infrastructure, Collection Code 982, Retrieved from Inorganic Crystal Structure Database (ICSD).

[197]FIZ Karlsruhe – Leibniz Institute for Information Infrastructure, Collection Code 64908, Retrieved from Inorganic Crystal Structure Database (ICSD).

[198]S. Dolabella, A. Borzì, A. Dommann, A. Neels, S Dolabella, A Borzì, A Dommann, and A Neels, "Lattice strain and defects analysis in nanostructured semiconductor materials and devices by high-resolution x-ray diffraction: theoretical and practical aspects", Small Methods **6**, 2100932 (2022).

[199]FIZ Karlsruhe – Leibniz Institute for Information Infrastructure, Collection Code 34475, Retrieved from Inorganic Crystal Structure Database (ICSD).

[200]FIZ Karlsruhe - ICSD, Inorganic crystal structure database (icsd), `https://icsd.fiz-karlsruhe.de/search/basic.xhtml`.

[201]Database of inorganic and organic data, PDF-#26-003 and PDF-#20-0043.

[202]Database of inorganic and organic data, PDF-#34-0719 and PDF-#48-0637.

[203]FIZ Karlsruhe – Leibniz Institute for Information Infrastructure, Collection Code 29288, Retrieved from Inorganic Crystal Structure Database (ICSD).

[204]L. E. Toth, Transition metal carbides and nitrides (Academic Press, New York, 1971).

[205]M. C. Burton, M. R. Beebe, K. Yang, R. A. Lukaszew, A.-M. Valente-Feliciano, and C. Reece, "Superconducting NbTiN thin films for superconducting radio frequency accelerator cavity applications", Journal of Vacuum Science & Technology A **34**, Publisher: American Vacuum Society, 021518 (2016).

[206]K. Makise, H. Terai, M. Takeda, Y. Uzawa, and Z. Wang, "Characterization of nbtin thin films deposited on various substrates", IEEE Transactions on Applied Superconductivity **21**, 139–142 (2011).

[207]T. S. Yeh, J. M. Wu, and W. H. Lan, "The effect of aln buffer layer on properties of alxin1 xn films on glass substrates", Thin Solid Films **517**, 3204–3207 (2009).

[208]A. D. Pogrebnjak, O. V. Bondar, G. Abadias, V. Ivashchenko, O. V. Sobol, S. Jurga, and E. Coy, "Structural and mechanical properties of nbn and nb-si-n films: experiment and molecular dynamics simulations", Ceramics International **42**, 11743–11756 (2016).

[209]L. Zhang, W. Peng, L. X. You, and Z. Wang, "Superconducting properties and chemical composition of nbtin thin films with different thickness", Applied Physics Letters **107**, `10.1063/1.4931943` (2015).

[210]FIZ Karlsruhe – Leibniz Institute for Information Infrastructure, Collection Code 31165, Retrieved from Inorganic Crystal Structure Database (ICSD).

[211]FIZ Karlsruhe – Leibniz Institute for Information Infrastructure, Collection Code 644538, Retrieved from Inorganic Crystal Structure Database (ICSD).

[212]FIZ Karlsruhe – Leibniz Institute for Information Infrastructure, Collection Code 150986, Retrieved from Inorganic Crystal Structure Database (ICSD).

[213]FIZ Karlsruhe – Leibniz Institute for Information Infrastructure, Collection Code 26252, Retrieved from Inorganic Crystal Structure Database (ICSD).

[214]FIZ Karlsruhe – Leibniz Institute for Information Infrastructure, Collection Code 82663, Retrieved from Inorganic Crystal Structure Database (ICSD).

[215]FIZ Karlsruhe – Leibniz Institute for Information Infrastructure, Collection Code 86061, Retrieved from Inorganic Crystal Structure Database (ICSD).

[216]A. Nigro, G. Nobile, M. G. Rubino, and R. Vaglio, "Electrical resistivity of polycrystalline niobium nitride films", Physical Review B **37**, 3970 (1988).

[217]W. Wagner, D. Ast, and J. R. Gavaler, "Electronmicroscopic evidence for a columnar-void-type structure in sputtered nbn films", Journal of Applied Physics **45**, 465–466 (1974).

[218]K. E. Gray, R. T. Kampwirth, D. M. Capone, and R. Vaglio, "Microscopic investigation of nbn sputtered films", Physica B+C **135**, 164–167 (1985).

[219]A. Nigro, G. Nobile, V. Palmieri, G. Rubino, and R. Vaglio, "Superconducting and normal state properties of niobium-nitride thin films", Physica Scripta **38**, 483 (1988).

[220]Y. M. Shy, L. E. Toth, and R. Somasundaram, "Superconducting properties, electrical resistivities, and structure of nbn thin films", Journal of Applied Physics **44**, 5539–5545 (1973).

[221]G. Horn and E. Saur, "Präparation und supraleitungseigenschaften von niobnitrid sowie niobnitrid mit titan-, zirkon- und tantalzusatz", Zeitschrift für Physik **210**, 70–79 (1968).

[222]C. M. Yen, L. E. Toth, Y. M. Shy, D. E. Anderson, and L. G. Rosner, "Superconducting hc-jc and tc measurements in the nb–ti–n, nb–hf–n, and nb–v–n ternary systems", Journal of Applied Physics **38**, Publisher: American Institute of Physics, 2268–2271 (1967).

[223]K. Vasu, M. G. Krishna, and K. A. Padmanabhan, "Effect of nb concentration on the structure, mechanical, optical, and electrical properties of nano-crystalline ti 1-x nb x n thin films", Journal of Materials Science **47**, 3522–3528 (2012).

[224]J. R. Gavaler, D. W. Deis, J. K. Hulm, and C. K. Jones, "Superconducting properties of niobium-titanium-nitride thin films", Applied Physics Letters **15**, 329–331 (1969).

[225]C. Kittel, Introduction to solid state physics, 8th ed. (John Wiley & Sons, New York, 2005).

[226] U. Johansson, H. Zhang, and R. Nyholm, "Thermal desorption of oxides on si(100): a case study for the scanning photoelectron microscope at max-lab", Journal of Electron Spectroscopy and Related Phenomena **84**, 45–52 (1997).

[227] K. Xue, J. B. Xu, and H. P. Ho, "Nanoscale in situ investigation of ultrathin silicon oxide thermal decomposition by hightemperature scanning tunneling microscopy", Nanotechnology **18**, 485709 (2007).

[228] L. S. Preece, "Magnetic characterization of peald coated thin films for srf cavity research", Master's Thesis (Universität Hamburg, Universität Hamburg, 2024).

[229] M. Delheusy, A. Stierle, N. Kasper, R. P. Kurta, A. Vlad, H. Dosch, C. Antoine, A. Resta, E. Lundgren, and J. Andersen, "X-ray investigation of subsurface interstitial oxygen at nb/oxide interfaces", Applied Physics Letters **92**, 101911 (2008).

[230] Q. Ma and R. A. Rosenberg, "Angle-resolved x-ray photoelectron spectroscopy study of the oxides on nb surfaces for superconducting r.f. cavity applications", Applied Surface Science **206**, 209–217 (2003).

[231] J. Halbritter, "On the oxidation and on the superconductivity of niobium", Applied Physics A Solids and Surfaces **43**, 1–28 (1987).

[232] L. Z. Zhang, A. L. Zhang, W. Lu, Q. L. Xiao, F. Chen, Z. Feng, S. Cao, J. Zhang, and J. Y. Ge, "Paramagnetic meissner effect observed in srbi3 with close to the critical regime", Journal of Superconductivity and Novel Magnetism **33**, 1691–1695 (2020).

[233] S. B. Roy, G. R. Myneni, and V. C. Sahni, "The influence of chemical treatments on the superconducting properties of technicalniobium materials and their effect on the performance of superconducting radio frequencycavities", Superconductor Science and Technology **22**, 105014 (2009).

[234] M. C. Burton, M. R. Beebe, K. Yang, R. A. Lukaszew, A.-M. Valente-Feliciano, and C. Reece, "Superconducting nbtin thin films for superconducting radio frequency accelerator cavity applications", Journal of Vacuum Science Technology A: Vacuum, Surfaces, and Films **34**, 21518 (2016).

[235] C. Antoine, "Materials for superconducting accelerators: beyond bulk nb", in Tutorials srf 2019 (2019).

[236] M. J. Sowa, Y. Yemane, F. B. Prinz, and J Provine, "Plasma-enhanced atomic layer deposition of tungsten nitride", Journal of Vacuum Science Technology A: Vacuum, Surfaces, and Films **34**, `10.1116/1.4961567/245491` (2016).

[237] N. Pessall, R. E. Gold, and H. A. Johansen, "A study of superconductivity in interstitial compounds", Journal of Physics and Chemistry of Solids **29**, 19–38 (1968).

[238] M. Hatano, T. Nishino, and U. Kawabe, "Sputtering: effects of thermal annealing on superconducting nb and nbn films", Journal of Vacuum Science Technology A: Vacuum, Surfaces, and Films **6**, 2381–2385 (1988).

[239] M. Guziewicz, W. Slysz, M. Borysiewicz, R. Kruszka, Z. Sidor, M. Juchniewicz, K. Golaszewska, J. Z. Domagala, W. Rzodkiewicz, J. Ratajczak, J. Bar, M. Wegrzecki, and R. Sobolewski, "Sputtering: technology of ultrathin nbn and nbtin films for superconducting photodetectors", Acta Physica Polonica A **120**, A76–A79 (2011).

[240] H. Ge, Y. R. Jin, and X. H. Song, "High quality nbtin films fabrication and rapid thermal annealing investigation", Chinese Physics B **28**, `10.1088/1674-1056/28/7/077402` (2019).

[241] D. W. Deis, J. R. Gavaler, J. K. Hulm, and C. K. Jones, "High field properties of pure niobium nitride thin films", Journal of Applied Physics **40**, 2153–2156 (1969).

[242] J. Y. Lee, D. W. Kim, W. S. Kang, J. O. Lee, M. Hur, and S. H. Han, "Growth mechanism of al2o3 film on an organic layer in plasma-enhanced atomic layer deposition", Journal of Physics D: Applied Physics **51**, 015201 (2017).

[243] C. Saribal et al., "Development of a thermal conductance instrument for niobium at cryogenic temperatures", in 21th international conference on rf superconductivity (srf'23), Paper MOPMB017 (2023).

[244] D. A. Turner, I. G. Díaz-Palacio, W. Hillert, T. Koettig, A. Macpherson, G. Rosaz, N. Stapley, A. G. Terricabras, and M. Wenskat, "Flux expulsion lens: concept and measurements", in 21th international conference on rf superconductivity (srf2023) (2023).

[245] I. Krylov, E. Zoubenko, K. Weinfeld, Y. Kauffmann, X. Xu, D. Ritter, and M. Eizenberg, "Obtaining low resistivity (100cm) TiN films by plasma enhanced atomic layer deposition using a metalorganic precursor", Journal of Vacuum Science & Technology A **36**, Publisher: American Vacuum Society, 051505 (2018).

[246] E. T. Norton and C. Amato-Wierda, "Kinetic and mechanistic studies of the thermal decomposition of ti(n(ch3)2)4 during chemical vapor deposition by in situ molecular beam mass spectrometry", Chemistry of Materials **13**, 4655–4660 (2001).

[247] K. Kasprzak, T. Buettner, A. Gössel, D. Klinke, D. Kostin, C. Müller, E. Vogel, and M. Wiencek, "Test-stand for conditioning of fundamental power couplers at desy", JACoW **SRF2023**, `10.18429/JACOW-SRF2023-WEPWB092` (2023).

[248] J. Landoulsi, M. J. Genet, S. Fleith, Y. Touré, I. Liascukiene, C. Méthivier, and P. G. Rouxhet, "Organic adlayer on inorganic materials: xps analysis selectivity to cope with adventitious contamination", Applied Surface Science **383**, 71–83 (2016).

[249] P. J. Cumpson and M. P. Seah, "Stability of reference masses. iv: growth of carbonaceous contamination on platinum-iridium alloy surfaces, and cleaning by uv/ozone treatment", Metrologia **33**, 507 (1996).

[250] C. Xia, X. Ma, X. Zhang, K. Li, J. Tan, Y. Qiao, and X. Liu, "Enhanced physicochemical and biological properties of c/cu dual ions implanted medical titanium", Bioactive Materials **5**, 377–386 (2020).

[251] A. Felten, I. Suarez-Martinez, X. Ke, G. V. Tendeloo, J. Ghijsen, J. J. Pireaux, W. Drube, C. Bittencourt, and C. P. Ewels, "The role of oxygen at the interface between titanium and carbon nanotubes", ChemPhysChem **10**, 1799–1804 (2009).

Acknowledgements

I would like to express my deepest gratitude to all those who have supported me over the past years and without whom this thesis would not have been possible.

In the first place, I would like to thank my supervisors, Prof. Dr. Robert Blick and Prof. Dr. Wolfgang Hillert, for giving me the opportunity to carry out this thesis and for allowing me to be part of their research groups. I would also like to thank Dr. Robert Zierold. I have been very fortunate to count on his guidance and support. I am very grateful for his help whenever needed and his encouragement, without which I would not have made it this far. I am also deeply grateful to Dr. Marc Wenskat for his support, guidance, and for always being there for me. His contagious enthusiasm for SRF cavities, his encouragement, and his belief in me have been a source of motivation for me. In addition, I would like to thank Prof. Dr. Michael Potthoff for chairing my oral examination.

I extend my thanks to all (present and former) colleagues who have created a supportive and comfortable working environment. Starting with the CHyN colleagues, I would like to give a special thanks to Vincent Strenzke, Dr. Chitra H. Sharma, and the members of the BioMat team, in particular to Dr. Carina Hedrich, Dr. Jun Peng, Kristian Deneke, Dr. Stefanie Haugg, and Malte Siegmund. I also want to thank Rakshith Venugopal, whose energy has made the time working side by side an enjoyable experience. From the Hillert's and MSL DESY group, I would like to express my gratitude to the members of the SRF Cavity team, particularly Dr. Detlef Reschke, Dr. Lea Steder, and Cornelius Martens, for their time, advice, and feedback over the years. I would also like to acknowledge my colleagues from the HF Lab, Dr. Ricardo Monroy-Villa, Chirag Banjare, Marco Voige, Dr. Julia Jirapon Goedecke, Giovanni Marconato, Artem Zaidman, and Cem Saribal. A very special thanks to Dr. Getnet Kacha Deyu for his willingness to help, his constructive feedback, and the many discussions about the results, but also for the good times and the laughs, both at work and beyond. I would also like to dedicate a particular thanks to Lea Preece, for her wonderful soul, which has made every moment brighter. Lastly, I want to express my gratitude to my Bangkok diggas, Dr. Christopher Bate, Jonas Wolff (Ë auch!), and Rezvan Ghanbari. I have enjoyed our endless discussions, the late-night co-working shifts at HF Lab, and the high-focus sessions at Stabi. I have been very fortunate to have you by my side through the ups and downs of my PhD and for the friendship we have built.

Quiero agradecer también a mis amigas y amigos por el apoyo durante estos años. Empezando por todos los que me han sostenido en la distancia, a mis Wachas, en especial a María, Mayka y Ainhoa por quererme y cuidarme tanto, a Alba por ser siempre un gran apoyo y a Sara por creer siempre en mi. También quiero agradecer de corazón a todos los que se han convertido en mi red de apoyo y familia estando lejos de casa, en especial a todo mi Komando, Irene, Nuria, Fran, Melania y sobre todo a David, por haber estado ahí con todas esas llamadas de control y más, sosteniéndome durante la etapa final. También quiero expresar mi profundo agradecimiento a Irene Zorroza.

Por último, quiero dar las gracias a mi familia por ser mi refugio. A mis padres, por animarme siempre a seguir y por hacerme sentir en casa llenándome la galería con fotografías de las perras. Y a mis hermanos y cuñados por su amor y apoyo incondicional. (*Amaia-La persona* y *Amaia-Auxiliar*)

A. Appendix: additional information on samples fabrication

A.1. Troubleshooting for the GEMStar PEALD system

A.1.1. Concerns about vacuum leaks: chamber door O-ring

The deposition temperature ($250\,°C$) and the chemicals involved impact the durability of the perfluoroelastomer (FFKM) O-ring responsible for vacuum sealing. It is designed to withstand temperatures from $-30\,°C$ to $327\,°C$ and provide broad chemical resistance. However, differences in durability have been observed among O-rings from various manufacturers. O-ring wear leads to vacuum leaks, causing CVD growth. Figure A.1 shows O-ring damages (worn, flattened, and fissures), which cause poor sealing and consequently vacuum leaks, leading to CVD growth (as seen in Figure A.1). Of the three manufacturers tested, ERIKS Deutschland GmbH supplied the most durable and reliable O-rings. Reducing the deposition temperature to below $200\,°C$ extends the o-ring durability.
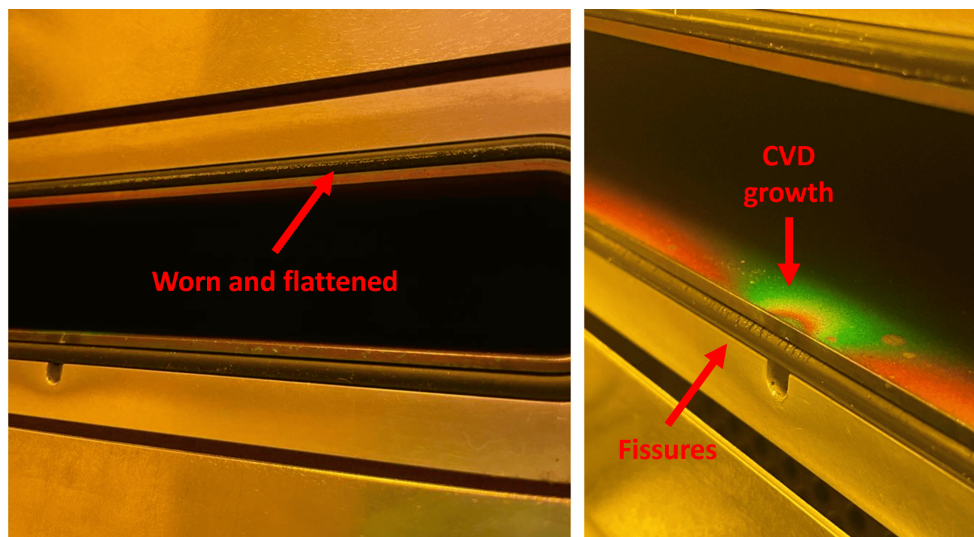

Figure A.1: Worn O-ring from the chamber door of the GEMStar XT-DP$^{\mathrm{TM}}$. The occurrence of CVD growth is a sign of a leak.

A.1.2. Plasma head troubleshooting: quartz tube replacement

To protect the quartz tube from the plasma head some actions have been taken. The plasma head is air-cooled and the plasma duration has been kept below 120 seconds to prevent its overheating. To keep the quartz tube clean and prevent precursor backflow, a 70 sccm Ar flow is used during precursor doses. However, residue accumulation in the quartz tube is inevitable with prolonged use, as visible in Figure A.1. Quartz degradation causes impedance mismatches, resulting in inefficient plasma ignition, power losses. and undesirable plasma fluctuations—visible by jittering of UV light; which restricts the system's capability to achieve controlled, high-quality, and reproducible depositions.
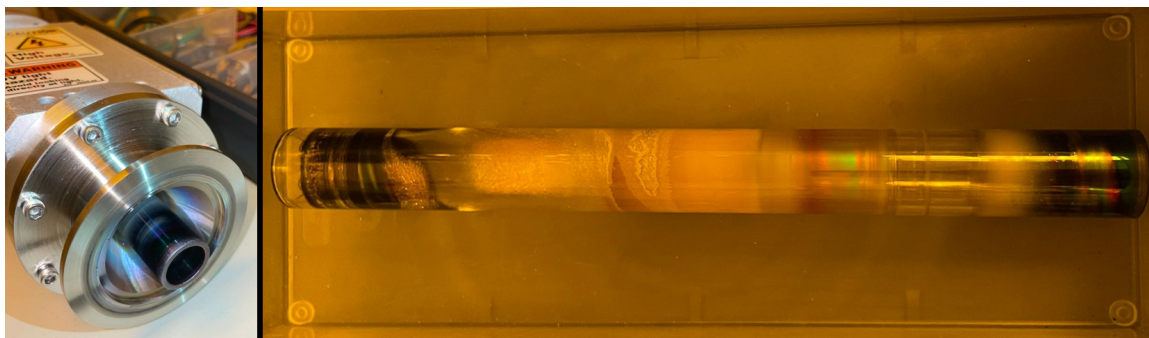
Figure A.2: Visible deterioration of the plasma head quartz tube

A.1.3. Concerns about precursors

Precursor decomposition

A drawback of the metalorganic alkylamide-based precursors is their thermal decomposition at low temperatures [54]. It may occur even during storage (see Figure A.3 *right*). Thus, they must be stored in tightly sealed containers (see Figure A.3 *left*) to avoid contact with water and reduce the risk of decomposition. Precursor decomposition results in impurities and non-self-limiting growth contributions. Hence, metalorganic alkylamide-based precursors are more suitable for PEALD rather than thermal ALD, as the latter often requires elevated deposition temperatures. The onset of thermal precursor decomposition may depend on temperature (deposition and storage), reactor pressure, and precursor pulse dose [245]. Previous studies have shown the onset for thermal decomposition is 300 °C for TBTDEN [84], 257 °C for TDMAT [246], and 370 °C for TMA [129]. However, it has been shown that for shorter precursor dose (<1 s) and low pressure ($\sim$mTorr) the impact on precursor decomposition rate is minimal, and high-quality films have been deposited at higher deposition temperatures [245].

Figure A.3: Photographs: *left* a precursor container from the system GEMStar XT-DP$^{\text{TM}}$ and *right* decomposed precursor (handle in a controlled atmosphere inside of a glove box).

Chromatic differences among the TBTDEN precursors

Despite the TBTDEN 98% purity ensured by the precursor supplier (Strem Chemicals), chromatic differences were noticed among the various bottles of TBTDEN. It has been observed that it may affect the purity of the deposited films, as indicated by a small variance in T_c^{NbTiN}.

Figure A.4: Two different TBTDEN bottles showing substantial discrepancy in colour. Both are 5g of minimum 98% purity TBTDEN however, their colour is notably distinct.

A.1.4. Plasma etching on high substrate

Figure A.5 shows the plasma-induced damage on TiN layer grown by PEALD on ceramic RF windows. It is assumed that the plasma ions impact the upper outer substrate surface with high energy, resulting in etching. Therefore, non-uniform coating is achieved, as evidence by the colour gradient.
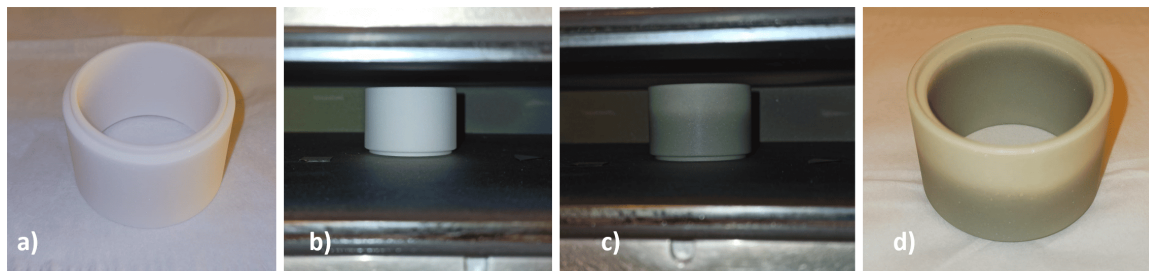

Figure A.5: Plasma-induced side effect: ion bombardment etching during deposition on high ceramic substrates, resulting in non-homogeneous TiN deposition. The ceramic RF windows are coated with a thin TiN layer, which suppresses secondary electron emission, as part of an investigation on conditioning of power couplers at DESY [247].

B. Appendix: additional characterisation results

B.1. Supplementary information for XRR studies from Section 5

Figure B.1 shows the reflectivity profiles for AlN-NbTiN and AlN-NbN multilayers, as-deposited and after RTA and STA. As-deposited the multilayers exhibit well-defined interfaces, indicated by the pronounced and sharp oscillations. After annealing the reflectivity profiles experience damping, indicating changes and reduce sharpness at the interfaces. This effect is more prominent for NbTiN than for NbN, suggesting that layer intermixing is more significant for NbTiN. Moreover, damping seems to be greater for STA than for RTA.
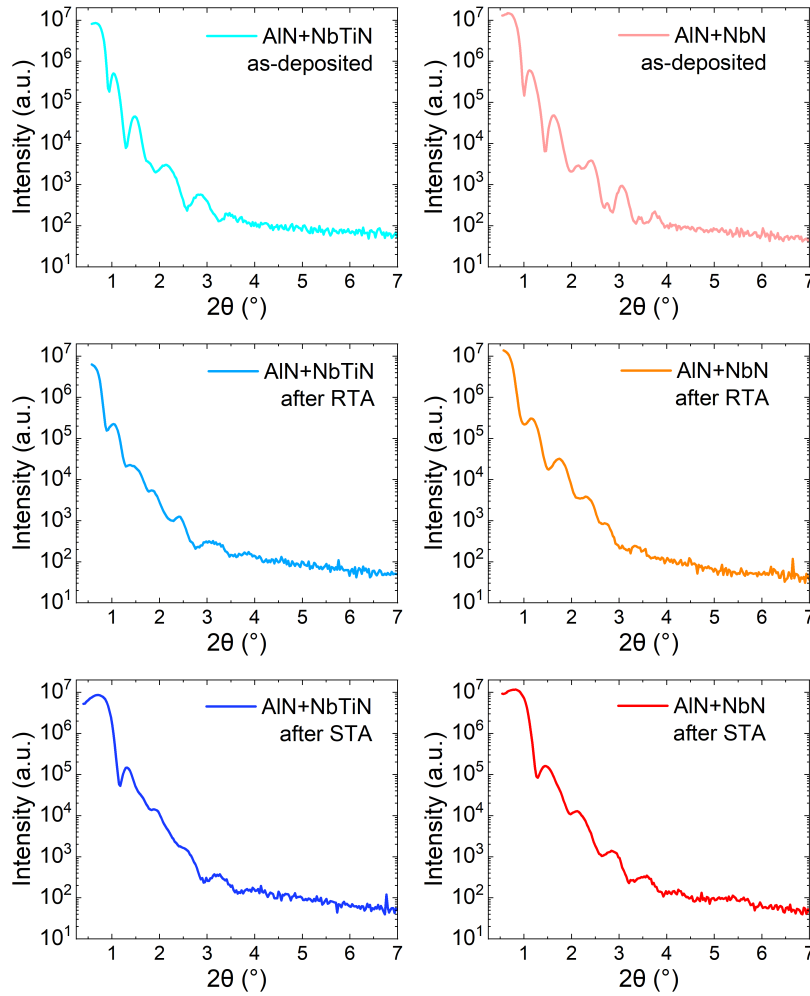

Figure B.1: XRR curves corresponding to: AlN-NbTiN (*left*) and AlN-NbN (*right*), as-deposited, RTA-, and STA-treated.

B.2. Supplementary information related to the morphology studies in Section 6

B.2.1. Impact of thin-film thickness on blistering

The impact of the thin-film thickness on blister density and size was examined for AlN films grown on Si. The thickness ranges from 10 to 25 nm. The greater the number of PEALD cycles, and thus the thicker the film, the higher the blister density. This observation supports the hypothesis that ion bombardment causes blistering, as compressive stress would be greater in thicker films. Although it also supports the hydrogen accumulation hypothesis, since the greater the number of PEALD cycles the more hydrogen would accumulate. The evaluation of blister density is not included, as the limited number of AFM scans and the significant variability in blister distribution (see Figure 6.10 a) reduce the statistical reliability. Blister height and diameter, measured via AFM for different film thicknesses, are shown in Figure B.2. Although both parameters show a slight upward trend with thickness, blister size varies significantly.
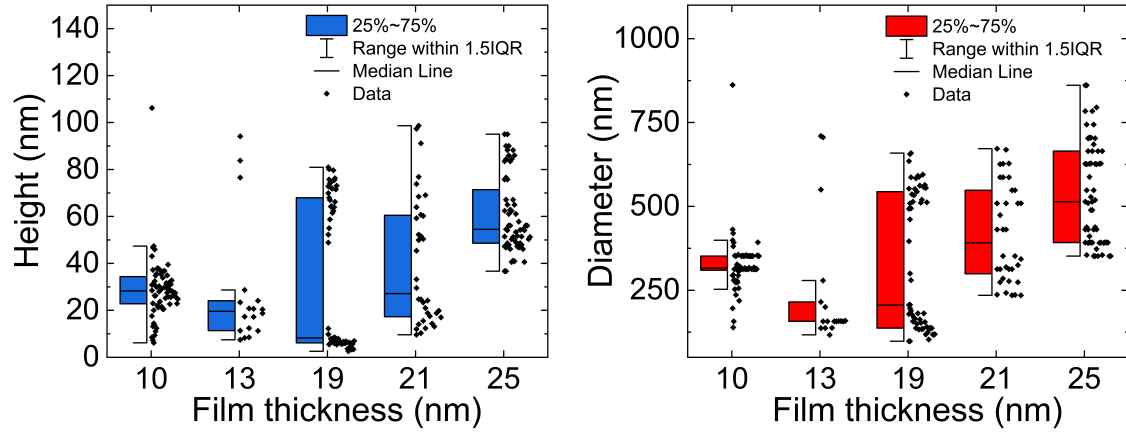

Figure B.2: Variation in blister size with thickness: blister height and diameter for AlN films of different thicknesses.

B.2.2. Inconsistencies on blister formation

Blister formation was investigated by varying the deposition temperature from $80\,°C$ to $250\,°C$, for 350 cycles of AlN. According to Fischer et al. [128], low temperatures ($80\,°C$, $95\,°C$, and $105\,°C$) do not produce blisters, while higher temperatures (125-$250\,°C$) lead to blister formation. However, Figure B.3 shows that repeated depositions at certain temperatures revealed inconsistencies in this trend.

To address the noted inconsistencies, a comprehensive evaluation was conducted. The deposition temperature was set at $175\,°C$, and the film thickness was maintained at approximately $25\,nm$. Various substrate positions within the PEALD reactor were used to investigate the potential influence of plasma distribution on blister formation; however, no differences were observed. The evaluation for blistering at the various films and substrates was repeated at $175\,°C$. Single-layer films of AlN, NbTiN, NbN, and TiN, as well as multi-
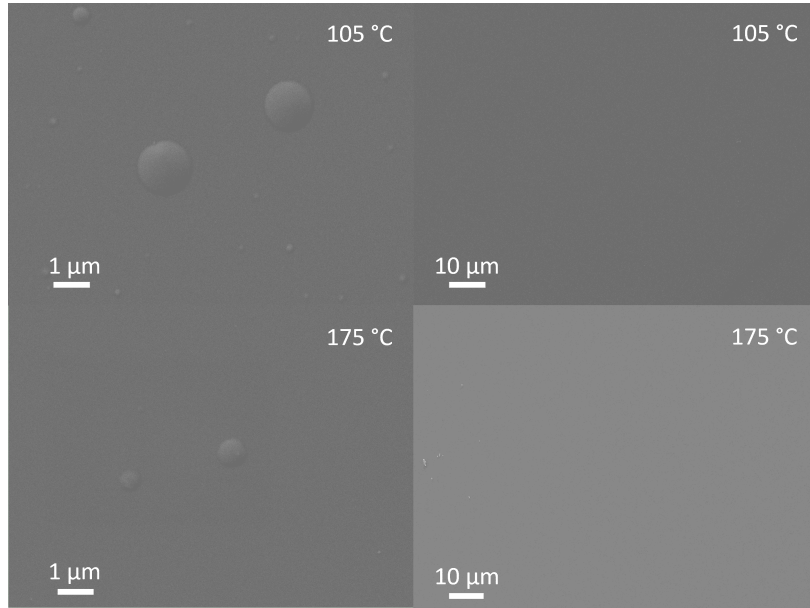
Figure B.3: Inconsistencies on blister formation. The SEM images correspond to 350 cycles of AlN grown at 105 °C and 175 °C. It can be observed that the same deposition temperature can result in the appearance or absence of blisters.

layer of AlN-NbTiN, AlN-NbN, and AlN-TiN, were deposited on both Si and Nb substrates. No blisters were observed in any scenario on Nb. However, on Si, single layers do not exhibit blister while multilayers do. Comparing AlN-NbN and AlN-TiN, blisters are more pronounced for AlN-NbN, even when using the same plasma process parameters. Reverse multilayers (NbTiN-AlN) were also examined, showing no blister formation. It is worth noting that blisters do not emerge under any circumstances in the event of deposition on Nb, which in this case refers to untreated Nb.

B.3. HPR Tests: Evaluating the compatibility of PEALD-SIS multilayers with cleaning standard procedures for SRF cavities

PEALD-SIS multilayers grown on Nb underwent the cleaning cavity procedure of high pressure rinsing (HPR) described in Section 3. The samples were evaluated with SEM and EDX before and after the treatment. The SEM inspection did not reveal any sign of damage. EDX spectra confirmed the presence of AlN and NbTiN thin films before and after seven HPRs (see Figure B.4).
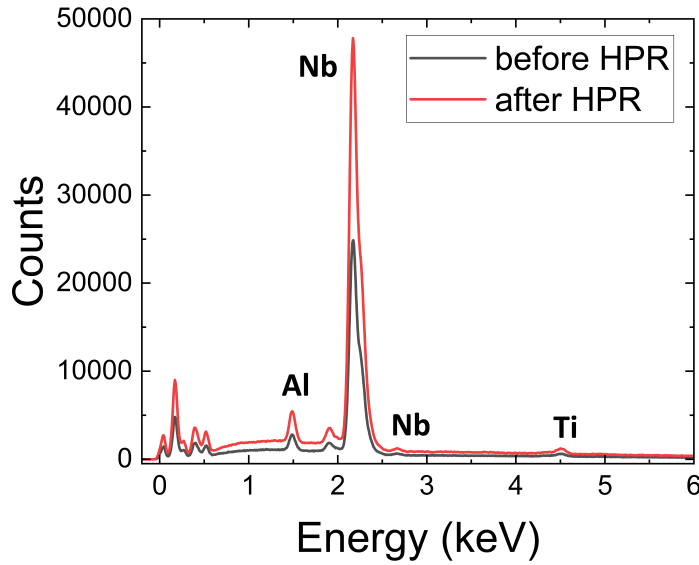

Figure B.4: EDX spectra taken before and after HPRs. The Al, Nb, and Ti peaks are visible.

B.4. Supplementary notes on XPS analysis in Section 7

B.4.1. Preliminary survey for element identification

A preliminary survey (pass energy of 50 eV and step size of 0.5 eV), for a binding energy (BE) ranging from 0 to 1200 eV is shown in Figure B.5, was performed to identify the elements present in the sample. Most elements have major photoelectron peaks below 1100 eV [169], thus a sweep up to 1200 eV is sufficient to identify all detectable elements. The measured survey clusters the observed peaks which correspond to the elements Nb, Ti, N, C, and O. No Al nor Si signal was detected in any of the measured spectra. Auger electrons were detected at binding energies above 900 eV. Note, that the as-deposited surface spectrum (green line) has a very low number of counts at the binding energies corresponding to Ti and Nb peaks. This is due to an inadequate setup alignment, likely adjusted based on the carbon peak instead of titanium or niobium.
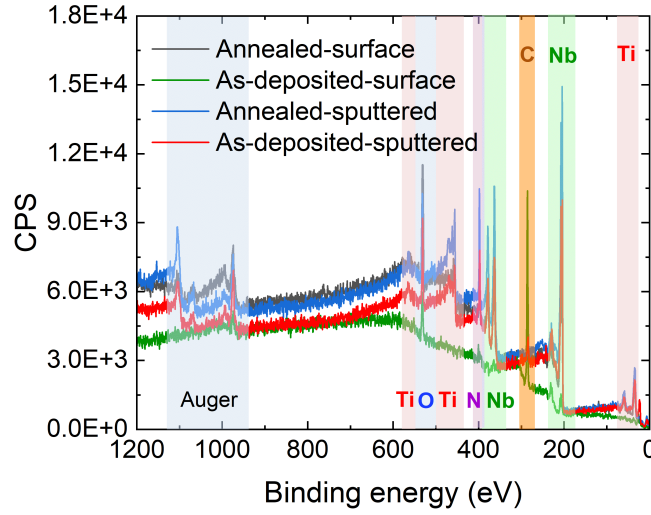

Figure B.5: Surface and sputtered XPS spectra, both in as-deposited and annealed states. Ranging from 0 to 1200 eV for element identification. Highlighted areas mark the detected peaks corresponding to Ti, Nb, N, C, O, and Auger electrons. Note the weak as-deposited surface survey signal (green line) due to a inadequate sample alignment.

B.4.2. Surface evaluation

It is well known that NbTiN surface oxidised when expose to air. As for NbN and TiN, the oxidation is a continuous substitution of nitrogen by oxygen [113]. This results in a mixture of Nb and Ti oxides and oxynitrides [113, 114, 116]. Oxides growth might not be planar; instead, oxides might serrate the metal surface on the nm scale. The serration was found to be smaller for hard NbTiN than for the soft Nb [116]. Angle-resolved XPS (ARXPS) studies concluded that Nb_2O_5 and TiO_2 build up on the surface—TiO_2 at the outer surface [113]—and the oxynitrides are sandwiched between the surface oxide and the bulk nitride [113, 116]. However, no real interface is built between the different compositions [113]. The

evaluation of the XPS spectra conducted at the surface of the as-deposited and annealed samples is presented here. Figure B.6 shows the high-resolution spectra of O 1s and C 1s. Both signals indicate common surface contamination, resulting from storage, handling, and water adsorption [117, 248, 249], which were satisfactorily removed by ion bombardment sputtering. No titanium carbide [163, 250, 251] or niobium carbide [90, 117] contributions are identified. TiO_2, Nb_2O_5 and oxynitrides are visible in the high-resolution spectra of O 1s and Ti 2p and Nb 3d respectively (see Figure B.7). The O 1s peak confirms the presence of metal oxides, (attributed to Nb and Ti oxides [90, 162]), metal oxynitrides [90]. The deconvolution of the Ti 2p peak indicates the presence of TiO_2 [113–115, 162], TiN_xO_y [162], and TiN. The Nb 3d peak is deconvoluted into four spin-orbit doublets, Nb_2O_5[113, 117, 164, 166], $Nb_2N_{2-X}O_{3+X}$ [113, 116], NbON [90, 113, 116, 164], and NbN [113, 116, 164, 165]. The N 1s peak is deconvoluted into a metal nitride, which coincides with NbN [113, 115] and TiN [162], and an oxynitride (TiN_xO_y [117, 162]) contributions. Lastly, it is visible in Figures B.6 and B.7 that annealing increases the surface oxidation of NbTiN films, in particular enhances TiO_2 (see Table B.2). This is further discussed in Appendix B.4.4.
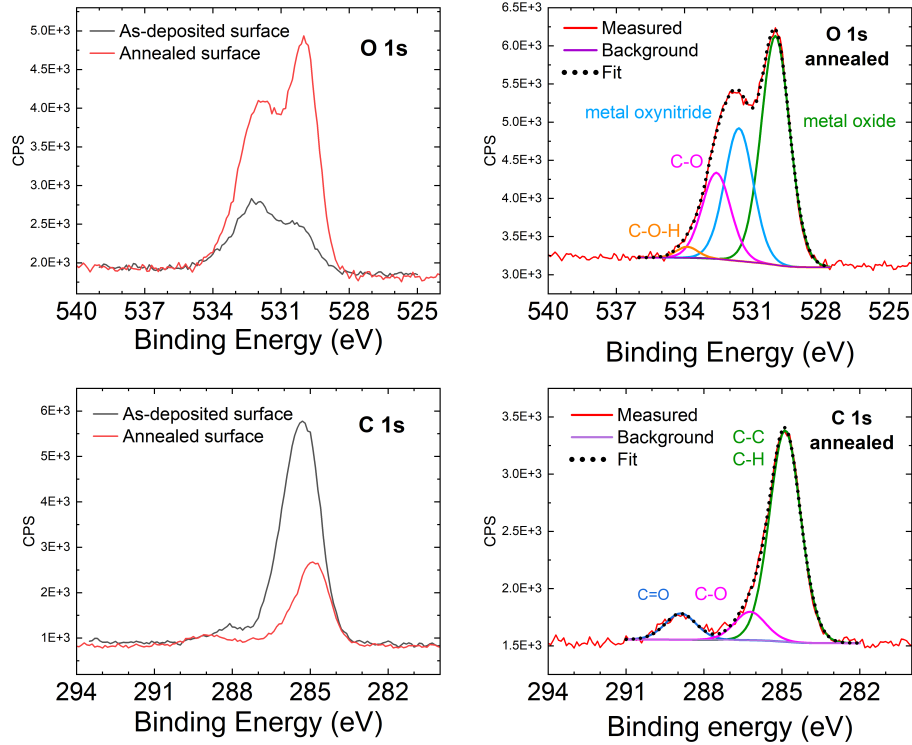

Figure B.6: Surface XPS high-resolution lines: O 1s and C 1s. The *left* column contrast as-deposited and annealed spectra. While the *right* column presents the deconvolution of the annealed lines. The presence of common surface contaminations is evident.
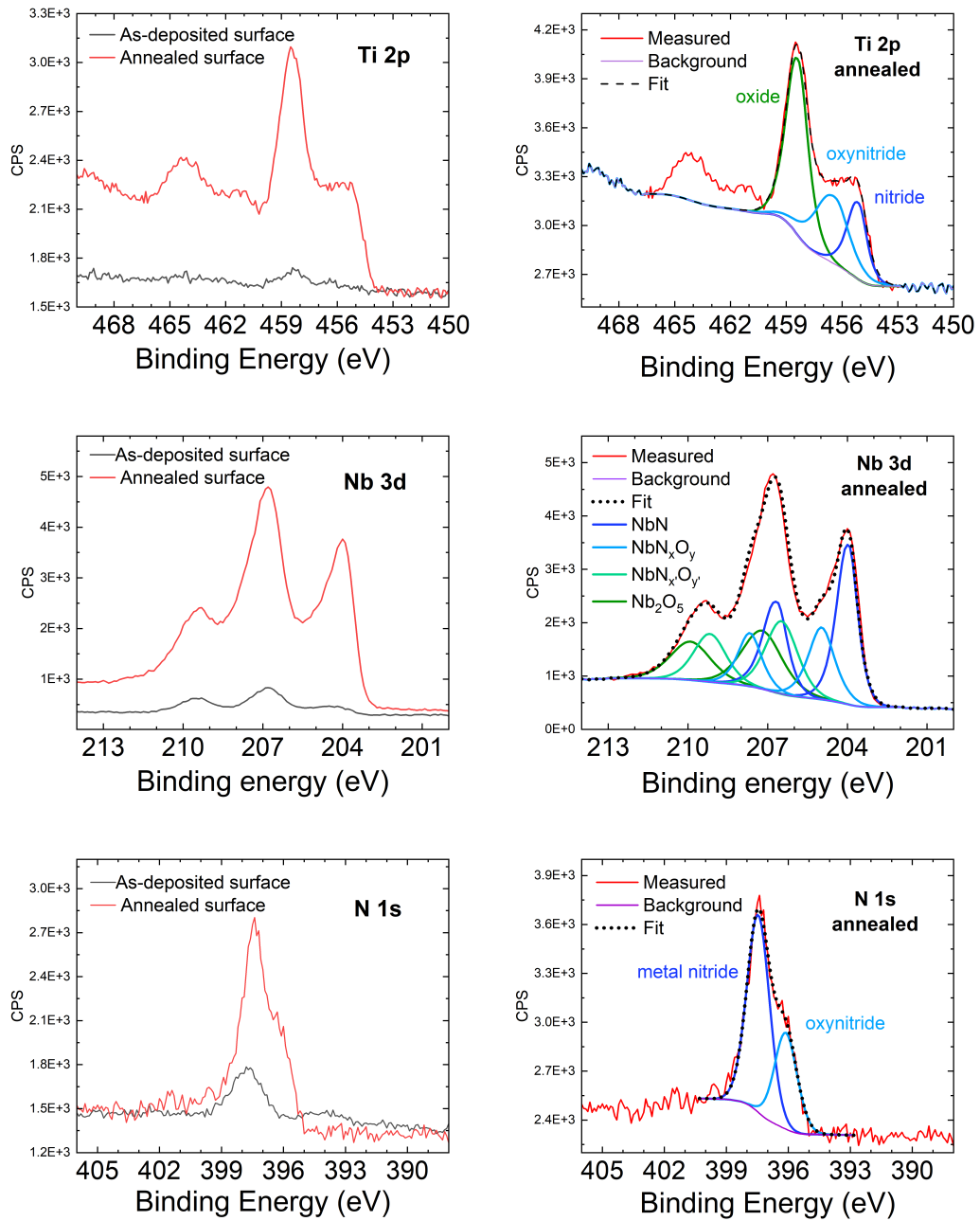
Figure B.7: Surface XPS high-resolution lines: Ti 2p, Nb 3d, and N 1s. The *left* column contrast as-deposited and annealed spectra. While the *right* column presents the deconvolution of the annealed lines. Nitrides, oxynitrides, and oxides of Ti and Nb are detected. Annealing increases both the surface oxidation (significantly for Ti) and the nitride character of the film.

B.4.3. Details of the XPS high-resolution peaks deconvolution

The details of the XPS analysis presented in Section 7 are given here. Table B.1 lists the binding energies assigned to each contribution identified in the deconvolution of the XPS high-resolution signals.

Table B.1: Binding energies associated with contributions in the deconvoluted XPS signals

O 1s	$W_{surface}$	$W_{sputter}$	$WSF_{surface}$	$WSF_{sputter}$
O-Nb/Ti	530.2	–	530.0	–
Nb-oxynitride	–	531.4	531.6	531.4
Ti-oxynitride	–	532.7	–	532.8
C-O	532.1	–	532.6	–
C-O-H	533.9	–	533.9	–
C 1s	$W_{surface}$	$W_{sputter}$	$WSF_{surface}$	$WSF_{sputter}$
C-Nb/Ti	–	282.3	–	–
C-C	285.2	284.8	284.9	–
C-O-C	286.0	–	286.2	–
O-C=O	288.1	–	288.9	–
N 1s	$W_{surface}$	$W_{sputter}$	$WSF_{surface}$	$WSF_{sputter}$
Ti-oxynitride	394.1	–	396.1	–
N-Nb/Ti	398.1	397.2	397.5	397.9
Nb-oxynitride	–	399.5	–	398.8
Ti 2p$_{3/2}$	$W_{surface}$	$W_{sputter}$	$WSF_{surface}$	$WSF_{sputter}$
TiN	–	455.0	455.1	455.5
TiN$_x$O$_y$	456.3	455.9	456.4	456.5
TiO$_2$	458.2	–	458.4	–
Nb 3d$_{5/2}$	$W_{surface}$	$W_{sputter}$	$WSF_{surface}$	$WSF_{sputter}$
NbN	204.3	203.9	204.0	203.9
NbN$_x$O$_y$	–	204.6	–	204.6
NbON	205.2	–	205.0	–
NbN$_{x'}$O$_{y'}$	–	205.9	–	206.0
Nb$_2$N$_{2-x}$O$_{3+x}$	206.7	–	206.5	–
Nb$_2$O$_5$	207.6	207.6	207.2	207.5

After sputtering, the binding energies of the oxynitride contributions attributed for the Nb 3d signal shift slightly. It may be attributed to defects introduced by Ar ion bombardment.

Lastly, Table B.2 summarise the relative concentration, calculated from the peak areas, for each of the contributions assigned for the spectra listed in Table B.1. Note that for some high-resolution peaks, a single contribution is assigned where it could potentially be split into two, one for Nb and one for Ti. This applies to the metal-oxide contribution in the O 1s peak, the metal-nitride contribution in the N 1s peak, and the metal-carbide contribution in the C 1s peak.

Table B.2: Relative concentrations for each constituent identified in the XPS spectra. The quantification has been obtained from the relative peak areas. In the case of Ti 2p line, the total peak area was considered and the satellites were not included.

	Surface		After ion bombardment	
O 1s	As-deposited (W)	Annealed (WSF)	As-deposited (W)	Annealed (WSF)
Metal-oxide	32.9	50.2	–	–
NbN_xO_y	–	29.1	69.2	72.0
TiN_xO_y	–	–	30.8	28.0
C-O	58.8	18.9	–	–
C-O-H	8.3	1.8	–	–
C 1s	As-deposited (W)	Annealed (WSF)	As-deposited (W)	Annealed (WSF)
C-C/C-H	67.5	79.5	90.3	–
O-C=O	6.1	9.9	–	–
C-O-C	26.4	10.7	–	–
C-Metal	–	–	9.7	–
N 1s	As-deposited (W)	Annealed (WSF)	As-deposited (W)	Annealed (WSF)
TiN_xO_y	30.9	32.8	–	–
Metal-nitride	69.1	67.2	84.3	79.9
NbN_xO_y	–	–	15.7	20.1
Ti 2p	As-deposited (W)	Annealed (WSF)	As-deposited (W)	Annealed (WSF)
TiN	–	19.8	45.2	64.5
TiN_xO_y	18.7	30.1	54.8	35.5
TiO_2	81.3	50.1	–	–
Nb 3d	As-deposited (W)	Annealed (WSF)	As-deposited (W)	Annealed (WSF)
NbN	20.2	34.5	37.6	43.4
NbN_xO_y	13.7	19.5	26.3	31.9
$NbN_{x'}O_{y'}$	57.3	22.9	19.7	10.6
Nb_2O_5	8.8	23.1	16.3	14.1

Table B.3 includes the elemental relative concentrations measured at the surface of the samples, as-deposited and annealed. The most evident observation is the presence of surface pollution and oxidation. Moreover, annealing may cause carbon outgassing, further surface oxidation, and enhance of the nitride character of the NbTiN film. Finally, the concentrations listed for the as-deposited sample, may be taken with caution. It can be observed in its high-resolution spectra and initial survey (Figures B.7 and B.5 in Appendix B.4), that the setup alignment for this measurement was incorrect, likely optimised the carbon signal. As a result, very low intensities were obtained for the major interest elements.

Table B.3: Quantitative surface analysis of the elemental composition of as-deposited and annealed samples.

% Atomic	As-deposited	Annealed
Oxygen	10.2	33.6
Carbon	83.4	33.0
Nitrogen	4.8	14.1
Titanium	0.2	4.5
Niobium	1.4	14.9

B.4.4. Additional XPS measurements

Six niobium-coated samples have been surface evaluated by XPS at the Institute of Solid State Physics Surface Physics from Universität Bremen. The aim is to evaluate both nitrides, NbTiN and NbN, as well as, the effect on them of the two different post-deposition thermal treatments, RTA and STA. The six samples include AlN-NbTiN and AlN-NbN multilayers in their as-deposited state and after RTA and STA procedures.The analysis conducted is less elaborate than the one in Section 7. However, some conclusions can still be drawn.

Firstly, the presence of a tiny fluorine line is appreciable in the survey of the six samples (see Figure B.8 *left*). The fluorine originates most likely from the perfluorelastomer o-ring used for the sealing of the PEALD chamber, which might be deteriorated (see Appendix A.1) and thus, fluorine may be incorporated into the films during deposition.

By comparing AlN-NbTiN and AlN-NbN multilayers, it is eit is evident that the NbTiN layer contains more nitrogen than NbN (see Figure B.8 *right*). It was observed that annealing may cause nitrogen desorption, which may be reduced or suppressed by the presence of titanium in the film. Additionally, annealing enhances the surface oxidation, which is observed to be more more pronounced for titanium. The same observation was extracted from the other XPS analysis. Differences between RTA and STA procedures are observed, but a detailed peak analysis would be required to draw further conclusions.
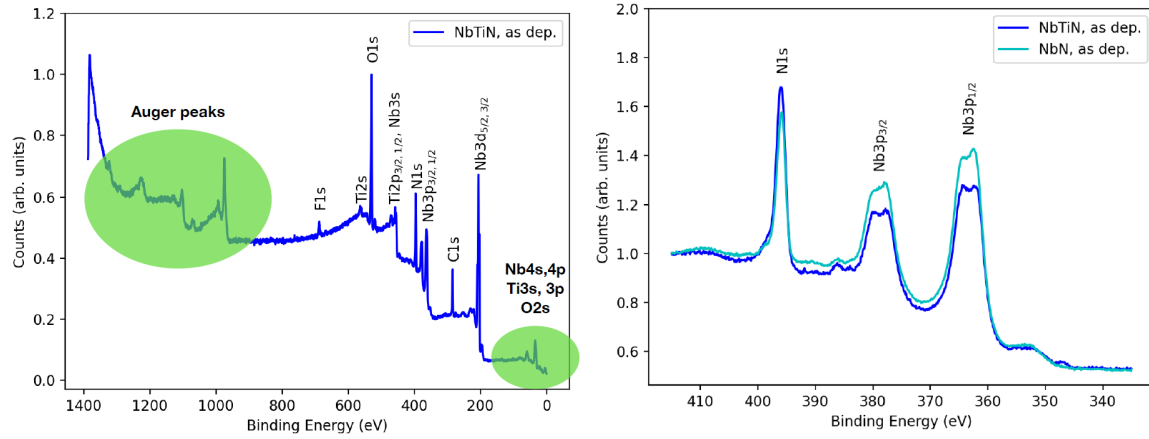
Figure B.8: Surface XPS analysis. *Left:* Binding energy sweep ranging from 0 to 1400 eV for the identification of the elements present in the sample. Note the small fluorine peak. *Right:* XPS spectra for the N 1s and Nb 3d lines for AlN-NbTiN and AlN-NbN multilayers, both in the as-deposited state.